



# City Research Online

## City, University of London Institutional Repository

---

**Citation:** Zimos, D.K. (2017). Modelling the Post-Peak Response of Existing Reinforced Concrete Frame Structures Subjected to Seismic Loading. (Unpublished Doctoral thesis, City, University of London)

This is the accepted version of the paper.

This version of the publication may differ from the final published version.

---

**Permanent repository link:** <https://openaccess.city.ac.uk/id/eprint/18531/>

**Link to published version:**

**Copyright:** City Research Online aims to make research outputs of City, University of London available to a wider audience. Copyright and Moral Rights remain with the author(s) and/or copyright holders. URLs from City Research Online may be freely distributed and linked to.

**Reuse:** Copies of full items can be used for personal research or study, educational, or not-for-profit purposes without prior permission or charge. Provided that the authors, title and full bibliographic details are credited, a hyperlink and/or URL is given for the original metadata page and the content is not changed in any way.



School of Mathematics, Computer Science and Engineering  
Research Centre for Civil Engineering Structures

PhD in Structural Engineering

MODELLING THE POST-PEAK RESPONSE OF EXISTING  
REINFORCED CONCRETE FRAME STRUCTURES SUBJECTED  
TO SEISMIC LOADING

by

**Dimitrios K. Zimos**

Dissertation submitted in fulfilment of the requirements for the award of  
DOCTOR OF PHILOSOPHY

October 2017



# Table of Contents

---

Table of Contents .....	iii
List of Tables .....	vi
List of Figures .....	vii
Acknowledgements.....	xix
Declaration.....	xx
Abstract.....	xxi
Chapter 1: Introduction .....	1
1.1 Background and Motivation .....	1
1.2 Objectives & Scope .....	2
1.3 Thesis Organisation.....	3
Chapter 2: Literature Review .....	7
2.1 Collapse of R/C Structures .....	7
2.2 Post-Peak Response of R/C Members.....	9
2.3 Modelling of R/C Members.....	21
PART I: INVESTIGATION OF THE POST-PEAK RESPONSE OF SHEAR-DEFICIENT R/C MEMBERS..	43
Chapter 3: Database Compilation.....	45
3.1 Descriptive Statistics .....	45
3.2 Data Collection and Processing.....	48
3.2.1 P- $\delta$ Correction.....	48
3.2.2 Critical Shear Crack Angle .....	51
3.2.3 Descending Branch .....	54
3.2.4 Displacement at Onset of Axial Failure.....	54
3.2.5 Load Control, Experimental Set-up and Uncertainty.....	55
Chapter 4: Empirical relationships for key shear response parameters.....	57
4.1 Conceptual Basis .....	57
4.2 Critical Shear Crack Angle .....	59
4.3 Post-Peak Response .....	65
4.4 Onset of Axial Failure .....	75
Chapter 5: Simultaneous Shear and Axial Failure.....	81

5.1	Dataset and Parameter of Interest.....	82
5.2	Assessment of Existing Observations .....	82
5.3	Proposed Criteria.....	84
5.4	Evaluation of Predictive Models.....	86
PART II: EXPERIMENTAL PROGRAMME.....		93
Chapter 6: Design of Experimental Programme.....		95
6.1	Conceptual Design.....	95
6.2	Design of Test Specimens .....	98
6.3	Test Set-up, Loading and Instrumentation.....	100
6.4	Numerical Blind Predictions .....	106
6.5	Fabrication of Specimens .....	111
6.6	Material Properties.....	114
Chapter 7: Experimental Results .....		117
7.1	Damage Propagation .....	117
7.2	Lateral Response .....	124
7.3	Axial Response.....	130
7.4	Deformation Analysis .....	134
7.5	Shear Failure Localisation.....	140
7.6	Stiffness .....	144
7.7	Energy Dissipation .....	147
7.8	Lash.....	147
7.9	Repeatability.....	149
7.10	Effect of Vertical Load Variation.....	150
PART III: BEAM-COLUMN ANALYTICAL MODEL.....		153
Chapter 8: Description and Implementation of Analytical Model .....		155
8.1	Hysteretic Shear Model .....	155
8.2	Beam-column Model Formulation .....	159
8.3	Software Implementation .....	164
Chapter 9: Verification of the Model .....		171

9.1	Analytical prediction accuracy .....	171
9.2	Flexure-shear Critical Specimens .....	171
9.2.1	Specimen-1 .....	171
9.2.2	FSC_1.....	175
9.2.3	C-2.....	178
9.3	Shear Critical Specimens.....	181
9.3.1	SC3 .....	181
9.3.2	SC_1 .....	183
9.4	Frame Specimens .....	186
9.4.1	Frame 1.....	186
9.4.2	Frame 2 .....	191
9.5	Specimens with Increasing Axial Load .....	196
Chapter 10:	Conclusions and Future Work.....	203
10.1	Summary and Conclusions .....	203
10.2	Recommendations for Future Work .....	212
Appendix A:	Database of R/C Column Tests .....	215
Appendix B:	Estimation of Critical Shear Crack Angle from Photographic Evidence.....	221
Appendix C:	Specimen Design Drawings.....	225
Appendix D:	Actual hysteretic response and smoothing.....	229
List of References	.....	233

## LIST OF TABLES

---

Table 3-1: Main specimen characteristics of the database.....	45
Table 4-1: Summary of the main statistics of accuracy and variation of Eq. 4-6 to 4-14.....	72
Table 4-2: Datasets and minimum and maximum limits of main design parameters defining the range of application of the proposed relationships. ....	72
Table 5-1: Comparison statistics of the predictive models against the experimentally observed values.....	88
Table 5-2: Confusion matrices of the predicted values of the empirical models (plus the classification criterion) compared to the observed values of the database. ....	89
Table 5-3: Comparison statistics of the predictive models' classification capabilities based on the experimentally observed values.....	90
Table 6-1: Flexure- and shear-controlled resistance (kN) predicted for each specimen set, based on M- $\phi$ analysis and various shear strength expressions. ....	99
Table 6-2: Schedule of specimen casting and testing. ....	112
Table 6-3: Concrete mix materials per batch (kg) and per cubic metre (kg/m <sup>3</sup> ).....	113
Table 6-4: Compressive strength of concrete samples for each specimen.....	115
Table 6-5: Flexure- and shear-controlled resistance (kN) predicted for each specimen set, based on M- $\phi$ analysis and various shear strength expressions. ....	115
Table 7-1: Evolution of crack widths in specimen FSC_1. ....	118
Table 7-2: Evolution of crack widths in specimen FSC_2. ....	118
Table 7-3: Evolution of crack widths in specimen FSC_3. ....	119
Table 7-4: Evolution of crack widths in specimen SC_1. ....	119
Table 7-5: Evolution of crack widths in specimen SC_2. ....	119
Table 7-6: Evolution of crack widths in specimen SC_3. ....	119
Table 7-7: Displacement ductilities of specimens at various levels. ....	126
Table 9-1: Accuracy measures of the analyses of Specimen-1, FSC_1 and C-2.....	175
Table 9-2: Accuracy measures of the analyses of SC3 and SC_1.....	183
Table 9-3: Accuracy measures of the analyses of Frame 1 and Frame 2. ....	190
Table 9-4: Accuracy measures of the analyses of specimens SC_2, SC_3, FSC_2 and FSC_3. ..	198
Table A-1: Specimens contained in the database, original publication and some of their most important characteristics. ....	215

## LIST OF FIGURES

---

Figure 2-1: (a) Specimen details and (b) test set-up. (Lejano et al. 1995).....	10
Figure 2-2: Deformation components of specimen C-2's response. (Lejano et al. 1995) .....	11
Figure 2-3: (a) Specimen-1 design and (b) test set-up. (Sezen & Moehle, 2006) .....	12
Figure 2-4: (a) Specimen design and (b) test set-up. (Ousalem et al. 2002).....	14
Figure 2-5: (a) Specimen design and (b) test set-up (Yoshimura & Yamanaka, 2000). (c) Specimen design (Yoshimura & Nakamura, 2002). (d) Design of specimen No. 1 (Yoshimura et al., 2003). (e) Test set-up (Nakamura & Yoshimura 2002). .....	16
Figure 2-6: Design details of (a) square specimens with aspect ratio of 2.4, (b) square specimens with aspect ratio of 1.7, (c) rectangular specimens with aspect ratio of 1.7. (d) Test set-up. (Tran, 2010) .....	18
Figure 2-7: Response of specimen 2 in terms of (a) lateral load vs. lateral drift, and (b) axial strain vs. axial force. (Matchulat, 2009).....	21
Figure 2-8: (a) Schematic representation of member-type model, and (b) shear hysteretic model. (Pincheira et al., 1999) .....	24
Figure 2-9: (a) Shear monotonic envelope, and (b) shear hysteresis rules. (Sezen & Chowdhury, 2009) .....	24
Figure 2-10: Fibre element scheme of beam element. (Spacone et al., 1996).....	25
Figure 2-11: (a) Sub-elements composing the beam element, and (b) hysteretic shear model. (Filippou et al., 1992) .....	25
Figure 2-12: (a) Fibre element scheme, and (b) truss idealisation of a beam segment for identification of shear monotonic response. (Ranzo & Petrangeli, 1998).....	26
Figure 2-13: (a) Possible shear envelopes, and (b) shear hysteretic model. (Marini & Spacone, 2006) .....	26
Figure 2-14: (a) Beam-column element in series with zero-length springs, and (b) hysteretic laws for zero-length springs. (Baradaran-Shoraka & Elwood, 2013) .....	27
Figure 2-15: Numerical localisation in force-based elements in the case of softening response. (Coleman & Spacone, 2001) .....	28
Figure 2-16: Example of numerical localisation (non-objective response) in the case of softening response. (Calabrese et al., 2010).....	28
Figure 2-17: R/C frame response with zero strain-hardening (a) without regularisation (non-objective response), and (b) with regularisation (objective response). (Coleman & Spacone, 2001) .....	29
Figure 2-18: The modified compression-field theory for membrane elements. (Vecchio & Collins, 1986) .....	30

Figure 2-19: (a) Shear spring in series with lumped or distributed inelasticity beam-column element, and (b) shear backbone curve and hysteretic laws. (LeBorgne & Ghannoum, 2013)	31
Figure 2-20: Shear hysteresis model. (Ozcebe & Saatcioglu, 1989)	31
Figure 2-21: Examples of cyclic strength degradation as a function of (a) increasing inelastic displacement, and (b) repeated cyclic displacement. (ATC, 2009)	32
Figure 2-22: Example of in-cycle strength degradation. (ATC, 2009)	32
Figure 2-23: Hysteretic response for systems subjected to two different loading protocols, (a, b) one with many cycles with a small displacement step, and (c, d) one with few initial cycles and a pulse-type displacement at the end. (a, c) The first system models only cyclic strength degradation, (b, d) while the second only in-cycle degradation. (ATC, 2009)	33
Figure 2-24: Concentration of damage after the onset of shear failure. (Elwood & Moehle, 2005a)	34
Figure 2-25: Mechanism at the onset of axial failure assumed by (a) Uchida & Uezono (2003), and (b) Ousalem & Kabeyasawa (2006)	37
Figure 2-26: Distinction between the (a) undisturbed (B-type), and (b) disturbed (D-type) region of a specimen, according to the shear cracks that are developed. (c) The most common case is a combination of both along the member. (Kim & Mander 1999)	40
Figure 3-1: Distribution of specimens' (a) concrete compressive strength, (b) longitudinal reinforcement yield strength, (c) transverse reinforcement yield strength, (d) axial load ratio, (e) longitudinal reinforcement ratio, and (f) transverse reinforcement ratio, in the database	46
Figure 3-2: Distribution of (a) aspect ratio, and (b) hoop spacing over effective depth, in the database	47
Figure 3-3: Distribution of (a) test configuration type, and (b) hoop type, in the database	47
Figure 3-4: Distribution of loading type in the database	47
Figure 3-5: Column test configuration types. (Berry et al., 2013)	47
Figure 3-6: Hoop configuration types. (Berry et al., 2013)	48
Figure 3-7: (a) Cantilever specimen undergoing constant vertical and cyclic lateral loading; its bending moment distribution (b) following the deflection shape of the specimen, or (c) with linear distribution simplifying assumption	49
Figure 3-8: Bending moment - storey drift relationship for a ductile sub-frame with and without P- $\delta$ . (Paulay, 1978)	49
Figure 3-9: Indicative response of an R/C element, upon which three different axial loads are applied	50
Figure 3-10: Different P- $\delta$ configuration cases (Berry et al., 2013)	51

Figure 3-11: Indicative extraction of critical shear crack angle from experimental photographic documentation: specimens by (a) Umehara & Jirsa (1982), and (b) Nakamura & Yoshimura (2014).....	53
Figure 3-12: Indicative extraction of descending branch curve from experimental data (Umehara & Jirsa, 1982).....	54
Figure 4-1: (a) Illustrative sketch of a shear-damaged column after the onset of shear failure. (b) Image of an actual experimental test of an axially failed shear-deficient R/C column (Wibowo, 2013).....	57
Figure 4-2: Shear crack angles measured experimentally against those calculated using the predictive models of (a) Chang (1993), (b) Kim & Mander (1999), (c) Ousalem et al. (2003), and (d) Elwood & Moehle (2005a).....	59
Figure 4-3: Correlation of the measured angle with (a) axial load ratio, (b) transverse reinforcement ratio, (c) longitudinal reinforcement ratio, (d) aspect ratio, (e) hoop spacing over effective depth, and (f) maximum average shear stress, divided into shear (S) and flexure-shear (FS) critical specimens.....	61
Figure 4-4: The (idealised) effect of aspect ratio on the critical shear crack angle. Fictitious column with increasing aspect ratio from left to right ( $(L_s/d)_5 > (L_s/d)_4 > \dots > (L_s/d)_1$ ) and the corresponding expected cracking (top). Pictures of specimens roughly corresponding to the above aspect ratios and failure types (Shear, Flexure-Shear and Flexural) (bottom); from left to right the specimens are: 3M (Yoshimura & Nakamura, 2002), S100 (Nakamura & Yoshimura, 2014), No. 6 (Yoshimura et al., 2003), Specimen 4 (Sezen, 2000) and BG-5 (Girra & Saatcioglu, 1996).....	63
Figure 4-5: Correlation of aspect ratio with maximum average shear stress in flexure-shear critical elements.....	63
Figure 4-6: Shear crack angles measured experimentally against the ones predicted by Eq. 4-2. ....	65
Figure 4-7: Critical shear crack angle predicted by Eq. 4-2 along the range of potential axial load and transverse reinforcement ratios, for (a) shear, and (b) flexure-shear critical specimens...	65
Figure 4-8: (a) Ratio of descending branch slopes in two “directions” of the response of the database specimens. (b) Curvature of the descending branch of the response of flexure-shear critical (FS) and shear critical (S) specimens of the database.....	67
Figure 4-9: Correlation of slope of the linear post-peak branch of the AS dataset with (a) axial load ratio, (b) longitudinal reinforcement ratio, (c) transverse reinforcement ratio normalised to the confined concrete area (stirrup spacing multiplied by the confined section width), and (d) average longitudinal bar diameter normalised to the effective depth. ....	70

Figure 4-10: Values of the post-peak descending branch slopes (dimensionless) measured experimentally against the ones predicted using Eq. 4-6 (a) to 4-14 (i) (from left to right and top to bottom). ..... 73

Figure 4-11: Descending branch slope ( $S_{pp}$ ) predicted by Eq. 4-6 along the range of potential longitudinal reinforcement ratios over relative confined concrete area ( $\rho_l/a_{conf}$ ), for different transverse reinforcement ratios over confined concrete area ( $\rho_{w,conf}$ ), for axial load ratios ( $v$ ) of (a) 0.2 and (b) 0.5. .... 75

Figure 4-12: Shear strength at the onset of axial failure normalised to the maximum shear strength for the specimens of the database. .... 75

Figure 4-13: Existing predictive relationships for the lateral displacement at the onset of axial failure applied in this database, against measured displacements: (a) Elwood & Moehle (2005a), (b) Zhu et al. (2007), (c) Yoshimura (2008), and (d) Ousalem et al. (2004). .... 76

Figure 4-14: Correlation of total post-peak shear strain at the onset of axial failure ( $\gamma_{t,pp}$ ) with (a) axial load ratio based on the capacity of the longitudinal reinforcement,  $v_l$ , (b) longitudinal reinforcement ratio divided by the percentage of confined area,  $\rho_l/\alpha_{conf}$ , (c) transverse reinforcement ratio multiplied by its yield strength,  $\rho_w \times f_{yw}$ , and (d) maximum average shear stress,  $\tau_{max}/vf_c$ . .... 77

Figure 4-15: Measured total post-peak shear strain at the onset of axial failure against the predicted one using Eq. 4-16. .... 79

Figure 4-16: Total post-peak shear strain predicted by Eq. 4-16 along the range of longitudinal reinforcement ratios (over confined area) and transverse reinforcement ratios (over confined concrete area), for longitudinal reinforcement axial load ratios of 0.2 (top) and 0.5 (bottom) and maximum shear stress of 0.25 (left) and 0.75 (right). .... 79

Figure 5-1: Indicative sketches of cyclic envelopes of the hysteretic lateral response of columns (a) failing axially after shear failure, or (b) failing in simultaneous shear and axial failure. (c) Example of specimen failing in simultaneous shear and axial failure (Matchulat, 2009). .... 81

Figure 5-2: Correlation of  $IDR_{,pp}$  with the longitudinal reinforcement axial load ratio. Some points are shown with arrows, indicating accurately one of their coordinates and that the other one is higher than the maximum of the range considered on the respective axis. .... 83

Figure 5-3: Values of  $IDR_{,pp}$  depicted against axial load ratio and transverse reinforcement ratio. Values greater than 1% are in grey colour. .... 84

Figure 5-4: Values of  $IDR_{,pp}$  depicted against longitudinal reinforcement axial load ratio and transverse reinforcement ratio over normalised hoop spacing. Values greater than 1% are in grey colour. Some points are shown with arrows, indicating accurately one of their coordinates and that the other one is higher than the maximum of the range of the respective axis. .... 85

Figure 5-5: Schematic representation of displacement derived from Elwood & Moehle model. .....	87
Figure 5-6: $IDR_{pp}$ predicted by the Elwood & Moehle model (2005a; 2005b) against longitudinal reinforcement axial load ratio and transverse reinforcement ratio over normalised hoop spacing. .....	88
Figure 5-7: $IDR_{pp}$ predicted by the Zimos et al. model against longitudinal reinforcement axial load ratio and transverse reinforcement ratio over normalised hoop spacing.....	89
Figure 6-1: Mechanism of axial load increase of columns neighbouring an axially failing column. .....	95
Figure 6-2: Design of (a) shear critical (SC) and (b) flexure-shear critical (FSC) specimens (lengths in m; bar and pipe diameters in mm). ....	98
Figure 6-3: Two-zone column classification criterion of failure type (Zhu et al., 2007). The values for SC and FSC specimens are shown with red on the diagram. ....	100
Figure 6-4: Experimental set-up shown schematically. ....	101
Figure 6-5: (a,b) Experimental set-up, and (c,d) vertical and horizontal actuators.....	102
Figure 6-6: Lateral displacement (left vertical axis) and vertical force (right vertical axis) histories of (a) reference specimens FSC-1 and SC-1, (b) specimens FSC-2 and SC-2, and (c) specimens FSC-3 and SC-3. ....	104
Figure 6-7: (a) Installation of strain gauges on the reinforcing bars, (b) their final arrangement, and (c) connecting them to the corresponding sensors. Draw-wire sensors measuring: (d) lateral displacement at the top of the column, (e) shear displacement, and (f) potential base uplift.	105
Figure 6-8: Instrumentation of the specimens: (a) draw-wire sensors and (b) strain gauges (drawn as circles on the respective rebars). ....	106
Figure 6-9: (a) Set-up for digital image correlation measurements, and (b) speckle pattern area on the front face of a specimen.....	106
Figure 6-10: Numerical 3D finite element model (concrete / reinforcement). ....	107
Figure 6-11: Response and failure modes (from ATENA analysis) of the (a) SC, and (b) FSC reference specimens.....	108
Figure 6-12: History of maximum tensile stress of longitudinal (red line) and transverse (blue line) reinforcement of the (a) SC, and (b) FSC reference specimens.....	109
Figure 6-13: Envelopes of flexural, bond-slip and shear sub-elements for the (a) SC, and (b) FSC specimens. ....	110
Figure 6-14: Comparison of obtained response for (a) SC, and (b) FSC reference specimens, according to the beam-column element (blue) and the 3D finite element analysis (red). ....	110
Figure 6-15: (a) Steel cage of FSC specimen, (b) completed, lubricated formwork, (c) steel cage placed inside the formwork prior to casting, and (d) casting and compaction of concrete.....	112

Figure 6-16: (a) Cast specimens just after concrete pouring, (b) curing of specimens inside formwork covered with wet cloth, (c,d) lifting and moving specimens inside the laboratory.	113
Figure 6-17: Shear critical (SC) and flexure-shear critical (FSC) specimens after construction.	114
Figure 6-18: (a) Concrete samples of all six specimens, and (b) a concrete sample under compression test.	115
Figure 6-19: Tensile response of ribbed B500C (a-c) $\varnothing$ 16 bars, and (d-f) $\varnothing$ 10 bars.	116
Figure 7-1: Example of crack width measurement (snapshot of SC3 at displacement level of +12 mm).	118
Figure 7-2: Damage state of specimens at displacement level of +12 mm.	120
Figure 7-3: Damage state of specimens at displacement level of +18 mm (besides FSC <sub>3</sub> , for which the second peak of +15 mm is included, right before its axial collapse).	121
Figure 7-4: Hysteretic response of bar elongation of (a, b) transverse and (c,d) longitudinal reinforcement against (a, c) lateral displacement and (b, d) force of specimen SC <sub>3</sub> .	123
Figure 7-5: Side view at the onset of axial collapse of (a) FSC <sub>2</sub> , (b) FSC <sub>3</sub> and (c) SC <sub>2</sub> .	123
Figure 7-6: State after the end of testing of specimens (a) FSC <sub>2</sub> , (b) SC <sub>2</sub> and (c) SC <sub>3</sub> .	124
Figure 7-7: Hysteretic response of specimens (a) FSC <sub>1</sub> , (b) FSC <sub>2</sub> , (c) FSC <sub>3</sub> , (d) SC <sub>1</sub> , (e) SC <sub>2</sub> and (f) SC <sub>3</sub> .	125
Figure 7-8: Side views of system of steel plates and bolts transferring the forces from the double-action horizontal actuator to the top of the specimen.	128
Figure 7-9 : Comparison of the maximum horizontal strength, for FSC and SC specimens.	128
Figure 7-10 : Comparison of experimental cyclic envelope with the ones predicted by codes as well as the proposed beam-column model (section 8), for (a) FSC <sub>1</sub> and (b) SC <sub>1</sub> .	129
Figure 7-11: Axial hysteretic response of specimens (a, b) FSC <sub>1</sub> , (c, d) FSC <sub>2</sub> , (e, f) FSC <sub>3</sub> ...	131
Figure 7-12: Axial hysteretic response of specimens (a, b) SC <sub>1</sub> , (c, d) SC <sub>2</sub> , (e, f) SC <sub>3</sub> ...	132
Figure 7-13: Vertical displacement of top of SC <sub>2</sub> at various displacement level peaks.	133
Figure 7-14: Comparison between shear displacement recorded by the Draw-Wire Sensors (DWS) and calculated via Digital Image Correlation (DIC) for specimens (a) SC <sub>1</sub> , and (b) FSC <sub>3</sub> .	135
Figure 7-15: Hysteretic response in terms of shear displacement of specimens (a) FSC <sub>1</sub> , (b) FSC <sub>2</sub> , (c) FSC <sub>3</sub> , (d) SC <sub>1</sub> , (e) SC <sub>2</sub> and (f) SC <sub>3</sub> .	136
Figure 7-16: Lateral displacement decomposition for (a, b) FSC <sub>1</sub> , (c, d) FSC <sub>2</sub> , and (e, f) FSC <sub>3</sub> in (left) absolute and (right) relative terms.	137
Figure 7-17: Lateral displacement decomposition for (a, b) SC <sub>1</sub> , (c, d) SC <sub>2</sub> , and (e, f) SC <sub>3</sub> in (left) absolute and (right) relative terms.	139
Figure 7-18: Lateral displacement decomposition for (a) FSC <sub>3</sub> , and (b) SC <sub>3</sub> , including the 'unaccounted for' component.	140

Figure 7-19: Lateral displacement decomposition for SC_2, including the bond-slip component, in (a) absolute and (b) relative terms. ....	140
Figure 7-20: Lateral displacement (in mm) profiles along the surface of specimen SC_1 from a displacement level of (a) 9 mm until (f) 24 mm.....	141
Figure 7-21: Lateral displacement (in mm) profiles along the surface of specimen SC_3 from a displacement level of (a) 9 mm until (f) 24 mm.....	142
Figure 7-22: Lateral displacement profiles along the centroidal axis of specimen (b) SC_2 (displacement levels +3 mm until +18 mm from left to right), and (c) FSC_3 (+3 mm until +15 mm from left to right). ....	143
Figure 7-23 : Horizontal displacement of the base of the specimens at each displacement level. ....	144
Figure 7-24: Lateral displacement secant stiffness for (a, b) FSC_1, (c, d) FSC_2, and (e, f) FSC_3 in (left) absolute and (right) relative terms. ....	145
Figure 7-25: Lateral displacement secant stiffness for (a, b) SC_1, (c, d) SC_2, and (e, f) SC_3 in (left) absolute and (right) relative terms. ....	146
Figure 7-26: Cummulative dissipated energy against displacement level for (a) FSC, and (b) SC specimens. ....	147
Figure 7-27: Recorded lash throughout experiments of (a) FSC, and (b) SC specimens. ....	148
Figure 7-28: Comparison of the first 9 cycles of the (a) FSC, and (b) SC specimens.....	149
Figure 7-29: (a) Experimentally obtained descending branch slopes of FSC and SC specimens. (b) Comparison of experimentally obtained against analytically predicted descending branch slopes of each specimen. ....	150
Figure 7-30: (a) Ultimate horizontal displacement reached by each specimen. (b) Comprarion of experimentally obtained and predicted values of ultimate horizontal displacement. ....	150
Figure 8-1: V- $\gamma$ primary curve of the proposed shear model (without shear-flexure interaction). ....	155
Figure 8-2: (a) Relationship between curvature ductility demand and strength of concrete shear resisting mechanisms (Mergos & Kappos, 2012). (b) Variation of shear resisting mechanisms (strut mechanism lumped with concrete mechanism); shear strain after shear cracking with curvature ductility demand in plastic hinge regions of R/C members (Mergos & Kappos, 2012). (c) Flexural primary curve and shear capacity in terms of member shear force and curvature ductility demand of the critical cross-section (left); shear (V - $\gamma$ ) primary curve before and after modelling shear-flexure (right) (Mergos & Kappos, 2013b). ....	156
Figure 8-3: Hysteresis rules after the onset of shear failure. ....	158

Figure 8-4: Finite element model: (a) geometry of R/C member; (b) beam–column finite element with rigid offsets; (c) flexural sub-element; (d) shear sub-element; (e) anchorage slip sub-element. (Mergos & Kappos 2012).....	161
Figure 8-5: (a) Flexural ( $M-\phi$ ) hysteretic model and (b) anchorage slip ( $M-\theta_{slip}$ ) hysteretic model. (Mergos & Kappos 2013b).....	161
Figure 8-6: (a) Reinforcing bar with 90° hook embedded in concrete; (b) steel stress distribution; (c) strain distribution; (d) bond stress distribution. (Mergos & Kappos 2012) .....	162
Figure 8-7: Spread inelasticity transition upon initiation of shear failure for: (a) a flexure-shear critical specimen, and (b) a shear critical specimen.....	164
Figure 8-8: Schematic representation of the implementation of in-cycle degradation.....	165
Figure 8-9: Algorithmic procedure for the implementation of in-cycle degradation inside the shear response sub-model. ....	166
Figure 8-10: Schematic representation of (a) the shear response with descending branch offset due to cyclic degradation and (b) the response with compensation for this offset. ....	167
Figure 8-11: Schematic representation of the influence of unloading stiffness of the other sub-models (left) simultaneously with in-cycle strength degradation of failed section (middle) on the shear force vs lateral displacement response (right). ....	167
Figure 8-12: Schematic representation of influence of reloading of the other sub-models (left) simultaneously with reloading of the failed section (middle) on the shear force - lateral displacement response (right).....	168
Figure 9-1: Comparison between the predicted response of Specimen-1 by the proposed model and the experimental one in terms of (a) shear force against lateral displacement, (b) shear displacement, (c) flexural displacement, and (d) anchorage slip displacement. (e) Displacement decomposition of the element’s lateral displacement components, and (f) flexural and shear inelastic zone lengths normalised to the clear member length, throughout the analysis.....	173
Figure 9-2: Comparison between the predicted response of Specimen-1 by the model proposed by Baradaran-Shoraka and Elwood (2013) and the experimental one in terms of (a) shear force against lateral drift ratio, (b) shear displacement over column height. ....	174
Figure 9-3: Comparison between the predicted response of FSC_1 by the proposed model and the experimental one in terms of (a) shear force against lateral displacement, and (b) shear displacement. (c) Decomposition of the element’s lateral displacement components throughout the analysis. (d) Comparison between predicted and experimentally obtained cumulative dissipated energy.....	176
Figure 9-4: Comparison between individual cycles of the predicted response of FSC_1 by the proposed model and the experimental one: (a, b) 3 <sup>rd</sup> cycle at +/- 15 mm, (c, d) 2 <sup>nd</sup> cycle at +/- 18	

mm, and (e, f) 1 <sup>st</sup> cycle at +/- 21 mm. (left) Total displacements and (right) shear displacements. .....	177
Figure 9-5: Comparison between the predicted response of C-2 by the proposed model and the experimental one in terms of (a) shear force against lateral displacement, (b) shear displacement and (c) flexural and bond-slip displacement; (d) cumulative dissipated energy throughout the experiment.....	179
Figure 9-6: Comparison between individual cycles of the predicted response of C-2 by the proposed model and the experimental one: (a, b) 2 <sup>nd</sup> cycle at +/- 5 mm, (c, d) 1 <sup>st</sup> cycle at +/- 6.5 mm, and (e, f) 1 <sup>st</sup> cycle at +/- 10 mm. (left) Total displacements and (right) shear displacements. .....	180
Figure 9-7: (a) Comparison between the predicted response of SC3 by the proposed model and the experimental one in terms of shear force against lateral displacement. (b)Decomposition of the element's lateral displacement components throughout the analysis.....	182
Figure 9-8: Comparison between the predicted response of SC_1 by the proposed model and the experimental one in terms of (a) shear force against lateral displacement, and (b) shear displacement. (c) Decomposition of the element's lateral displacement components throughout the analysis. (d) Comparison between predicted and experimental cumulative dissipated energy. .....	183
Figure 9-9: Comparison between individual cycles of the predicted response of SC_1 by the proposed model and the experimental one: (a, b) 1 <sup>st</sup> cycle at +/- 15 mm, (c, d) 1 <sup>st</sup> cycle at +/- 21 mm, and (e, f) 2 <sup>nd</sup> cycle at +/- 24 mm. (left) Total displacements and (right) shear displacements. .....	185
Figure 9-10: Frame 1 layout (dimensions in mm) and applied finite element model (Mergos & Kappos, 2012). .....	187
Figure 9-11: Comparison between response history of Frame 1 predicted by the proposed model and the experimental test in terms of (a) lateral displacement of the frame's first storey as well as (b) its base shear.....	187
Figure 9-12: Comparison between predicted response of Frame 1 by the proposed model and the experimental test in terms of (a) base shear against lateral displacement of the first storey of the frame and (b) shear force against lateral displacement of the middle column; (c) cumulative dissipated energy throughout the experiment. (d) Analytical prediction of shear force against local shear deformation, $\gamma$ , of top and bottom plastic hinges of the mid-column. .....	188
Figure 9-13: (a) Photographic documentation of the damage sustained by Frame 1 (Elwood & Moehle, 2008b); (b) predicted damage by the proposed model. ....	189

Figure 9-14: Comparison between the analytically predicted response of Frame 1 without considering shear failure and the experimental test in terms of (a) base shear against lateral displacement of the first storey of the frame, (b) shear force against lateral displacement of the middle column and (c) base shear history. .... 190

Figure 9-15: Comparison between response history of Frame 2 predicted by the proposed model and the experimental test in terms of (a) lateral displacement of the frame’s first storey as well as (b) its base shear. .... 192

Figure 9-16: Comparison between predicted response of Frame 2 by the proposed model and the experimental test in terms of (a) base shear against lateral displacement of the first storey of the frame, (b) shear force against lateral displacement of the middle column, and (c) cumulative dissipated energy throughout the experiment. (d) Analytical prediction of shear force against local shear deformation,  $\gamma$ , of top and bottom plastic hinges of the mid-column. .... 193

Figure 9-17: (a) Photographic documentation of the damage sustained by Frame 2 (Elwood & Moehle, 2008b); (b) predicted damage by the proposed model. .... 194

Figure 9-18: Comparison between response history predicted by the proposed model (Frame 2 low) and the experimental test in terms of (a) lateral displacement of the frame’s first storey as well as (b) its base shear. .... 194

Figure 9-19: Comparison between predicted response by the proposed model (Frame 2 low) and the experimental test in terms of (a) base shear against lateral displacement of the first storey of the frame and (b) shear force against lateral displacement of the middle column; (c) cumulative dissipated energy throughout the experiment. (d) Analytical prediction of shear force against local shear deformation,  $\gamma$ , of top and bottom plastic hinges of the mid-column. .... 195

Figure 9-20: Comparison between the predicted response of FSC\_2 by the proposed model and the experimental one in terms of (a) shear force against lateral displacement, and (b) shear displacement. (c) Decomposition of the element’s lateral displacement components throughout the analysis. (d) Comparison between predicted and experimental cumulative dissipated energy. .... 197

Figure 9-21: Comparison between the predicted response of FSC\_3 by the proposed model and the experimental one in terms of (a) shear force against lateral displacement, and (b) shear displacement. (c) Decomposition of the element’s lateral displacement components throughout the analysis. (d) Comparison between predicted and experimental cumulative dissipated energy. .... 198

Figure 9-22: Comparison between the predicted response of SC\_2 by the proposed model and the experimental one in terms of (a) shear force against lateral displacement, and (b) shear

displacement. (c) Decomposition of the element’s lateral displacement components throughout the analysis. (d) Comparison between predicted and experimental cumulative dissipated energy. ....	199
Figure 9-23: Comparison between the predicted response of SC_3 by the proposed model and the experimental one in terms of (a) shear force against lateral displacement, and (b) shear displacement. (c) Decomposition of the element’s lateral displacement components throughout the analysis. (d) Comparison between predicted and experimental cumulative dissipated energy. ....	200
Figure B-1: Cross-section of the rotated column and observed dimensions, instead of the actual ones.....	222
Figure B-2: Distortion of the column dimensions, due to the perspective; downwards (top), upwards (middle) and the common realistic case (bottom). ....	223
Figure C-1: As-built design drawings of sub-base. ....	225
Figure C-2: As-built design drawings of SC specimens.....	226
Figure C-3: As-built design drawings of FSC specimens.....	227
Figure D-1: Response of specimen FSC_1 without smoothing.....	224
Figure D-2: Response of specimen FSC_2 without smoothing.....	224
Figure D-3: Response of specimen FSC_3 without smoothing.....	225
Figure D-4: Response of specimen SC_1 without smoothing.....	225
Figure D-5: Response of specimen SC_2 without smoothing.....	226
Figure D-6: Response of specimen SC_3 without smoothing.....	226



## ACKNOWLEDGEMENTS

---

A doctoral project is a long and arduous endeavour. Although single-handedly performed, there are many persons, who contribute to a lesser or greater extent in their own way and ought to be duly acknowledged.

First and foremost, I would like to thank my first supervisor, Prof Andreas Kappos. His continuous guidance and support, his meticulousness, wisdom and foresight through all these years have been defining for the successful completion of my PhD. Working with him has been an inspiration and taught me a lot outside the narrow boundaries of doctoral work.

Additionally, my second supervisor, Dr Panagiotis Mergos, has been there every step of the way, supporting, helping and sharing his insights more than any PhD student could hope from a second supervisor and for that I am sincerely grateful.

The experimental part of this work would not have been a success, had it not been for my external supervisor, Dr Vassilis Papanikolaou. His grasp of problems before they even arise, his involvement atop an extremely busy workload, and his valuable pieces of advice are greatly appreciated.

I would also like to thank all the staff of the Laboratory of Reinforced Concrete and Masonry Structures, Aristotle University of Thessaloniki for their help in completing the tests successfully and timely.

I would also like to gratefully acknowledge the funding provided by City, University of London for the first three years of the project, through its Doctoral Studentship, and the partial funding by A.G. Leventis Foundation for the fourth year, through an Educational Grant.

I am very grateful to all my fellow PhD candidates and friends outside of the university for their love and support and for making these years an unforgettable experience. It would certainly not have been the same without each and every one of them.

Last and most importantly, I would like to thank from the bottom of my heart and dedicate this work to my beloved parents, sister and partner, without whose sustained psychological and emotional support this PhD would have certainly not come to fruition.

## DECLARATION

---

I grant powers of discretion to the University Librarian to allow this dissertation to be copied in whole or in part without further reference to me. This permission covers only single copies made for study purposes, subject to normal conditions of acknowledgements.

## ABSTRACT

---

Structural members of reinforced concrete (R/C) buildings designed according to older, less stringent seismic codes are often vulnerable to shear or flexure-shear failure followed by axial failure. Thus, such substandard R/C structures are susceptible to vertical collapse, which pertains to the exceedance of vertical resistance of columns and connecting beams and can lead to the whole structure – or a substantial part of it – undergoing collapse.

The largest database of shear and flexure-shear critical R/C columns cycled well beyond the onset of shear failure and/or up to the onset of axial failure is compiled and empirical relationships are developed for key parameters affecting the response of such members after the initiation of shear failure. A novel shear hysteresis model is proposed employing these relationships, based on experimental observations that deformations after the onset of shear failure tend to concentrate in a specific member region.

A computationally efficient finite element model of the member-type is proposed, using the above shear hysteretic model and combining it with displacements arising from flexural and bond-slip deformations to get the full lateral force-lateral displacement response. It accounts for the interaction between flexural and shear deformations inside the potential plastic hinges, the distribution of flexural and shear flexibility along the element, as well as the location and extent of post-peak shear damage, without relying on assumptions about the bending moment distribution and avoiding shortcomings of previous beam-column models pertinent to numerical localisation. Thus, the full-range hysteretic response of substandard R/C elements can be predicted up to the onset of axial failure subsequent to shear failure with or without prior flexural yielding, while simultaneously accounting for potential flexural and anchorage failure modes.

The proposed model is implemented in a finite element structural analysis software and its predictive capabilities are verified against quasi-static cyclic and shake-table test results of column and frame specimens. The model is shown to be sufficiently accurate not only in terms of total response, but more crucially in terms of individual deformation components. Overall, it is believed that the accuracy, versatility and simplicity of this model make it a valuable tool in seismic analysis of complex substandard R/C buildings.

An experimental investigation of shear and flexure-shear critical R/C elements is carried out with the aim of independently validating the beam-column model. Furthermore, an opportunity is provided to verify the model's underlying assumptions, which is of paramount importance for the reliability of its analytical predictions. The experiments were designed in such a manner as to investigate the effect of vertical load redistribution from axially failing members on the lateral post-peak response of neighbouring columns.



# Chapter 1: INTRODUCTION

---

## 1.1 BACKGROUND AND MOTIVATION

Reinforced concrete (R/C) buildings designed according to older, less stringent seismic codes – or even without adhering to any code – represent a large part of the total building stock worldwide. Naturally, this applies to developing earthquake-prone countries, where the state of the art in construction technology and structural design is lagging – or at least was lagging in previous decades–, and where regulation of construction and policies on the required safety margins of structures has followed a slow pace. Nevertheless, this also applies to many developed earthquake-prone countries, largely due to the building boom of the decades following the 2<sup>nd</sup> World War that resulted in creating a sizeable stock of buildings perhaps compliant to contemporary guidelines, but largely considered substandard given the current seismic codes, technology and state-of-the-art.

Such buildings, often referred to as substandard or non-ductile buildings owing to their limited deformability, are susceptible to progressive collapse. This comprises the succession of failure of structural elements leading to the whole structure – or a substantial part of it – undergoing collapse. The types and causes of progressive collapse can vary; they are broadly classified into side-sway collapse that takes place when seismic lateral forces exceed the lateral resistance of the structure and vertical collapse, which pertains to the exceedance of vertical resistance of columns and connecting beams (Matsukawa *et al.*, 2012). Post-earthquake reconnaissance has shown that the latter is the most common scenario for R/C frame buildings, primarily due to failure of columns or beam-column joints (Ghannoum *et al.*, 2008), and non-ductile R/C buildings are reportedly much more prone to vertical collapse compared to modern ductile structures (Liel, 2008).

This is not surprising, since the quality of construction in older buildings is typically much lower than buildings designed nowadays – including lower-strength concrete, lower longitudinal reinforcement content, inadequate, widely spaced or poorly detailed transverse reinforcement and insufficient anchorage of longitudinal bars –, and modern design concepts like capacity design and the provision of dissipative zones are lacking. This renders the vertical elements of these buildings vulnerable to various failure modes, for instance flexural hinging, buckling of

steel bars or crushing of concrete due to excessive axial loading, anchorage failure, as well as shear failure; the latter may occur subsequently, or even prior, to yielding of their longitudinal reinforcement and can eventually lead to loss of axial load capacity of vertical elements, through disintegration of the poorly confined concrete core and the consequent axial load resistance decrease (Sezen & Moehle, 2006).

This research work will focus on the latter mode of failure, i.e. axial failure of R/C columns subsequent to shear failure and (potentially) yielding. This is a rather complex phenomenon governed by highly non-linear softening response, progressive damage accumulation and it is subject to many uncertainties. It must be appropriately modelled, in order to describe the full-range response (up to collapse) of sub-standard R/C frame and dual structures to strong ground motions. Previous research has focussed on modelling this type of response to some extent, however disregarding important aspects of this phenomenon, as will be highlighted later on.

Full-range analysis of structures is a necessity if vulnerability assessment is sought that would include the critical limit states of significant damage and collapse. This is not just a desirable step forward for structural engineering research, but also relevant to further improving the safety of millions of people residing, working or spending part of their leisure time in such sub-standard buildings.

## 1.2 OBJECTIVES & SCOPE

An experimental investigation of shear and flexure-shear critical R/C elements is carried out with the objective of demonstrating that displacements beyond the onset of shear failure are attributed to shear and concentrate in a region defined by diagonal failure planes. Furthermore, the effect of vertical load redistribution from axially failing members on the lateral post-peak response of neighbouring columns is investigated for the first time.

The main objective of this research project is to put forward a computationally efficient finite element model of the beam-column type able to accurately predict the hysteretic non-linear response of elements of sub-standard R/C structures up to the onset of axial failure following shear failure with or without prior flexural yielding, while simultaneously accounting for potential flexural and anchorage failure modes. In order to achieve this, it ought to appropriately account for shear and flexural deformations at a local level, the interaction between them inside the potential plastic hinges of an element, the distribution of flexural and shear flexibility along the element, as well as the location and extent of shear damage, without relying on assumptions about the bending moment distribution, which generally changes during seismic loading.

Some R/C columns may sustain simultaneous shear and axial failure with substantially reduced deformation capacity, which jeopardises the entire structure, thus constituting a priority in a pre-seismic retrofit context. Therefore, simplified criteria will be sought for this particular class of elements, in order for their identification to be accelerated and not require analysis of the entire structure or even individual members.

The contributions summarised in the aforementioned objectives are believed to have noteworthy implications regarding the more accurate and reliable assessment and collapse analysis of existing R/C structures. Moreover, they advance the state-of-the-art in vulnerability assessment using nonlinear analysis methods that directly capture member collapse rather than accounting for it using simplifying (and often arbitrary) assumptions.

### 1.3 THESIS ORGANISATION

The stated objectives of the PhD are met as described in the next chapters, divided into three major parts: (i) the compilation of a database and – based on this – proposed empirical relationships and simplified failure criteria, (ii) the design of, and the obtained results from, an experimental investigation involving six cantilever shear and flexure-shear critical columns, and (iii) the development and verification of a beam-column finite element model.

Chapter 2 provides a comprehensive summary of existing literature regarding the aforementioned topics. A critical review of member-type models predicting the response of sub-standard R/C elements is included as well as existing empirical relationships used to predict various key post-peak response parameters. Moreover, observations regarding specimens susceptible to simultaneous shear and axial failure and conclusions drawn from experimental investigations of R/C members' post-peak response are summarised.

In chapter 3, the compilation of the largest database (to date) of shear and flexure-shear critical elements, which were cycled well beyond the onset of shear failure and/or up to the onset of axial failure, is presented. Descriptive statistics of the main characteristics of the specimens as well as data extraction and processing considerations are provided.

In chapter 4, the theoretical basis adopted herein for the modelling of the post-peak response of shear and flexure-shear critical specimens is presented. Appropriate empirical relationships are put forward for key parameters, i.e. the inclination of the diagonal shear failure plane, the rate of strength degradation after the initiation of shear failure as well as the shear deformation associated with the onset of axial failure.

In chapter 5, sub-standard R/C columns failing simultaneously in shear and axial failure are investigated. Existing observations on the circumstances leading to specimens being susceptible to such failure are evaluated. Novel criteria aiming to identify members susceptible to simultaneous failure without the need for analysis of the entire structure or even individual components, are put forward. The empirical relationship previously proposed for the post-peak deformability as well as a well-established existing model are evaluated in the context of simultaneous shear-axial failure.

In chapter 6, the design and fabrication of an experimental series of six cantilever columns is presented. The purpose is to investigate the effect of vertical load redistribution on the lateral post-peak response of shear and flexure-shear critical R/C columns neighbouring axially failing vertical members. Therefore, cyclic tests are carried out, with the axial load increasing just before or after the onset of shear failure. Furthermore, another objective is to investigate if displacements beyond the onset of shear failure are attributed to shear and concentrate in a region defined by diagonal failure planes.

In chapter 7, the results of this experimental campaign are presented in detail. All relevant information in terms of damage progression, lateral and axial response is included. Furthermore, light is shed on various issues regarding the overall response of the specimens, for instance their energy dissipation capacity, stiffness variation throughout the tests, concentration of damage after the onset of shear failure and some topics related to the testing procedure per se.

In chapter 8, a novel shear hysteretic model is proposed, based on the previously proposed empirical relationships and the afore-described concentration of damage after the onset of shear failure. A computationally efficient member-type finite element model for the hysteretic response of shear and flexure-shear critical R/C frame elements up to the onset of axial failure is presented, incorporating this shear hysteresis model. Being based on local deformation quantities in lieu of inter-storey displacements, it can account in an unbiased way for the interaction of inelastic flexural and shear deformations, including the gradual decrease of an element's shear resistance, and more reliably predict the location and extent of shear damage subsequent to shear failure, avoiding shortcomings of previous models.

In chapter 9, the beam-column element is verified against a multitude of experimental tests, including quasi-static R/C column tests and dynamic shake-table tests on R/C frames. Wherever feasible, comparisons are shown not only in terms of total response, but also with regard to individual deformation components. Additionally, the specimens tested in this study with increasing axial load are analysed.

In the final chapter (10) of the thesis, the work performed is summarised and the main conclusions are outlined. Last but not least, recommendation for future research work in this area are made.



## Chapter 2: LITERATURE REVIEW

---

A summary as well as critical evaluation of the existing literature pertinent to the subjects touched upon in this thesis will be herein included. Topics relevant to the collapse of R/C structures, post-peak response of sub-standard R/C components as well as modelling of this response will be presented.

### 2.1 COLLAPSE OF R/C STRUCTURES

Many existing R/C structures have been designed according to older, less stringent seismic codes compared to current guidelines or might not have been designed to withstand seismic loads at all. Therefore, they are quite vulnerable to damage from earthquake loading, potentially even leading to collapse of the whole structure or a major part of it. This takes place in a progressive manner starting with the failure of one or few elements and propagating through the structure, thus termed progressive collapse (Starossek, 2008). Progressive collapse scenarios are broadly classified into (1) side-sway collapse, which takes place when seismic lateral forces exceed the lateral capacity of the structure, and (2) vertical collapse that pertains to exceeding the structure's vertical bearing capacity (Matsukawa *et al.*, 2012). The former is more common in ductile frames, which can attain larger lateral displacements and are influenced considerably by P- $\delta$  phenomena. On the other hand, non-ductile R/C frames usually undergo the latter mode of collapse, their elements losing their vertical capacity before excessive lateral displacements can be reached (Liel, 2008; Adam & Ibarra, 2014).

Loss of axial load capacity of vertical R/C elements has been shown through post-earthquake reconnaissance to be one of the most common reasons of vertical collapse of older R/C frame buildings (Ghannoum *et al.*, 2008). Axial failure of a column can occur after the onset of shear failure, subsequently, or even prior, to yielding of the longitudinal reinforcement, through disintegration of the poorly confined concrete core of the column with continuous lateral cycling (Sezen & Moehle, 2006). A large fraction of the vertical load carried by a failing member is subsequently redistributed to neighbouring vertical elements through the adjacent horizontal members, which leads to a significant increase of axial load acting on the neighbouring R/C columns. The ability of a structural system to resist progressive collapse in such a 'scenario' hinges on both the ability of horizontal elements (beams and slabs) to transfer the loads being redistributed to adjacent vertical elements and the vertical elements' ability to resist them without considerably losing their strength and deformability (Lodhi, 2012).

Existing research work has looked extensively into the adjacent horizontal elements' capacity to redistribute vertical loads, neglecting the neighbouring columns or assuming they are capable of bearing the extra axial load. Several analytical studies, experimental programmes and field studies have highlighted that R/C beams and slabs adjacent to a failing column redistribute the loads initially via frame (or Vierendeel) action, followed by compressive arch action of the beams and membrane action of the slabs, as the vertical displacement increases, eventually turning into catenary action with the whole depth being in tension (Sasani *et al.*, 2007; Sasani & Sagioglu, 2008; He & Yin, 2008; Izzuddin *et al.*, 2008; Vlassis *et al.*, 2008; Yi *et al.*, 2008; Sasani & Sagioglu, 2010; Li *et al.*, 2011; Choi & Kim, 2011; Jahromi *et al.*, 2012; Yu & Tan, 2013; Lew *et al.*, 2014; Li *et al.*, 2014; Palmisano, 2014). The General Services Administration guidelines (GSA, 2013) also focus on load redistribution systems of gravity loads to neighbouring vertical load-bearing elements without any particular mention to the neighbouring vertical elements themselves.

Nonetheless, an abrupt increase of the axial load in vertical elements neighbouring an axially failing column takes place – in addition to potential increase of shear or deformation demands – and they ought to be checked in order to perform an accurate assessment of the ability of the structure to arrest progressive collapse. Xu & Ellingwood (2011) accounted for this via considering the potential buckling of neighbouring vertical elements in a design procedure against progressive collapse of steel buildings. However, only in one noteworthy study of R/C buildings has it been attempted to account for this effect, modelling shear and axial failure of the columns of an R/C frame building that were judged as the most critical based on preliminary analyses (Murray & Sasani, 2013). Their shear strength model could take the variation of axial load into consideration. Nonetheless, the post-peak shear strength degradation rate was assigned a value based on results from similar columns cycled under constant axial load, without considering the effect of axial load increase or decrease. Additionally, the onset and rate of axial strength degradation were also assumed based on past experimental results. Furthermore, although the structure was representative of older construction, the anchorage slip as well as shear deformations were not taken into account in the analyses. Naturally, the effect of vertical load redistribution can be readily taken into account using member-type elements that account for axial-flexure interaction, in the case of flexure-critical elements. However, this is not the case for shear or flexure-shear critical elements of older R/C structures – which are the focus of this thesis – modelled through beam-column models explicitly accounting for shear response, where this effect has not been modelled appropriately yet.

Another common assumption in collapse analysis is that of undamaged vertical elements, e.g. assuming uncracked cross-sections. This might be appropriate for blast-induced, vehicular

impact or similar collapse scenarios, where damage can be largely assumed localised in a single structural element or a small set of elements. Nevertheless, earthquake-induced collapse scenarios pose a further difficulty in that there is global damage in a large part, if not all, of the building even before the loss of a column's vertical load-bearing capacity. Therefore, the damage state of a column neighbouring an axially failed vertical member has to be appropriately taken into account in a realistic earthquake-induced progressive collapse assessment, e.g. as attempted to be done by Murray & Sasani (2013).

Previous experimental studies looking into the non-linear, especially the post-peak, lateral response of substandard R/C columns have looked extensively at the response under constant vertical load (e.g. Lynn *et al.*, 1996; Yoshimura & Yamanaka, 2000; Yoshimura & Nakamura, 2002; Nakamura & Yoshimura, 2002; Ousalem *et al.*, 2003; Yoshimura *et al.*, 2004; Matamoros & Woods; 2010) as well as variable axial load corresponding to an exterior column case, i.e. axial load proportional to the lateral force acting on the column (e.g. Ramirez & Jirsa, 1980; Ousalem *et al.*, 2002; Sezen & Moehle, 2006). Recently, Nakamura & Yoshimura (2014) investigated the effect that decreasing axial load has on the lateral non-linear response of substandard columns, thus simulating the response of a column that starts failing axially and its axial load starts decreasing correspondingly due to vertical load redistribution. All these studies are presented in the next section; the most relevant conclusions are presented and the subsequent parts of the project are based upon them to a greater or lesser extent.

To the writer's best knowledge, the effect of vertical load redistribution on the non-linear post-peak response of shear and flexure-shear critical R/C columns neighbouring failing vertical members has thus far not been investigated at all.

## 2.2 POST-PEAK RESPONSE OF R/C MEMBERS

Traditionally, experimental tests of R/C columns would terminate after a slight degradation of strength, at around 80-85% of the maximum strength, being conservative as to the available displacement capacity of R/C members. The experiments falling into this category do not provide sufficient information on the post-peak response of R/C members. Similarly, analytical models would consider the peak of the response or the point of 80-85% of the maximum strength as the ultimate state. Nonetheless, there has been a recent shift of interest in the post-peak domain inside the engineering research community, chiefly during the last 20 years. This has produced a sizeable amount of data with regard to the post-peak response in general and particularly to the onset of axial failure of columns. Some of the most salient experimental and analytical works along with their main observations will be presented herein.

Ramirez & Jirsa (1980) performed experimental tests on similar 2/3-scaled short columns under cyclic lateral loading and varying or constant compressive or tensile axial load. Compressive load was found to increase the shear strength degradation, while tension decreased it, compared with a specimen with no axial load. They claim that tension results in a smaller part of the concrete core resisting shear, so more transverse reinforcement capacity can contribute to carrying the shear force experienced by the column, instead of being used as concrete core confinement, and less damage is inflicted on the concrete crack surfaces during cycling. Varying axial loads between tension and compression seemed to decrease the deterioration as much as applying a constant tensile axial force.

Lejano *et al.* (1995) conducted an experimental programme to study the deformation characteristics of short double-curvature R/C columns with high-strength concrete under quasi-static cyclic loading as well as high or fluctuating axial load (Figure 2-1). It was observed that specimens under compressive axial loads tend to exhibit high shear deformations in the post-peak part of the response. As an example, the deformation components of the response of one specimen (C-2), which was subjected to very high compressive axial load, is shown herein (Figure 2-2).  $\delta_s$  denotes shear deformation,  $\delta_f$  flexural deformation and the additional deformation,  $\delta_a$ , is assumed to derive mainly from anchorage slippage.

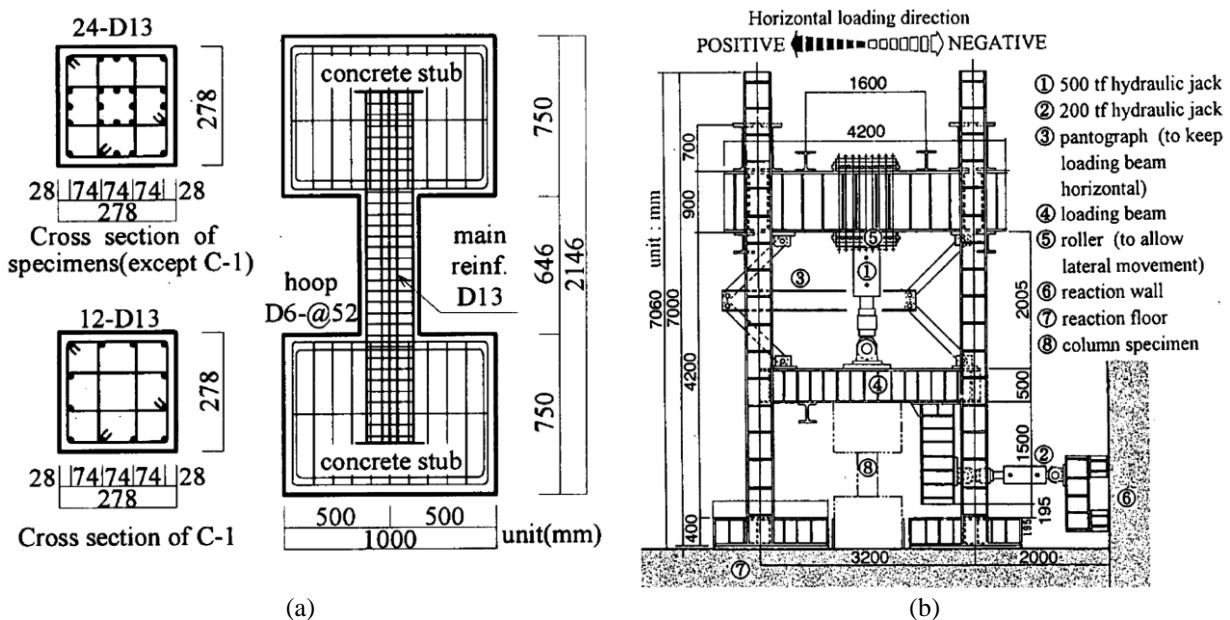


Figure 2-1: (a) Specimen details and (b) test set-up. (Lejano *et al.* 1995)

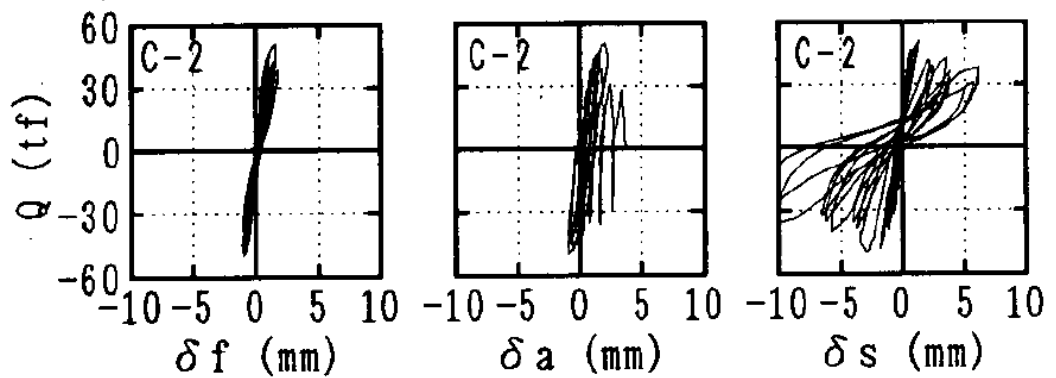


Figure 2-2: Deformation components of specimen C-2's response. (Lejano *et al.* 1995)

Lynn *et al.* (1996) conducted tests on eight full-scale square R/C columns with light and poorly detailed reinforcement, undergoing quasi-static cyclic lateral loading, while having a constant axial load. Sezen & Moehle (2006) performed four more tests on similar specimens, including one with monotonic lateral loading under constant axial load, as well as cyclic tests with varying, high constant and low constant axial load (Figure 2-3). Subsequently, four more specimens with similar geometry and test configuration were conducted (Matamoros *et al.*, 2008; Matchulat, 2009; Woods, 2009), to record the response of specimens after the onset of axial failure. Lastly, eight more experiments were carried out (Henkhaus *et al.*, 2013), including columns with two different aspect ratios as well as uniaxial and biaxial loading. These compose an experimental series amounting to 24 similar specimens, which is very important for studying the effects of individual variables on the post-peak response. Some of their main conclusions and findings regarding post-peak response of sub-standard R/C columns were:

- Loss of gravity load capacity occurred soon after the loss of lateral load capacity, in specimens governed by shear. On the contrary, in flexure-shear specimens, the gravity load capacity was lost at relatively large lateral displacements (Lynn *et al.*, 1996).
- Higher axial load was found to shift the failure type from flexure-shear to shear and to reduce the lateral displacement at the onset of shear as well as axial failure significantly, leading in general to a more brittle response (Sezen & Moehle, 2006; Matchulat, 2009; Woods, 2009). Moreover, it leads to a far higher post-peak degradation of axial as well as lateral resistance (Matchulat, 2009; Matamoros *et al.*, 2008), although it is beneficial for the pre-peak lateral resistance of a column, as is well-known.
- Monotonic loading, as compared to cyclic, allows for higher lateral displacement at axial failure (Sezen & Moehle, 2006).
- Larger longitudinal reinforcement ratio results in higher lateral drift ratio at the onset of shear as well as axial failure (Woods, 2009).

- Increased number of cycles per displacement level (6 cycles as opposed to 3) were found to decrease the lateral drift ratio at the onset of shear as well as axial failure, based on the aforementioned tests (Woods, 2009; Henkhaus *et al.*, 2013) and a subsequent comparative analysis of the results (Simpson & Matamoros, 2012).
- Higher aspect ratio and transverse reinforcement ratio increase the lateral drift ratio at the onset of axial failure (Henkhaus *et al.*, 2013). Shorter specimens were found to attain a higher drift at axial failure in another study, however (Simpson & Matamoros, 2012).
- The use of larger ties at larger spacing, the general reduction of transverse reinforcement, increased number of cycles per displacement level and biaxial loading instead of uniaxial were found to cause a higher post-peak lateral strength degradation (Henkhaus *et al.*, 2013). Biaxial loading has been found to be even more influential than the number of cycles per displacement level (Simpson & Matamoros, 2012).
- Columns with higher initial axial load ratio run a higher risk of sudden collapse after the onset of axial failure, as they can maintain a far lower fraction of axial load, as opposed to columns with lower initial axial load ratio that can carry a reduced axial load for higher drifts. So, redistribution of axial loads in case of progressive collapse might not be possible in the former, contrary to the latter category (Woods & Matamoros, 2010).
- Sudden decrease of axial strength and increase of axial shortening take place at the onset of axial failure (Matchulat, 2009).
- Damage was observed to concentrate at a localised region along the specimen after the onset of shear failure (Henkhaus *et al.*, 2013).

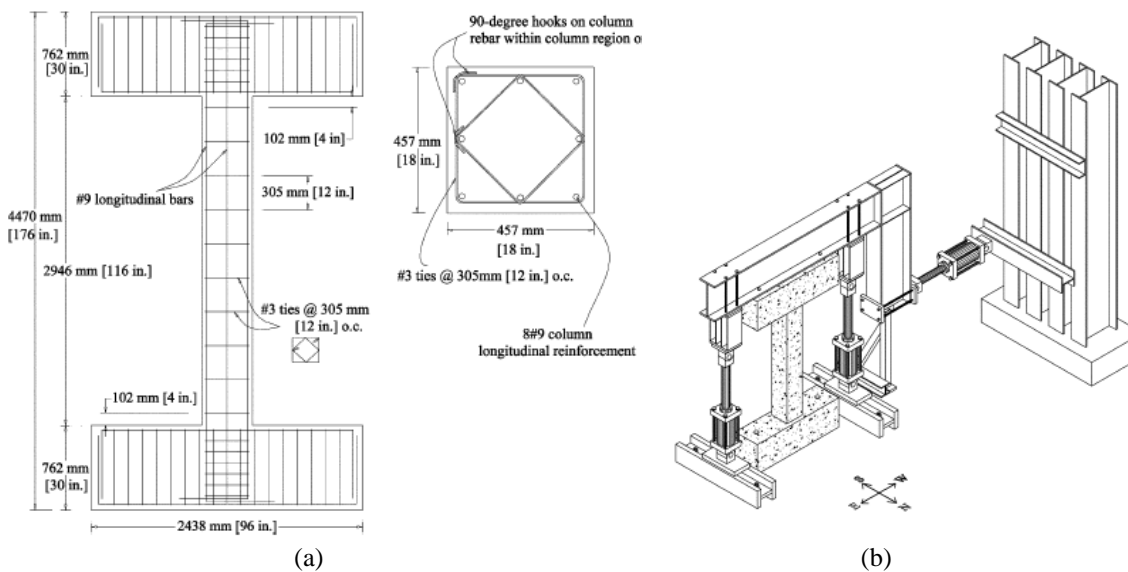


Figure 2-3: (a) Specimen-1 design and (b) test set-up. (Sezen & Moehle, 2006)

Ghannoum *et al.* (2012) performed tests pseudo-statically and dynamically at various velocities. The columns were flexure-shear critical, a 1/3-scale version of the aforementioned (Figure 2-3).

They observed that there was a 30% increase in strength in dynamic tests (as compared to the quasi-static one), due to the strain rate effect on the yield strength of the longitudinal bars, which increases the flexural resistance of the column. However, this increase was constant regardless of the velocity of the test, although the strength increase would be expected to be proportional to the strain rate. The dynamic tests also showed higher displacement capacities, but also higher cyclic shear strength degradation rates.

Ousalem *et al.* (2002) performed experimental tests on six square one-third-scaled R/C columns undergoing cyclic lateral loading and constant or variable axial loads (Figure 2-4). Ousalem *et al.* (2003) conducted seven more experiments on similar specimens, except for two of them having a lower aspect ratio, with different loading protocols. Comparative analysis was subsequently carried out (Ousalem *et al.*, 2004). Relevant conclusions drawn were:

- Higher transverse reinforcement ratio resulted in higher maximum shear strength and lateral displacement at axial failure (Ousalem *et al.*, 2002).
- Increased axial load led to higher shear strength as expected, but lower lateral displacement at axial failure as well as axial deformations of the column. It also resulted in a steeper failure plane (Ousalem *et al.*, 2002; Ousalem *et al.*, 2004).
- Varying axial load led to milder degradation of axial stiffness, higher shear resistance, larger lateral displacement and lower shear degradation (Ousalem *et al.*, 2002; Ousalem *et al.*, 2004).
- Shear strength had degraded to nearly zero when axial collapse occurred along inclined planes. At the onset of axial collapse, longitudinal bars were found to buckle simultaneously with hoops opening (Ousalem *et al.*, 2003).
- Fewer reversals of larger displacement amplitude resulted in less but wider cracks, which led in turn to less pronounced shear strength degradation and higher deformability. In specimens with low transverse reinforcement, however, the lateral loading type had no effect on the maximum lateral drift attained. Moreover, fewer reversals led to higher shear strength in the primary direction, attributed to the lack of low-amplitude reversal damage. Nevertheless, lower shear strength was attained in the opposite direction, due to the influence of shear cracking and shear strength degradation in the primary direction (Ousalem *et al.*, 2003; Ousalem *et al.*, 2004).
- Lower aspect ratio resulted in increased shear strength, but decreased lateral deformability (Ousalem *et al.*, 2003).
- Axial load ratio as well as transverse reinforcement were found to have a significant effect on the failure plane inclination, especially in the case of varying axial load. The

lateral loading protocol type did not have a significant influence on it (Ousalem et al., 2004).

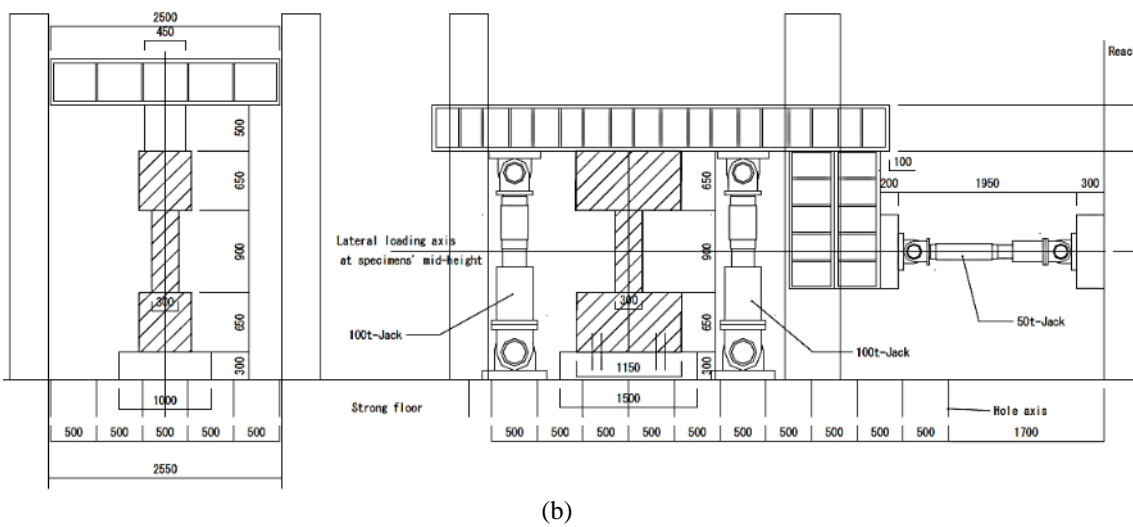
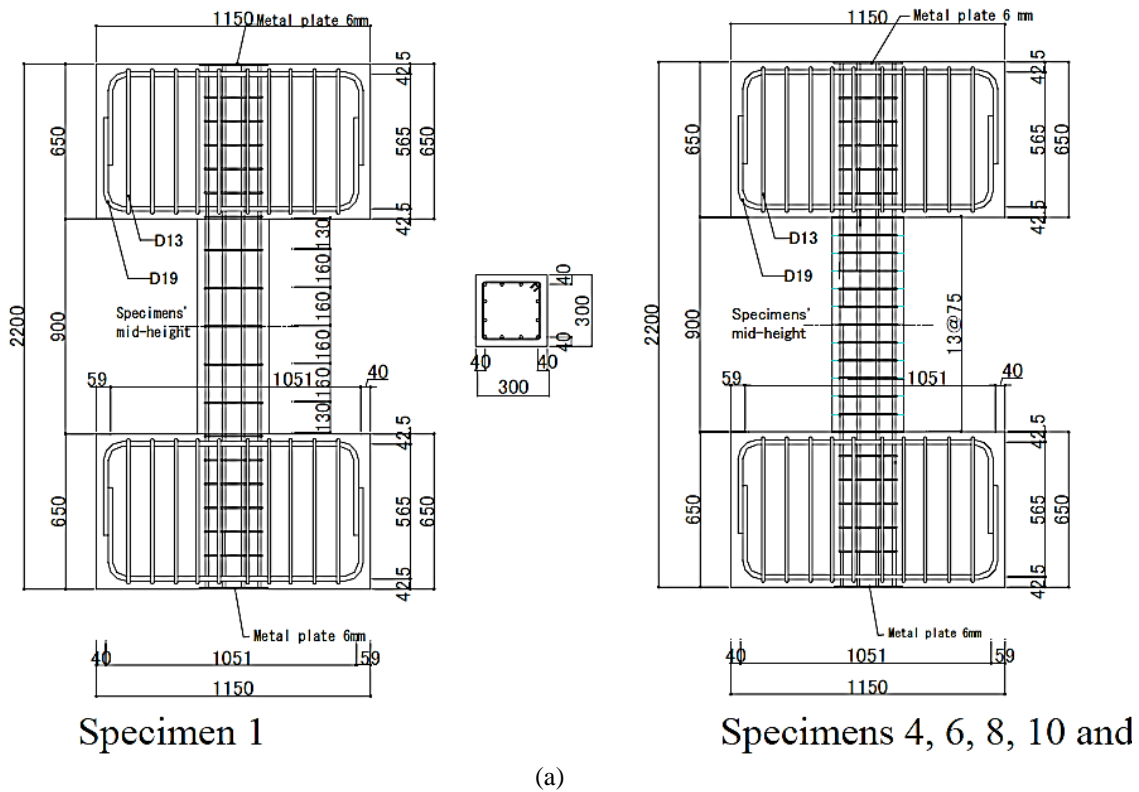


Figure 2-4: (a) Specimen design and (b) test set-up. (Ousalem et al. 2002)

Yoshimura & Yamanaka (2000) carried out experiments on six cantilever R/C columns, with monotonic, uniaxial and biaxial cyclic lateral loading and relatively low constant axial loading. Half of them were designed to fail in shear prior to flexural yielding and half of them after yielding. Nakamura & Yoshimura (2002) tested four short specimens in a double-curvature setup, with monotonic and cyclic lateral loading. Yoshimura & Nakamura (2002) tested six specimens similarly, designing them to fail in shear. Yoshimura *et al.* (2003) tested eight more specimens of a slightly higher aspect ratio. Comparisons within this large series of specimens resulted in plenty of conclusions drawn in later publications (Yoshimura *et al.*, 2004; Yoshimura,

2008). Nakamura & Yoshimura (2012) performed shake-table tests on half- and full-scale R/C columns up to axial collapse, with natural earthquake recordings of increasing amplitude. Nakamura & Yoshimura (2014) undertook an extensive experimental programme, including sixteen full-scale column specimens, which were loaded with lateral monotonic or cyclic load and a constant axial force, which was decreased to a fraction of the initial value in the post-peak domain of the response. Figure 2-5 summarises the specimen design and test set-up characteristics of most of the aforementioned experimental programmes. Many conclusions have been drawn throughout these years of experimental work, the most important of which are:

- Shear strength at the onset of axial failure reaches about 10% of the maximum strength (Yoshimura & Yamanaka, 2000). It was found to degrade to about zero in other studies (Yoshimura & Nakamura, 2002; Nakamura & Yoshimura, 2002). Later, it was found to be negligible in shear critical elements, but much larger (about 90% of the maximum strength) in flexure-shear critical ones, based on the two flexure-shear and five shear critical specimens of this study (Yoshimura *et al.*, 2003).
- Axial load ratio plays a major role in lateral and vertical displacements as well as dissipated energy at the onset of axial collapse, i.e. increased axial load results in a decrease in all of them (Nakamura & Yoshimura, 2002).
- The maximum attainable displacement seems to decrease as the longitudinal reinforcement ratio decreases. This is also reinforced by the finding that longitudinal bars sustain much higher strains near the diagonal failure plane than in the rest of the column, so they transfer a larger part of the axial force at the crack, where concrete is not able to (Yoshimura & Nakamura, 2002). Later, it was concluded that there is a positive correlation between these two quantities for shear critical elements, but a negative one for flexure-shear critical ones (Yoshimura, 2008).
- As a consequence of the previous comments, the longitudinal reinforcement axial load ratio (defined as the axial load over the axial yield strength of the longitudinal reinforcement), seems to correlate better with the lateral drift at axial failure than the classical axial load ratio (Yoshimura & Nakamura, 2002). Later, they claim that this parameter is a very good predictor for shear critical specimens, but not for flexure-shear critical ones (Yoshimura *et al.*, 2003).
- Loading history seems to be an important factor affecting deformability. Cyclic tests achieve around 30% less maximum drift ratio than monotonic ones (Yoshimura & Nakamura, 2002). It was still around 30% with small deviations depending on the axial load history, in later experiments (Nakamura & Yoshimura, 2014). On the other hand, it

was found that for columns with small hoop ratio that fail in shear, collapse drifts are almost independent of the loading history (Nakamura & Yoshimura, 2012).

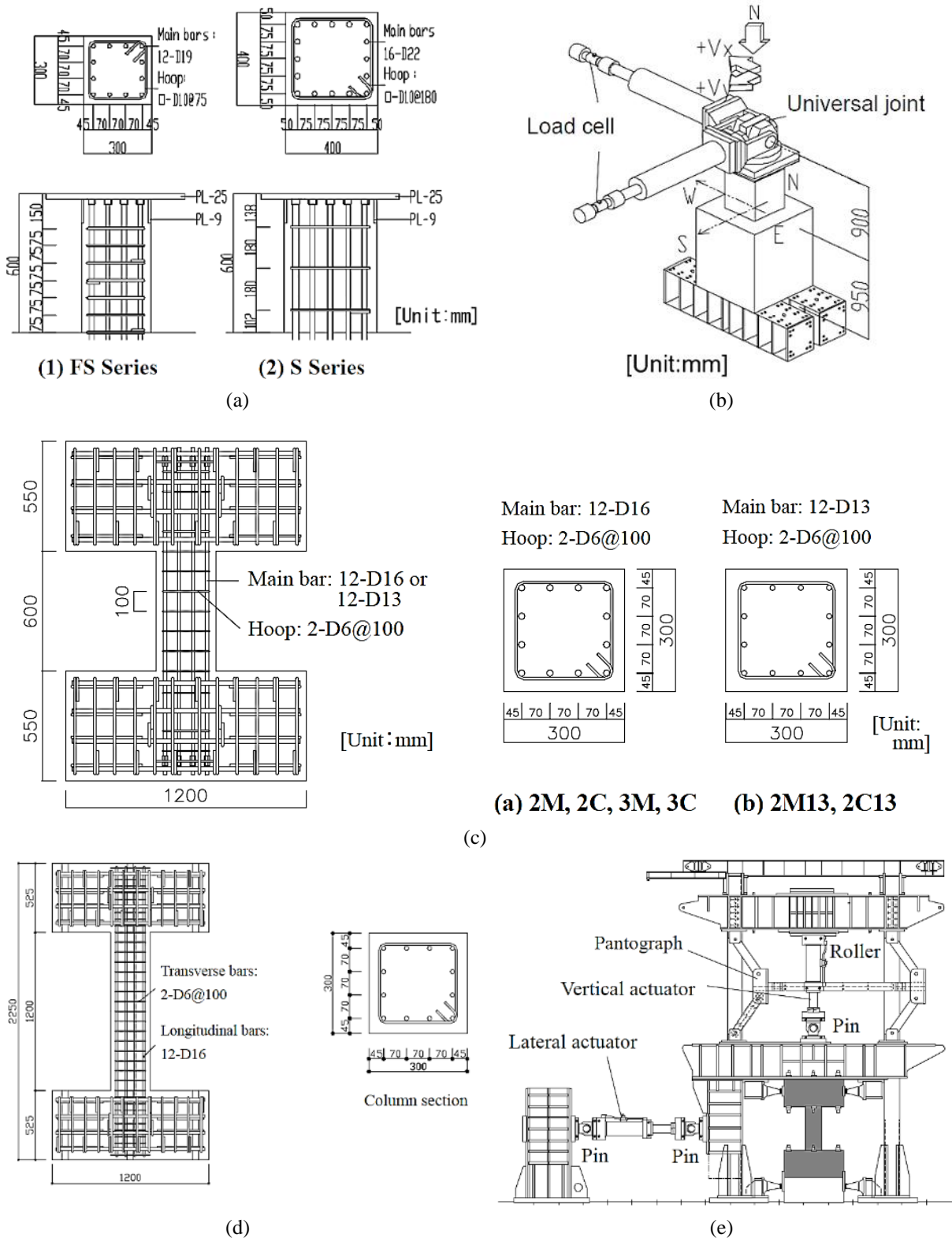


Figure 2-5: (a) Specimen design and (b) test set-up (Yoshimura & Yamanaka, 2000). (c) Specimen design (Yoshimura & Nakamura, 2002). (d) Design of specimen No. 1 (Yoshimura et al., 2003). (e) Test set-up (Nakamura & Yoshimura 2002).

- Sudden increase of axial shortening is observed at the onset of axial failure (Nakamura & Yoshimura, 2002).

- In shear critical elements, a diagonal crack is formed at the column mid-height at shear failure. This crack widens as lateral deformation increases and collapse occurs due to the reduction of the axial capacity due to buckling of the reinforcement bars, simultaneously with an increase in the axial force carried by them (Yoshimura *et al.*, 2003).
- Columns whose axial load is reduced at some point inside the post-peak response, exhibit higher lateral drifts at the onset of axial failure as well as lower post-peak strength degradation rate. The larger the decrease and the sooner it happens, the higher the displacement attained (Nakamura & Yoshimura, 2014).
- It was observed that drifts tend to shift in one direction for columns under seismic motions. Therefore, it is suggested that monotonic tests could be more suitable as capacity indicators rather than cyclic ones, when quasi-static tests are conducted (Nakamura & Yoshimura, 2012).

The last remark seems to agree well with that of Lignos & Krawinkler (2012). They reason that approaching collapse member hysteresis loops tend to become extremely asymmetric, observing a ratcheting phenomenon of lateral deformation. Therefore, symmetric cyclic lateral loading that has been the norm in experimental testing does not really provide useful information on the expected behaviour. On the contrary, cyclic deformation to low inelastic displacements followed by monotonic loading to collapse would be ideal for this purpose. The ideal case would be to have both monotonic and cyclic experiments with many different deformation protocols, in order to calibrate correctly all degradation mechanisms (Haselton *et al.*, 2009).

Kato *et al.* (2006) conducted lateral cyclic experiments on 26 specimens with variable concrete strength, axial loads and hoop detailing. They concluded that the effect of hoop detailing on the lateral deformation at axial failure was significant for small axial load ratio; as the latter increases, this impact fades. Moreover, it is shown that axial failure can initiate long before the shear strength of an R/C member degrades significantly.

Tran (2010) performed experimental tests on ten R/C columns of square or rectangular section, with different aspect and axial load ratios (Figure 2-6). It was concluded that:

- Increasing axial load and decreasing aspect ratio had a detrimental effect on both lateral deformation at axial failure and total dissipated energy up to that point. In addition, they resulted in a predominance of shear over flexural displacements, potentially shifting the failure mode from flexure-shear to shear.

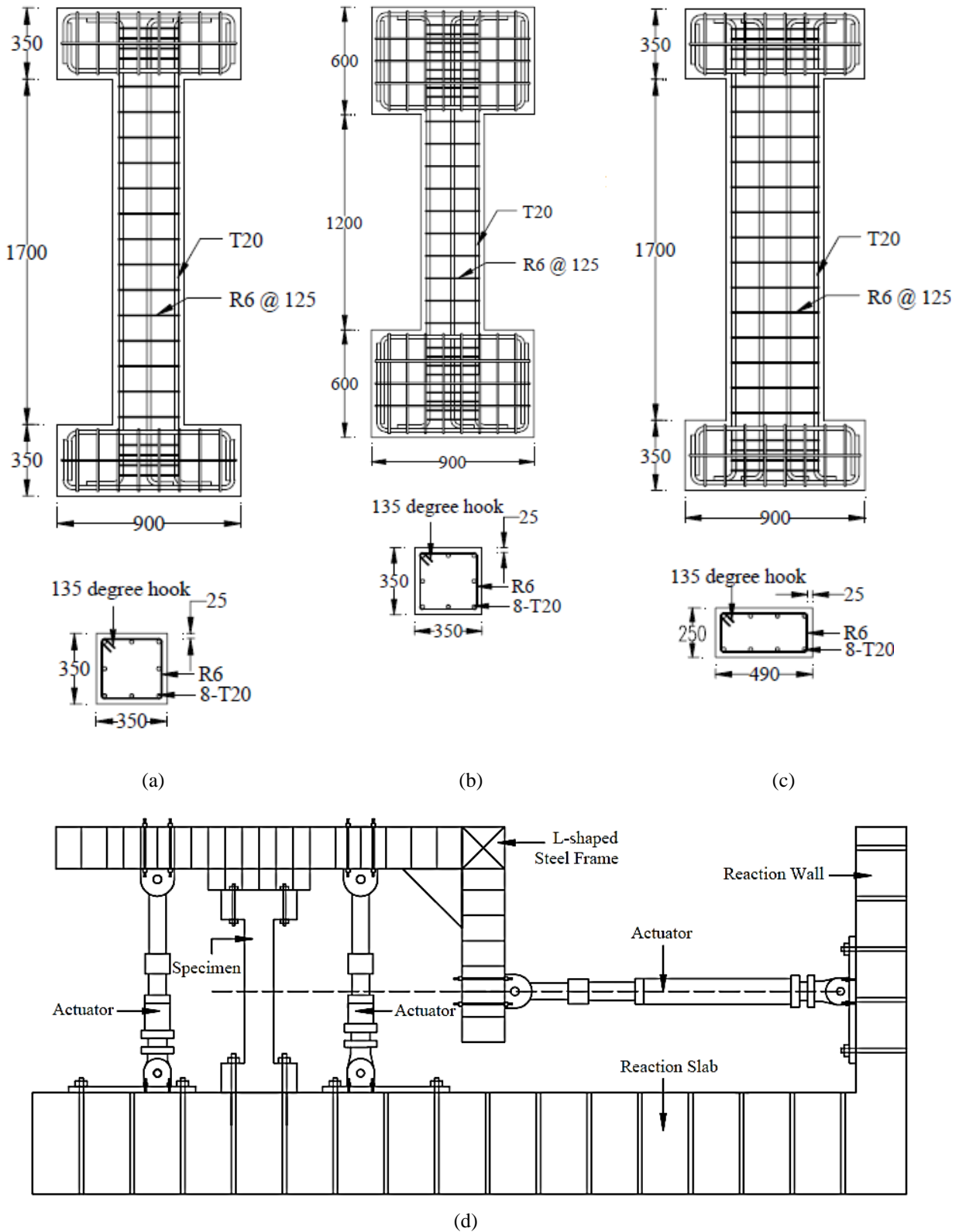


Figure 2-6: Design details of (a) square specimens with aspect ratio of 2.4, (b) square specimens with aspect ratio of 1.7, (c) rectangular specimens with aspect ratio of 1.7. (d) Test set-up. (Tran, 2010)

- There were two distinct failure modes in the tests. In square columns, a steep shear crack was formed at shear failure, along which sliding occurred at axial failure. At that stage, longitudinal bar buckling and fracture of transverse bars took place along the

developed failure plane. On the other hand, the rectangular columns were controlled by a combination of shear and bond-split, with vertical cracks forming along the height of the column. At axial failure, crushing of concrete, buckling of longitudinal bars and fracture of transverse bars occurred across a damaged zone.

In NIST GCR 10-917-7 (NEHRP, 2010), it was observed that the axial failure drift increases with decreasing aspect and axial load ratio, increasing longitudinal and transverse reinforcement ratio, lower number of displacement cycles, hoops of smaller diameter placed at closer spacing (under constant transverse reinforcement ratio) and uniaxial instead of biaxial displacement protocol.

#### *Simultaneous shear and axial failure*

As a rule, shear and flexure-shear critical vertical load bearing members do possess some displacement capacity even after initiation of shear failure, in fact rather significant in some cases. In other words, after the onset of shear failure, their lateral displacement can increase further accompanied by the corresponding deterioration of their lateral strength. Nonetheless, there is a subset of columns that can collapse axially immediately after their shear failure (Henkhaus *et al.*, 2009). This most daunting phenomenon is commonly referred to as “simultaneous shear and axial failure” in the literature. It is of paramount significance, because the collapse mode of the whole structure can be adversely affected by such members, leading to redistribution of vertical loads at usually low lateral drifts, and the probability that the structure collapses can thus be greatly increased.

Determining which columns are susceptible to such failure, however, is not a straightforward task. Relevant observations have been made by researchers in the past on possible circumstances leading to this phenomenon, but no criterion has been proposed. Some experimental evidence suggests that simultaneous shear and axial failure occurs when the applied axial load is about equal to, or greater than, the axial capacity of the longitudinal reinforcement (Matchulat, 2009). Elsewhere, it was shown that columns that experienced such failure had a ratio of axial load over yield strength of longitudinal reinforcement greater than 0.65 and had the highest ratios of axial load to buckling capacity of the longitudinal reinforcement in a subset of 11 columns examined (Matamoros & Woods, 2010). Henkhaus *et al.* (2009) studied a dataset of 40 columns cycled up to axial failure. They noted that the 4 of them that did fail in simultaneous shear and axial failure had transverse reinforcement ratios of  $\rho_w \geq 0.06\%$  and axial load levels of  $v \leq 0.3$ , contrary to what ASCE/SEI 41-06 (ASCE 2006) predicted for members with such characteristics. Yoshimura *et al.* (2003) observed that axial

failure occurred simultaneously with shear failure in shear-flexure critical elements quite suddenly and pertaining to crushing of concrete and buckling of longitudinal bars at the plastic hinge region. On the other hand, in shear critical specimens, axial collapse occurred when shear strength degraded almost completely. Their finding was based on an experimental series comprising 8 column tests. Eurocode 8-3 (CEN, 2005), on the other hand, does not provide for post-peak response of elements undergoing shear failure, considering it as a brittle failure and merely adopting a maximum strength criterion, due to the code-like conservative nature of basing on a significant-damage rather than a near-collapse damage state.

### *Frame effect*

Elwood & Moehle (2003) conducted a shake-table test on two RC Frames, studying their behaviour up to axial collapse. Gradual redistribution of vertical loads was observed through a dynamic process of oscillation of the mass above an axially failed column and bending of the connecting beam. During axial failure, there seemed to be few large pulses that decreased the axial resistance and axial column deformation rapidly, combined with smaller oscillations that slowly decreased them even further. Of course, due to the nature of the phenomenon, there was a transient dynamic amplification of the redistributed vertical loads owing to the inertial forces arising from the vertically accelerating mass associated with the loss of axial load support. The dynamic amplification factor was not that high because the complete loss of axial resistance happened over 5.5 s, reaching a maximum of 1.5 and subsequently converging to 1.0 with minor oscillations.

Another shake-table test, conducted by Wu *et al.* (2008a), reveals that there are dynamic oscillations of a column's axial load during experiments, occasionally substantial. Therefore, applying any axial failure criterion in an absolute sense could lead to underestimation of axial collapse. In other words, the axial load might decrease to nearly zero at the highest lateral displacement of a cycle, but it picks up again when passing through the balance (i.e. vertical) position. Another study (Wu *et al.*, 2008b) showed that the shear strength of R/C short columns was greater for dynamic shake-table tests than for cyclic static tests, probably attributed to the strain rate effect. Displacements at the onset of shear failure were similar, however.

Last but not least, judging from shake-table frame tests as well as from Matchulat's (2009) individual column tests, there seems to be "life after axial failure". Matchulat (2009) has shown that columns can continue being cycled after axial failure, albeit with reduced lateral strength and stiffness (e.g. specimen 2 in Figure 2-7). Ghannoum & Moehle (2012) also underlined the frame-effect on an individual column: due to partial redistribution of the axial load to

neighbouring elements, the axial strength will not be suddenly lost as in individual-specimen experiments; even after it is reduced, the system can find a balance state and cycling can normally proceed, provided that neighbouring columns can bear the higher axial load of the axially failed column, while the latter will continue being cycled with decreased axial and lateral strength and stiffness.

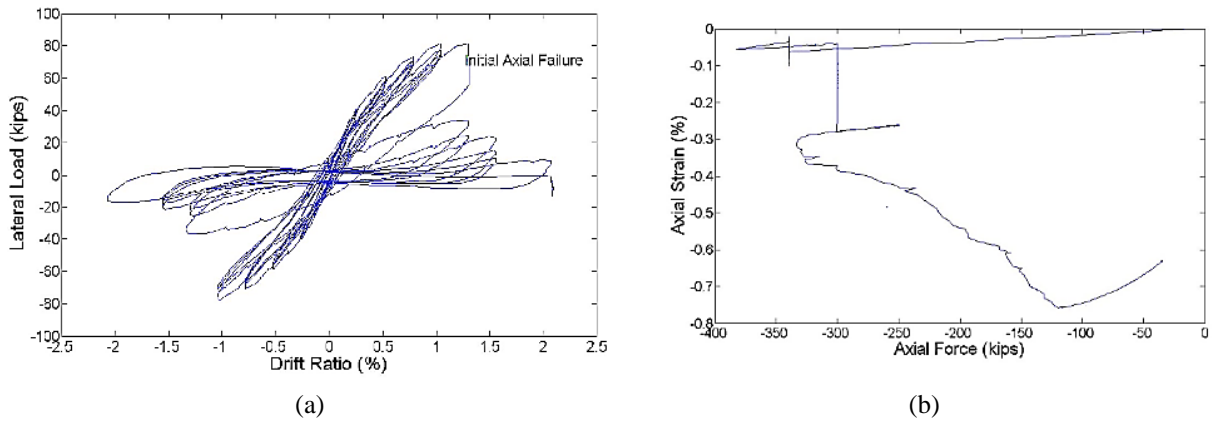


Figure 2-7: Response of specimen 2 in terms of (a) lateral load vs. lateral drift, and (b) axial strain vs. axial force. (Matchulat, 2009)

Ghannoum & Moehle (2012) also highlight the influence of low-cycle fatigue on strength deterioration of a column, especially when subjected to long-duration seismic motions. Therefore, they claim that both cyclic-based as well as deformation-based damage should be taken into account in analytical models.

### 2.3 MODELLING OF R/C MEMBERS

There are generally three different modelling approaches for the seismic structural analysis of an R/C structure (Mazars & Millard, 2009):

- a) Macro-scale or global approach, i.e. empirical macro-models that represent the behaviour of R/C members, like beams, columns, walls, or even larger subassemblies of a building. These connect deformation quantities – curvature, shear strain, extension, lateral displacement etc. – with global stress quantities – moment, shear or axial load.
- b) Meso-scale or semi-global approach, i.e. multi-fibre or multi-layer models. These rely on a finer discretisation of an element in layers or fibres and the assignment of the uniaxial law of each material, in order to get a representative behaviour of the whole element through integration.
- c) Micro-scale approach, i.e. fine 2D or 3D models. These represent the material behaviour at a much smaller scale and can reveal both the local as well as global response of a

structure with great accuracy, contingent on the quality of the chosen constitutive laws, assigned boundary conditions and discretisation.

In principle, the accuracy improves moving down the scale of modelling. However, the computational cost involved increases proportionally. This is the main reason, why a micro-scale approach can only be used for more detailed representations of R/C elements, without too complex geometrical or loading conditions, e.g. for better understanding of models during an experiment (Mazars & Millard, 2009). Meso- and macro-scale approach can be used in analyses of more complex subassemblies or even entire R/C structures.

#### *Member-type analytical models*

Modelling of R/C members under lateral loading should consider all three components of deformation, i.e. flexural, anchorage slip, and shear (Mergos & Kappos, 2012). The former can be captured quite accurately by the available finite element models providing an accurate prediction of the hysteretic response of code-conforming members. Nevertheless, the other two deformation components readily become significant, when dealing with sub-standard members. Furthermore, the post-peak response of shear and flexure-shear critical R/C elements has to be appropriately captured, in order to correctly assess the degrading behaviour of sub-standard structures, especially when it comes to predicting the initiation and cascade of progressive collapse.

In addition, for analytical models to be realistic and reliable in describing the response of R/C members up to significant-damage and/or near-collapse damage states, they should be able to reliably predict the location and extent of shear damage after the onset of shear failure, duly accounting for localisation effects. Localisation is a ubiquitous and multifaceted phenomenon in structural engineering. Simple, yet well-known examples are “necking” in tensile loading of steel and other metals as well as the concentration of damage at a specific region of a concrete specimen under compressive loads or the tensile crack region under tension (e.g. Calabrese *et al.*, 2010).

It has been observed experimentally that in plastic hinge regions shear strength decreases, even if no yielding of the transverse reinforcement has taken place (Ozcebe & Saatcioglu, 1989; Lee & Watanabe, 2003). Also, shear deformations increase considerably, despite the fact that shear demand remains practically constant (Mergos & Kappos, 2012). The cause of these is the increase of the tensile strains perpendicular to the existing cracks, which decreases the effective compressive strength of concrete, hence the concrete contribution to shear strength. This phenomenon is known as shear-flexure interaction and it impacts the response of flexure-shear

critical members, i.e. members that fail in shear after having experienced flexural yielding. Several models have been developed to predict the maximum shear strength of a member and its degradation with ductility demand, accounting for the aforementioned interaction. Amongst them are the model by Priestley *et al.* (1994), Sezen & Moehle (2004), and a more recent one based on statistical analysis of a large number of tests of flexure-shear critical column specimens, by Biskinis *et al.* (2004).

Initial efforts to model the seismic response of R/C elements were focused on flexural response and used concentrated inelasticity models (e.g. Giberson, 1967), assuming that inelasticity is lumped in rotational springs at the member ends. In these models, shear deformation can be taken into account either by modifying the hysteretic rules of the rotational springs (e.g. Roufaiel & Meyer, 1987) or by adding translational shear springs (e.g. Thom, 1983). There have been several lumped inelasticity models for the cyclic lateral behaviour of shear-deficient R/C elements that take into account shear deformation and the effect of shear-flexure interaction (Figure 2-8) (e.g. Ricles *et al.*, 1998; Pincheira *et al.*, 1999; Lee & Elnashai, 2001; Sezen & Chowdhury, 2009). Some of them also extend into the post-peak domain of the response, even predicting the onset of axial failure of an element (e.g. Sezen & Chowdhury, 2009) (Figure 2-9), which is a critical point in assessing the behaviour of an existing structure, as it signals the initiation of vertical load redistribution and possibly progressive collapse. Lumped inelasticity models, albeit computationally efficient, are bound by limitations regarding their ability to predict inelastic response. Specifically, they cannot capture the gradual spread of inelasticity, they rely on assumptions regarding the moment distribution in structural elements and they cannot provide information regarding the actual distribution of deformations and damage along structural elements.

To tackle these limitations, 'distributed' inelasticity models (e.g. Soleimani *et al.* 1979; Valles *et al.* 1996; Mergos & Kappos 2012; Helleland & Scordelis 1981; Spacone *et al.*, 1996; Ranzo & Petrangeli 1998; Filippou *et al.* 1992; Ceresa *et al.* 2007; Lee & Filippou, 2009) were proposed. These either capture the inward penetration of inelasticity from the ends of an element (plastification zones of variable length) or define inelasticity at cross-section level (Figure 2-10). Distributed inelasticity models can be divided into two main categories: displacement-based (e.g. Helleland & Scordelis, 1981) and force-based (e.g. Spacone *et al.*, 1996). The latter do not rely on assumptions regarding the displacement and curvature fields and, therefore, are considered more effective in modelling the inelastic response of structural elements.

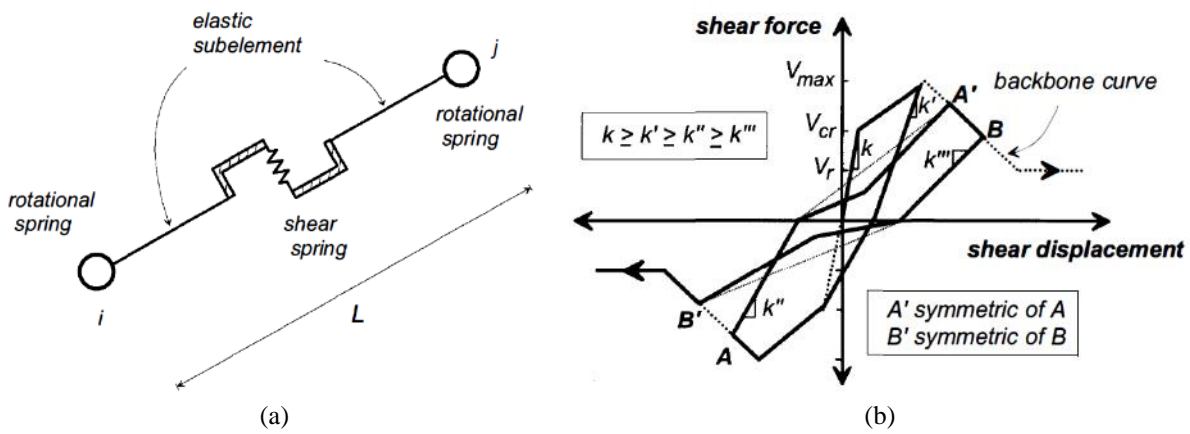


Figure 2-8: (a) Schematic representation of member-type model, and (b) shear hysteretic model. (Pincheira et al., 1999)

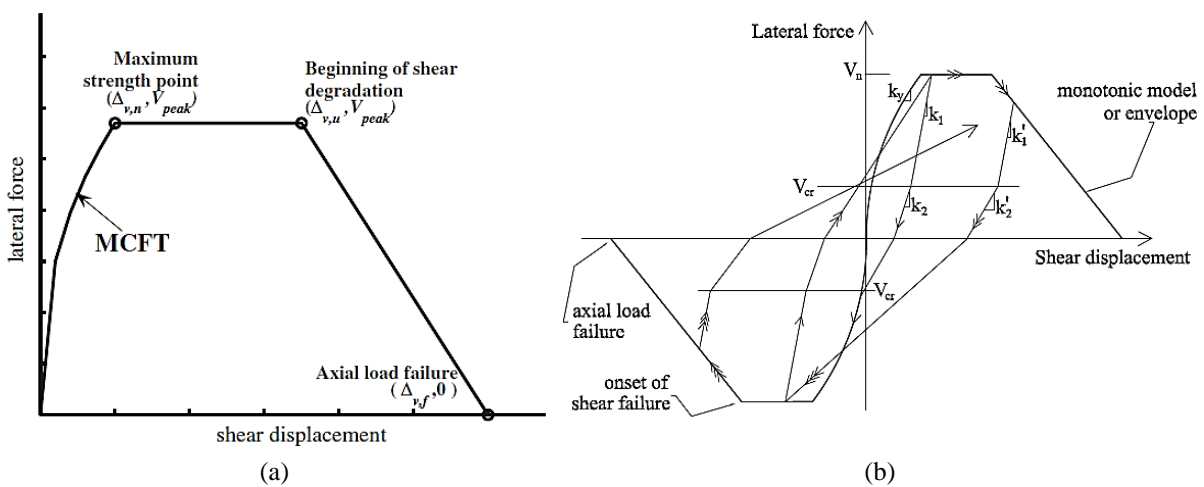


Figure 2-9: (a) Shear monotonic envelope, and (b) shear hysteresis rules. (Sezen & Chowdhury, 2009)

The first distributed inelasticity elements, both force and displacement-based, focused solely on flexural response (e.g. Soleimani et al., 1979; Helleland & Scordelis, 1981; Spacone et al., 1996). These models are generally able to capture adequately the response of flexure-dominated R/C elements. In addition, a significant number of distributed inelasticity models have been developed to account for shear flexibility and shear-flexure interaction effects (e.g. Filippou et al., 1992; Vecchio & Emara, 1992; Ravi Mullapudi & Ayoub, 2010; Saritas & Filippou, 2009; Ranzo & Petrangeli, 1998; Petrangeli et al., 1999; Martinelli, 2008; Ceresa et al., 2007; Ceresa et al., 2009; Bairan & Mari, 2007; Mohr et al., 2010; Mazars et al., 2006; Guner & Vecchio, 2012; Marini & Spacone, 2006) (Figure 2-11 and Figure 2-12). These elements consider interaction of flexural and shear deformations at section level, either by using mechanical models like the smeared crack theory, damage mechanics, or micro-plane theory (Ceresa et al., 2007; Ceresa et al., 2009), or by adopting phenomenological  $V-\gamma$  (shear force vs shear strain) laws (e.g. Marini & Spacone, 2006; Mergos & Kappos, 2012). Few amongst these models (e.g. Marini & Spacone, 2006; Baradaran-Shoraka & Elwood, 2013) can also address the response after the onset of shear failure (Figure 2-13 and Figure 2-14).

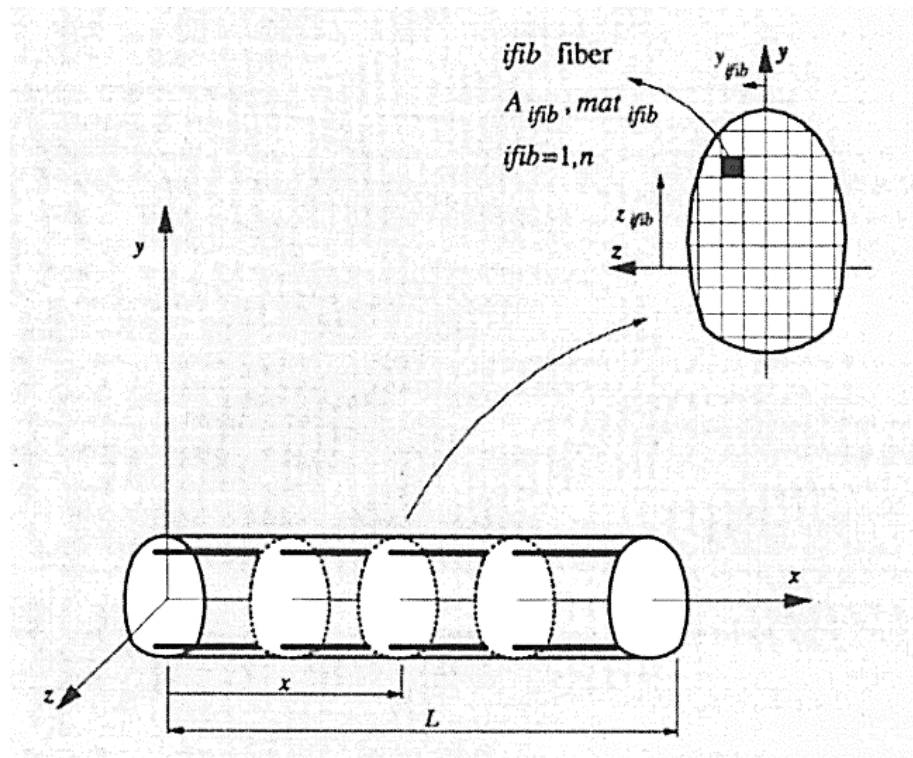


Figure 2-10: Fibre element scheme of beam element. (Spacone et al., 1996)

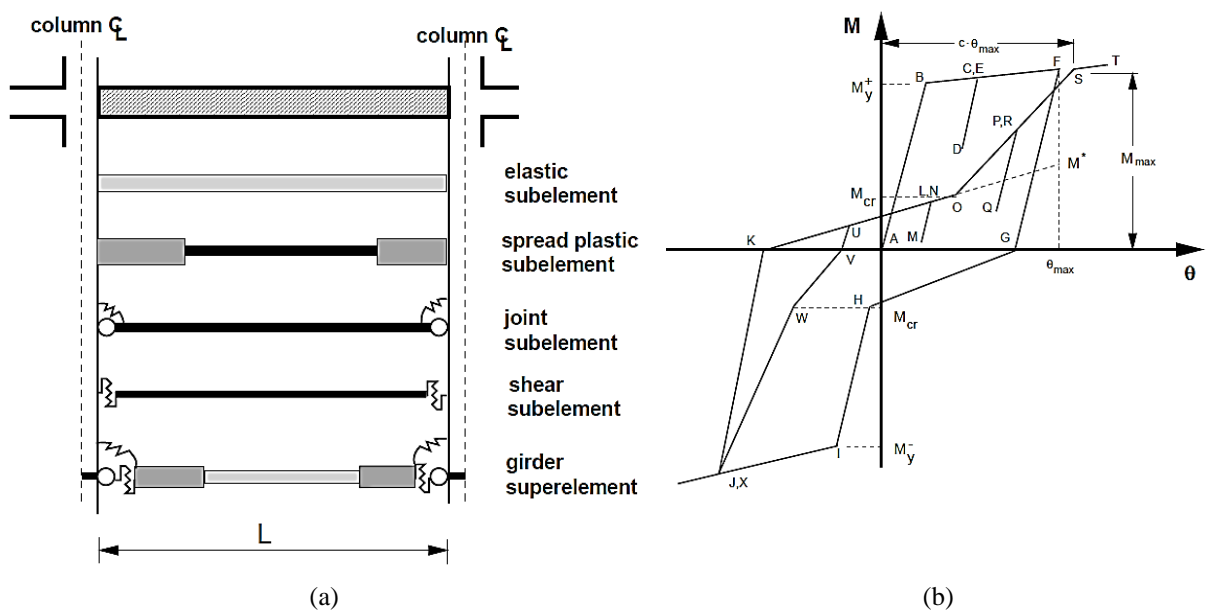


Figure 2-11: (a) Sub-elements composing the beam element, and (b) hysteretic shear model. (Filippou et al., 1992)

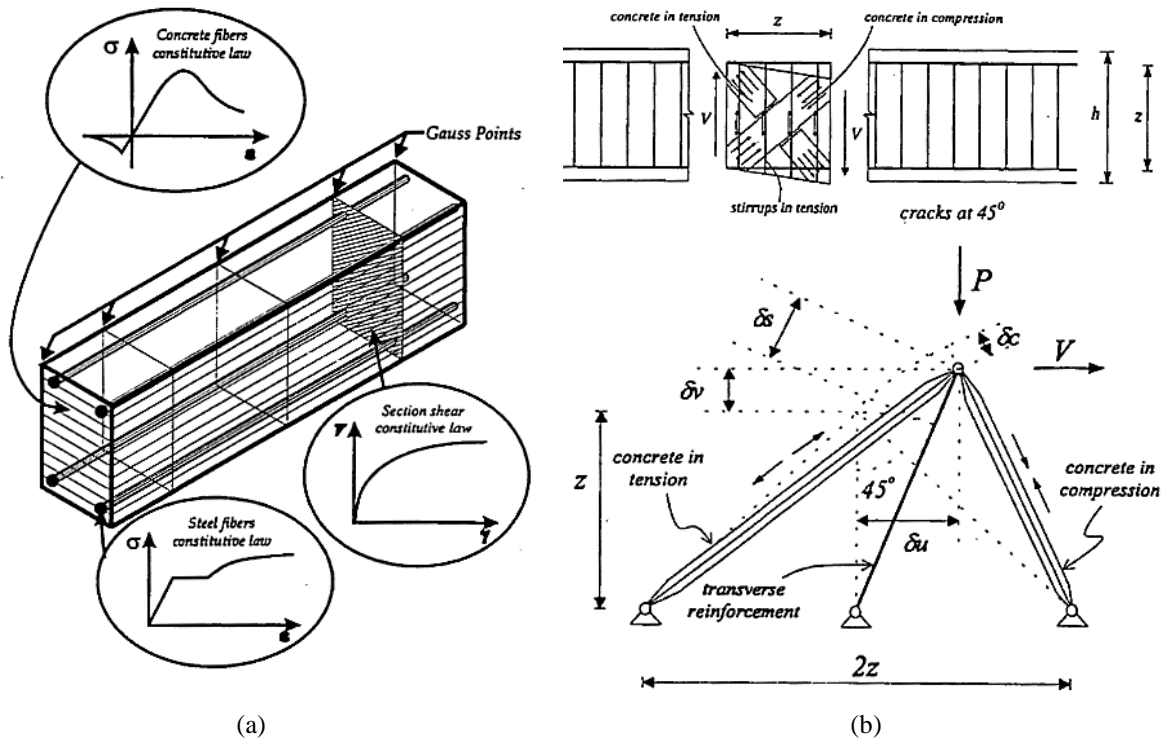


Figure 2-12: (a) Fibre element scheme, and (b) truss idealisation of a beam segment for identification of shear monotonic response. (Ranzo & Petrangeli, 1998)

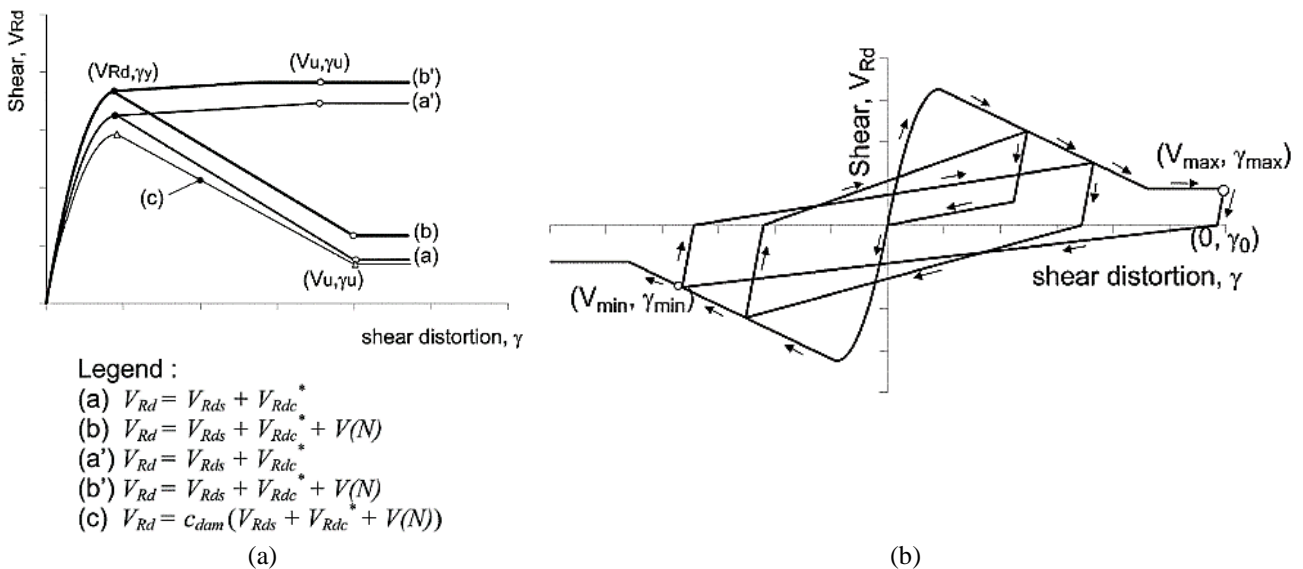


Figure 2-13: (a) Possible shear envelopes, and (b) shear hysteretic model. (Marini & Spacone, 2006)

Distributed inelasticity models have been found to suffer from numerical localisation issues in the post-peak range of the response, i.e. in the softening regime (Calabrese *et al.*, 2010). Numerical localisation should not be confused with the physical localisation occurring in structural elements during their softening response, as described previously; it is actually an inherent flaw of these finite elements, owing to their numerical formulation. It manifests as a steady increase of local deformations at the section where failure initiates as the number of integration points and/or mesh refinement increases, at the same value of total displacement demand. This occurs because when softening is developed, inelasticity is concentrated solely at

the most stressed integration point (controlling section) and the associated integration length (Figure 2-15). Therefore, the global and local predictions of distributed inelasticity elements depend on the applied finite element mesh or adopted numerical integration scheme (number and location of integration points) and therefore are not objective (Figure 2-16). To restore objectivity, several researchers have proposed regularisation techniques to overcome the problem of numerical localisation in the case of softening flexural response (e.g. Scott & Fenves, 2006; Coleman & Spacone, 2001; Calabrese *et al.*, 2010). These techniques aim at providing objective solutions that are realistic and physically meaningful in terms of the magnitude and spread of local deformations after the onset of flexural failure (Figure 2-17). Nonetheless, to the best of the writer's knowledge, no previous study has addressed regularisation of the post-peak response in the case of shear failure; addressing this could lead to objective prediction of the shear response at a local as well as global level.

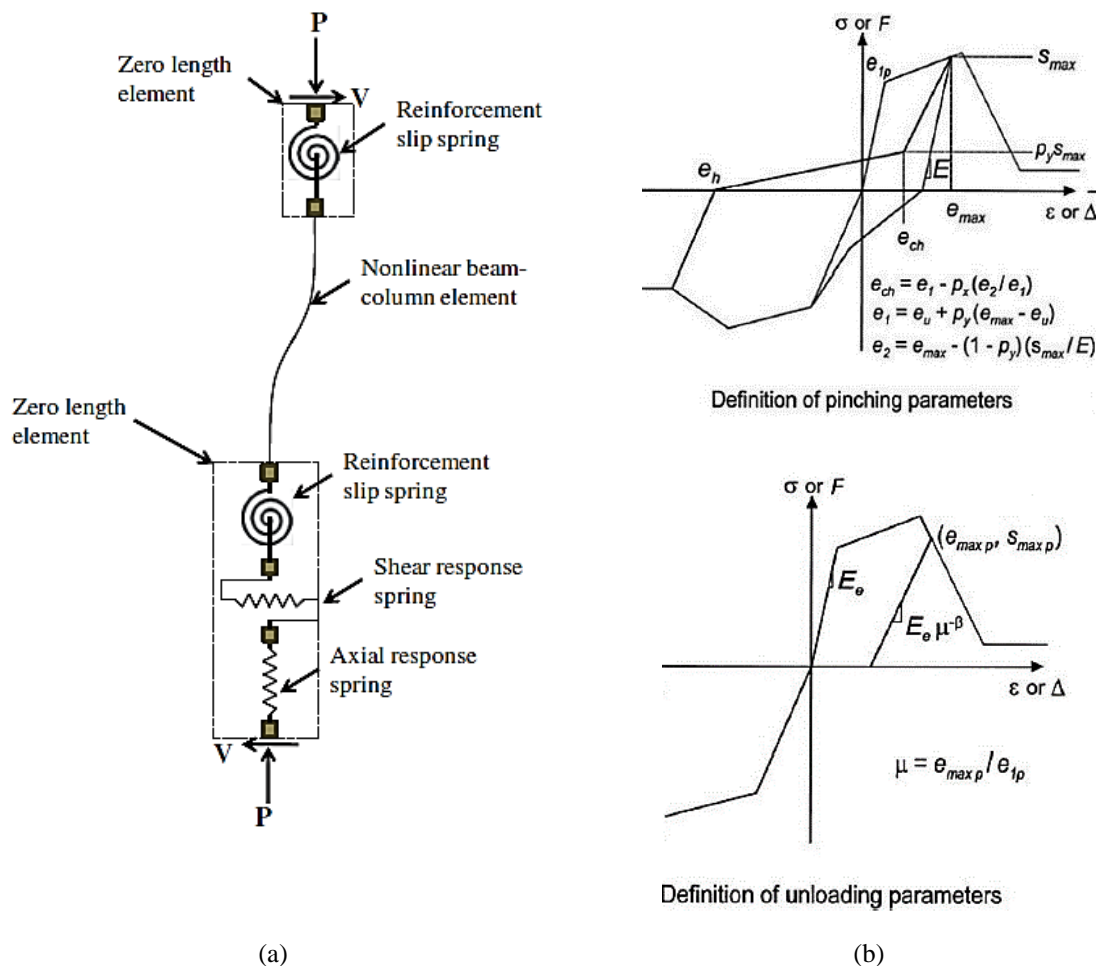


Figure 2-14: (a) Beam-column element in series with zero-length springs, and (b) hysteretic laws for zero-length springs. (Baradaran-Shoraka & Elwood, 2013)

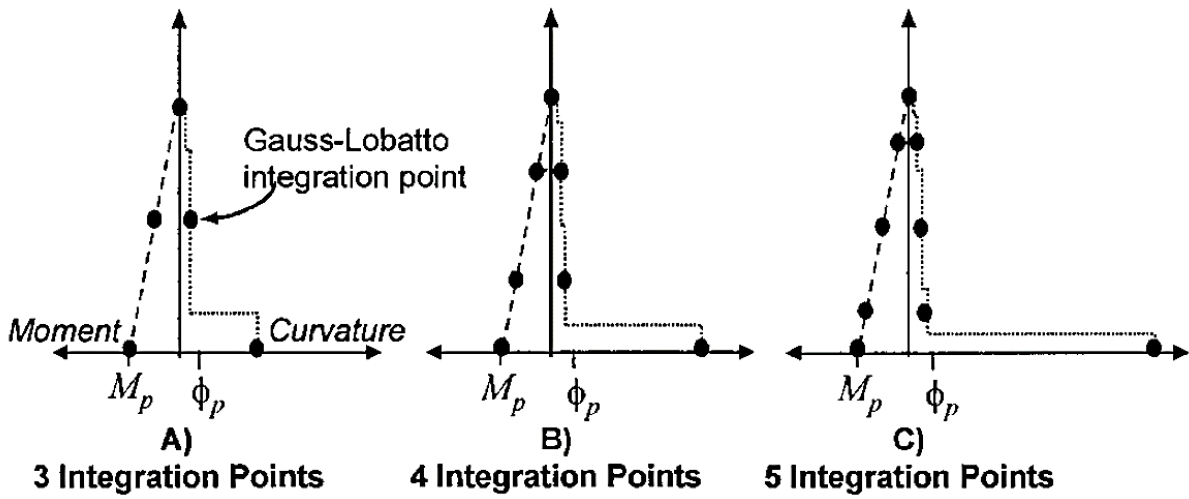


Figure 2-15: Numerical localisation in force-based elements in the case of softening response. (Coleman & Spacone, 2001)

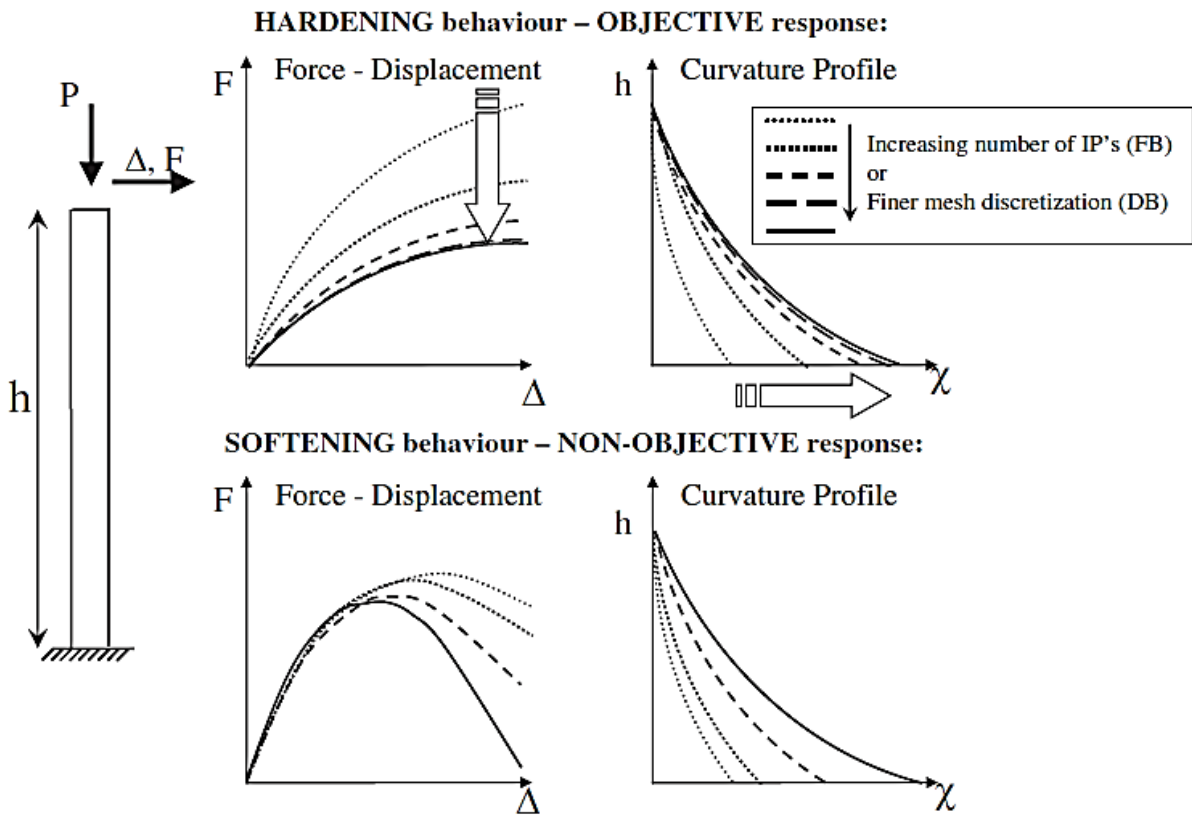
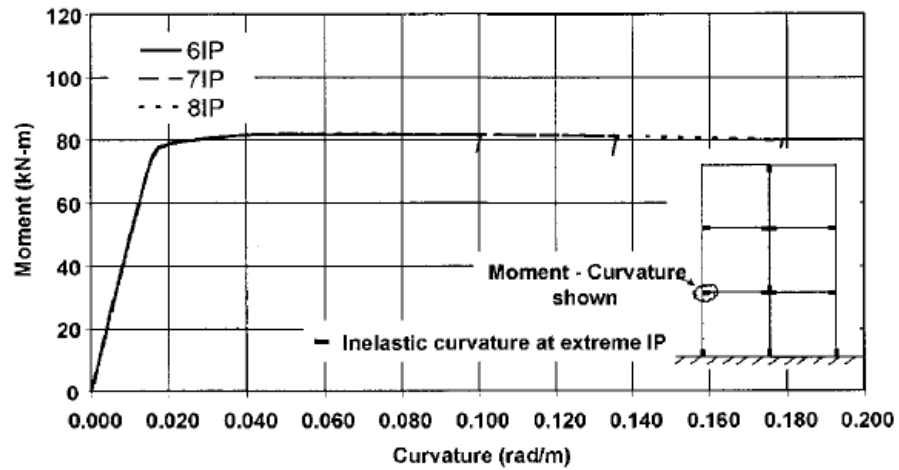
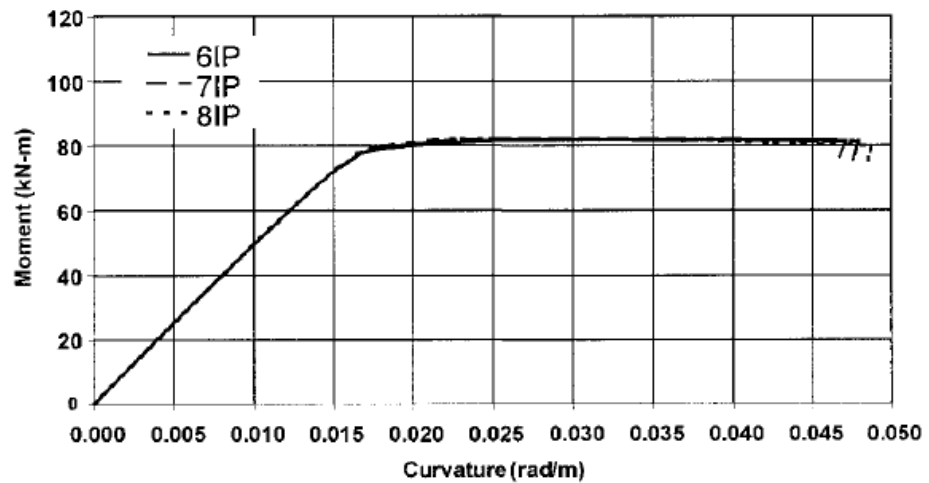


Figure 2-16: Example of numerical localisation (non-objective response) in the case of softening response. (Calabrese et al., 2010)



(a)



(b)

Figure 2-17: R/C frame response with zero strain-hardening (a) without regularisation (non-objective response), and (b) with regularisation (objective response). (Coleman & Spacone, 2001)

Advanced, structural-mechanics-based, shear models like the Modified Compression Field Theory (e.g. Vecchio & Collins, 1986) (Figure 2-18) or the Softened Truss and Membrane Models (Hsu, 1988; Hsu & Zhu, 2002), have proven to be rather accurate, but are limited to pre-peak shear behaviour. More recently, the Axial-Shear-Flexure Interaction approach was proposed (Mostafaei & Kabeyasawa, 2007), addressing post-peak shear response in addition to pre-peak. Nonetheless, these approaches involve high computational demand due to their iterative nature and do not capture the hysteretic response of R/C elements, hence do not readily lend themselves to use in seismic analysis of complex R/C structures.

There is a multitude of simplified shear models proposed over the years, predicting the shear response of an R/C member in terms of shear force against shear deformation or displacement (e.g. Takayanagi *et al.*, 1979; Maruyama & Jirsa, 1979; Ozcebe & Saatcioglu, 1989; Elwood, 2004; Sezen, 2008; LeBorgne & Ghannoum, 2013) (Figure 2-19b). They can be used in series with any element predicting flexural and possibly anchorage slip displacements to calculate the complete

lateral response of a member, no matter if it is a concentrated or distributed inelasticity model (e.g. Figure 2-19a). The most widely used model is arguably the cyclic model proposed by Ozcebe & Saatcioglu (1989) for the up-to-peak response of flexure-shear critical members (Figure 2-20). Various improvements on the original model have been proposed in later publications (e.g. Lee & Elnashai, 2001; Mergos & Kappos, 2008), mainly with a view to incorporating it into an inelastic dynamic analysis framework.

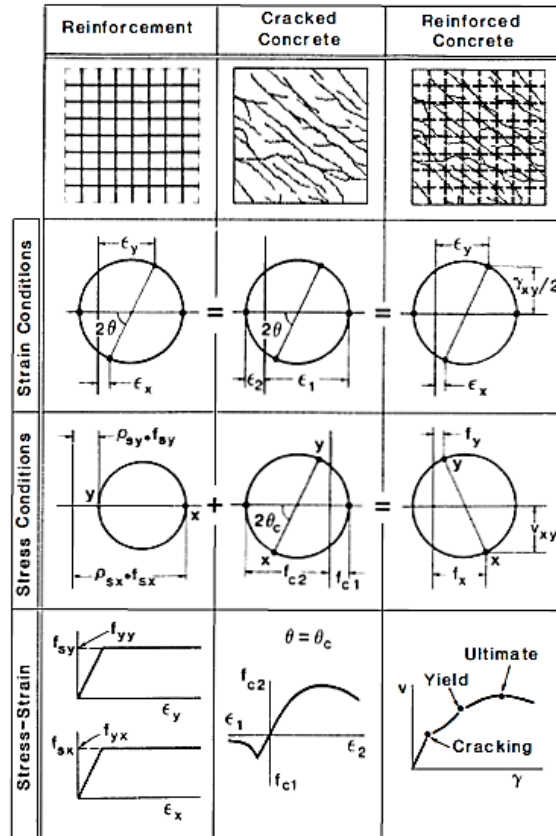


Figure 2-18: The modified compression-field theory for membrane elements. (Vecchio & Collins, 1986)

Several models adopt assumptions in the post-peak range that are not always appropriate and might lead to deviations in the resulting behaviour. For instance, the shear strength is typically considered zero at the point of axial failure, although this is not always the case. On top of this, the post-peak descending branch slope is not explicitly considered, i.e. the descending branch is assumed to be the “connecting line” between the points of shear and axial failure (e.g. Sezen, 2008; Elwood, 2004) (Figure 2-19a), falling short of predicting the experimentally recorded response. Moreover, some models consider a residual strength branch without solid experimental basis (e.g. Ricles *et al.*, 1998; Pincheira *et al.*, 1999; Leborgne & Ghannoum, 2013) (Figure 2-8b and Figure 2-19b). Such assumptions will be addressed in this thesis (see sections 4.3 and 4.4).

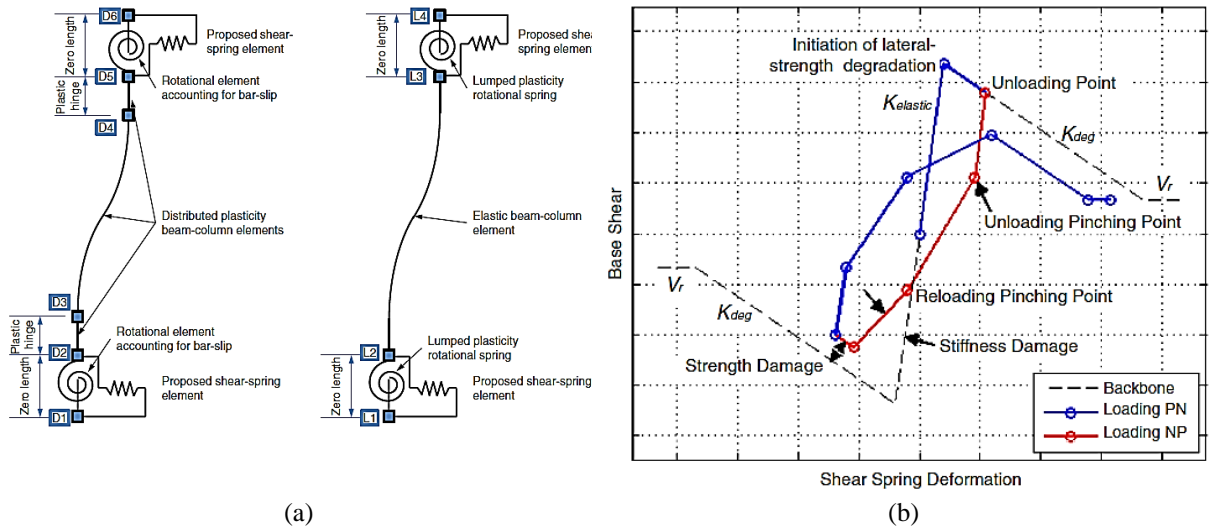


Figure 2-19: (a) Shear spring in series with lumped or distributed inelasticity beam-column element, and (b) shear backbone curve and hysteretic laws. (LeBorgne & Ghannoum, 2013)

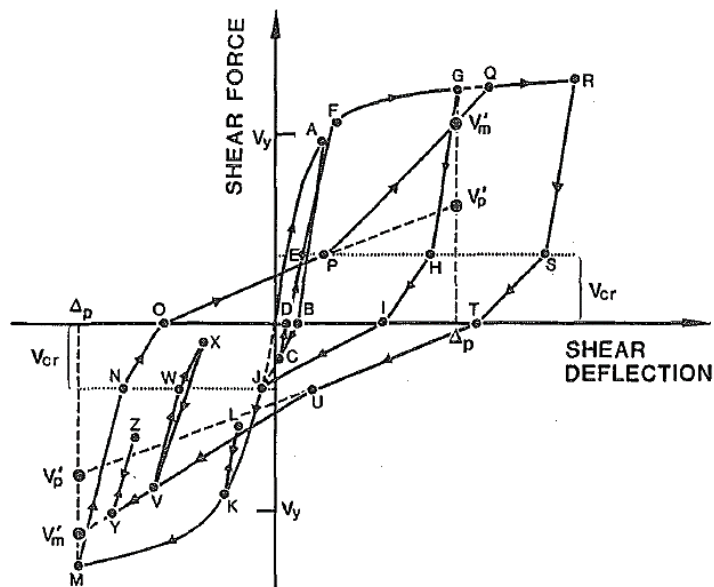


Figure 2-20: Shear hysteresis model. (Ozcebe & Saatcioglu, 1989)

A clear distinction should be made between different kinds of strength degradation, i.e. cyclic and in-cycle. It is a matter of importance, as highlighted by FEMA P440A (ATC, 2009), especially in the pursuit of realistically capturing the progressive collapse of a structural system. Cyclic strength degradation is the reduction of the strength of an R/C member or a system resulting from cyclic load reversals. This can be modelled as a function of the peak displacement reached (Figure 2-21a) or of the total hysteretic energy dissipated (Figure 2-21b) or as a combination of both. In-cycle strength degradation, on the other hand, is the strength reduction occurring within a cycle (Figure 2-22). This results from P- $\delta$  effects as well as longitudinal reinforcement bar buckling or fracture, concrete strength softening and other phenomena related to material nonlinearities in reinforced concrete structures (ATC, 2009).

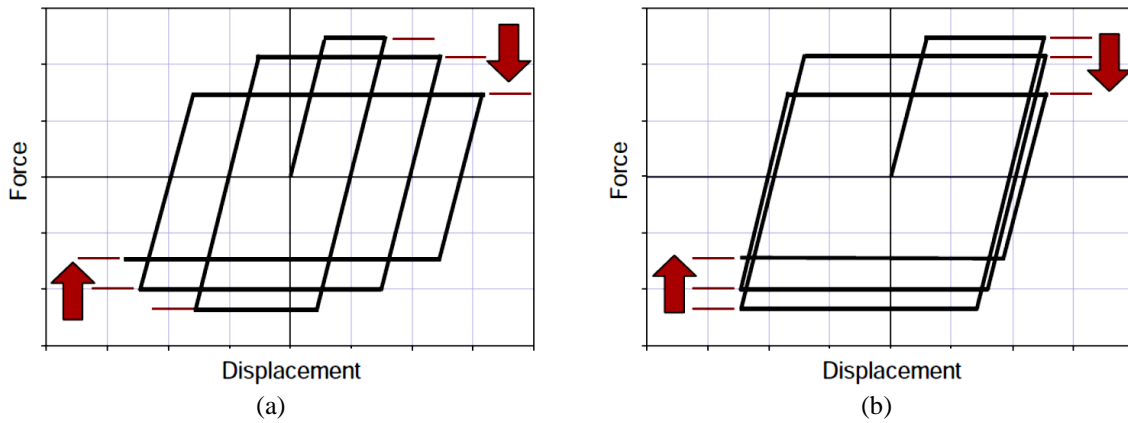


Figure 2-21: Examples of cyclic strength degradation as a function of (a) increasing inelastic displacement, and (b) repeated cyclic displacement. (ATC, 2009)

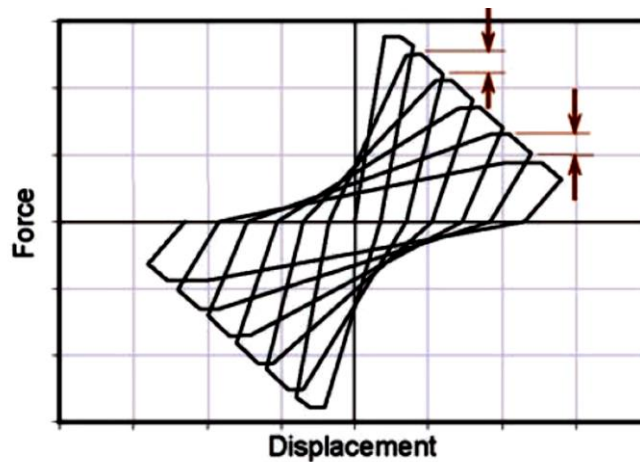


Figure 2-22: Example of in-cycle strength degradation. (ATC, 2009)

An example of how vital this differentiation is, particularly in the study of structural collapse, is displayed in Figure 2-23, wherein the response of two different systems following two different loading protocols is shown (ATC, 2009). The first system models only cyclic strength degradation (Figure 2-23a,c), while the other only in-cycle (Figure 2-23b,d). In the first loading protocol (Figure 2-23a,b), the resulting response is very similar in both systems. In the case of the second protocol (Figure 2-23c,d), however, the behaviour is similar in the beginning, but diverges vastly after the second cycle. The first system experiences high deformation, maintaining a considerable level of lateral resistance, whereas the second one is led to total loss of strength. Therefore, significant attention should be paid to the calibration of each type of strength degradation. An apparent degradation in lateral strength of a test specimen can often be misleading and lead to wrong categorisation between the two, hence rendering the calibrated parameters potentially useless for other loading paths.

Similarly, the distinction between the *capacity boundary* and the *cyclic envelope* should be underlined (ATC, 2009). The former refers to the maximum strength attainable by a structural member at any given displacement level, hence defining an outer limit of the force-displacement

relationship. The latter, however, constitutes the envelope of the cyclic behaviour of a structural member from a given test and is largely dependent on the loading protocol (ASTM-E2126, 2011). The ideal method for obtaining the capacity boundary of a member or a structural system is through a monotonic test (ATC, 2009). The cyclic degradation parameters are to be estimated, naturally, through cyclic tests; ideally, cyclic tests should have been conducted with various loading protocols. Nonetheless, the availability of sets of monotonic and cyclic (with multiple loading paths) tests is very limited. Considerable judgment must be exercised and the results must be treated with caution, since many different combinations of initial capacity boundary and degradation parameters might lead to the same result observed in one particular test. If a given cyclic envelope is used as capacity boundary in another test with equal or lower displacement steps, not much discrepancy will arise. Nevertheless, in cases of larger displacement steps, the response will be affected, underestimating the member's capacity.

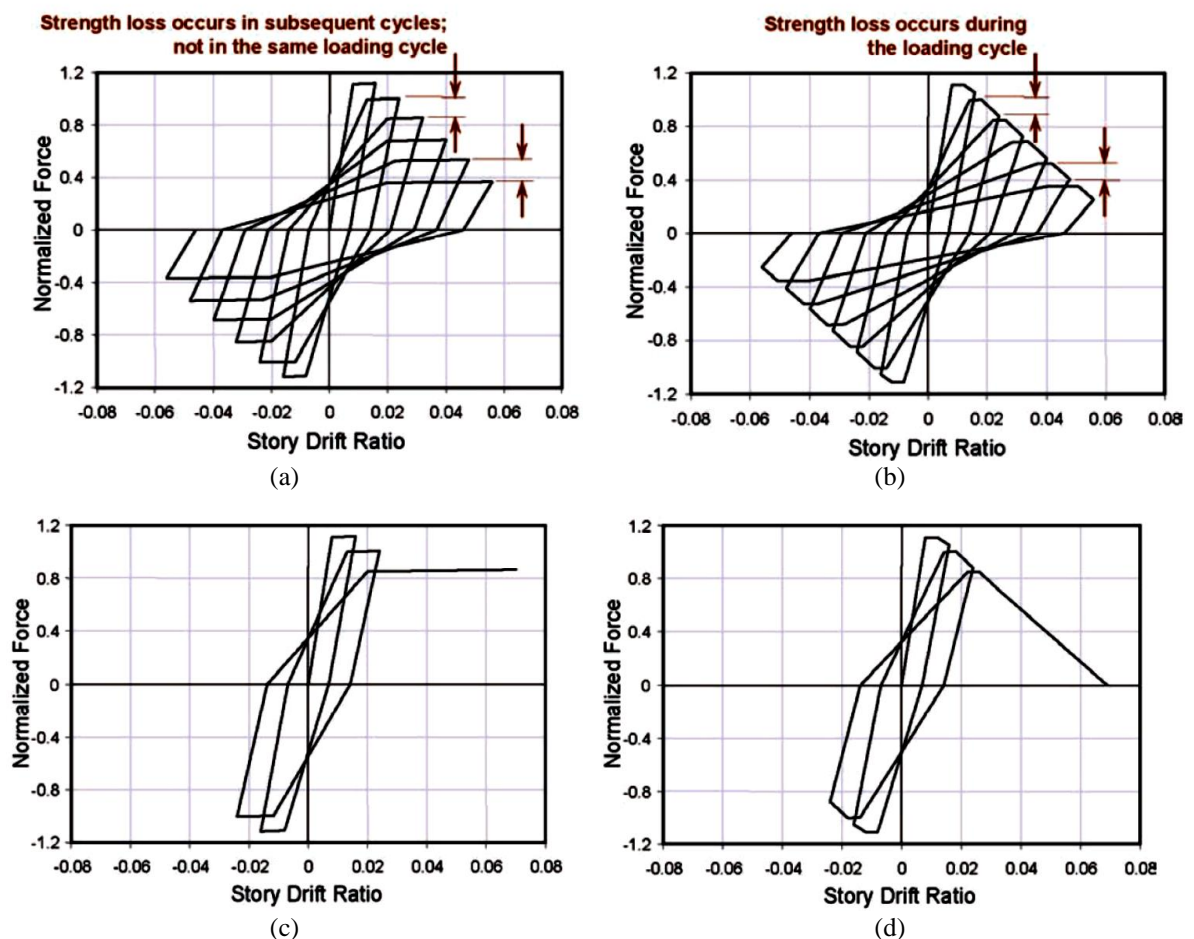


Figure 2-23: Hysteretic response for systems subjected to two different loading protocols, (a, b) one with many cycles with a small displacement step, and (c, d) one with few initial cycles and a pulse-type displacement at the end. (a, c) The first system models only cyclic strength degradation, (b, d) while the second only in-cycle degradation. (ATC, 2009)

*Analytical prediction of onset of axial failure*

Several studies have focussed on predicting the onset of axial failure of an R/C column. The pioneering work towards this goal was performed by Elwood & Moehle (2005a) and was based on the concept of the shear-friction model, i.e. the idealisation of a distinct inclined failure plane forming at shear failure with friction between the discrete upper and lower parts of the column (including aggregate interlock and dowel action of the reinforcement), a compression force normal to the crack and forces from the longitudinal and transverse reinforcements. When external loads exceed friction and sliding of one part of the column against the other along the diagonal crack starts or the axial capacity of the longitudinal bars is exceeded, axial failure of the column initiates. The proposed semi-empirical equation is the following:

$$\frac{\Delta_a}{L} = \frac{4}{100} \frac{1 + (\tan 65^\circ)^2}{\tan 65^\circ + N \left( \frac{s}{A_{sw} f_{yw} d_c \tan 65^\circ} \right)} \quad (2-1)$$

where  $\Delta_a/L$  is the lateral inter-storey drift of the column at axial failure,  $65^\circ$  is the assumed shear failure plane inclination with respect to the cross-section line,  $N$  is the axial load,  $s$  is the spacing between consecutive hoops,  $A_{sw}$  and  $f_{yw}$  the area and yield strength of transverse reinforcement and  $d_c$  the depth of the column core from centreline to centreline of the ties. This equation was based on 12 uniaxially loaded columns (Lynn *et al.*, 1996; Sezen & Moehle, 2006), which experienced flexural yielding, shear failure and axial collapse and which had quite a limited range of characteristics; shear strength is assumed to have degraded to zero when sliding begins.

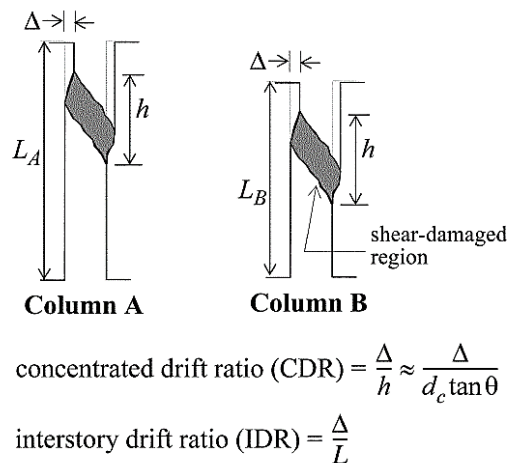


*Figure 2-24: Concentration of damage after the onset of shear failure. (Elwood & Moehle, 2005a)*

Elwood & Moehle (2005a) also mention that after shear failure, damage concentrates at a specific region (Figure 2-24), hence a Concentrated Drift Ratio (CDR) might be more appropriate than the Inter-storey Drift Ratio (IDR), however the latter is more consistent with the parameters

used in performance-based design methodologies. For instance, Figure 2-24 shows columns with the same CDR, nevertheless resulting in different IDR due to their difference in aspect ratio.

Elwood & Moehle's (2005a) model predicted a significantly conservative value of drift at axial failure for a column with high longitudinal reinforcement (Woods & Matamoros, 2010), indicating that longitudinal reinforcement should be taken into account in an axial capacity model. Yoshimura *et al.* (2003) also applied this model to their specimens. It has good correlation with those that had an axial load over longitudinal reinforcement yield capacity higher than 0.6, but very poor with the rest. They propose that longitudinal reinforcement be taken into account in the compression carrying capacity, to improve the model's accuracy. Furthermore, it has been proposed to include reduction factors for protocols with more cycles per displacement level, as well as biaxial loading (Simpson & Matamoros, 2012). Last but not least, it was proposed that the axial limit curve be shrank or be made steeper with increasing damage of the column (Elwood & Moehle, 2003).

Ousalem *et al.* (2004) developed a similar model, adopting slightly different assumptions. They assumed that the column shear strength at axial failure is negligible, they took into account the dowel action of the longitudinal reinforcement as a separate force, but they neglected its axial capacity due to probable buckling of the bars at that stage. They expressed the lateral drift ratio at axial failure as:

$$\frac{\Delta_a}{L} = \frac{1}{k} \sqrt[0.36]{\frac{0.97 - 1.33k}{\sqrt{0.03 + 1.33k}}}$$

$$k = \frac{\rho_w f_{yw}}{\nu f_c} \quad (2-2)$$

where  $\rho_w$  is the transverse reinforcement (volumetric) ratio,  $f_c$  is the concrete compressive strength and  $\nu$  the axial load ratio ( $\nu = N / (A_g \cdot f_c)$ ). Their expression was not very accurate and was based on a pool of data from 24 flexure-shear critical column tests, half of which were taken into account in the previously mentioned model (Elwood & Moehle, 2005a). They proposed that more parameters, like the column slenderness and the type of loading, be taken into account to improve the model. They also proposed that an upper limit be considered for Eq. 2-2 at a displacement level, which sub-standard columns would not be expected to exceed; based on the available dataset they proposed 9%, which could be refined with the addition of further data.

Matamoros & Von Ramin (2005) studied the deterioration of shear carrying mechanisms, which were identified as aggregate interlock, compression zone strength, arch and truss action. They take into account the decrease of the shear carried by the concrete in the damaged hinge region

as the lateral deformation increases, with the consequent higher demand on the transverse reinforcement. They assume this strength reduction begins at yielding. Furthermore, the truss shear strength component degrades with increasing drift ratio, albeit much less and not up to total loss of strength, i.e. there is a residual truss strength. Through analysing this residual strength, they proposed an expression of the drift ratio at axial failure. However, the data used for calibration were quite limited, i.e. only 11 flexure-shear critical lightly reinforced columns.

Zhu *et al.* (2007) developed a probabilistic model for the lateral drift of flexure-shear critical R/C columns at axial failure, largely based on, and very similar to, the aforementioned shear-friction model (Elwood & Moehle, 2005a), calibrated against 28 experimental tests. The median prediction is defined as:

$$\frac{\Delta_{a,median}}{L} = 0.1835e^{-1.45\mu}$$

$$\mu = \frac{\frac{N \cdot s}{A_{sw} f_{yw} d_c} - 1}{\tan 65 + \frac{N \cdot s}{A_{sw} f_{yw} d_c \tan 65}}$$
(2-3)

More information on the this model can be found in the original publication by Zhu *et al.* (2007). They propose that a larger range of parameters be taken into account to improve its predictive strength; an important extension would be to take into account columns having failed in pure shear failure.

Yoshimura (2008) proposed two purely empirical models for the prediction of the drift ratio at axial failure, one for shear and one for flexure-shear critical R/C columns. A very interesting feature of these models is that, although the axial load and transverse reinforcement ratios influence the drift similarly in both failure modes, the longitudinal reinforcement ratio seems to have inverse effect on each one. In shear critical members, it increases their deformability, while it decreases it in members that have yielded in flexure. This has to do with the mechanisms of failure in each mode, which have been analysed further above. The expressions are as follows:

$$\frac{\Delta_{a,S}}{L} = 62.2\rho_w - 51.9v + 6.07\rho_l - 9.91 \geq 1.5$$

$$\frac{\Delta_{a,FS}}{L} = 28.0\rho_w - 42.3v - 8.60\rho_l + 20.6 \geq 1.5$$
(2-4)

where S and FS denote shear and flexure-shear critical specimens, respectively, and  $\rho_l$  is the longitudinal reinforcement ratio.

Ousalem & Kabeyasawa (2006) studied axial failure, based on a previously proposed model by Uchida & Uezono (2003). They assumed the existence of a shear-damaged zone (Figure 2-25b), rather than a clear diagonal crack that was assumed in the previous model (Figure 2-25a). Results from previously published experiments carried out by the same authors as well as others exhibited the assumed behaviour of localisation of the damage at a given region leading up to axial collapse.

Based on the photographic documentation of a plethora of shear-failed members assembled herein (see chapter 3 and chapter 4), the failure mode along a diagonal crack (Figure 2-25a) is the norm. A well-defined shear-damaged zone mode (Figure 2-25b) is very rare and was only seen in specimens under monotonic lateral loading or limited cycling and subsequent monotonic push until collapse (Nakamura & Yoshimura, 2002; Yoshimura *et al.*, 2003). It is not clear if and how it could develop under purely cyclic lateral loading.

Kato *et al.* (2009) proposed two models for axial failure drift capacity, one for shear and one for flexure-shear critical R/C columns, both based on the shear-friction concept. The former consists of two components, the deformation up to the peak point and the descending branch one. The flexure-shear model additionally includes the flexural yielding deformation plus the plastic deformation up to the point of the onset of lateral failure. It was assumed that the longitudinal reinforcement does not contribute in the case of prior flexural yielding and that the deformation up to the peak point of shear-critical elements is almost negligible, when compared to the post-peak deformation.

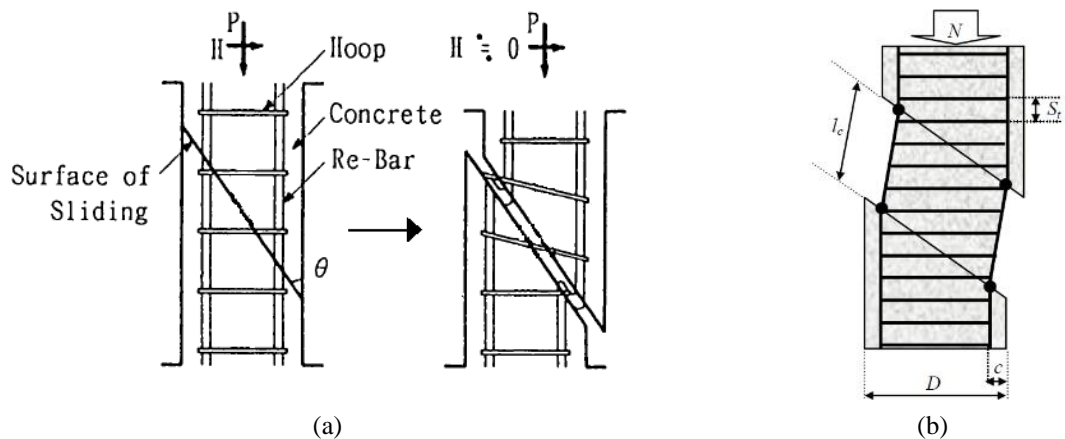


Figure 2-25: Mechanism at the onset of axial failure assumed by (a) Uchida & Uezono (2003), and (b) Ousalem & Kabeyasawa (2006).

Matsukawa *et al.* (2012) developed a theoretical model for the deterioration of the axial capacity of a column, based on the assumptions that: the cover concrete has spalled off completely due to cyclic loading, the influence of the transverse reinforcement on the axial load capacity is negligible, all axial capacity is attributed to the longitudinal reinforcement, the steel follows an elastic-perfectly-plastic behaviour (i.e. no hardening) and the lateral strength of the column

deteriorates to zero at axial failure. The basic concept is that, besides vertical loads, extra stresses act on the longitudinal bars due to  $P-\delta$  effects, the compressive part of which is added on the initial axial stress. Equilibrium of stresses at axial failure gives the maximum lateral drift possible, i.e. the lateral drift at axial failure. Rearranging the equation, one can get the residual axial capacity at any deformation level.

Matsukawa *et al.* (2013) improved the model, adding the effect of transverse reinforcement on the axial load capacity, via confining the crushed concrete core. They applied their complete analytical model to five different R/C frames that they tested. The shear behaviour prediction was not very satisfactory in the pre-peak region, but it was better in the post-peak part of the response, capturing decently the overall trends. The axial capacity along with the axial collapse prediction was in reasonable agreement with the experimental results in the case of the two more brittle frames, while the agreement was poor in the other specimens, underestimating their resistance and deformability.

Tran & Li (2013) proposed another shear-friction model, based on a database of 47 columns of various characteristics, which sustained axial failure. The semi-empirical model is based on reinforcement characteristics, concrete strength, cross-section area, axial force and displacement ductility of the member and is applicable in elements with or without prior yielding of the longitudinal reinforcement. It is assumed that lateral demand is negligible when axial collapse is reached, the failure plane inclination is considered constant and when the shear strength starts degrading, the subsequent deformation is assumed to derive solely from sliding across the shear failure plane. Comparing some experimental results with the predicted deformation from this model and a previous one (Elwood & Moehle, 2005a), the proposed one seems to yield slightly better predictions (Tran, 2010); however, the failure type and the characteristics of the compared elements are different from what the latter model was calibrated against. The model by Tran & Li (2013) was calibrated against a database with much broader characteristics, including columns of various aspect ratios, with more dense transverse reinforcement and higher longitudinal reinforcement ratio, but it is much more complex than the model proposed by Elwood & Moehle (2005a).

Pham & Li (2013), based on their experimental work, observed there are two distinct modes of axial failure. The first one is the aforementioned sliding along the critical shear failure plane. The second one, though, derives from vertical bond-splitting cracks and they concluded that Elwood & Moehle's (2005a) model, which is based on the assumption of a critical shear failure plane having formed, cannot predict the axial failure lateral drift in this case. This was also observed by Tran (2010). It is also noted that in specimens failing in bond-split there seems to be a residual branch, unlike specimens failing along a diagonal plane.

*Analytical prediction of inclination of shear failure plane*

The inclination of the diagonal shear failure plane, or herein termed *critical shear crack angle*, does not necessarily coincide with the angle of the first shear cracks that appear on a specimen. It is the angle corresponding to the failure plane that forms at shear failure and is generally different from the initial crack inclination. According to Elwood & Moehle (2005a), a first principles approach – i.e. calculating the nominal principal tension stress angle when the tensile capacity of concrete is reached under combined shear and axial load – will result in angles steeper than those experimentally recorded. They proposed a simple relation (although they used an average value of 25° for their axial capacity model), based only on the 12 columns tested by Sezen & Moehle (2006) and Lynn *et al.* (1996), and impose a geometrical minimum, which would apply in cases of columns with low aspect ratio:

$$\theta = 35 - 35 \frac{N}{0.85 f_c (A_g - A_{sl}) + f_{yl} A_{sl}} \quad (2-5)$$

$$\theta_{\min} = \tan^{-1} \left( \frac{h}{L_{cl}} \right)$$

where  $\vartheta$  is herein measured from the longitudinal axis,  $A_g$  is the gross cross-section area of the member,  $A_{sl}$  is the area of the longitudinal reinforcement,  $f_{yl}$  is the yield strength of the longitudinal reinforcement and  $L_{cl}$  is the clear length of the member.

Chang (1993) used limit analysis to calculate the shear crack angle, differentiating between three different categories, corresponding to (1) simultaneous yielding of longitudinal and transverse reinforcement (Eq. 2-6a), (2) yielding of transverse reinforcement and crushing of concrete (Eq. 2-6b), and (3) crushing of concrete while the reinforcement remains elastic in both directions (Eq. 2-6c):

$$\tau_u = \sqrt{\rho_l \frac{h}{d_c} \rho_w f_{yl} f_{yw}}, \tan \theta = \sqrt{\frac{\rho_w f_{yw}}{\rho_l \frac{h}{d_c} f_{yl}}} \quad (2-6a)$$

$$\tau_u = \sqrt{(f_c - \rho_w f_{yw}) \rho_w f_{yw}}, \sin \theta = \sqrt{\frac{\rho_w f_{yw}}{f_c}} \quad (2-6b)$$

$$\tau_u = \frac{1}{2} f_c, \theta = 45^\circ \quad (2-6c)$$

$$\tan \theta_{\min} = \frac{d_c}{2L_{cf}} \quad (2-6d)$$

with  $L_{cf}$  being the length of the column up to the contraflexure point. The lowest value of  $\tau_u$  defines the failure mode, and the corresponding angle is to be used. The minimum reportedly corresponds to the rocking effect (Eq. 2-6d) and is exactly the same as the one imposed by Elwood & Moehle (2005a) above, assuming that the top bending moment is equal to the bottom.

Kim & Mander (1999) used an energy minimisation of external work approach, taking into account shear and flexural displacements, to calculate the angle where shear cracking will occur:

$$\tan \theta = \sqrt[4]{\frac{\rho_w n + \zeta \frac{\rho_w b d_c}{\rho_l A_g}}{1 + \rho_w n}} \quad (2-7)$$

where  $\zeta$  is a boundary condition constant, equal to 0.5704 for fixed-fixed and 1.5704 for fixed-pinned columns;  $n$  is the ratio of the modulus of elasticity of steel over that of concrete. In their study, the (well-known from strut-and-tie models) assumption of two separate region types along elements with respect to cracking was made (Figure 2-26). In the B-region, the Bernoulli hypothesis applies, while the other is the D-region or disturbed region, which occurs near concentrated loads, corners, openings and other discontinuities. The cracking inclination is constant in the former and variable in the latter and they assumed that the steepest angle of the disturbed region is equal to the constant crack angle of the undisturbed region (Figure 2-26c).

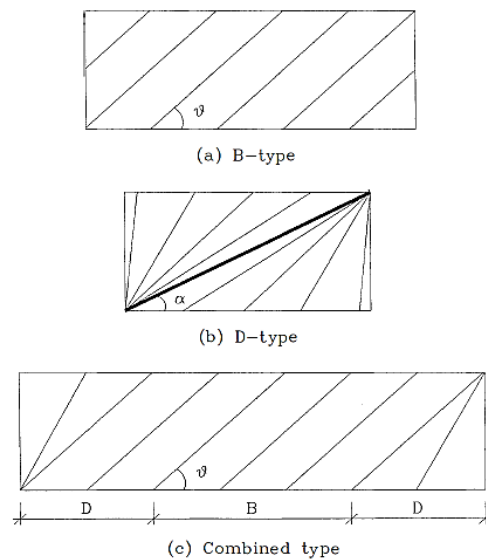


Figure 2-26: Distinction between the (a) undisturbed (B-type), and (b) disturbed (D-type) region of a specimen, according to the shear cracks that are developed. (c) The most common case is a combination of both along the member. (Kim & Mander 1999)

Ousalem *et al.* (2003) developed an empirical relationship for the inclination of the critical shear crack angle as part of a shear-friction model. The expression is the following:

$$\tan \theta = 3 \frac{\rho_w f_{yw}}{(\rho_l f_{yl} + f_c) v} + 0.15 \quad (2-8)$$



PART I: INVESTIGATION OF THE POST-PEAK RESPONSE OF  
SHEAR-DEFICIENT R/C MEMBERS



## Chapter 3: DATABASE COMPILATION

For the purpose of investigation of R/C member post-peak response, a large database of shear and flexure-shear critical elements, which were cycled well beyond the onset of shear failure or for which clear photographic evidence of their shear cracking was available, was compiled. It comprises 151 rectangular R/C columns, 68 of which have sustained flexure-shear failure (hereafter noted as “FS”) and 83 shear failure (hereafter noted as “S”). To the best of the writer’s knowledge, it includes the largest collection (to date) of rectangular R/C columns cycled well into the post-peak domain after the onset of shear failure (116) and/or eventually failing axially (89). Their main characteristics are summarised below and the specimens are presented in detail in Table A-1 (Appendix A: Database Specimens, below). Some of them were taken from the [SERIES database](#) (Perus *et al.*, 2014), while most of them were obtained directly from original sources.

### 3.1 DESCRIPTIVE STATISTICS

The ranges of the main characteristics of the database specimens in terms of longitudinal reinforcement ratio ( $\rho_l$ ), transverse reinforcement ratio ( $\rho_w$ ), stirrup spacing over effective depth ( $s/d$ ), aspect ratio ( $L_s/d$ ), maximum shear stress ratio ( $\tau_{max}/\sqrt{f_c}$ ) and axial load ratio ( $v$ ) (3 specimens in tension are presented separately) are summarised in Table 3-1 and are presented in detail further on, using histograms (Figure 3-1 to Figure 3-4). The most important design parameters provided by the researchers in the respective reports/papers as well as dimensionless parameters, derived from combination of primary parameters, are included (Figure 3-1 and Figure 3-2). Qualitative parameters are also included (Figure 3-3 and Figure 3-4); these are used to describe each specimen and its behaviour, categorising it without resorting to numerical values, as opposed to the measurable quantitative parameters.

Table 3-1: Main specimen characteristics of the database.

	Min	Mean	Max
$\rho_l$ (%)	0.16	2.25	4.76
$\rho_w$ (%)	0.08	0.38	1.59
$s/d$	0.11	0.44	2.52
$L_s/d$	0.90	1.94	4.29
$\tau_{max} / \sqrt{f_c}$	0.22	0.57	1.23
$v$ (compressive)	0.00	0.27	0.80
$v$ (tensile)	-0.26	-0.15	-0.07

The test configuration type is divided into cantilever (C), double-curvature (DC) and hammer-head specimens (HH) (Figure 3-5), in line with the PEER categorisation (Berry *et al.*, 2013). The hoop configuration is divided into multiple types, again in line with the PEER categorisation;

there are specimens with interlocking (I), rectangular (R), rectangular and diagonal (RD), rectangular and interlocking (RI) ties, rectangular ties and J-hooks (RJ) and U-bars with J-hooks (UJ) (Figure 3-6). The loading type is annotated as CD for specimens with cyclic response exhibiting post-peak descending branch parts (i.e. in-cycle strength degradation, or parts with negative stiffness), CS for cyclic ones without in-cycle strength degradation, M for specimens with purely monotonic response, MC for specimens with monotonic response after initial cycling up to a point (before the onset of shear failure) and NO for the specimens without post-peak response, due to simultaneous shear-axial failure (Figure 3-4).

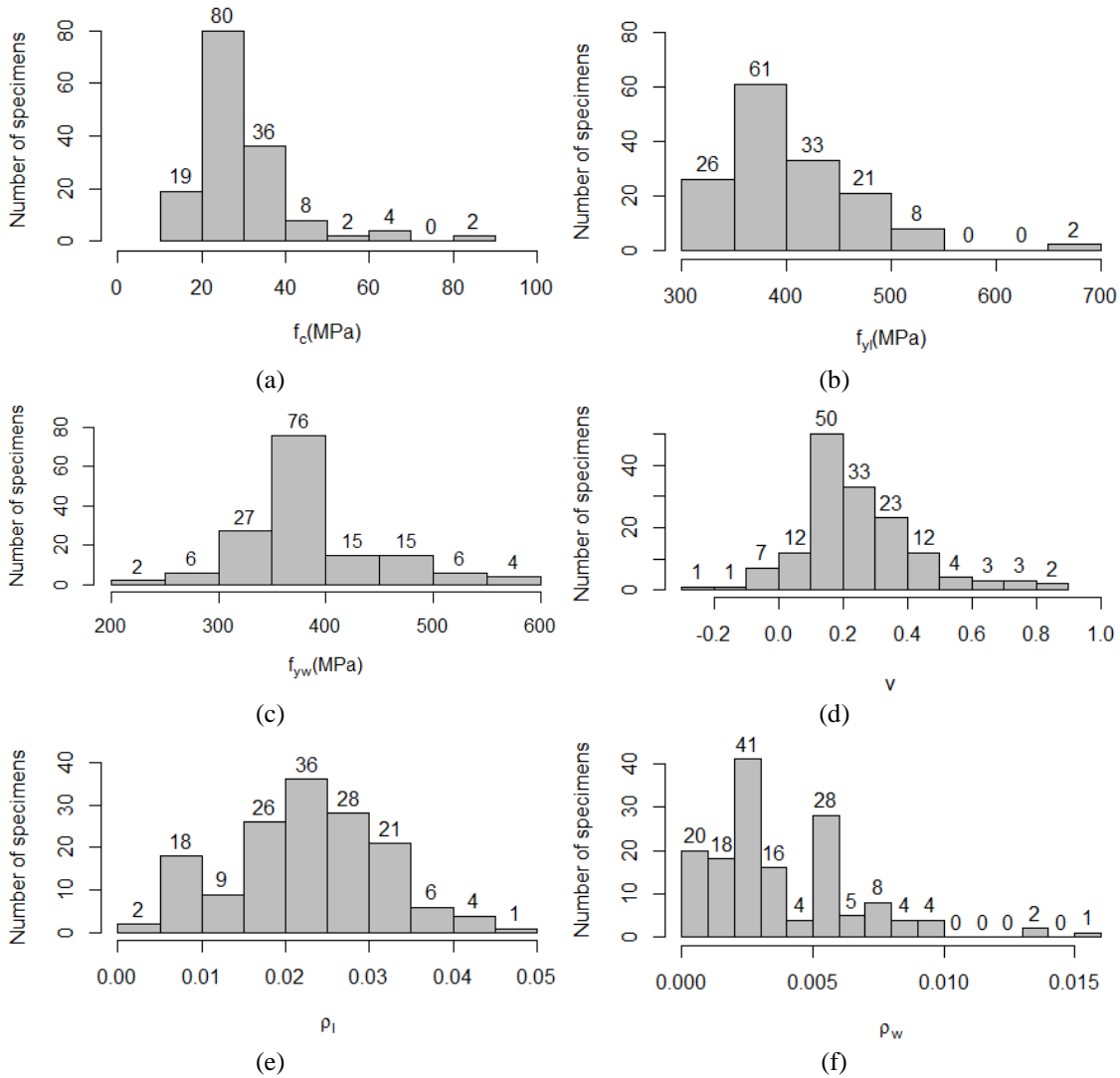
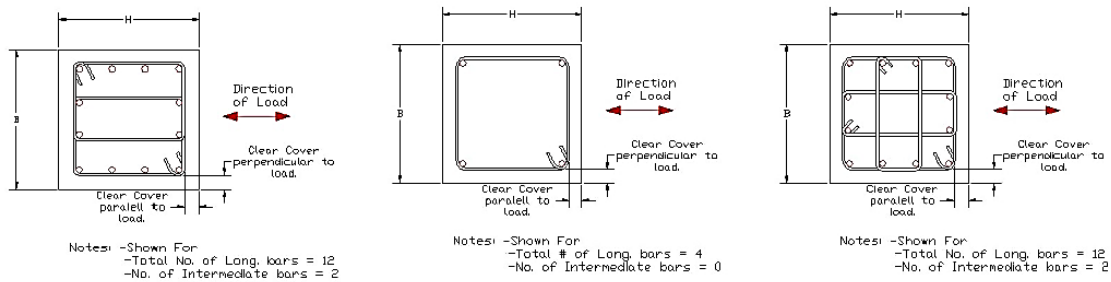


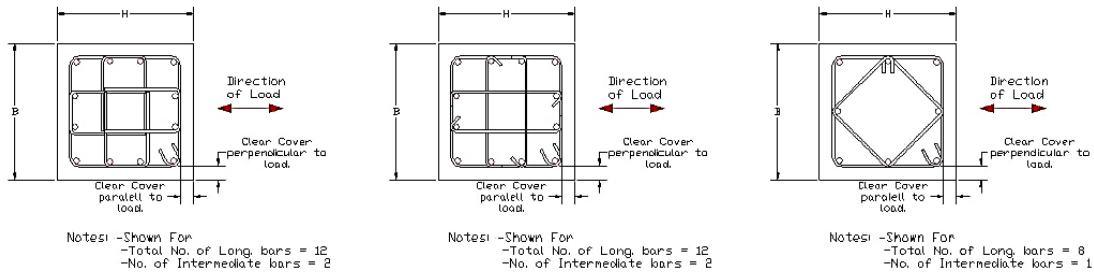
Figure 3-1: Distribution of specimens' (a) concrete compressive strength, (b) longitudinal reinforcement yield strength, (c) transverse reinforcement yield strength, (d) axial load ratio, (e) longitudinal reinforcement ratio, and (f) transverse reinforcement ratio, in the database.



Confinement Type I    Confinement Type R    Confinement Type RI



Confinement Type RU    Confinement Type RJ    Confinement Type RD



Confinement Type RD    Confinement Type RIJ    Confinement Type UJ

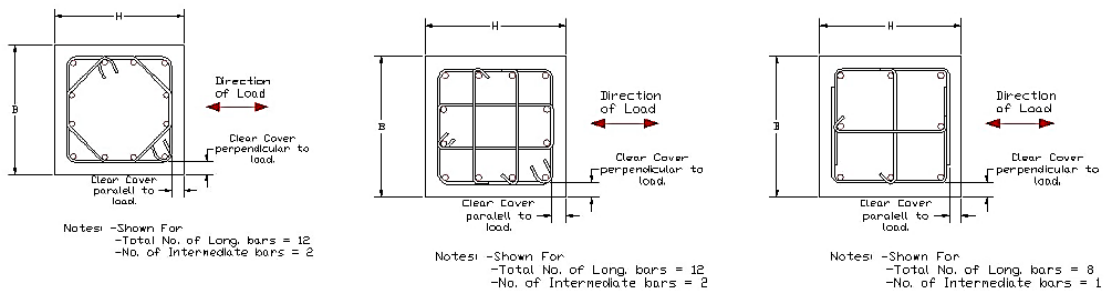


Figure 3-6: Hoop configuration types. (Berry et al., 2013)

## 3.2 DATA COLLECTION AND PROCESSING

### 3.2.1 P-δ Correction

Due to lateral deflections during cycling, the axial load acting on the specimen produces a secondary moment at the cantilever base ( $P \times \delta$ ) (Figure 3-7). This can be considered a linear function along the height of the specimen (Figure 3-7c). In reality, however, the secondary moment follows the deflected shape of the specimen (Figure 3-7b). P-δ correction has been applied to the force data gathered in this database considering the distribution of moments linear, being the conservative as well as the traditionally followed approach.

An explanation of the influence of P-δ on the hysteretic behaviour of elements is provided in Figure 3-8. In effect, as far as the 1<sup>st</sup> and 3<sup>rd</sup> quadrants are concerned, the P-δ-moment “consumes” part of the total lateral capacity of the specimen. So, the problem is not that the member’s lateral resistance decreases in an absolute sense, but that this secondary action takes

up part of it, so only a fraction of the resistance of the lateral loading remains available. In the 2<sup>nd</sup> and 4<sup>th</sup> quadrants, one can see that there is an ostensible increase in the resistance of the specimen, i.e. it seems more resistant than it should normally be. It is easy to grasp why, since there is an extra destabilising moment ( $P \times \delta$ ) that has to be counteracted before the member can return to its original position.

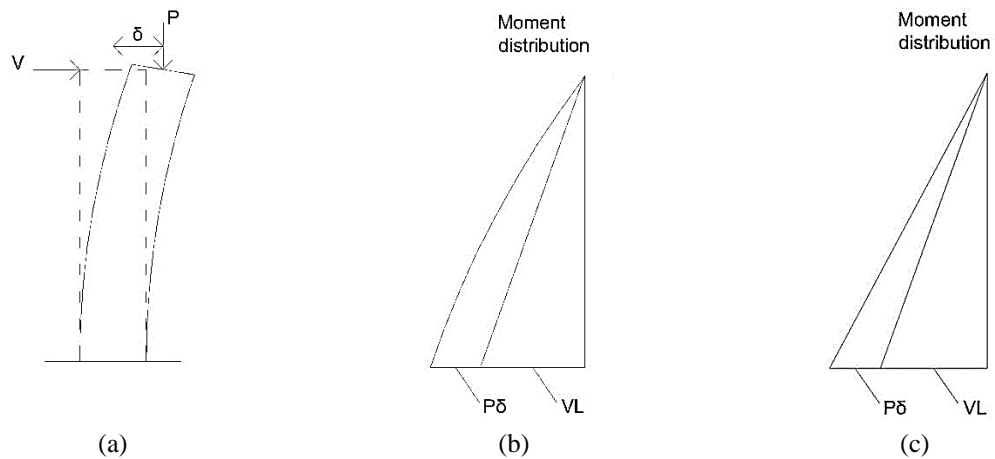


Figure 3-7: (a) Cantilever specimen undergoing constant vertical and cyclic lateral loading; its bending moment distribution (b) following the deflection shape of the specimen, or (c) with linear distribution simplifying assumption.

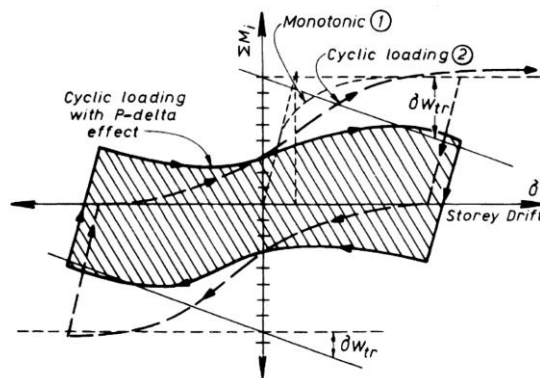


Figure 3-8: Bending moment - storey drift relationship for a ductile sub-frame with and without P- $\delta$ . (Paulay, 1978)

The target is to treat hysteretic response in a uniform way while being compatible with the procedures used in [IDARC 2D v. 7.0](#) (Reinhorn *et al.* 2009; Valles *et al.* 1996), where the beam-column model will be coded. In IDARC as well as several other programs, a matrix similar to a geometric stiffness matrix is computed at each step; it is calculated from the equivalent moments (secondary moments) produced at each story level due to P- $\delta$ . This matrix is subtracted from the stiffness matrix of the whole structure in the beginning of the next step (Reinhorn *et al.*, 2009). It is an "exact" method, assuming that the axial loads on the members do not change during lateral loading (which is not generally the case, especially at the end columns of frames) and that the lateral displacements are small compared to the structural dimensions (which is a typical assumption), as explained by Wilson (2002). There are other

iterative methods, which approximate the phenomenon more accurately, but are computationally inefficient and not well-fitting to nonlinear dynamic analysis, due to the lengthening of the structural periods of vibration caused by P- $\delta$ .

At this point, the distinction should be made between:

- $F_{eff} = M_{base} / L$ , i.e. the effective shear force.
- $F_H$ , the net horizontal shear force acting on the column.
- Another force component,  $F_{P-\delta}$ , i.e. the equivalent shear force caused by vertical loads and the lateral drift of the member.

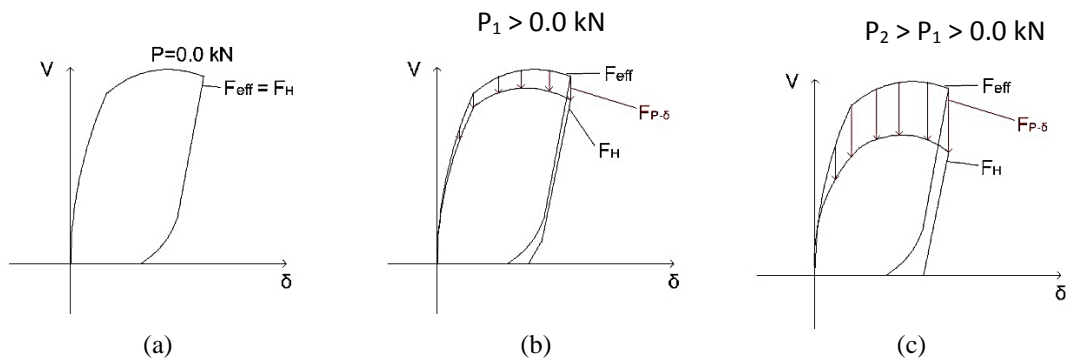


Figure 3-9: Indicative response of an R/C element, upon which three different axial loads are applied.

Of course, the relation  $F_{eff} = F_H + F_{P-\delta}$  holds. This distinction between the actual shear caused by horizontal loads ( $F_H$ ) and by P- $\delta$  ( $F_{P-\delta}$ ) becomes clearer in Figure 3-9 with the help of an indicative example. The lateral response of an R/C element is shown, upon which three different axial loads (compression positive) are applied. It is obvious that (at a given displacement) the higher the axial load, the higher the  $F_{P-\delta}$ , hence reducing the capacity available for the actual horizontal force  $F_H$ , which leads to the eventually recorded response.

The most effective and reasonable method in this case is to obtain the hysteretic behaviour of the full shear from the experimental results ( $F_{eff}$ ), no matter the axial load. In case a P- $\delta$ -free curve is given ( $F_H$ ),  $F_{P-\delta}$  should be added to the reported shear accordingly. Having this as input, the P- $\delta$  effects will be introduced automatically by IDARC, depending on the magnitude of the axial load during the analysis, and the final  $F_H$  curve can be produced.

Depending on the loading setup, there are different P- $\delta$  configurations. The distinction followed in the [PEER database](#) (Berry *et al.*, 2013) will be employed (Figure 3-10). The explanation as well as correction equations for each case are:

- Case I  
 $F_{eff}$  is directly reported by the respective researcher, no correction needed.

- Case II  
 $F_H$  is reported, so  $F_{P-\delta}$  needs to be added to get the full response:  
 $F_{eff} = F_H + P \Delta / L$

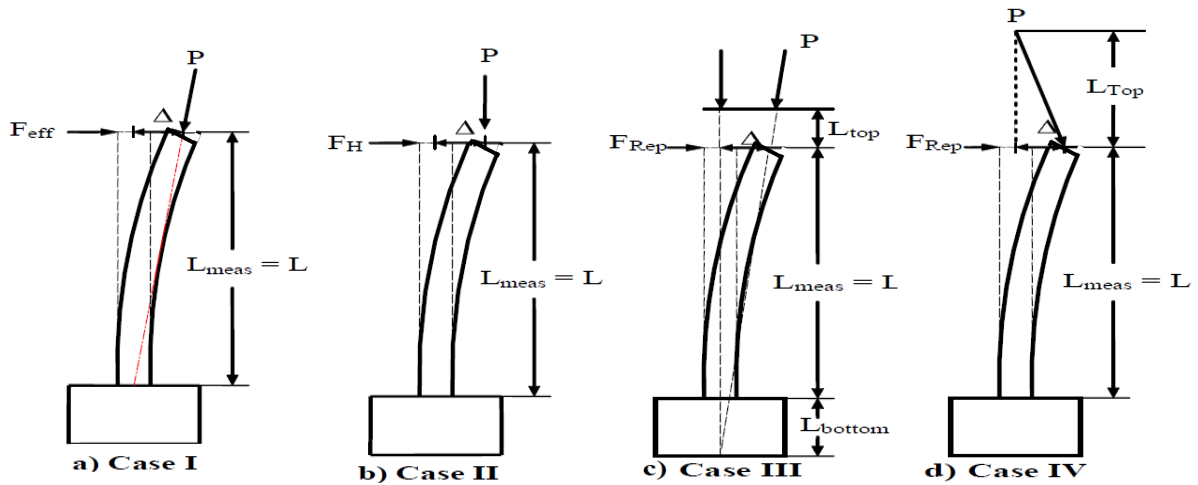


Figure 3-10: Different  $P-\delta$  configuration cases (Berry et al., 2013).

- Case III  
 $F_{Rep}$  is reported and the axial load acts at a higher elevation than the horizontal actuator or its line of action does not pass through the column base:  
 $\alpha = \tan^{-1}(\Delta / (L + L_{bot}))$   
 $F_{eff} = F_{Rep} + P L_{bot} \sin \alpha / L$
- Case IV  
 $F_{Rep}$  is reported and the top of the vertical actuator is pinned:  
 $\alpha = \tan^{-1}(\Delta / L_{top})$   
 $F_{eff} = F_{Rep} + P (L + L_{top}) \sin \alpha / L$

Notation:

$L$  : shear span length

$P$  : gravity (vertical) load

$\Delta$  : measured displacement at cantilever elevation  $L_{meas}$

$L_{meas}$  : elevation at which lateral column displacement was measured

$F_H$  : net horizontal force

$F_{Rep}$  : reported force, lateral load applied by the horizontal actuator

$F_{eff}$  : total (effective) shear force

$\alpha$  : angle pertinent to direction of vertical force (calculated accordingly in Cases III and IV)

### 3.2.2 Critical Shear Crack Angle

The critical shear crack angle, or the inclination of the idealised diagonal shear failure plane, is herein measured with respect to the longitudinal axis of the member. Very few such angle values were provided by researchers. The rest of them were obtained from available photographic documentation of specimens exceeding the onset of shear failure (e.g. Figure 3-11). This angle does not necessarily correspond to the first shear cracks that appear on a specimen along the

principal compressive stress trajectories, when the tensile strength of concrete is exceeded. These can be readily calculated according to structural mechanics principles and generally result in steeper angles than the experimentally observed ones (Elwood & Moehle, 2005b).

However, measuring this angle is not always so straightforward, for example due to the state of the specimens after collapse, as reported by Elwood & Moehle (2005b) who tried to subjectively estimate this angle from photographic evidence of columns after axial failure, and in general due to the complex and sometimes chaotic patterns of cracking. Therefore, the following procedure and assumptions are adopted for the angle measurement:

- The objective of the angle measurements, is to appropriately estimate the length of the shear-damaged region, or herein called *critical shear length*, which forms part of the conceptual basis of the proposed model, as will be explained in section 4.1 in more detail.
- In shear critical specimens, the major apparent shear crack is taken into account, if there is a clear one; Umemura & Ichinose (2004) mention that the slippage between the two parts of the column is concentrated along the thickest of the cracks, which dominates shear failure. Even when there is a major shear crack, however, its inclination may vary; in that case, an average inclination was considered, with a view to appropriately measuring the critical shear length, as mentioned above.
- If there is no clear major crack, the average inclination of the shear-cracked zone was taken into account (e.g. Figure 3-11a), with a view to appropriately measuring the critical shear length, as mentioned above.
- When shear failure takes place near the ends of a specimen, as typically is the case in flexure-shear critical elements, the phenomenon becomes more complex. Kim & Mander (1999) adopt the (well-known from strut-and-tie models) distinction between the B-Region, which is governed by beam-action and Bernoulli's hypothesis of plane sections remaining plane holds, and the D-Region, where the strain section distribution is disturbed and may be significantly non-linear (Figure 2-14a,b). In most cases, one can see a combination of these two regions, as shown in Figure 2-14c. In these cases, they claim that "*the steepest crack angle to the longitudinal axis of the fan-shaped cracks at the disturbed region of the column will be equal to the constant crack angle at the undisturbed region*" or  $\alpha = \vartheta$ , according to the notation of Figure 2-14; this assumption is also adopted by Collins & Mitchell (1997). So, in the cases that the cracked zone lies in the disturbed region, the steepest angle (in other words, the lowest-value angle with respect to the longitudinal reinforcement) is selected as the critical one.

- Moreover, shear cracks of flexure-shear critical elements tend to turn to horizontal flexural cracks towards the end. This part was disregarded in the estimation of the angle.

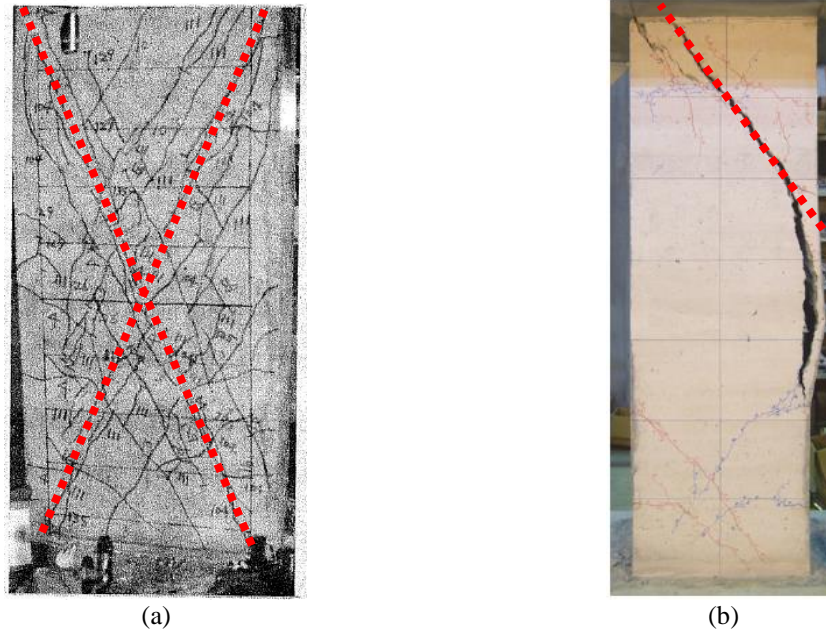


Figure 3-11: Indicative extraction of critical shear crack angle from experimental photographic documentation: specimens by (a) Umehara & Jirsa (1982), and (b) Nakamura & Yoshimura (2014).

- Matsukawa *et al.* (2013) provide photos both at the onset of shear and axial failure of their specimens and it is estimated that the average crack angle measured is practically identical. Therefore, the angle can be measured no matter which state of response is provided, so long as the critical shear crack has formed, i.e. at or after the onset of shear failure.
- Nonetheless, it is observed in Matchulat's (2009) specimens (for which photos both at the onset of axial failure and at an advanced axial failure stage are provided) that after axial failure there can be considerable shortening of a member, especially due to buckling of reinforcement along the shear crack critical angle. This can lead to an ostensibly shorter critical shear length, hence higher measured angle. The angles prior to such shortening are gathered in the database; if no other photograph is available, the shortening is taken into consideration through engineering judgement, which however needed to be done in very few specimens.
- Cracks parallel to the longitudinal axis, typically caused by bond-split of the longitudinal reinforcement, are disregarded in measurements (e.g. Figure 3-11b).
- In most cyclic tests, shear cracks appear in both directions with the characteristic X-pattern (e.g. Figure 3-11a); in these cases the average of both directions is used.

Besides the aforementioned procedure, corrections were applied to account for the rotation of the specimen about its longitudinal axis in the photograph and the downward or upward perspective, in order to get the correct shear crack angle. These corrections are presented in detail in Appendix B.

### 3.2.3 Descending Branch

The post-peak behaviour of specimens with at least 30% shear strength degradation (reaching beyond 70% of  $V_{max}$  post-peak) was considered, in order to have a genuine descending response. Thus, experiments conducted up to 85% or 80% of  $V_{max}$ , which constituted the overwhelming majority until recently, were excluded. For the graph digitisation, the software [GetData Graph Digitizer 2.26](#) was used. The descending branch of the curve was obtained by the peaks of the first cycles at each displacement level of the post-peak domain (e.g. Figure 3-12), as well as any parts of in-cycle strength degradation of these first cycles, starting off from the point of maximum strength in the respective direction of the response (i.e. points B and A in Figure 3-12). In many experiments, the response in the two directions can be different, especially when it comes to the post-peak range. Therefore, the descending branches in both directions were recorded and were compared later on (section 4.3).

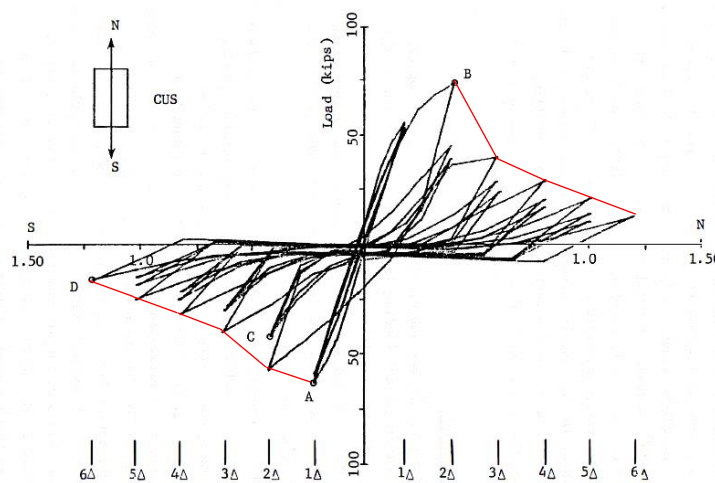


Figure 3-12: Indicative extraction of descending branch curve from experimental data (Umehara & Jirsa, 1982).

### 3.2.4 Displacement at Onset of Axial Failure

In cases where a specimen's shear strength degrades to zero, the abscissa of the intersection of the descending branch with the zero-strength line is recorded as the displacement at the onset of axial failure. Otherwise, the maximum displacement developed by the specimen is conventionally defined as the one at onset of axial failure, although in some cases the actual onset of axial failure takes place during a load reversal.

### 3.2.5 Load Control, Experimental Set-up and Uncertainty

As the focus of this project is on post-peak response of R/C members, all experiments included in the database are displacement-controlled, not force-controlled. Experiments adopting either method of displacement control, namely internal or external, are included in the database. Internal displacement-control is based on displacement measurement from inside of the actuator, while external is based on an independent displacement measurement outside of the actuator. As demonstrated later on (chapter 7), the difference in the results between these two methods can be very significant (considerably more than 100% in some cases) in the pre-peak domain. Nonetheless, this difference is much less significant in the post-peak domain, whereupon this project concentrates.

As mentioned previously (section 3.1), tests with different experimental setups are included in the database. For some of these there is no in-depth account of all the details of the experimental setup used. This means that there might be differences causing inconsistent resulting behaviours in some cases, besides the  $P-\delta$  effect, which was taken into account (section 3.2.1). As an example, different support conditions of the actuators used might result in different lateral as well as axial response, due to the potential extra stiffness introduced in the system. Another example would be measuring the displacements in such a fashion as to include horizontal slippage of the base/footing against the strong floor, which would produce a response more flexible than it ought to be.

The extra uncertainty that is perhaps introduced by the choice to add all of these data is herein appreciated. The majority of the tests have consistent conditions, but some of them might not. These inconsistencies might potentially add to the uncertainty of the proposed equations and criteria. Nonetheless, this uncertainty increase is considered to be outweighed by the advantage of increased sample size and the subsequent increase of the reliability of the proposed empirical relationships and criteria. Bigger datasets can lead to the emergence of patterns, which might otherwise be obscured.

In most cases, reported experimental data are not completely error-free. For the response range of interest in this study, i.e. "Significant damage" to "Near-collapse", experimental data are in general clearly subject to high uncertainty. Nevertheless, empirical data from actual earthquakes, where the input motion may be poorly defined and damage is assessed in a qualitative and subjective way, do entail even higher uncertainty. Therefore, experimental and analytical results can be invaluable for assessing these advanced damage states compared to the empirical data, on the basis of which most of the existing vulnerability and fragility curves for these damage states are derived.



# Chapter 4: EMPIRICAL RELATIONSHIPS FOR KEY SHEAR RESPONSE PARAMETERS

## 4.1 CONCEPTUAL BASIS

With regard to the response of an R/C member after the onset of shear failure, the assumption adopted in this study is that flexural and slip-induced deformations do not increase further than their values at peak strength, i.e. the entire post-peak lateral displacement is attributed to shear deformations. This assumption has also been adopted in other similar models (e.g. Elwood, 2004; Sezen, 2008) and is supported by experimental evidence (e.g. Shirai *et al.*, 1996).

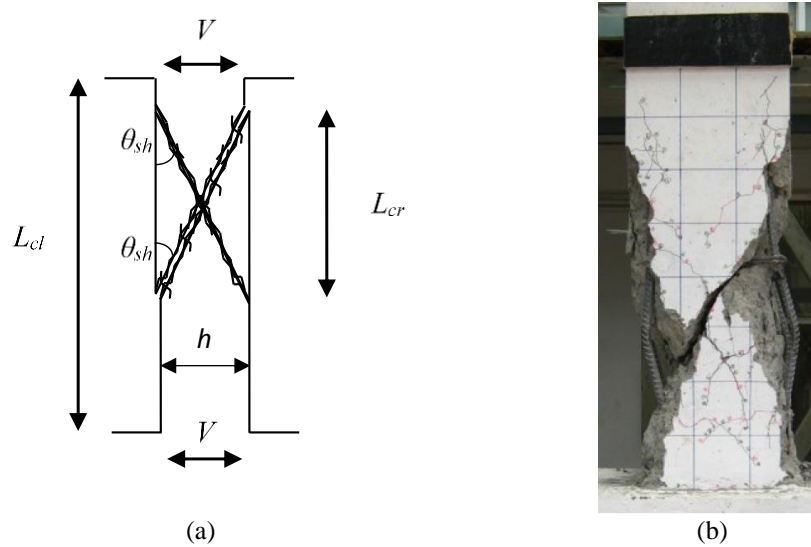


Figure 4-1: (a) Illustrative sketch of a shear-damaged column after the onset of shear failure. (b) Image of an actual experimental test of an axially failed shear-deficient R/C column (Wibowo, 2013).

Furthermore, it has been previously established based on experimental observations (e.g. Elwood & Moehle, 2005a; Henkhaus *et al.*, 2013; Ousalem & Kabeyasawa, 2006) that deformations after the onset of shear failure tend to concentrate in a specific member region, the critical shear length, defined by the diagonal failure plane(s); the clear length of a column,  $L_{cl}$ , the critical shear length,  $L_{cr}$ , the cross-section height,  $h$ , and the critical shear crack angle,  $\vartheta_{sh}$ , are illustrated in Figure 4-1a. The localisation of post-peak shear strains in the critical length is herein termed *shear failure localisation*. In essence, it mainly represents the relative rigid body displacement between the discrete upper and lower parts of the column along the shear crack; this can be seen in the image of an actual experimental test of a shear-deficient R/C column in Figure 4-1b (Wibowo, 2013). This phenomenon will be further investigated experimentally in Part II of this thesis (chapters 6 and 7).

Following this approach, after the onset of shear failure, shear deformations in the critical shear length will be expressed as:

$$\gamma = \gamma_{sh,f} + \frac{\delta_{pp}}{L_{cr}} = \gamma_{sh,f} + \frac{\delta_{pp}}{h \cot \theta_{sh}} \quad (4-1)$$

where  $\gamma$  is the average shear strain in the critical shear length;  $\gamma_{sh,f}$  is the shear strain at the onset of shear failure in the critical shear length;  $\delta_{pp}$  is the post-peak lateral displacement.

Prior to lateral loading of a specimen, there is an available axial load resistance, clearly greater than the axial load demand (i.e. the axial force acting upon the column). With lateral displacement reversals, resistance degrades, due to gradual disintegration of the confined core concrete, until it reaches the axial load demand (Sezen & Moehle, 2006). Axial failure initiates at the point where resistance and demand become equal, whereupon sudden decrease of axial load and increase of axial shortening take place (e.g. Nakamura & Yoshimura, 2002; Matchulat, 2009; Leborgne, 2012). This constitutes a vital turning point in the non-linear response of the entire structure, since it signals the initiation of a process of loss of an individual vertical R/C element's axial load support simultaneously with the redistribution (through the floor system) of vertical loads to its neighbouring members, potentially initiating vertical progressive collapse of the structure. The onset of axial failure is physically manifested as loss of friction and initiation of sliding of one part of the column against the other along a diagonal shear failure plane, in line with the shear-friction concept (e.g. Elwood & Moehle, 2005a; Tran & Li, 2013; Ousalem *et al.*, 2004).

Based on the aforementioned conceptual 'model', the key parameters that have to be defined, in order to model the local post-peak hysteretic shear response of an R/C element in the shear-damaged region, are: (1) the critical shear length, hence the angle of the critical shear crack angle, (2) the rate of shear strength degradation or the post-peak descending branch slope of the hysteretic response, and (3) the shear deformation limit corresponding to the onset of axial failure.

Although a mechanics-based approach would in principle be preferable to obtain such parameters, it is currently not feasible given the complexity and inherent uncertainty of the post-peak cyclic shear response. This is influenced considerably by the effect of the history of demands (e.g. number of cycles per displacement level and magnitude of displacement step) that usually cannot be accounted for, the experimental set-up used in each case (e.g. the displacement control type and out-of-plane support), as well as the randomness of the succession of degrading phenomena taking place at a lower level. This fact is corroborated by the high variability of results from similar models for the post-peak response of shear-deficient R/C elements (e.g. Leborgne & Ghannoum, 2014), by the adoption of empirical models even for the pre-peak response of existing structures in Eurocode EN1998-3 (CEN, 2005; Fardis, 2014) and, lastly, by the fact that even when trying to develop a mechanics-based model, shear

deformations might need to be accounted for through an empirical correction factor (Biskinis & Fardis, 2013).

As explained in section 3.2.5, experimental data for the damage states of interest are in general subject to high uncertainty. Nevertheless, it is reiterated that empirical data from actual earthquakes, where the input motion may be poorly defined and damage is assessed in a qualitative and subjective way, do entail even higher uncertainty. Therefore, experimental and analytical results can be invaluable for assessing these advanced damage states compared to the empirical data, on the basis of which most of the existing vulnerability and fragility curves for these damage states are derived.

## 4.2 CRITICAL SHEAR CRACK ANGLE

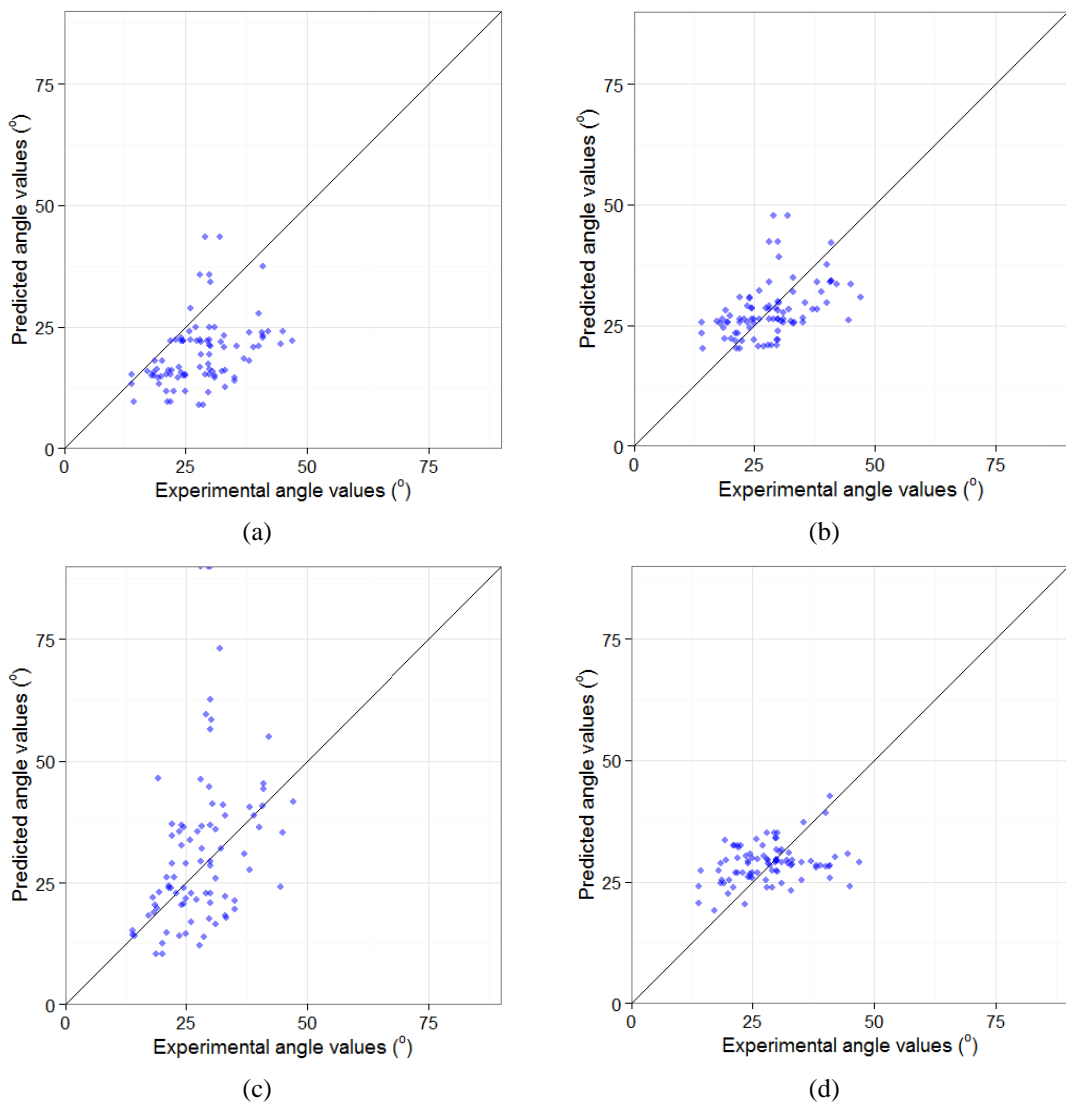


Figure 4-2: Shear crack angles measured experimentally against those calculated using the predictive models of (a) Chang (1993), (b) Kim & Mander (1999), (c) Ousalem et al. (2003), and (d) Elwood & Moehle (2005a).

The critical shear crack angle has often been assumed to be independent of column properties (e.g. 30°) in the process of developing shear strength (e.g. Priestley *et al.*, 1994) or axial capacity models (e.g. Elwood & Moehle, 2005a). As this angle affects (through  $L_{cr}$ ) the modelling of the post-peak part of the shear force vs shear deformation curve, a realistic estimate of its value would be in order, hence an appropriate expression for this angle was sought.

It is emphasised again that this angle corresponds to an idealised inclined failure plane, which forms at the onset of shear failure and its definition and prediction include a lot of difficulties and uncertainties, or as expressed in a previous publication “*it is noticed that inclination of failure planes is tremendously random and complex to formulate simply by means of columns characteristics*” (Ousalem *et al.*, 2004).

Existing shear crack angle relationships were tested against experimentally measured values, to select an appropriate one to use in the context of the model to be developed (Figure 4-2). Chang's (1993) model seems to heavily underestimate the angle; perhaps because it is theoretically derived and not calibrated against experimental results. Ousalem *et al.*'s (2003) relationship produces great scatter, which can be largely attributed to the axial load ratio; both low as well as high values can lead it to great over- or underestimation, as it was developed based on specimens roughly in the range  $0.05 \leq \nu < 0.35$ . Kim & Mander's (1999) and Elwood & Moehle's (2005a) relationships can represent the angles observed in these experiments comparatively better than the previous ones. The former has a mean experimental-to-predicted value of 1.03 and a Coefficient of Variation (CoV) of 23.74%, but a Coefficient of Determination ( $R^2$ ) of only 0.10; additionally, it is more complicated than the other models and it does not take into account the axial load ratio, which is thought to be a crucial parameter with regard to the critical shear crack angle. The latter results in 0.99, 26.38% and 0.03, which means that although it gives a close estimate the variation is not explained adequately by the proposed model (it is reminded that an  $R^2$  of 0.0 would mean that the model explains as much variation in the data as a constant value equal to their average).

As no existing relationship was found to provide reasonable estimates of the observed angles and simultaneously account for all the influential parameters, statistical analysis was carried out, using the software package [R 3.1.0](#). It was performed on the subset of the database (chapter 3), for which either the angle was provided by the research team or there was enough photographic evidence to measure it directly. Double-curvature specimens, as well as flexure-shear critical cantilever ones were taken into account; the few shear critical cantilever specimens were observed to develop higher angle values due to corner-to-corner cracking, which might not be representative of an actual building column. There were 54 shear (S) and 34 flexure-shear critical

(FS) specimens satisfying the aforementioned criteria. Based on this dataset, the following patterns emerged (Figure 4-3):

- In line with structural mechanics principles, increasing axial load ratio ( $\nu$ ) tends to decrease the shear crack angle, since the trajectories of the principal compressive stresses - along which the first shear cracks will form – are oriented closer to the longitudinal axis of the member.

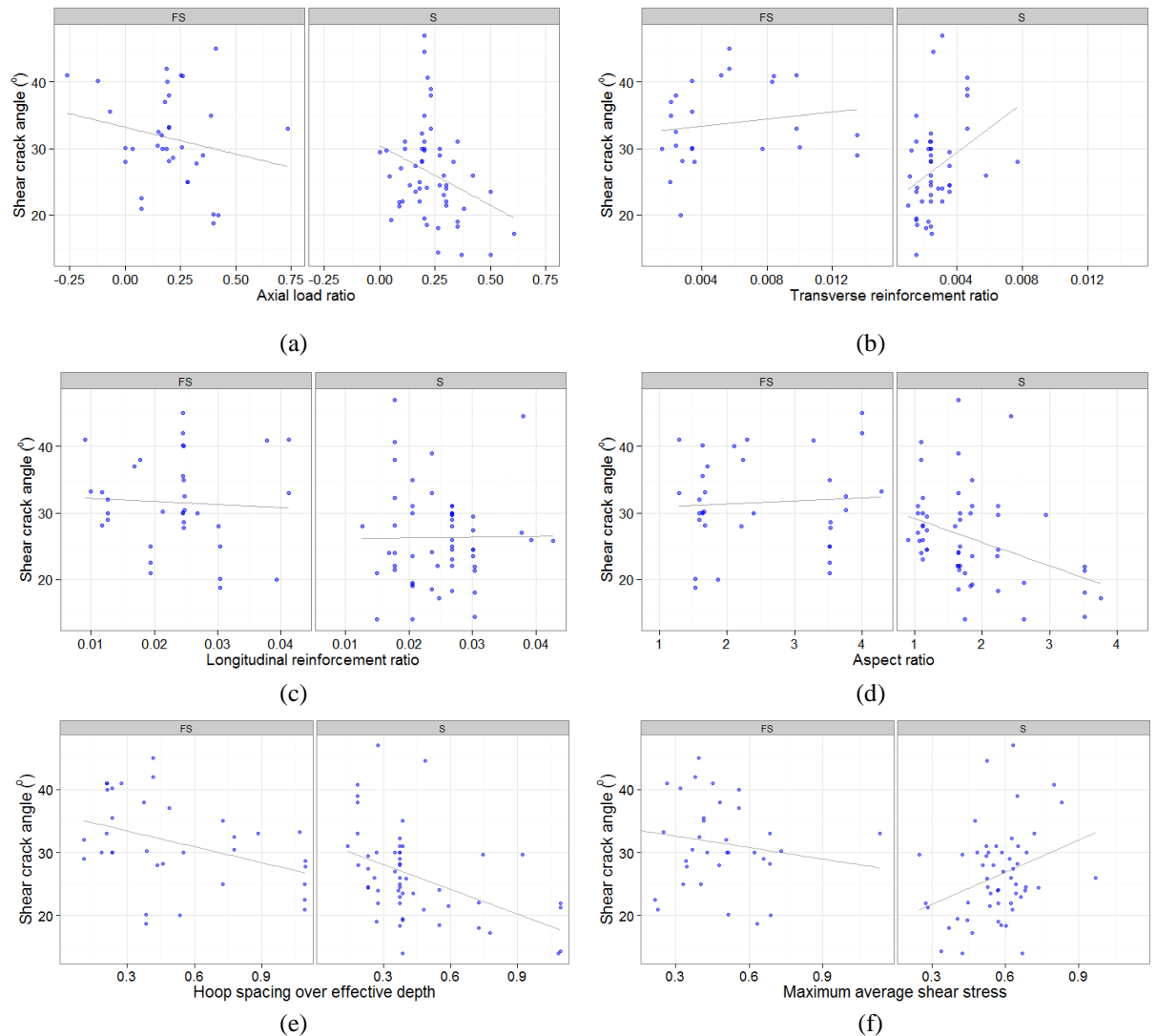


Figure 4-3: Correlation of the measured angle with (a) axial load ratio, (b) transverse reinforcement ratio, (c) longitudinal reinforcement ratio, (d) aspect ratio, (e) hoop spacing over effective depth, and (f) maximum average shear stress, divided into shear (S) and flexure-shear (FS) critical specimens.

- Transverse reinforcement ratio ( $\rho_w$ ) is shown to have a positive correlation with the angle, although transverse reinforcement has hardly any influence on the principal stress trajectories prior to shear cracking, hence on the initial crack inclination. However, the angle of interest in the present model seems to include the propagation of shear crack at varying angles, the angle change being significantly affected by the yielding transverse reinforcement (Hsu, 1998).

- Longitudinal reinforcement ratio ( $\rho_l$ ) seems to play no role whatsoever in either case (S or FS). This is consistent with the mechanics of shear cracking, while it contradicts previous studies (e.g. Hsu, 1998; Kim & Mander, 1999) that have considered it an important parameter.
- Aspect ratio ( $L_s/d$ ) has a strong negative correlation in the case of shear critical elements, as expected, because of the influence on the trajectories of the principal compressive stresses. However, in flexure-shear critical elements it has a slightly positive correlation, which is not in line with the previous observation. Although the first shear cracks form similarly to what was described for shear critical elements, the shear strains subsequently concentrate in the end-regions, where flexural yielding has already taken place. The idealised critical shear crack that will form will have a larger angle, mostly confined at the plastic hinge region. What could explain the positive aspect ratio-shear crack angle trend is that as the shear span ( $M/V$ ) increases, the influence of flexure over shear becomes more pronounced, which probably leads to even “flatter” idealised critical shear crack angles, closer to the horizontal flexural cracks. This is illustratively shown in Figure 4-4.
- The maximum average shear stress (normalised to the square root of concrete compressive strength) ( $\tau_{max}/\sqrt{f_c} = V_{max}/bd\sqrt{f_c}$ ) has the expected correlation in the case of shear critical elements, i.e. the higher the shear stress, the higher the angle. However, in flexure-shear critical specimens, the inverse is true. This is probably due to the aforementioned aspect ratio effect, since these two quantities are partly correlated; the more slender a column is, the lower the shear that will be developed for a given flexural resistance (Figure 4-5).
- Hoop spacing over effective depth ( $s/d$ ) has the inverse correlation of transverse reinforcement ratio. This comes as no surprise, since the two parameters are highly correlated. Therefore, only one of them will be included in the final relationship.
- In general, FS members seem to have higher values of critical shear crack angle, the crack being confined in the end-region of the member that has yielded.
- Other important parameters that influence the shear crack angle, like cross-section shape and loading conditions, were beyond the scope of the current investigation, which was based on a database including only rectangular specimens – the majority of them square –, mostly with a double-curvature loading condition with forces acting at the ends of the members.

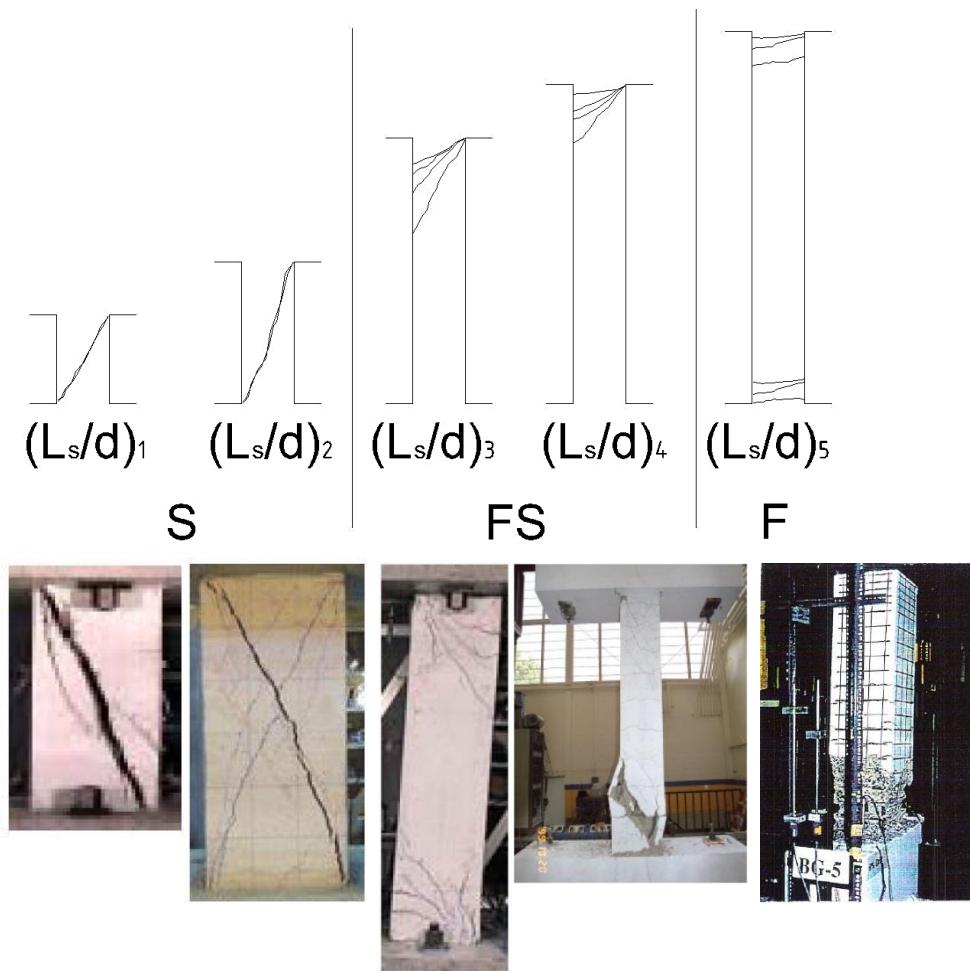


Figure 4-4: The (idealised) effect of aspect ratio on the critical shear crack angle. Fictitious column with increasing aspect ratio from left to right ( $(L_s/d)_5 > (L_s/d)_4 > \dots > (L_s/d)_1$ ) and the corresponding expected cracking (top). Pictures of specimens roughly corresponding to the above aspect ratios and failure types (Shear, Flexure-Shear and Flexural) (bottom); from left to right the specimens are: 3M (Yoshimura & Nakamura, 2002), S100 (Nakamura & Yoshimura, 2014), No. 6 (Yoshimura et al., 2003), Specimen 4 (Sezen, 2000) and BG-5 (Gira & Saatcioglu, 1996).

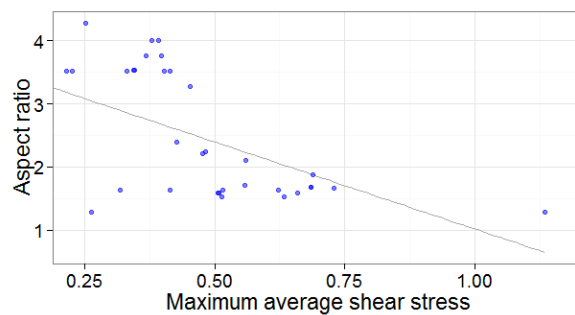


Figure 4-5: Correlation of aspect ratio with maximum average shear stress in flexure-shear critical elements.

The statistical methods used are presented in the following. First of all, a step-wise predictor variable elimination procedure was followed; in other words, the approach taken was to start with the most complex model, including all the potential explanatory variables, and move to simpler models, thus ending up to the model with the least terms that could explain the data adequately.

Non-linear least-squares fitting was performed using the Levenberg-Marquardt nonlinear least-squares algorithm (Levenberg, 1944; Marquardt, 1963). It is an iterative non-linear optimisation algorithm, interpolating between the Gauss-Newton and the steepest descent methods, in order to avoid shortcomings of both. It is a popular solution, not least because of its robustness.

Using more flexible models, i.e. models of higher degree, can potentially lead to over-fitting to the experimental data, in effect confusing noise for data patterns; this, of course, might lead to higher performance in the experimental dataset, but can lead to by far larger errors, when new data points are predicted. To avoid bias in the models, 10-fold-cross-validation (Refaeilzadeh *et al.*, 2009) was used. The available dataset is initially split into 10 sub-sets (folds); subsequently, models are fit on 9 of them (training dataset) and tested on 1 of them (testing dataset); this is repeated 10 times, so that all folds are used exactly once as testing datasets; this simulates the potential fit of models to a generalised sample, i.e. to “new data”. The models developed using the non-linear optimisation algorithm were thus compared against best-fitting models based on linear least-squares fitting, which is assumed to have by default the least potential for over-fitting, in order to validate their predicting ability.

Based on the aforementioned trends and significance tests of the predictor variables, various empirical relationships were explored. Using the abovementioned statistical methods, the best relationship developed was:

$$\theta_{\min} = \tan^{-1} \frac{h}{L_{cl}} < \theta_{sh} = 164.87 \frac{\beta \times \rho_{w,conf}^{0.0393}}{(v + 2.6)^{0.33}} - 66.288 < \theta_{\max} = 45^{\circ} \quad (4-2)$$

where  $h$  is the height of the cross-section;  $L_{cl}$  is the clear length of the member;  $\beta$  is a parameter that differentiates between shear and flexure-shear critical members, equal to 1.00 for S and 1.06 for FS elements;  $\rho_{w,conf}$  is the transverse reinforcement ratio using the confined concrete area (stirrup spacing multiplied by the confined section width), introduced with its actual value (not in %);  $v$  is the axial load ratio ( $v = N / (A_g \times f_c)$ ). The minimum value is a geometrical limitation of the shear crack applying to columns with a very low aspect ratio, as also explained by Elwood & Moehle (2005a). Were this limit not imposed, the angle could be lower than the angle of the diagonal connecting the two ends of the column (corner-to-corner crack), essentially leading to an  $L_{cr}$  exceeding the length of the column itself.

Eq. 4-2 yields a mean experimental-to-predicted value of 1.00, a median of 0.97, a CoV of 21.89% and an  $R^2$  of 0.344 (Figure 4-6). Of course, as mentioned previously, predicting the critical shear crack angle involves high uncertainty, hence the resulting variability.

Eq. 4-2 applies to specimens in the following range of parameters:  $-0.26 \leq \nu < 0.75$ ,  $0.08 < \rho_{w,conf} \leq 1.35$  (%),  $0.91 \leq \rho_l < 4.28$  (%),  $330 < f_{yl} \leq 700$  (MPa),  $270 \leq f_{yw} \leq 587$  (MPa),  $13.5 \leq f_c \leq 86$  (MPa),  $0.9 < L_s/d < 4.3$ . Figure 4-7 shows the values of the critical shear crack angle that Eq. 4-2 would result in, across the whole range of relevant parameters, i.e. axial load and transverse reinforcement ratios, for shear and flexure-shear critical specimens. For shear and flexure-shear critical R/C columns with characteristics in the ranges of  $0.2 \leq \nu \leq 0.3$  and  $0.2 \leq \rho_w \leq 0.6$  (%), angles of approximately  $25^\circ$ - $30^\circ$  and  $30^\circ$ - $35^\circ$  would be expected, respectively.

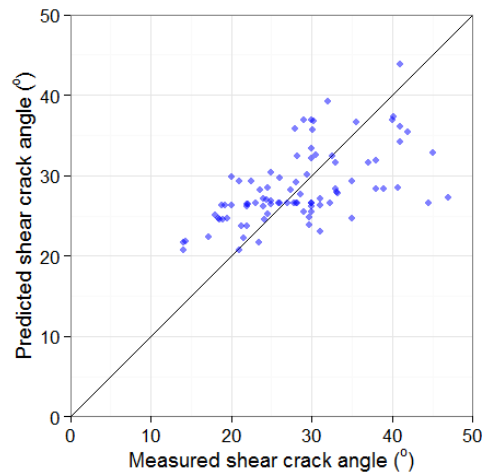


Figure 4-6: Shear crack angles measured experimentally against the ones predicted by Eq. 4-2.

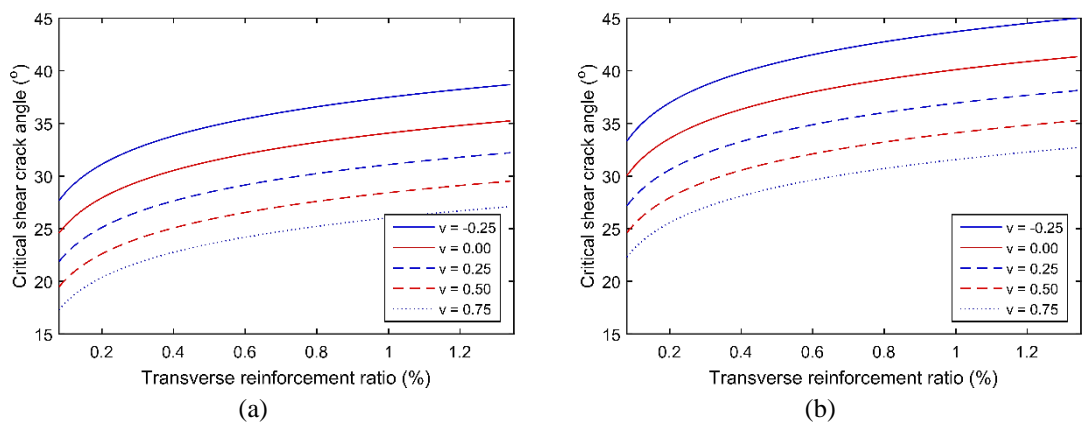


Figure 4-7: Critical shear crack angle predicted by Eq. 4-2 along the range of potential axial load and transverse reinforcement ratios, for (a) shear, and (b) flexure-shear critical specimens.

### 4.3 POST-PEAK RESPONSE

Shear failure initiating in one direction was hypothesised to influence the behaviour in the other direction, so the overall relation between the slopes of the descending branches in either direction was investigated more closely. According to the boxplot in Figure 4-8a, it seems that the difference is not really significant, with the majority of specimens ranging between 0.9 and 1.3, i.e. having approximately equal slopes in both directions. Therefore, the average of the

response in the two directions was used to calculate the descending branch slope for each specimen.

The shape of the post-peak descending branch has been investigated using the experimental data in the database (chapter 3). Initially the possibility of a non-linear branch was investigated, which would be able to represent both concave and convex descending curves. The relationship that was assumed was:

$$\frac{V}{V_{max}} = 1 - a \cdot (\gamma - \gamma_{sh,f})^c \quad (4-3)$$

where  $V_{max}$  is the maximum shear strength that occurs at the onset of shear failure,  $V \leq V_{max}$  the strength at any loading level after the onset of shear failure and  $\gamma \geq \gamma_{sh,f}$  the corresponding average shear strain in the critical shear length (Eq. 4-1),  $a$  a constant affecting the average slope, and  $c$  the curvature of the descending branch. However, no strong correlation emerged between the geometric and loading parameters of specimens and the curvature. Therefore, a non-linear curve concept was no further pursued and simpler linear forms were explored.

Nonetheless, a noteworthy finding from this investigation was that shear critical specimens tend to exhibit mostly convex post-peak descending branch shapes, while flexure-shear critical specimens mostly exhibit approximately linear curves with some convex and some concave ones (Figure 4-8b).

The former observation is probably related to the following: It was observed in the database that some specimens exhibit a sudden degradation of their shear strength (anywhere between 5% and 50%) immediately after shear failure, herein termed *shear failure leap*. It occurs only in shear critical specimens. Also, it occurs in specimens with lower transverse reinforcement and lower axial load levels. A possible explanation could be that during the formation of the critical shear crack, a considerable portion of the shear strength attributed to concrete is lost. Hence, part of the shear demand is instantly transferred to the other shear transfer mechanisms. Due to little transverse reinforcement, this force cannot be carried, thus a sudden decrease of strength is observed. Of course, in flexure-shear critical specimens, the strength attributed to concrete has degraded substantially by the time shear failure initiates owing to inelastic curvatures in the plastic hinge, so no such phenomenon could take place. This would also explain why it occurs in specimens with moderate to low levels of axial load, since a high axial load would increase the other shear transfer mechanisms. Overall, however, the correlations cannot be considered so significant and reliable as to model shear failure leap as a potential initial part of the post-peak descending branch at this stage.

Subsequently, modelling the descending branch with a linear segment was considered, taking into account its simplicity, its compatibility with the proposed shear model and its match with experimental results – the  $R^2$  of fitting a least-squares line to the experimental post-peak response has an average value of 0.95 and a CoV of 7.4%.

The linear descending branch is herein defined by fitting a least-squares line starting from the onset of shear failure. Were it defined by a line connecting the onset of shear and axial failure instead (e.g. Elwood, 2004; Sezen, 2008), the energy dissipated by an element could be significantly under- or overestimated. For instance, in the case of the convex curve of Figure 3-12, this would lead to an overestimation of the dissipated energy. The opposite would happen in concave curves; the deviation would generally be larger the farther away from a linear descending branch a specimen's post-peak strength degradation curve is.

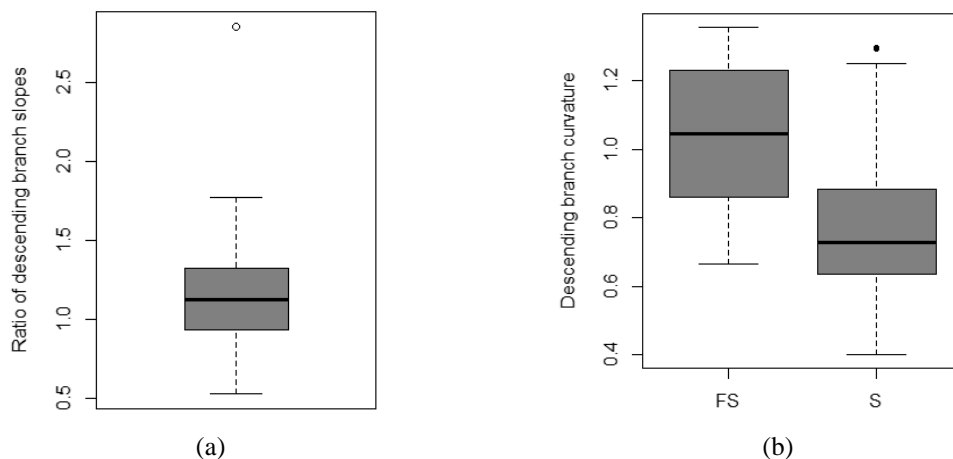


Figure 4-8: (a) Ratio of descending branch slopes in two “directions” of the response of the database specimens. (b) Curvature of the descending branch of the response of flexure-shear critical (FS) and shear critical (S) specimens of the database.

A bilinear curve with a horizontal branch representing residual strength, assumed by previous studies (e.g. LeBorgne & Ghannoum, 2013; Pincheira *et al.*, 1999), was judged to be a viable choice for less than 10% of all specimens in the database. Many of these specimens were found to be influenced to a lesser or greater extent by bond-splitting, which probably hints that the ostensible residual branch is probably attributable to this phenomenon; such a behaviour can also be seen for other specimens failing in bond-splitting shear failure (e.g. Pham & Li, 2013). This suggests either that practically no residual strength is developed in most shear and flexure-shear critical R/C members (at least those with the characteristics of this database), or that axial failure occurs in these specimens before they reach their residual capacity; hence, such an approach was no further pursued.

Nevertheless, a bilinear branch with two independent slopes was pursued, with the breaking point located at 50% strength degradation. The slopes of the two branches were obtained by

fitting a least-squares line starting from the onset of shear failure and from the 50% strength degradation point, for the first and the second branch, respectively. For the linear least-squares fitting of the former, the points up to 50% strength degradation were considered, while for the latter the rest of them. This approach was believed to lead to a more accurate representation of the post-peak descending branch overall, as it is much more flexible and can represent linear, convex and concave responses, observed experimentally (Figure 4-8b), e.g. specimen U1 (Saatcioglu & Ozcebe, 1989) and specimens 4 and 12 (Ousalem, Kabeyasawa, Tasai, & OHSUGI, 2002). Additionally, the latter part of the response seems to be very set-up-dependent. Following such a calibration procedure, the slope of the first segment (from the onset of shear failure until 50% strength degradation) can be independent from the second segment's slope. Thus, it could be used instead of the slope taking 100% of the response into account, the latter being considered more setup-dependent.

Only specimens with at least 80% strength degradation were used to measure the value of the slope of the second segment of their post-peak response, hence only 37 specimens were taken into account in this case.

The proposed linear and bi-linear shear strength degradation relationships are the following:

$$\frac{V}{V_{\max}} = 1 - S_{pp} \times (\gamma - \gamma_{sh,f}) \quad (4-4)$$

$$\frac{V}{V_{\max}} = \begin{cases} 1 - S_{pp,1} \times (\gamma - \gamma_{sh,f}), & \gamma \leq \gamma_{u2} \\ 0.5 - S_{pp,2} \times (\gamma - \gamma_{u2}), & \gamma > \gamma_{u2} \end{cases} \quad (4-5)$$

where  $S_{pp}$  is a dimensionless parameter expressing the shear strength degradation normalised to  $V_{\max}$  per unit of post-peak shear strain for the linear descending branch case,  $S_{pp,1}$  and  $S_{pp,2}$  are the respective slopes of the two segments of the bi-linear descending branch case,  $\gamma \geq \gamma_{sh,f}$  the corresponding average shear strain in the critical shear length (Eq. 4-1) and  $\gamma_{u2}$  the shear strain corresponding to 50% strength degradation, i.e. where the bi-linear descending branch's breaking point is located.

As explained in chapter 2, it has been pointed out (e.g. in FEMA P440A (ATC, 2009)) that in-cycle strength degradation should not be confounded with cyclic strength degradation; in other words the monotonic capacity boundary of an element's response, which is considered unique, should not be confounded with its cyclic envelope, which is loading-protocol-dependent. This has also been shown experimentally, for instance by observing the apparent difference in the descending branch slope of nominally identical specimens that were cycled under different loading protocols (Ousalem et al., 2004). Therefore, they should be, and have been herein, treated

separately. Specimens with at least 30% degradation of their total shear strength being attributed to in-cycle degradation were termed “quasi-monotonic” (**QM**), i.e. it was assumed that their strength degradation was mainly due to in-cycle degradation mechanisms, while the rest were considered “cyclic specimens” (**CS**). The former amounted to a total of 30, the latter to 86, i.e. a total of 116 specimens in the database were available - hereafter called “all specimens” (**AS**).

- Empirical equations developed for **QM** will be more appropriate for modelling specimens with high in-cycle degradation due to the displacement history used (purely monotonic or cyclic with large displacement steps) or members of actual structures which are expected to exhibit high in-cycle degradation, e.g. when subjected to near-field, pulse-like, ground motions.
- **CS** will be more appropriate for cyclic tests with loading protocols with more than one cycles at each displacement level and small displacement steps, i.e. the typical cyclic quasi-static symmetrical loading protocols.
- **AS** will be more appropriate for ‘scenarios’ wherein a mix of both types of strength degradation is expected, i.e. structures subjected to earthquakes, exhibiting both cyclic and in-cycle degradation.

Based on these datasets, several patterns emerged examining the correlation of the descending branch slopes (in terms of  $V/V_{max}$  vs  $\gamma$ ) with geometric, material and loading parameters (in Figure 4-9, the trends observed in the case of a linear descending branch in the dataset **AS** are shown, being indicative of the other cases and datasets):

- Higher axial load ratio increases the shear strength degradation rate, as has been often noted in similar studies (e.g. Ousalem *et al.* , 2002). Notably, this effect of axial load is different from that on the pre-peak shear resistance of a member.
- Increased longitudinal reinforcement leads to a decreased post-peak slope, mainly through the dowel action of the longitudinal bars, as well as carrying an (occasionally significant) part of the vertical load.
- It is noteworthy that the longitudinal reinforcement ratio divided by the ratio of the confined to the total cross-section area gives a better prediction than the unnormalised ratio, the latter being more common a variable in pre-peak models. This can be attributed to the fact that after the critical shear crack has formed at the onset of shear degradation, the effective concrete area is the confined one; the unconfined cover concrete either has already spalled off within the critical shear length or it does not actively contribute to shear resistance, due to substantial reduction in its strength.

- Higher transverse reinforcement is beneficial, as expected; the transverse steel bars crossing the critical crack are one of the main shear resistance mechanisms.
- The average diameter of longitudinal bars over the effective depth,  $\Phi_{l,ave}/d$ , seems to play an important role, too, decreasing the degradation rate as it increases.
- Aspect ratio was investigated, as it was considered important in a previous model (Wibowo *et al.*, 2014), but was herein found to hold limited predictive strength. This is attributed to the fact that the localisation of shear strains in the critical length was considered, hence minimising the effect of aspect ratio, which is pronounced when taking into account the inter-storey drift ratio, disregarding shear failure localisation.

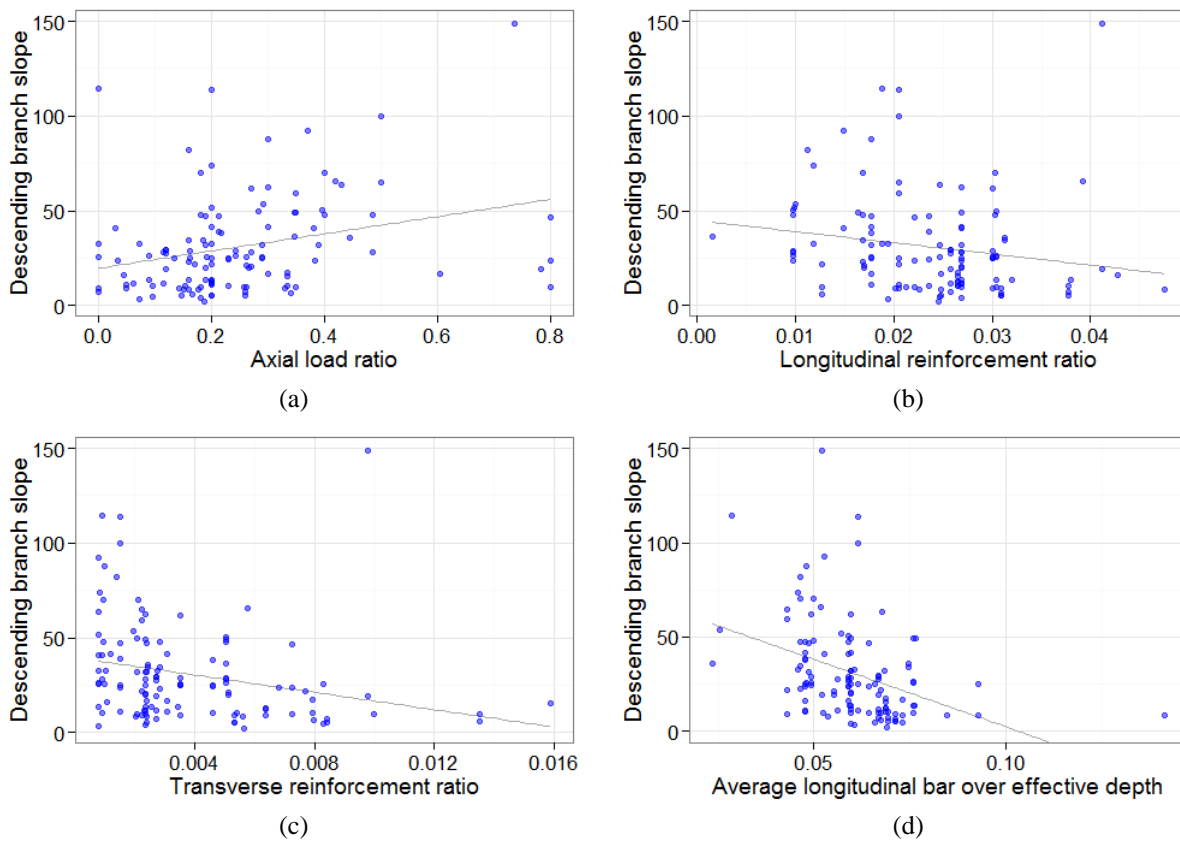


Figure 4-9: Correlation of slope of the linear post-peak branch of the AS dataset with (a) axial load ratio, (b) longitudinal reinforcement ratio, (c) transverse reinforcement ratio normalised to the confined concrete area (stirrup spacing multiplied by the confined section width), and (d) average longitudinal bar diameter normalised to the effective depth.

Based on these trends and significance tests of the predictor variables, various potential predictive relationships were explored. The final expressions were developed through a step-wise predictor variable elimination procedure, 10-fold-cross-validation (Refaeilzadeh *et al.*, 2009) and optimisation using the Levenberg-Marquardt nonlinear least-squares algorithm (e.g. Levenberg, 1944). For a linear post-peak branch, where the entire post-peak response is taken into account, the following expressions are proposed (for **QM**, **CS** and **AS** specimens, respectively):

$$S_{pp} = \frac{0.01341(v + 0.05)^{0.533}}{(\rho_{w,conf} + 0.0003)^{0.6331} \left( \frac{\rho_l}{\alpha_{conf}} + 0.700 \right)^{15.382}} - 3.758 \geq 2 \quad (4-6)$$

$$S_{pp} = \frac{0.00302(v + 0.3)^{0.8352}}{(\rho_{w,conf} + 0.0155)^{2.484} \left( \frac{L_s}{d} - 0.9 \right)^{0.1585}} - 9.247 \geq 2 \quad (4-7)$$

$$S_{pp} = \frac{1.981 \cdot 10^{-6} (v + 0.255)^{1.056} \left( \frac{\tau_{max}}{\sqrt{f_c}} - 0.21 \right)^{0.0528}}{(\rho_{w,conf} + 0.0039)^{1.711} \left( \frac{L_s}{d} - 0.9 \right)^{0.207} (\rho_l + 0.3495)^{8.669}} + 1.985 \geq 2 \quad (4-8)$$

In the case of a bilinear post-peak descending branch, for the first segment, up to 50% loss of  $V_{max}$ , the following expressions are proposed (for **QM**, **CS** and **AS** specimens, respectively):

$$S_{pp,1} = \frac{0.000128(v_l - 0.20)^{0.201}}{(\rho_{w,conf} + 0.0075)^{2.7952} \left( \frac{L_s}{d} - 1.05 \right)^{0.1831}} - 4.382 \geq 2 \quad (4-9)$$

$$S_{pp,1} = \frac{0.801(v + 0.145)^{0.2324}}{(\rho_{w,conf} + 0.0033)^{0.587} \left( \frac{L_s}{d} - 0.408 \right)^{0.2497} \left[ \frac{\rho_l}{\alpha_{conf}} \left( \frac{\Phi_{l,ave}}{d} \right) + 0.0053 \right]^{0.379}} - 40.505 \geq 2 \quad (4-10)$$

$$S_{pp,1} = \frac{2.649 \cdot 10^{-5} (v + 0.0618)^{0.3861} \left( \frac{\tau_{max}}{\sqrt{f_c}} - 0.20 \right)^{0.115}}{(\rho_{w,conf} + 0.0077)^{2.422} \left( \frac{L_s}{d} - 0.90 \right)^{0.207} (\rho_l + 0.2077)^{2.604}} - 5.513 \geq 2 \quad (4-11)$$

For the second segment of a bilinear post-peak branch, after 50% loss of  $V_{max}$  (Fig. 1), the following expressions are proposed (for **QM**, **CS** and **AS** specimens, respectively):

$$S_{pp,2} = 40.19(v_l - 0.07564)^{0.5377} \left( \frac{s}{d} + 0.4254 \right)^{1.262} - 8.1577 \geq 2 \quad (4-12)$$

$$S_{pp,2} = \frac{231.69(v_l - 0.1154)^{0.0236} \left( \frac{s}{d} + 0.1595 \right)^{0.033}}{(\rho_{w,conf} + 0.1253)^{1.05} \left( \frac{\rho_l}{\alpha_{conf}} + 1.7595 \right)^{2.766}} - 363.11 \geq 2 \quad (4-13)$$

$$S_{pp,2} = \frac{0.206(v_l - 0.15)^{0.1597} \left( \frac{s}{d} + 0.0003 \right)^{0.393}}{\left( \rho_{w,conf} + 0.0018 \right)^{0.149} \left( \frac{\rho_l}{\alpha_{conf}} + 0.2194 \right)^{3.505}} - 15.145 \geq 2 \quad (4-14)$$

Table 4-1: Summary of the main statistics of accuracy and variation of Eq. 4-6 to 4-14.

Eq.	(4-6)	(4-7)	(4-8)	(4-9)	(4-10)	(4-11)	(4-12)	(4-13)	(4-14)
<b>R<sup>2</sup></b>	0.80	0.44	0.54	0.64	0.51	0.58	0.73	0.54	0.51
<b>mean</b>	1.00	1.03	1.01	1.00	1.02	1.02	1.00	1.00	1.00
<b>median</b>	0.97	0.94	0.90	0.93	0.94	0.94	0.96	0.83	0.89
<b>CoV (%)</b>	40.3	56.9	49.6	45.0	47.5	53.5	31.2	63.7	61.2

Table 4-2: Datasets and minimum and maximum limits of main design parameters defining the range of application of the proposed relationships.

Dataset / No. of specimens	$v$	$\rho_{w,conf}$ %	$\Phi_{l,ave}/d$ [ $\times 10^{-3}$ ]	$\rho_l/\alpha_{conf}$ %	$f_{yl}$ [MPa]	$f_{yw}$ [MPa]	$f_c$ [MPa]	$L_s/d$
<i>Linear branch and first segment of bilinear branch (at least 30% degradation)</i>								
<b>QM / 30</b>	[0.07, 0.60]	[0.00, 0.85]	[45, 75]	[1.50, 5.45]	[330, 700]	[250, 590]	[13.5, 86]	[1.1, 3.8]
<b>CS / 86</b>	[0.00, 0.80]	[0.00, 1.60]	[25, 140]	[0.20, 6.50]	[330, 540]	[295, 560]	[13.5, 86]	[0.9, 4.3]
<b>AS / 116</b>	[0.00, 0.80]	[0.00, 1.60]	[25, 140]	[0.20, 6.50]	[330, 700]	[250, 590]	[13.5, 86]	[0.9, 4.3]
<i>Second segment of bilinear branch (at least 80% strength degradation)</i>								
<b>QM / 16</b>	[0.15, 0.30]	[0.12, 0.85]	[46, 75]	[2.20, 5.45]	[330, 550]	[355, 475]	[22, 31]	[1.1, 3.8]
<b>CS / 21</b>	[0.05, 0.40]	[0.08, 0.56]	[45, 75]	[1.65, 4.85]	[340, 460]	[290, 475]	[18, 32.5]	[1.1, 3.8]
<b>AS / 37</b>	[0.05, 0.40]	[0.08, 0. 85]	[45, 75]	[1.65, 5.45]	[330, 550]	[290, 475]	[18, 32.5]	[1.1, 3.8]

Table 4-1 summarises the accuracy and variation statistics of the above presented relationships (mean and median refer to the ratio of experimental to predicted values). Table 4-2 includes the size of the datasets used for the derivation of each expression as well as the ranges of the main parameters, inside which these models are valid. Regarding the parameters used,  $\rho_l$  is the longitudinal reinforcement ratio, introduced with its actual value (not in %);  $\alpha_{conf}$  is the ratio of the confined to the total cross-section area;  $\tau_{max}/\sqrt{f_c}$  is the maximum average shear stress normalised to the square root of concrete compressive strength;  $v_l$  is the longitudinal reinforcement axial load ratio, i.e. axial load divided by the axial strength of the longitudinal reinforcement bars;  $L_s/d$  is the member aspect ratio;  $\Phi_{l,ave}/d$  is the average diameter of longitudinal bars normalised to the effective depth (to avoid scaling issues);  $s/d$  is the spacing of

stirrups over the effective depth of the cross-section. The lower threshold used in all equations is the value 2.00, corresponding to the lowest slope value encountered in the database.

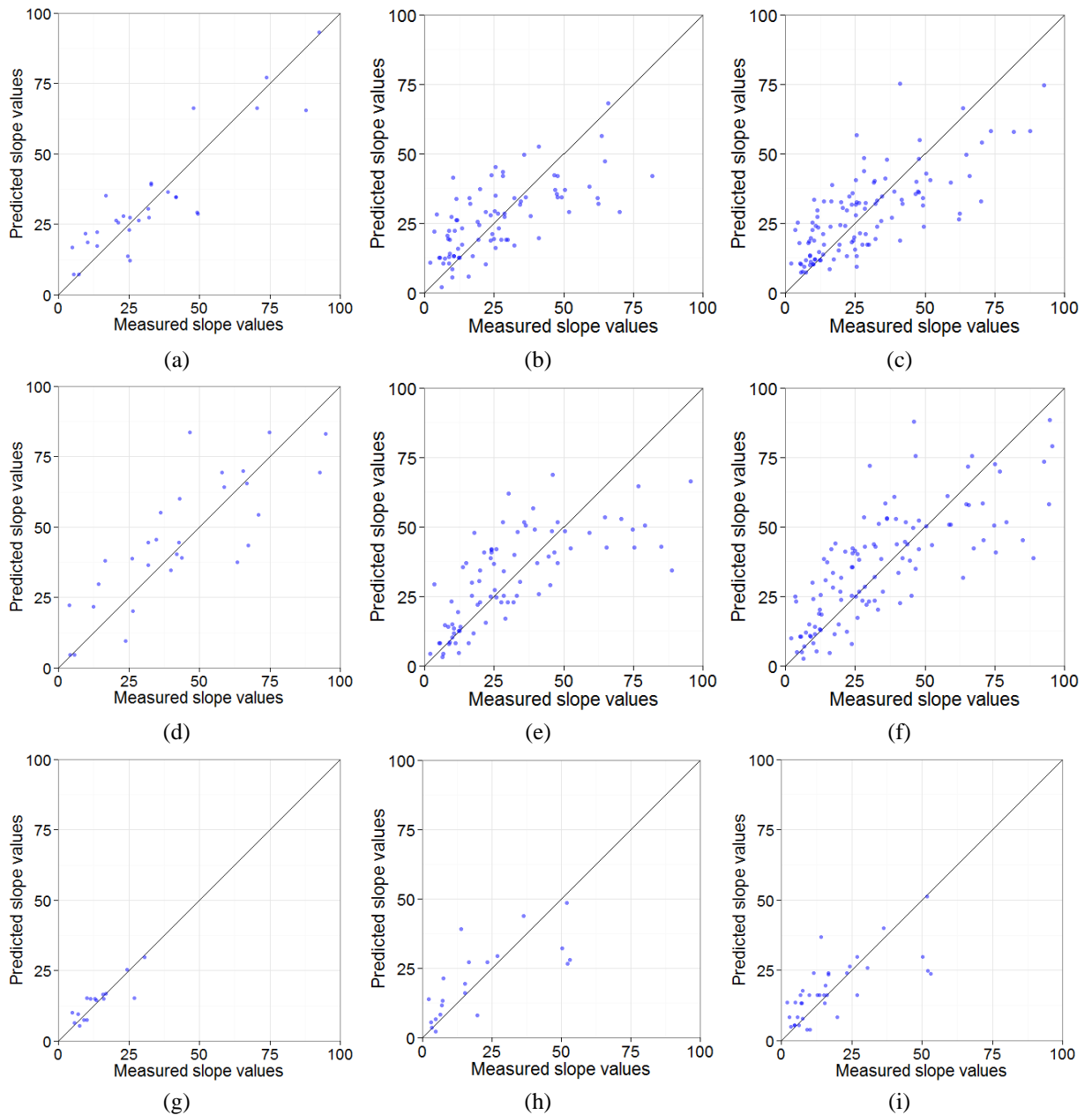


Figure 4-10: Values of the post-peak descending branch slopes (dimensionless) measured experimentally against the ones predicted using Eq. 4-6 (a) to 4-14 (i) (from left to right and top to bottom).

Scatter plots of experimental against predicted values of the descending branch are presented for all equations in Figure 4-10. The scatter is influenced by the very high uncertainty inherent in post-peak phenomena, arising among other factors from the difference in the history of demands (e.g. number of cycles per displacement level and magnitude of displacement step) and experimental set-up used in each case (e.g. the way that the displacement was controlled and whether and how the specimen was supported against out-of-plane displacements), as well as the randomness of the succession of degradation phenomena taking place at a lower level, e.g. aggregates and concrete surfaces being smoothed with cyclic loading, softening of

concrete strength, bending, buckling and fracturing of longitudinal bars. The randomness in each of them affects the accuracy of the total prediction. Even if the exact same experiment is repeated, the probability that differences will exist in the post-peak behaviour is quite high, as opposed to an expected more or less similar pre-peak response. This is obvious also in similar existing models that exhibit high variation (e.g.  $R^2$  of 0.6 Leborgne & Ghannoum, 2014). Thus, the equations are not expected to yield an accurate value every time, but a roughly accurate estimation, subject to the aforementioned variability. Of course, the proposed relationships would fit more in a probabilistic rather than a deterministic context.

Naturally, the relationships for **QM** specimens have lower variation compared to **CS** and **AS** in all cases. This is due to the fact that only in-cycle degradation is captured via these relationships, while the slopes of **CS** specimens are substantially affected by the displacement pattern used for each test leading to potentially lower or higher cyclic strength degradation, thus producing extra uncertainty.

In Figure 4-11, the values of the descending branch slope predicted by Eq. 4-6 are plotted against the longitudinal reinforcement ratio, for different transverse reinforcement ratios, for a low and a high axial load ratio. Figure 4-11 demonstrates that the higher the axial load and the lower the transverse and longitudinal reinforcement of the member, the steeper the slope of the descending branch is going to be, i.e. the higher the strength degradation after the onset of shear failure.

Additionally, it can be seen from Eq. 4-6 to 4-14 that the maximum shear stress applied on the specimen and its aspect ratio generally have a positive and negative correlation, respectively, with the slope of the descending curve; this means that shorter specimens with higher applied shear stresses tend to have steeper slopes. The parameter  $s/d$  was not important in the linear as well as the 1<sup>st</sup> segment of the bilinear curve, however it was defining in the 2<sup>nd</sup> segment, featuring in all of Eq. 4-12 to 4-14 and holding substantial predictive strength; this underlines the predominant role of an element's confinement in maintaining its vertical as well as part of its lateral resistance for higher displacement levels. Another noteworthy point is that both longitudinal and transverse reinforcement ratios seem to have better correlation with the slope when normalised to the confined core, instead of the gross section; as mentioned above, this can be attributed to the fact that after the onset of shear failure, the effective concrete area is the confined one, as the unconfined cover concrete either has already spalled off within the critical shear length or it does not actively contribute to shear resistance, due to substantial reduction in its strength.

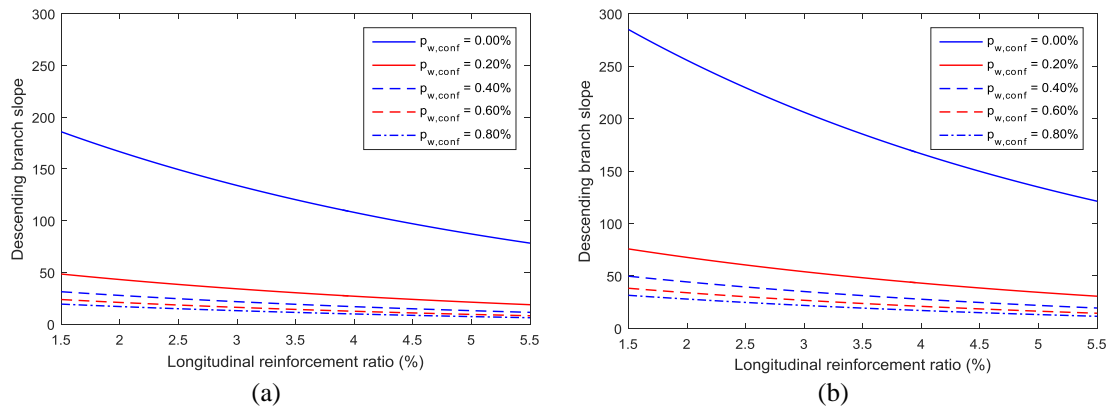


Figure 4-11: Descending branch slope ( $S_{pp}$ ) predicted by Eq. 4-6 along the range of potential longitudinal reinforcement ratios over relative confined concrete area ( $\rho_l/a_{conf}$ ), for different transverse reinforcement ratios over confined concrete area ( $\rho_{w,conf}$ ), for axial load ratios ( $\nu$ ) of (a) 0.2 and (b) 0.5.

#### 4.4 ONSET OF AXIAL FAILURE

It has long been claimed, based on a limited amount of experimental data (e.g. Yoshimura & Nakamura, 2002), that the onset of axial failure occurs when shear strength degrades to zero (or becomes negligible). Several post-peak models have been based on this assumption (e.g. Elwood, 2004; Sezen, 2008). Nonetheless, experimental evidence shows that this cannot be assumed for all specimens. In fact, for many of them it is considerably misleading as shown in Figure 4-12, where the shear strength at the onset of axial failure is shown for the specimens that have sustained axial failure in this database; it is normalised by the respective strength at the onset of shear failure. The ostensibly unrealistic values equal to or near 1.00 are in fact due to specimens having undergone simultaneous shear and axial failure.

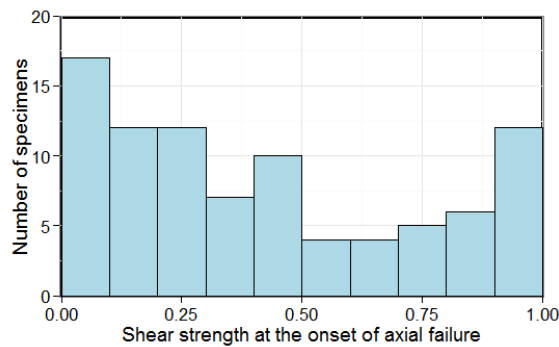


Figure 4-12: Shear strength at the onset of axial failure normalised to the maximum shear strength for the specimens of the database.

Apparently, the shear strength of only a fraction of specimens has degraded to negligible values (10% or even 20%) of the maximum strength. Consequently, the assumption of zero shear strength at the onset of axial failure is certainly not experimentally justified; adopting it could potentially lead to high discrepancies i.e. much steeper descending branches and consequent

great underestimation of the energy dissipation capacity, especially in cases where axial failure initiates before significant shear strength degradation.

Therefore, a deformation-based criterion is sought, instead. Existing relationships predicting the lateral displacement at the onset of axial failure were applied in this extensive dataset of 89 specimens having sustained axial failure. The predictive ability of these models is shown in Figure 4-13. The models by Ousalem *et al.* (2004) and Yoshimura (2008) seem to exhibit very high scatter, in some cases overestimating and in other cases underestimating the lateral displacement by large. Elwood & Moehle's (2005a) and Zhu *et al.*'s (2007) models seem to capture the displacements well on average, but they also exhibit high scatter. Most of these models (Elwood & Moehle, 2005a; Ousalem *et al.*, 2004; Zhu *et al.*, 2007) have been calibrated only to flexure-shear critical specimens and they are all based on rather limited datasets.

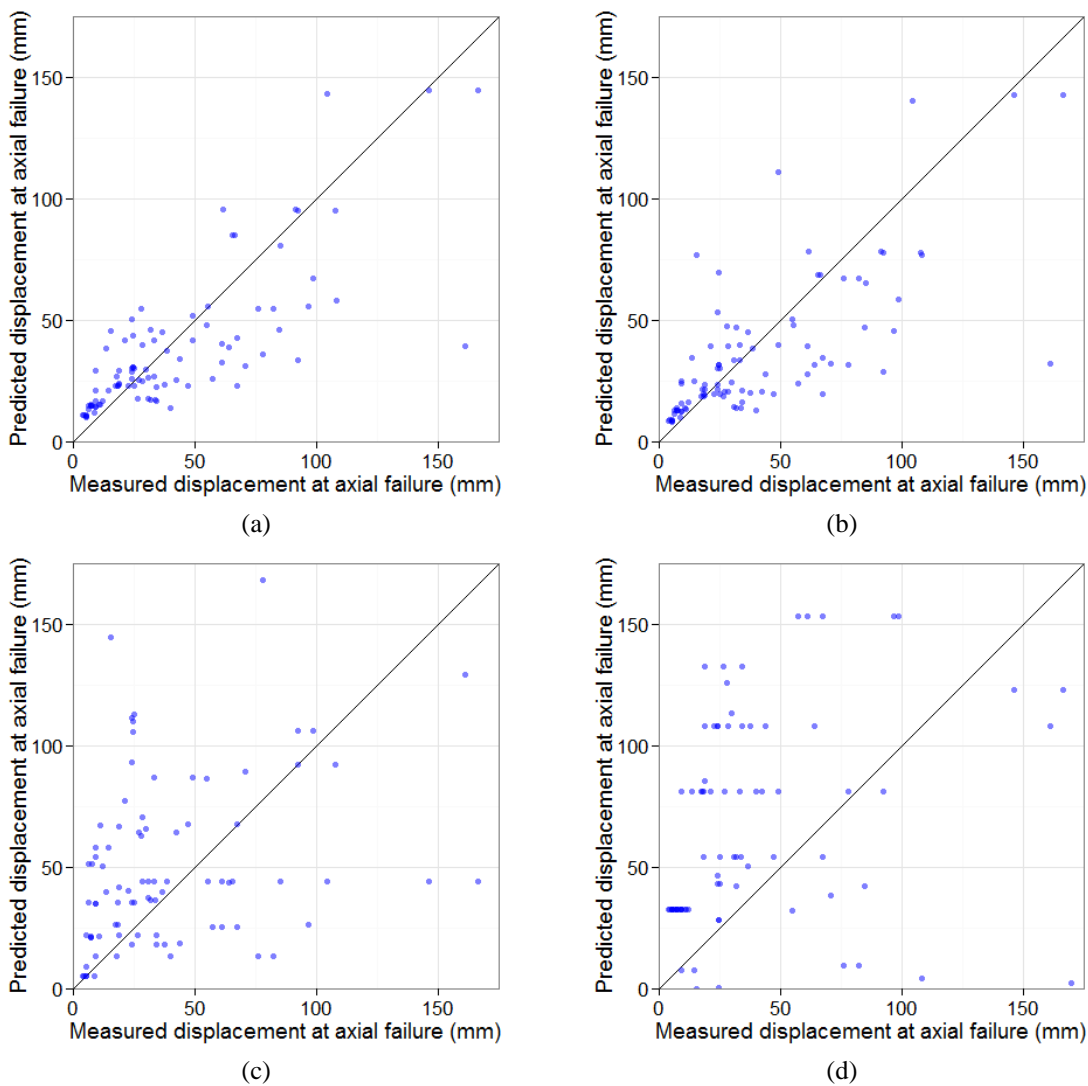


Figure 4-13: Existing predictive relationships for the lateral displacement at the onset of axial failure applied in this database, against measured displacements: (a) Elwood & Moehle (2005a), (b) Zhu *et al.* (2007), (c) Yoshimura (2008), and (d) Ousalem *et al.* (2004).

To improve the prediction accuracy, a new deformation-based empirical model is herein developed to capture the onset of axial failure of an R/C element. In line with the local shear hysteretic model to be described in section 8.1, the deformation parameter used is the average post-peak shear strain  $\gamma_{t,pp}$  in the critical shear length  $L_{cr}$  at the onset of axial failure determined by the following equation:

$$\gamma_{t,pp} = \frac{\delta_{ax,f} - \delta_{sh,f}}{L_{cr}} \quad (4-15)$$

where  $\delta_{ax,f}$  is the lateral displacement at the onset of axial failure, and  $\delta_{sh,f}$  is the lateral displacement at the onset of shear failure.

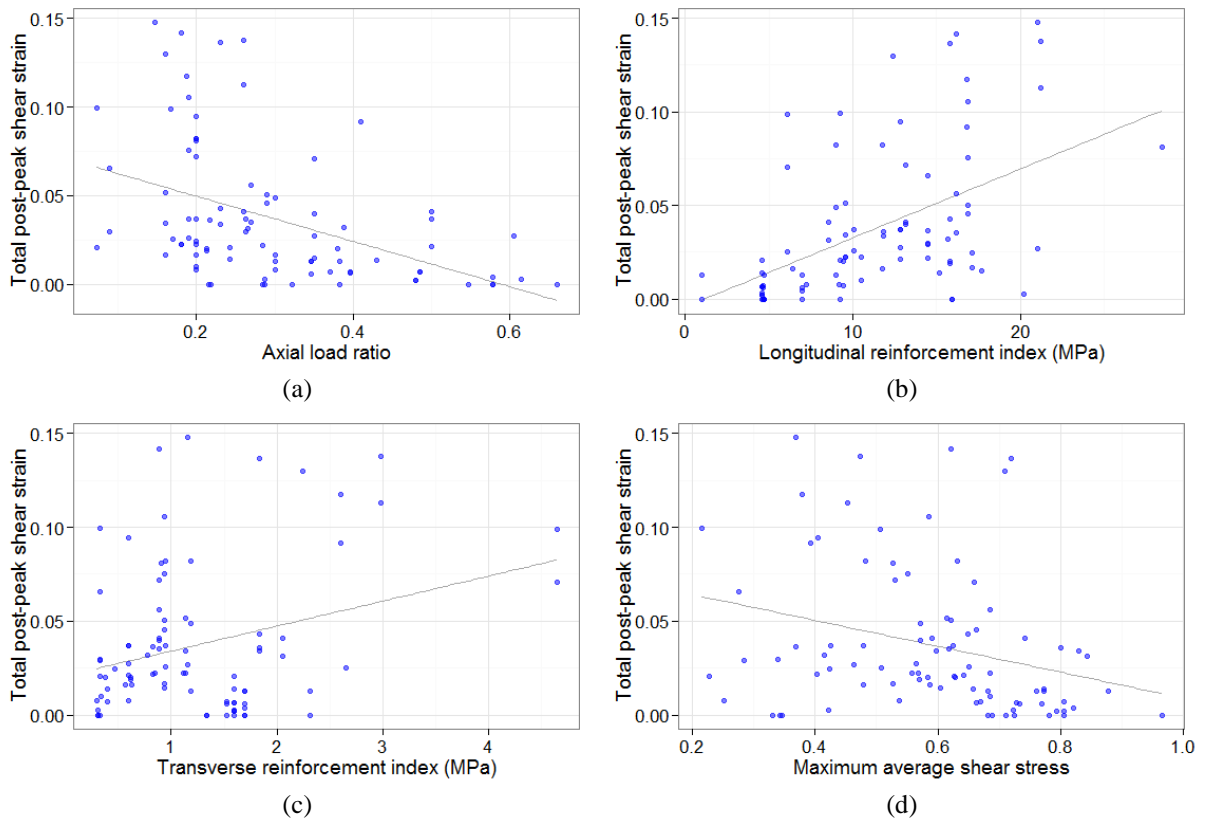


Figure 4-14: Correlation of total post-peak shear strain at the onset of axial failure ( $\gamma_{t,pp}$ ) with (a) axial load ratio based on the capacity of the longitudinal reinforcement,  $v_l$ , (b) longitudinal reinforcement ratio divided by the percentage of confined area,  $\rho_l/\alpha_{conf}$ , (c) transverse reinforcement ratio multiplied by its yield strength,  $\rho_w \times f_{yw}$ , and (d) maximum average shear stress,  $\tau_{max}/\sqrt{f_c}$ .

Based on this dataset, the following patterns emerged, examining the correlation of the local post-peak average shear strain with design and loading parameters (Figure 4-14):

- Axial load ratio is a pivotal parameter, associated with decrease in member deformability, as has been noted in many similar studies (e.g. Elwood & Moehle, 2005a; Ousalem *et al.*, 2002).
- Higher longitudinal reinforcement is beneficial, increasing the post-peak deformability, as also observed in previous studies (e.g. Yoshimura & Nakamura, 2002). Longitudinal

bars take up part of the axial load, partially relieving the confined concrete core from damage inflicted during the displacement reversals. Also, it allows for redistribution of a higher percentage of the axial load from concrete to steel at later stages.

- As expected, transverse reinforcement is beneficial, a fact underlined repeatedly in the past (e.g. Elwood & Moehle, 2005a; Ousalem *et al.*, 2002). It confines the concrete core, allowing for higher bearing capacity and takes up a significant part of the shear force, decreasing the shear strength degradation of the member and the damage inflicted to the core along the shear failure plane.
- The higher the maximum average shear stress, the lower seems to be the achieved deformation at the onset of axial failure.
- There are other influential factors, too, e.g. load history and failure type among others. As noted time and time again (e.g. Sezen & Moehle, 2006), monotonic response leads to higher deformability than cyclic. Flexure-shear critical specimens (FS) also seem to exhibit higher deformability on average, when contrasted with shear critical ones (S).

Based on these trends and significance tests of the predictor variables, various potential predictive relationships were explored. The final expression was developed through a step-wise predictor variable elimination procedure, 10-fold-cross-validation (Refaeilzadeh *et al.*, 2009) and optimisation using the Levenberg-Marquardt nonlinear least-squares algorithm (e.g. Levenberg, 1944):

$$\gamma_{t,pp} = \frac{0.01926(\rho_{w,conf} - 0.00074)^{0.4222} \left( \frac{\rho_l f_{yl}}{\alpha_{conf}} - 0.985 \right)^{0.8988}}{(v + 0.504)^{3.851} \left( \frac{\tau_{ave,max}}{\sqrt{f_c}} - 0.2154 \right)^{0.162}} - 5.768 \cdot 10^{-4} \geq 0 \quad (4-16)$$

where  $\rho_l$ ,  $\rho_{w,conf}$  are introduced with their actual value (not in %). Eq. 4-16 yields a mean experimental-to-predicted value of 1.02, a median of 0.78, a CoV of 84.8% and an  $R^2$  of 0.69, including all specimens. However, the inclusion of specimens having a very low value of deformation (close to zero) results in extreme values; excluding the ones equal to or lower than 0.01, the following values are obtained instead: 1.01, 0.85, 69.1% and 0.64. Despite the fact that the experimental-to-predicted ratios statistics are worse for  $\gamma_{t,pp}$  lower than 0.01, this is not considered a serious problem, because in terms of absolute values the errors are negligible. This is also verified by the very high  $R^2$  value achieved in both cases. The predictive ability of the expression, for all specimens, can also be seen in Figure 4-15. As explained previously (e.g. section 4.3), the high variability of the post-peak response influences the scatter produced by

this empirical relationship, hence it is not expected to yield a completely accurate value for each case it is used, but a roughly accurate estimate of this deformation quantity.

Eq. 4-16 is valid in the following range of parameters:  $0.07 < \nu < 0.66$ ,  $0.08 < \rho_w \leq 1.35$  (%),  $0.15 < \rho_l \leq 3.8$  (%),  $331 \leq f_{yl} \leq 700$  (MPa),  $303 \leq f_{yw} \leq 587$  (MPa),  $13.5 \leq f_c \leq 33.6$  (MPa),  $1 < L_s/d \leq 4.25$ .

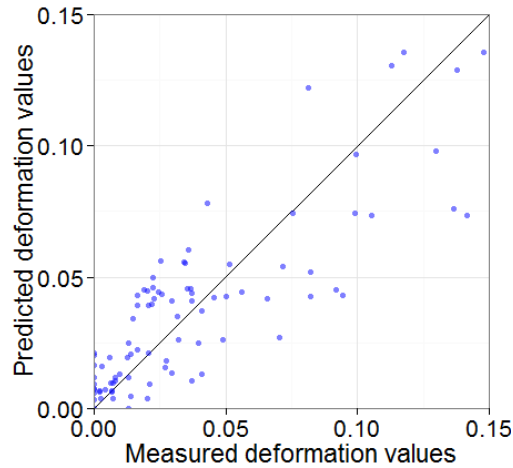


Figure 4-15: Measured total post-peak shear strain at the onset of axial failure against the predicted one using Eq. 4-16.

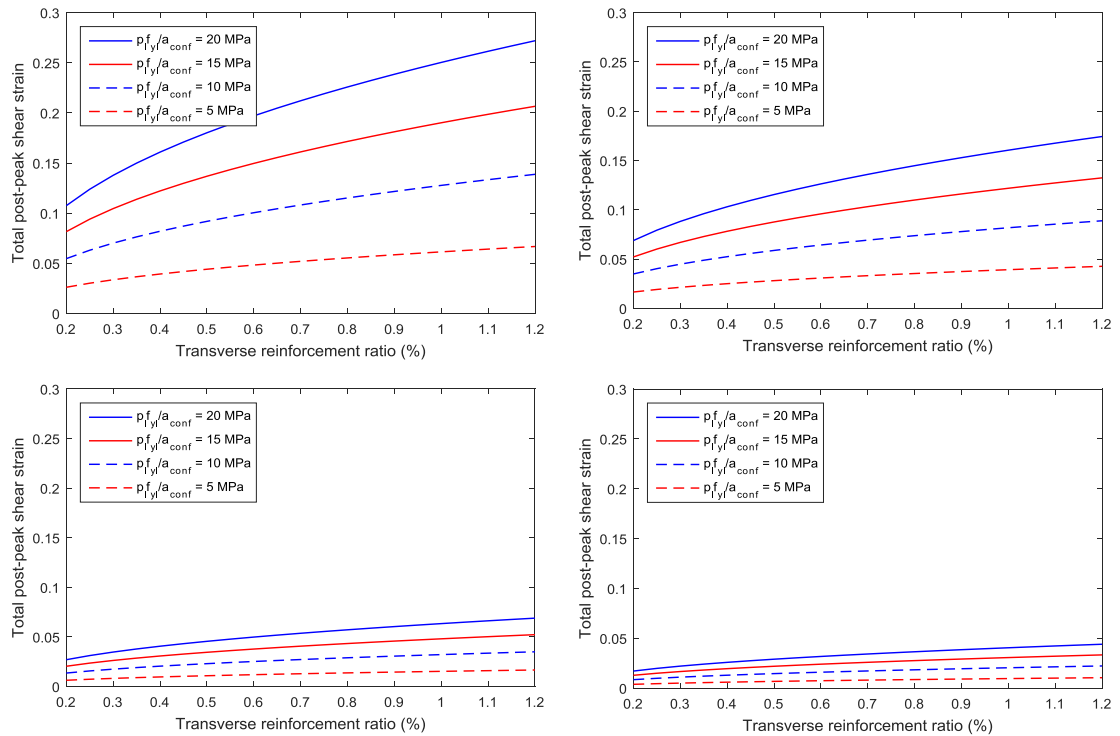


Figure 4-16: Total post-peak shear strain predicted by Eq. 4-16 along the range of longitudinal reinforcement ratios (over confined area) and transverse reinforcement ratios (over confined concrete area), for longitudinal reinforcement axial load ratios of 0.2 (top) and 0.5 (bottom) and maximum shear stress of 0.25 (left) and 0.75 (right).

In Figure 4-16, the values of the total post-peak shear strain ( $\gamma_{t,pp}$ ) predicted by Eq. 4-16 are plotted against the transverse reinforcement ratio normalised to the confined concrete volume ( $\rho_{w,conf}$ ), for four different longitudinal reinforcement indices ( $\rho_{f_{yl}}/\alpha_{conf}$ ), for axial load ratios ( $\nu$ )

of 0.2 and 0.5 and for maximum shear stress ratios ( $\tau_{max}/\sqrt{f_c}$ ) of 0.25 and 0.75. It is obvious that the higher the axial and shear loads and the lower the transverse and longitudinal reinforcement of a member, the lower its deformability, i.e. the lower the average post-peak shear strain at the onset of axial failure.

## Chapter 5: SIMULTANEOUS SHEAR AND AXIAL FAILURE

Generally, shear and flexure-shear critical vertical load bearing members possess some displacement capacity even after initiation of shear failure, as has been shown in the previous chapter. In other words, after the onset of shear failure, they can reach higher ductility levels accompanied by a corresponding deterioration of their lateral strength (Figure 5-1a). Nonetheless, some columns are susceptible to simultaneous shear and axial failure (Figure 5-1b, c). Determining which columns are prone to such failure is not a straightforward task, but it is of paramount significance, as the collapse mode of the structure can be adversely affected and the probability of collapse greatly increased, as explained in chapter 2. Therefore, a top priority in a pre-seismic retrofit attempt of an existing structure should be to strengthen these particularly vulnerable elements.

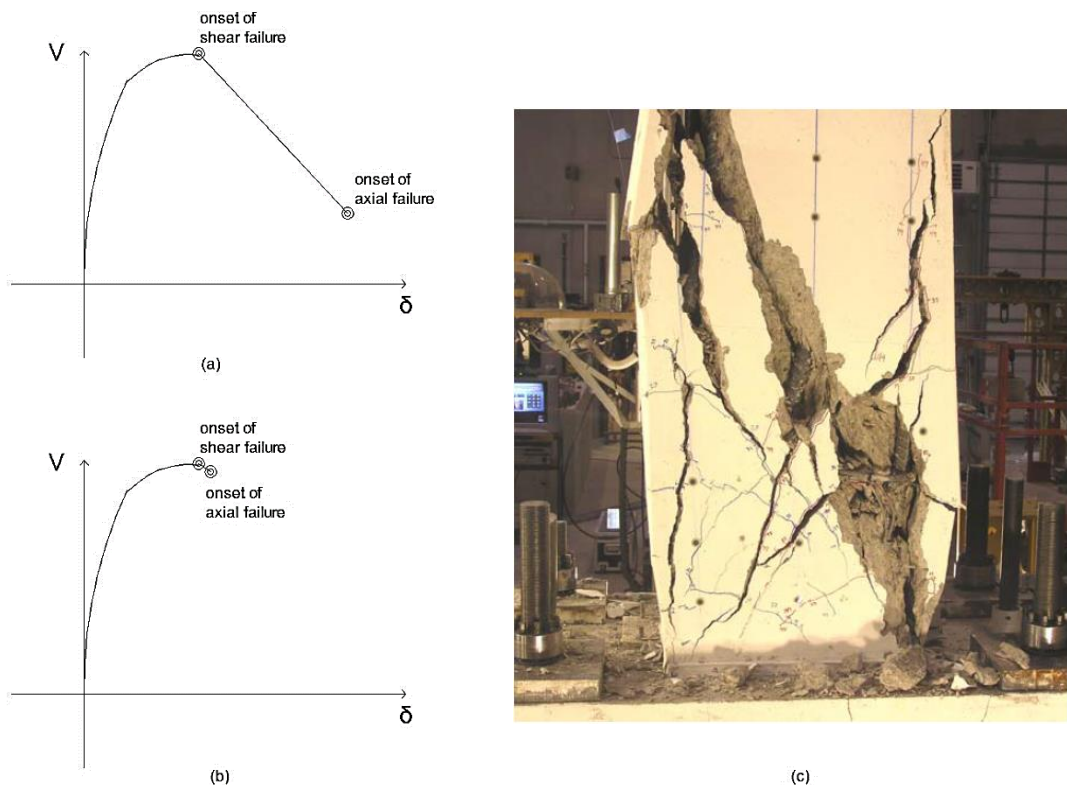


Figure 5-1: Indicative sketches of cyclic envelopes of the hysteretic lateral response of columns (a) failing axially after shear failure, or (b) failing in simultaneous shear and axial failure. (c) Example of specimen failing in simultaneous shear and axial failure (Matchulat, 2009).

In this chapter, the validity of previous suggestions on this phenomenon is explored in detail and the necessary conditions of simultaneous shear and axial failure of R/C columns are empirically identified. Subsequently, the empirical model proposed in the previous chapter (Eq. 4-16) is compared against an existing established model from the literature based on the ability to predict this type of failure.

## 5.1 DATASET AND PARAMETER OF INTEREST

A subset of the database (chapter 3) will be used, in order to investigate empirically the phenomenon of simultaneous shear and axial failure. In total, 89 specimens have sustained axial failure; another 44 have been included due to their post-peak behaviour, which means that at least 30% lateral strength degradation has been recorded, so it is clear that no simultaneous failure has occurred. Hence, a dataset of 133 specimens will be employed in total.

The main parameter explored herein is the post-peak Inter-storey Drift Ratio,  $IDR_{pp}$ , which is equal to the post-peak lateral displacement up to the onset of axial failure normalised by the length of the specimen. This is a parameter expressing a column's post-peak displacement capacity, which the earthquake engineering community would be very familiar with, making it an appropriate choice.

When this quantity is zero or close to zero for a given specimen, its post-peak response is practically non-existent, sustaining axial failure simultaneously with shear failure. However, it remains to define how much could be considered "close to zero". The post-peak Inter-storey Drift Ratio ranges from 0.0% to almost 12.0% in this database, with the main bulk of specimens lying between 0.6% and 3.2% (first and third quartile, respectively). Taking into account the typical heights of existing building storeys, even a 0.5% drift ratio would translate into 15 to 20 mm; this is a large value with regard to post-peak response.

Consequently, a value of 0.2%, i.e. up to 6-8 mm post-peak displacement for typical building columns, was chosen as a conventional upper limit in order to consider a specimen as having failed simultaneously in shear and axial failure. Out of the 133 specimens of the database, about 9.0% have sustained simultaneous shear and axial failure following this definition.

In order to get a better understanding of the magnitude, a limit of 0.1%, 0.4% or 0.6% would have resulted in 11, 15 or 25 specimens being deemed as failed in simultaneous shear-axial failure, respectively.

## 5.2 ASSESSMENT OF EXISTING OBSERVATIONS

The first hypothesis that is tested is the claim that flexure-shear – as opposed to shear – critical specimens sustain simultaneous shear and axial failure (Yoshimura *et al.*, 2003). This can readily be shown not to apply in all cases, since:

- about half the specimens sustaining such failure herein are shear critical, and
- the majority of flexure-shear critical specimens (88.1%) have not failed simultaneously in shear and axial failure.

The next hypotheses tested are the ones pertaining to the longitudinal reinforcement axial load ratio. Matchulat's (2009) finding that simultaneous shear and axial failure occurs when the applied axial load is (about) equal to, or greater than, the axial capacity of the longitudinal reinforcement cannot be generalised; however, Matamoros & Woods's (2010) remark about the ratio of 0.65 seems to provide indeed a lower threshold for the occurrence of the phenomenon. The upper threshold, above which the occurrence is highly probable seems to be the ratio of 2.25, as all of the specimens with greater  $v_l$  exhibit  $IDR_{pp}$ 's less than 1.0% and nearly half of them fail in simultaneous axial-shear failure. These patterns can be more clearly seen in Figure 5-2, where the lower ( $v_l = 0.65$ ) and upper thresholds ( $v_l = 2.25$ ) for the occurrence of simultaneous shear and axial failure are depicted. Note that the 44 specimens that showed no sign of axial failure have values of  $0 \leq v_l \leq 2.25$  and are not depicted on the diagram. Nonetheless, it is clear that this parameter alone cannot provide a comprehensive criterion, since the range of specimens in-between the two limits – where the behaviour is unpredictable – is quite extensive.

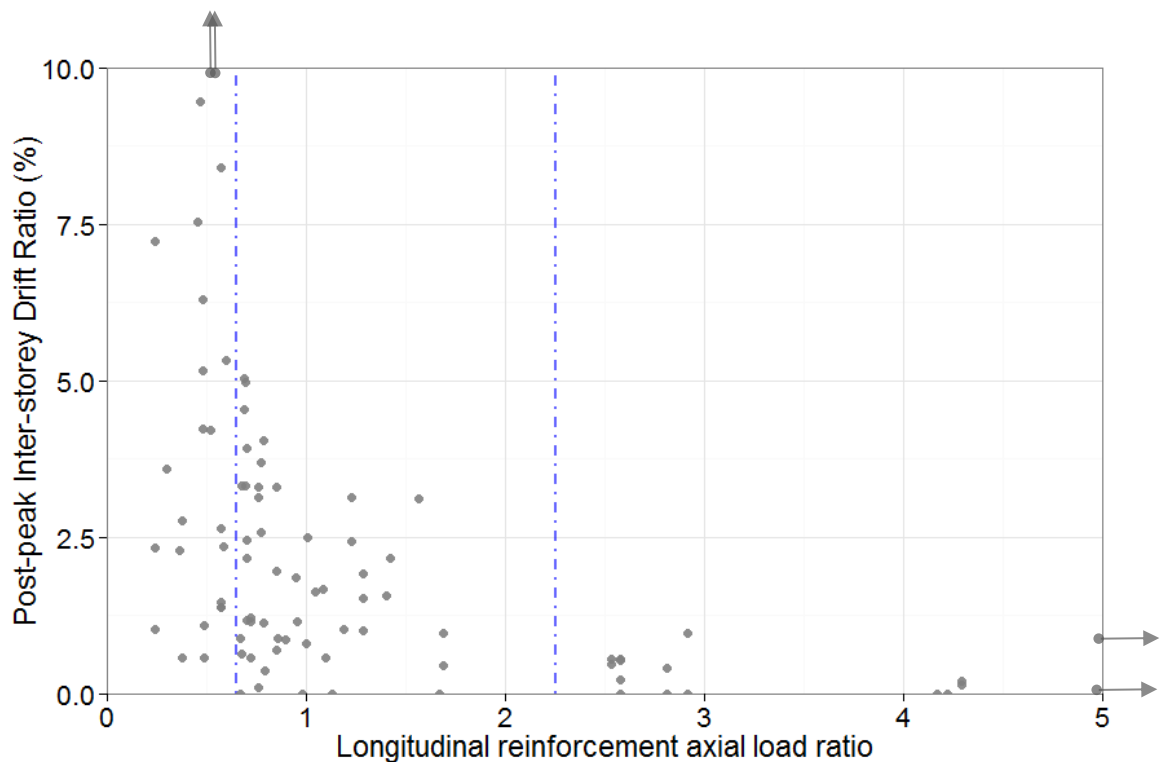


Figure 5-2: Correlation of  $IDR_{pp}$  with the longitudinal reinforcement axial load ratio. Some points are shown with arrows, indicating accurately one of their coordinates and that the other one is higher than the maximum of the range considered on the respective axis.

Henkhaus *et al.*'s (2009) study claims that the axial load ratio and the transverse reinforcement ratio limits of ASCE/SEI 41-06 (ASCE, 2006) are not sound, since all of the specimens sustaining simultaneous failure examined in their dataset would be deemed safe from it. It is established in the present study that a transverse reinforcement ratio of  $\rho_w \geq 0.05\%$  and a compressive axial load ratio of  $v \leq 0.6$ , or even  $\rho_w \geq 0.06\%$  and  $v \leq 0.3$ , do not ensure that simultaneous failure will not occur, as can be seen in Figure 5-3. The vast majority (83.3%) of the specimens that failed

simultaneously satisfy the former limits ( $v = 0.60$  and  $\rho_w = 0.05\%$ , shown with blue dashed lines). One third of them are even inside the latter, more stringent limits ( $v = 0.30$  and  $\rho_w = 0.06\%$ , shown with green dashed lines).

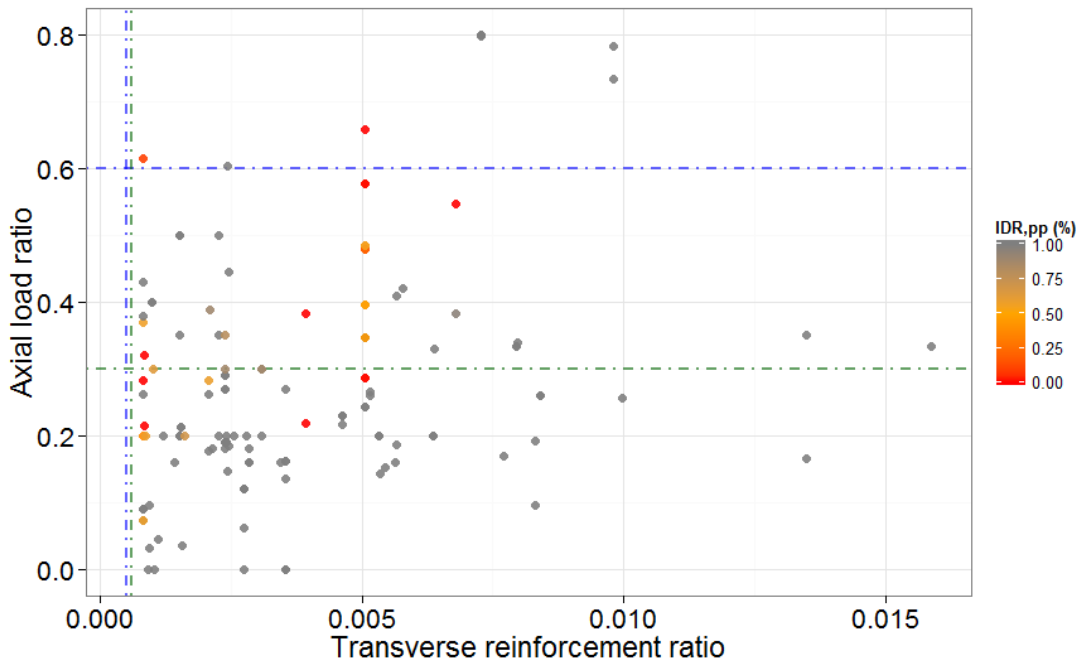


Figure 5-3: Values of  $IDR_{pp}$  depicted against axial load ratio and transverse reinforcement ratio. Values greater than 1% are in grey colour.

### 5.3 PROPOSED CRITERIA

Based on the remarks made in the previous section, a simplified criterion is extracted, which can be used if a limited amount of data is known for a given column or if only a preliminary estimation is to be made. This criterion is based on the ratio of axial load over yield strength of longitudinal reinforcement ( $v_l = P / (A_{sl} \cdot f_{yl})$ ) and reads as follows (Figure 5-2):

- If  $v_l \leq 0.65$  (compression positive), the column can be considered safe.
- If  $v_l \geq 2.25$ , the column will most likely fail in simultaneous shear and axial failure.

In the intermediate zone ( $0.65 \leq v_l \leq 2.25$ ), the behaviour cannot be reliably determined, as there are specimens belonging to both categories.

Subsequently, a more reliable and accurate criterion is sought. Besides  $v_l$  and  $v$ , other parameters are studied, in order to discover suitable classification variable(s). The transverse reinforcement was used in the ASCE/SEI 41-06 (ASCE, 2006) classification and is generally believed to play an important role in this phenomenon. Therefore, many different relevant

parameters including  $s/d$ ,  $\rho_w$ ,  $f_{yw}$  and combinations of these variables have been tried out, since the transverse reinforcement ratio is shown not to be adequate by itself (Figure 5-3).

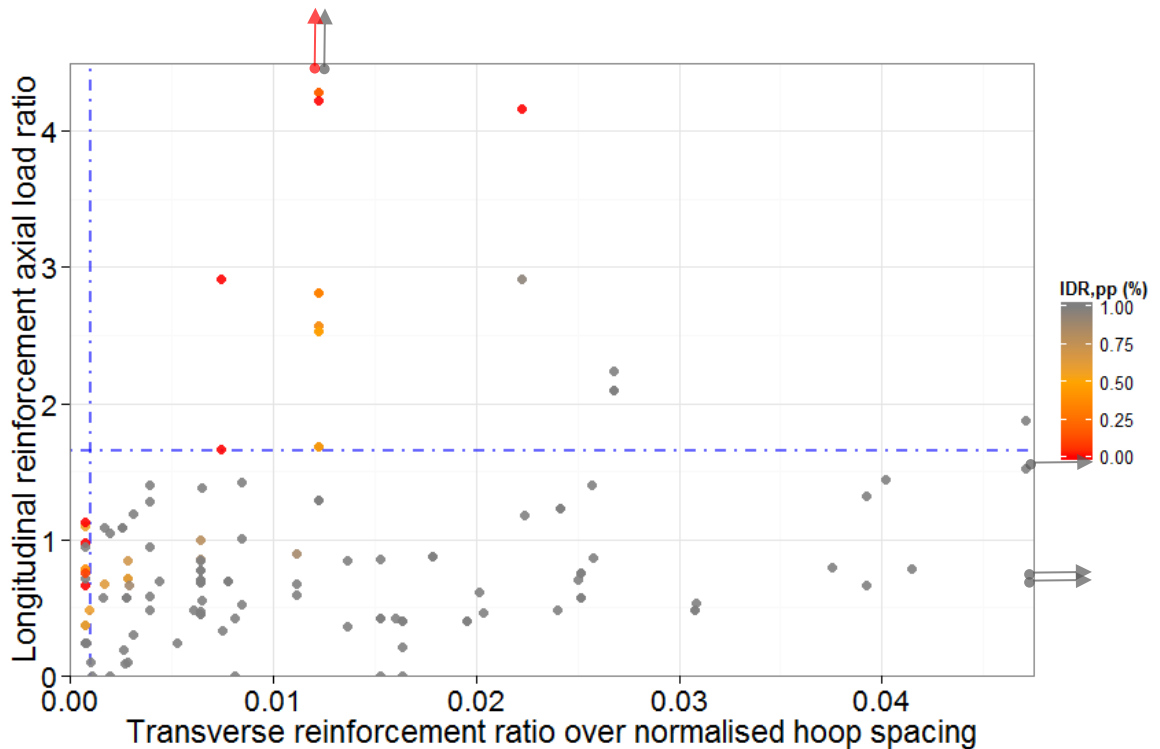


Figure 5-4: Values of  $IDR_{pp}$  depicted against longitudinal reinforcement axial load ratio and transverse reinforcement ratio over normalised hoop spacing. Values greater than 1% are in grey colour. Some points are shown with arrows, indicating accurately one of their coordinates and that the other one is higher than the maximum of the range of the respective axis.

Eventually, the combination of the parameters  $v_l$  and  $\rho_w / (s/d)$  was found to be the best one to classify the specimens. Its classification capability can be seen in the scatter plot of Figure 5-4. The latter parameter expresses the content of transverse reinforcement further reduced or enhanced by sparse or dense hoop spacing, respectively.

The criterion defines a "safe area" for columns and reads as follows (Figure 5-4, with blue dashed lines showing the limits of the safe area at  $v_l = 1.65$  and  $\rho_w / (s/d) = 0.1\%$ ):

- If  $v_l \leq 1.65$  and  $\rho_w / (s/d) \geq 0.1\%$ , the column is considered safe, i.e. it is not going to fail in simultaneous shear and axial failure.
- If  $v_l > 1.65$  or  $\rho_w / (s/d) < 0.1\%$ , the column might fail in simultaneous shear and axial failure, i.e. the necessary conditions are met. Nevertheless, there are specimens falling into this category that do not fail thus, as the conditions are not sufficient and necessary at the same time.

Leaning towards the conservative side (i.e. in a code of practice context), if the goal is to avoid a post-peak Inter-storey Drift Ratio lower than 1.0%, one can use one of the two following "extra-safe zones" criteria:

- $v_l \leq 1.65$  and  $\rho_w / (s/d) \geq 1.15\%$ , or
- $v_l \leq 0.85$  and  $\rho_w / (s/d) \geq 0.3\%$ .

Summarising, having knowledge of the axial load carried by a given column, its longitudinal and transverse reinforcement, one can define if it is safe from this type of failure or if it meets the necessary conditions for it.

Of course, as mentioned in previous sections (e.g. 3.2.5 or 4.3), there is high uncertainty associated with this damage state. Therefore, variability in the data might mean that specimens marginally falling into the safe area might actually fail in simultaneous shear and axial failure. Therefore, slightly stricter limits might be worth considering, in order to compensate for this uncertainty.

## 5.4 EVALUATION OF PREDICTIVE MODELS

Two empirical models predicting the post-peak response of R/C members are tested against the experimental observations of the aforementioned dataset. The first one comprises the Elwood & Moehle equations (Elwood & Moehle, 2005a; Elwood & Moehle, 2005b) that predict the drift ratio at the onset of shear and axial failure, respectively, and which have been incorporated into several member-type constitutive models. The onset of shear failure has been defined as 20% loss of shear strength, while the onset of axial failure as complete loss of strength. Therefore, a factor of 1.25 will be applied to get the entire predicted post-peak displacement, namely from the point of maximum strength that has been herein defined as onset of shear failure, so that the results presented below be directly comparable (see Figure 5-5):

$$\frac{\Delta_s}{L} = \frac{3}{100} + 4\rho_w - \frac{1}{40} \frac{\tau_{\max}}{\sqrt{f_c}} - \frac{1}{40} \frac{N}{A_g f_c} \geq \frac{1}{100} \quad (5-1)$$

$$IDR_{,pp} = 100 \cdot 1.25 \left( \frac{\Delta_a}{L} - \frac{\Delta_s}{L} \right) = 100 \cdot 1.25 \left( \frac{4}{100} \frac{1 + (\tan 65)^\circ}{\tan 65 + N \left( \frac{s}{A_{sw} f_{yw} d_c \tan 65} \right)} - \frac{\Delta_s}{L} \right) \geq 0 \quad (5-2)$$

where  $IDR_{,pp}$  is calculated in %,  $\rho_w$  is the transverse reinforcement ratio introduced with its actual value (not in %),  $f_c$  is the concrete compressive strength,  $N$  is the axial load applied on the column,  $A_g$  is the cross-section area,  $A_{sw}$  and  $f_{yw}$  are the area and yield strength of the transverse reinforcement, the angle in the tangent is in degrees ( $65^\circ$ ),  $s$  is the spacing between the transverse reinforcement ties and  $d_c$  is the depth of the column core from centreline to centreline of ties.

The second empirical model is based on Eq. 4-16, henceforth referred to as Zimos *et al.* model, which predicts the post-peak shear deformation of an R/C member, described by the following equation:

$$IDR_{,pp} = 100 \frac{L_{cr}}{L} \left[ \frac{0.01926 (\rho_{w,conf} - 0.00074)^{0.4222} \left( \frac{\rho_l f_{yl}}{\alpha_{conf}} - 0.985 \right)^{0.8988}}{(v + 0.504)^{3.851} \left( \frac{\tau_{ave,max}}{\sqrt{f_c}} - 0.2154 \right)^{0.162}} - 5.768 \cdot 10^{-4} \right] \geq 0 \quad (5-3)$$

where  $IDR_{,pp}$  is calculated in %,  $\rho_l$ ,  $\alpha_{conf}$  and  $\rho_{w,conf}$  are introduced with their actual value (not in %), and  $L_{cr}$  is the shear critical length defined by the critical shear crack angle (Eq. 4-2). For consistency, the predicted post-peak displacements from both models have been normalised to the clear length of the member, instead of the critical shear length.

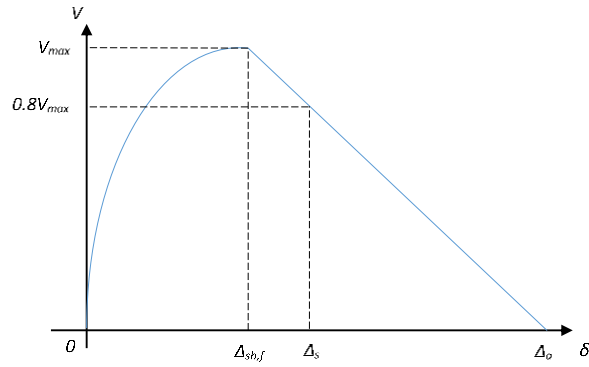


Figure 5-5: Schematic representation of displacement derived from Elwood & Moehle model.

The first model seems to estimate well the occurrence of simultaneous shear and axial failure overall, which is shown in Figure 5-6 (limits of previously defined safe area shown with blue dashed lines, for comparison). However, there are specimens into the safe zone that are predicted to have post-peak drifts equal to or very close to zero. On the other hand, the Zimos *et al.* model seems to underestimate the occurrence of simultaneous failure, predicting close to zero deformation for very few specimens (Figure 5-7); these, however, mostly fall into the not-safe zone, which is a positive sign.

For a more objective comparison, initially the models' predicted values are compared to the observed values and comparison statistics are produced (Table 5-1), including  $R^2$ , Mean Absolute Error (*MAE*) and Root Mean Squared Error (*RMSE*). Reading the statistics, one realises that the first model is doing clearly worse in explaining the variation of the observed values (i.e. much lower  $R^2$ ) compared to the second model. The second model has an  $R^2$  roughly equal to the one obtained by Eq. 4-16. The difference in the other two statistics further complements this finding, with the first model producing systematically a roughly 70% higher error than the other.

Subsequently, the models' classification capabilities are compared based on the observed values and confusion matrices are constructed (Table 5-2). Therein, the number of cases that a model predicted correctly that a specimen is safe or that it will fail simultaneously lie on the diagonal (classification as "safe" and "failed" is based on an  $IDR_{pp} \leq 0.2\%$ , as previously mentioned in section 5.1). Conversely, in the other cells one can spot the number of specimens that were falsely predicted as due to fail in shear-axial failure while being actually safe or the opposite. The classification with the aforementioned two-parameter classification criterion (section 5.3) is also included, for comparison purposes. From these, statistics are computed to compare the classification strength of each model (Table 5-3).

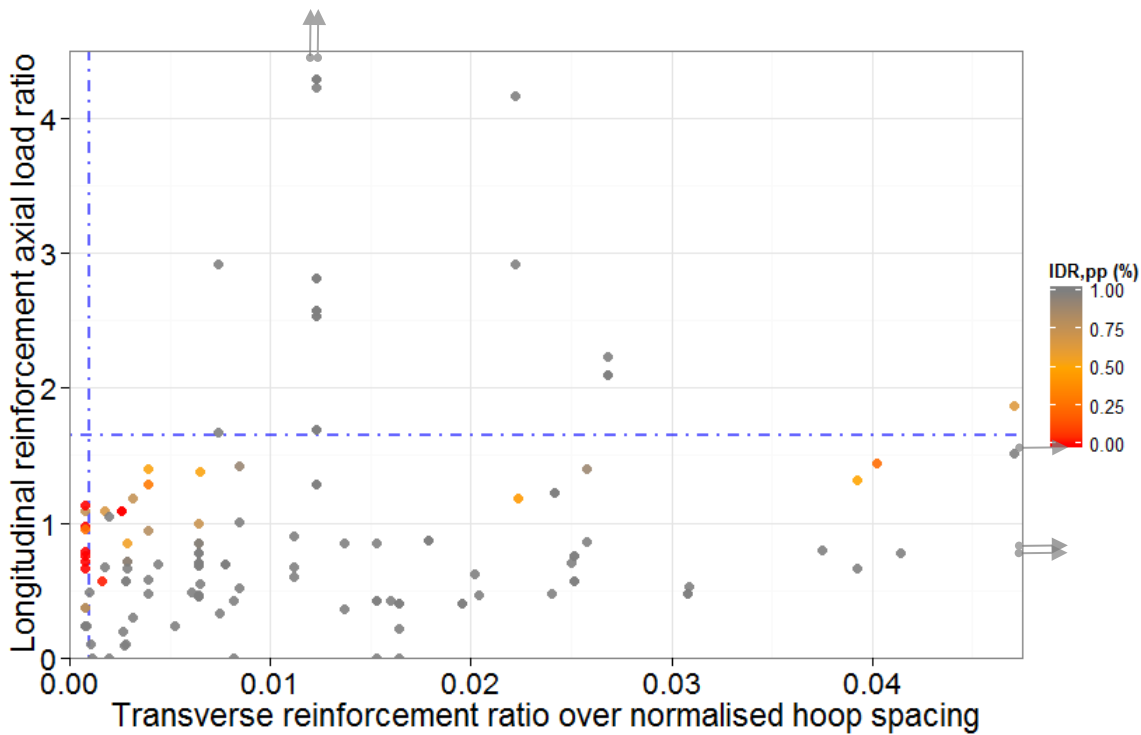


Figure 5-6:  $IDR_{pp}$  predicted by the Elwood & Moehle model (2005a; 2005b) against longitudinal reinforcement axial load ratio and transverse reinforcement ratio over normalised hoop spacing.

Table 5-1: Comparison statistics of the predictive models against the experimentally observed values.

Model	$R^2$	MAE	RMSE
Elwood & Moehle	0.08	1.645	2.294
Zimos <i>et al.</i>	0.69	0.983	1.336

It is observed that – in line with the previously presented statistics – the Zimos *et al.* model is clearly the more accurate one, having the highest accuracy and producing the lowest error rate, i.e. it predicts the most correct cases overall even compared to the classification criterion. The Elwood & Moehle model follows suit with just a minor decrease in accuracy, while the classification criterion has an even lower accuracy.

However, the classification criterion results in zero Type I error, which is exactly its objective of providing the necessary conditions of failure, i.e. that each specimen it predicts as safe be indeed safe. If the conditions were necessary and sufficient, Type II error would also be zero, i.e. each specimen that it would predict as due to fail in axial-shear failure would indeed fail. The other two models result in very high Type I error, largely because they systematically overestimate the deformability of each member (Figure 5-6 and Figure 5-7). This is corroborated by the fact that the Type II error is very low, so the overwhelming majority of the specimens they predict as safe are indeed safe.

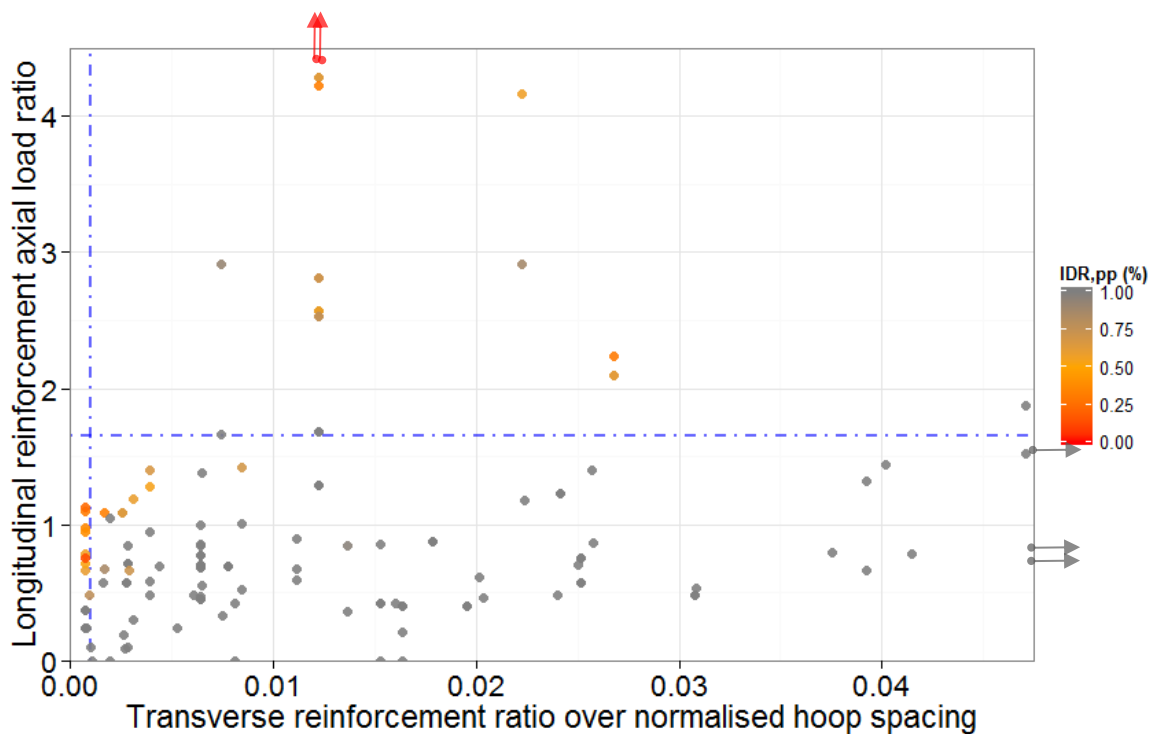


Figure 5-7:  $IDR_{pp}$  predicted by the Zimos *et al.* model against longitudinal reinforcement axial load ratio and transverse reinforcement ratio over normalised hoop spacing.

Table 5-2: Confusion matrices of the predicted values of the empirical models (plus the classification criterion) compared to the observed values of the database.

Elwood & Moehle		
<b>observed \ predicted</b>	“safe”	“failed”
“safe”	116	5
“failed”	8	4
Zimos <i>et al.</i>		
<b>observed \ predicted</b>	“safe”	“failed”
“safe”	120	1
“failed”	10	2
Classification Criterion		
<b>observed \ predicted</b>	“safe”	“failed”
“safe”	96	25
“failed”	0	12

Comparing Figure 5-6 and Figure 5-7 to Figure 5-4 reveals that the Zimos *et al.* model is closer to the actual deformation in each case, but it slightly overestimates the specimens' deformability, hence many specimens marginally do not qualify for the "failed" category; visually, this is understood by the fact that several specimens in the "failed" area that have indeed failed (Figure 5-4) are closer to orange than red in Figure 5-7 (i.e. slightly higher than the limit of 0.2%). At the same time, those being in the safe area are correctly mostly grey or yellow/orange, with no specimen predicted as failing simultaneously. This is why it performed markedly better in absolute terms (Table 5-1), but not in terms of classification capability (Table 5-3).

Table 5-3: Comparison statistics of the predictive models' classification capabilities based on the experimentally observed values.

Model	Accuracy	Error Rate	Error I	Error II
Elwood & Moehle	0.90	0.10	0.67	0.04
Zimos <i>et al.</i>	0.92	0.08	0.83	0.01
Classification criterion	0.81	0.19	0	0.21

On the other hand, the Elwood & Moehle model seems to predict failed specimens inside the safe zone, while resulting in many grey dots in the not-safe area. This is not observed as much in the left area as in the top one, which is governed by exceedance of the longitudinal reinforcement axial load ratio. This is because, as explained in chapter 2, this model does not account for the longitudinal reinforcement's influence on the deformation at the onset of axial failure. It is believed that if this parameter were duly considered, the model's prediction with regard to that part of the plot could improve.

In conclusion, the Zimos *et al.* model (Eq. 5-3) seems to be much better in predicting the post-peak displacement capacity of an R/C member in absolute terms compared to the Elwood & Moehle model (Eq. 5-1, 5-2). This is largely due to the lack of the effect of longitudinal reinforcement in the latter model and the range of parameters of the databases to which these empirical equations (Eq. 5-1, 5-2) were calibrated being much narrower compared to the extensive database used herein. Of course, it has to be noted that this database partly comprises of the subset used to calibrate the Zimos *et al.* model (Eq. 5-3), which increases the expected accuracy of this model.

On the other hand, when it comes to predicting the safety of a specimen, i.e. each specimen predicted as safe being indeed safe, the two-parameter classification criterion is unequivocally

the best, producing no error as was its development objective. In this respect, the Elwood & Moehle model performs better than the Zimos *et al.* model for the reasons mentioned above.



## PART II: EXPERIMENTAL PROGRAMME



## Chapter 6: DESIGN OF EXPERIMENTAL PROGRAMME

### 6.1 CONCEPTUAL DESIGN

Axial failure of a column can occur after the onset of shear failure, subsequently, or even prior, to yielding of the longitudinal reinforcement, through disintegration of the poorly confined concrete core of the column with continuous lateral cycling (Sezen & Moehle, 2006). The biggest part of the vertical load carried by a failing member is subsequently redistributed to neighbouring vertical elements through the adjacent horizontal members, as shown in Figure 6-1. This leads to a significant increase of axial load acting on the neighbouring R/C columns; the non-linear lateral response of the latter will be altered due to this increase of axial loading and this is a problem not addressed in previous studies.

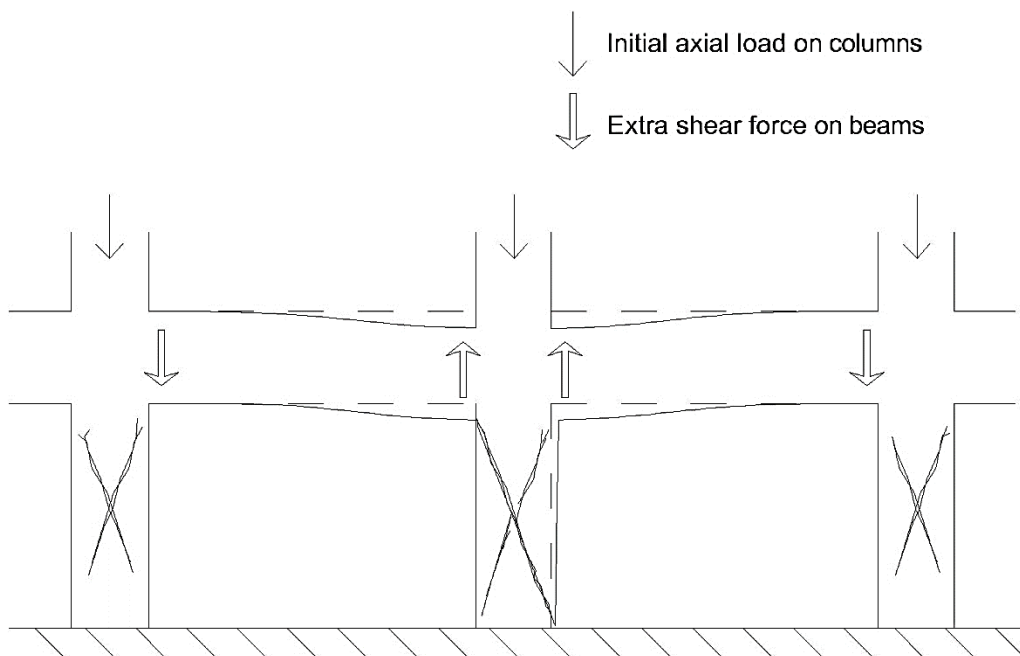


Figure 6-1: Mechanism of axial load increase of columns neighbouring an axially failing column.

The ability of a structural system to resist progressive collapse in such a 'scenario' hinges both on the ability of horizontal elements to transfer the loads being redistributed to adjacent vertical elements and on the latter's ability to resist them without losing a considerable part of their strength and deformability (Lodhi, 2012). Existing research work has looked extensively into the adjacent horizontal elements' capacity to redistribute vertical loads, neglecting the vertical elements neighbouring axially failing columns or assuming they are capable of bearing the extra axial load, as explained in chapter 2.

Another common assumption in progressive collapse analysis is that of undamaged vertical elements, e.g. assuming uncracked cross-sections; this might be appropriate for blast-induced, vehicular impact or similar collapse scenarios, where damage can be largely assumed localised

in a single structural element or a small set of elements. Nevertheless, earthquake-induced collapse scenarios pose a further difficulty in that there is global damage in a large part of the, if not the entire, building even before the loss of a column's vertical load-bearing capacity. Therefore, the damage state of a column neighbouring an axially failed vertical member has to be appropriately taken into account in a realistic earthquake-induced progressive collapse assessment, e.g. as attempted to be done by Murray & Sasani (2013).

Previous experimental studies looking into the non-linear, and especially post-peak, lateral response of substandard R/C columns have looked extensively at the response under constant vertical load (e.g. Lynn *et al.*, 1996; Yoshimura & Nakamura, 2002) as well as variable axial load corresponding to an exterior column case, i.e. axial load proportional to the lateral force acting on the column (e.g. Ramirez & Jirsa, 1980; Sezen & Moehle, 2006). Recently, Nakamura & Yoshimura (2014) investigated the effect that decreasing axial load has on the lateral non-linear response of substandard columns, attempting to experimentally simulate the response of a column that starts failing axially and its axial load starts decreasing correspondingly due to vertical load redistribution. Nonetheless, to the writer's best knowledge, the effect of the axial load increase of the neighbouring R/C columns has thus far not been investigated at all. The main objective of this part of the present study is to shed further light on this phenomenon, i.e. the effect of vertical load redistribution on the non-linear response of shear- and flexure-shear-critical R/C columns neighbouring failing vertical members.

Cantilever specimens of length corresponding to the length between the floor and the contraflexure point of a building R/C column have been selected to be tested. Two series of specimens were constructed, one failing in flexure-shear and another in shear, so that both types of members can be investigated. The focus is on older R/C construction lacking modern design and detailing rules, thus not focussing on flexure dominated members.

A lateral cyclic load along with a constant vertical load acting at the specimens' top simulate the conditions before redistribution of any extra loads. One specimen in each test series will be thus tested, to establish the reference pre- and post-peak response. In the other specimens, at some point the lateral cycling will pause, the vertical load will be increased to the desired level and subsequently lateral cycling will resume; this simulates the response to a) an earthquake loading up to a given point, b) redistribution of vertical loads from a neighbouring column, and c) continuation of the earthquake action up to vertical collapse of the given column.

An important issue is the damage state at the point of vertical load increase over the response history of the column. As mentioned previously, in earthquake-induced collapse scenarios there is substantial damage in most of the building before the loss of a column's vertical load-bearing

capacity and the difference in the damage state considered might have a significant impact on the resulting response. For instance, an axial load increase at the early stages of pre-peak response might be beneficial for the overall response of the member, increasing its strength and stiffness, while the same increase in the post-peak stage might prove detrimental. As the main focus of this study is on the peak and post-peak response of flexure-shear and shear critical R/C columns, two different points of axial load increase were selected in order to observe the response difference. The first one is before the start of the displacement level where the onset of shear failure occurs and the second one immediately after it.

Another important issue is the percentage of axial load increase. Usually, neighbouring columns carry vertical loads of comparable values and after axial failure of one of them, this is redistributed to three or four neighbouring columns, so normally it should increase by 20% to 35%. However, there are cases where higher load increase can take place, as in neighbouring columns with different tributary areas or cross-section dimensions. Additionally, a higher increase will lead to a more pronounced effect on lateral response. Therefore, a 50% increase of the axial load is selected here as a reasonably conservative value.

It is highly likely that this axial load increase will initiate at or close to the extreme displacement excursions of the displacement history of the specimens. Nonetheless, according to previous shake-table tests (e.g. Elwood & Moehle, 2003; Ghannoum & Moehle, 2012), the procedure of vertical resistance loss of a column and redistribution of the previously carried axial loads to neighbouring columns takes place gradually over several load reversals. In absence of a specific “point” and leaning towards the side of safety, the zero displacement point of a cycle was chosen as the point of vertical load increase during the tests.

Besides the aforescribed effect that will be investigated, the design characteristics of the specimens are selected with a view to supplementing the existing experimental literature on post-peak response (see Figures 3-1, 3-2), particularly with respect to the aspect ratio. It is important to obtain insight in areas of characteristics with sparse data, so as to verify the capabilities of existing empirical relationships and improve the reliability of proposed ones in the future.

Additionally, these tests provide an excellent opportunity for independent verification of the analytical model under development (see chapter 8). In other words, these tests not being included in the database, they allow for an ‘external’ validation of the model’s predictive capabilities.

Of course, carrying out a limited experimental programme is not expected to furnish enough results to recalibrate a model that is based on such a large number of specimens, but can allow us to identify some trends as to the role of the axial load change. Most of the empirical relationships used in the analytical model have been based on about or more than 100 tests, thus carrying out 6 more could not possibly lead to a significant change.

Furthermore, it is of very high importance to test the underlying assumptions of the model under development regarding the post-peak response of substandard columns (see theoretical basis in section 4.1). Such columns have been assumed to deform mainly in shear after the onset of shear failure (their flexural and bond-slip deformations not increasing any further than their values at the onset of shear failure) and these deformations have been assumed to be concentrated at a specific shear-damaged region, defined by the diagonal shear full-depth cracks. This is perhaps the most crucial point, as the whole post-peak response prediction hinges on the validity of this theoretical basis.

## 6.2 DESIGN OF TEST SPECIMENS

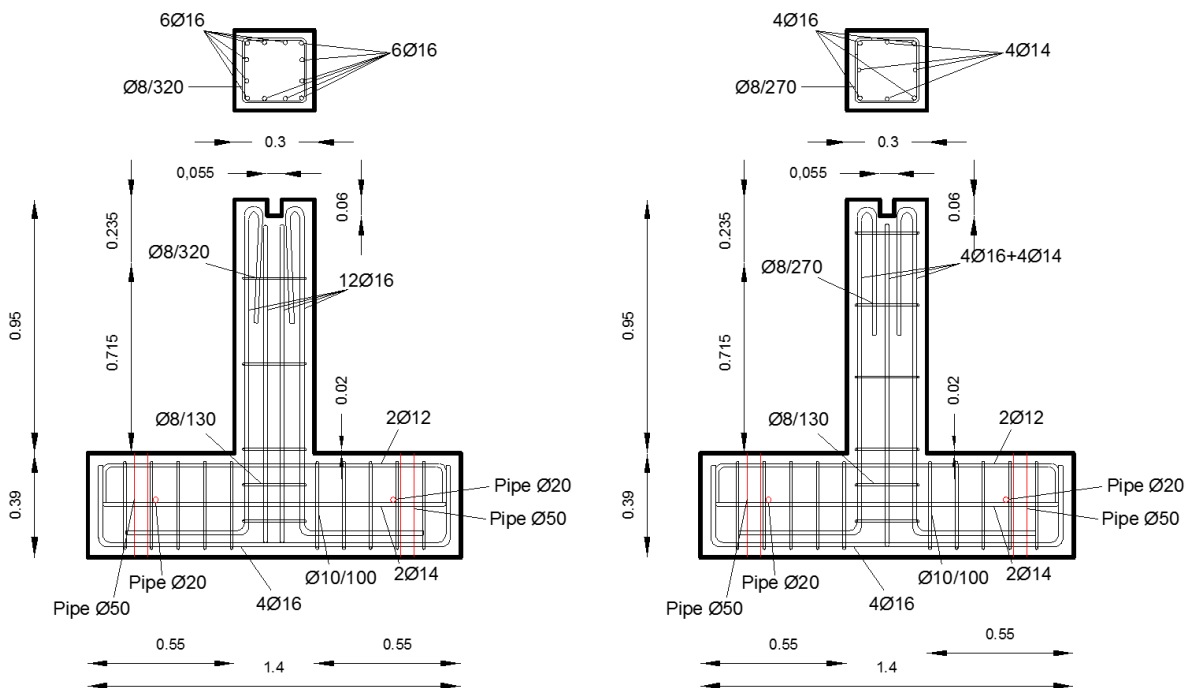


Figure 6-2: Design of (a) shear critical (SC) and (b) flexure-shear critical (FSC) specimens (lengths in m; bar and pipe diameters in mm).

Two sets of three geometrically and materially identical columns (6 columns, in total) with different reinforcement characteristics were designed and fabricated (Figure 6-2). The specimens are short columns with an aspect ratio of slightly less than 3.0, with detailing representative of older construction. The cross-section is square, 300 × 300 (mm), and the

cantilever length is 715 mm. The target material characteristics are concrete grade C12/15 representative of older R/C construction, while both the transverse and longitudinal reinforcement consist of B500C steel ribbed bars. Consistent with old practice, the transverse reinforcement is quite sparse i.e.  $\varnothing 8/320$  and  $\varnothing 8/270$  for the shear critical (SC) and flexure-shear critical (FSC) specimens, respectively (Figure 6-2).

The longitudinal reinforcement was designed so as to achieve the desired response and failure type; it is  $12\varnothing 16$  and  $4\varnothing 16+4\varnothing 14$ , resulting in a total reinforcement ratio of 2.68% and 1.58%, respectively. Yield and ultimate moments were calculated from  $M-\varphi$  analysis using *RCCOLA.NET* (Kappos & Panagopoulos, 2011). The predicted shear resistance was calculated based on five shear strength models (Biskinis *et al.*, 2004; Priestley *et al.*, 1994; Sezen & Moehle, 2004; fib, 2010; CEN, 2005) predicting the maximum resistance, i.e. before shear strength degradation with increasing inelastic flexural deformations (Table 6-1). The Priestley *et al.* (1994) model's predictions using shear crack angles of both  $30^\circ$  and  $45^\circ$  are presented. The Biskinis *et al.* (2004) equation is also the one proposed by Eurocode 8-3 (CEN, 2005), using mean material values and disregarding partial factors;  $\mu_{\Delta,pl}$  and  $\chi$  (compression zone depth) corresponding to yielding have been used for the maximum strength, as the shear strength arising using values before yielding was judged not to be representative and it was not necessary for these tests. For the Model Code 2010 (fib, 2010) shear strength equation partial factors are disregarded and it is based on a level III approximation. This design can be understood to lead the SC specimens most likely to pure shear tension failure, i.e. before longitudinal reinforcement yielding takes place. The FSC specimens, on the other hand, will most likely yield in flexure and subsequently fail in tension shear, with the Priestley *et al.* (1994) model predicting it will fail in flexure and the Model Code 2010 (fib, 2010) model predicting it will fail in shear before reaching flexural yield.

Table 6-1: Flexure- and shear-controlled resistance (kN) predicted for each specimen set, based on  $M-\varphi$  analysis and various shear strength expressions.

Specimen series	Flexural strength ( $M-\varphi$ analysis)		Shear strength				
			Priestley <i>et al.</i>		Biskinis <i>et al.</i> / EC8-3	Sezen & Moehle	MC2010
			30°	45°			
SC	Yield	Ultimate	173	149	151	119	119
FSC	121	128	184	156	127	126	123

It is clear from Table 6-1 that the prediction of the maximum shear resistance of an R/C element is subject to very high variability and different models can lead to great differences. In order to validate the findings, the classification criterion proposed by Zhu *et al.* (2007) was also used (Figure 6-3). The SC and FSC specimens have a  $V_p/V_n$  (maximum strength according to flexural response over the shear strength predicted by Sezen's model) of 1.50 and 1.02, respectively, as well as a shear span ratio  $L_s/d$  of 2.81. Hence, FSC are near the border of the flexure critical and

shear critical specimens, with the experiments lying nearby being all flexure-shear critical. On the other hand, the SC specimens are shown to be way further above with mostly shear as well as some flexure-shear critical specimens, thus reinforcing the belief that these designs will lead to the desired failure types.

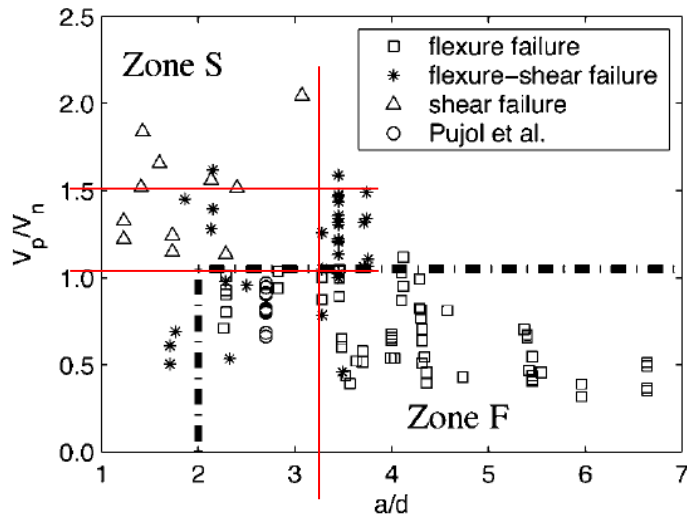


Figure 6-3: Two-zone column classification criterion of failure type (Zhu et al., 2007). The values for SC and FSC specimens are shown with red on the diagram.

The specimen detailing, also including the bases of the columns, is shown in Figure 6-2. The bases were quite wide (1.40 m) and designed with high reinforcement content, so as to avoid any unwanted base failure altogether and to make the base very stiff, thus minimising the deformations of the column top due to cracking and elastic deformations of the base.

Detailed design drawings of both specimen series and the ‘sub-base’ (see section 6.3, below) are included in Appendix C.

### 6.3 TEST SET-UP, LOADING AND INSTRUMENTATION

The full experimental set-up is depicted in Figure 6-4 (schema based on Salonikios *et al.*, 1999) and from various angles in Figure 6-5. It simulates a 2D loading condition, i.e. the specimens are simultaneously subjected to uniaxial bending and axial loading. The loading centre of the horizontal actuator is located at 2.04 m from the strong floor, hence a sub-base was cast to support the specimens and reduce the necessary height, so as to achieve the selected column slenderness. The vertical actuator operates at a higher level, 23.5 cm further up, at the upper edge of the specimens (Figure 6-5). Both actuators are anchored against the stiff reaction frame of the laboratory where the tests were carried out (Laboratory of Reinforced Concrete and Masonry Structures, Aristotle University of Thessaloniki), which can be seen in Figure 6-4 and Figure 6-5. The specimens are anchored to the strong floor via anchoring bolts passing through

the specimen base and the sub-base. No out-of-plane support was provided to the specimens, but the precise concentric application of loading during the test minimised out-of-plane deflection.

The double-acting double-hinged horizontal actuator (Figure 6-5) applies a quasi-static cyclic load, operating in external displacement-control mode. The standard actuator-based internal displacement-control is deemed to introduce considerable 'lash' into the results, largely due to the mounting setup and the non-negligible elastic deformations of the reaction frame, thus overestimating the actual lateral displacement of the tested specimens (Pilitsis *et al.*, 2015). Therefore, an external draw-wire sensor for displacement control was used, instead; this removes any such source of error. The loading protocol used is typical for quasi-static cyclic tests (e.g. see ISO Displacement Schedule in ASTM-E2126, 2011), comprising of three cycles at each lateral displacement level with a displacement step of 3.0 mm.

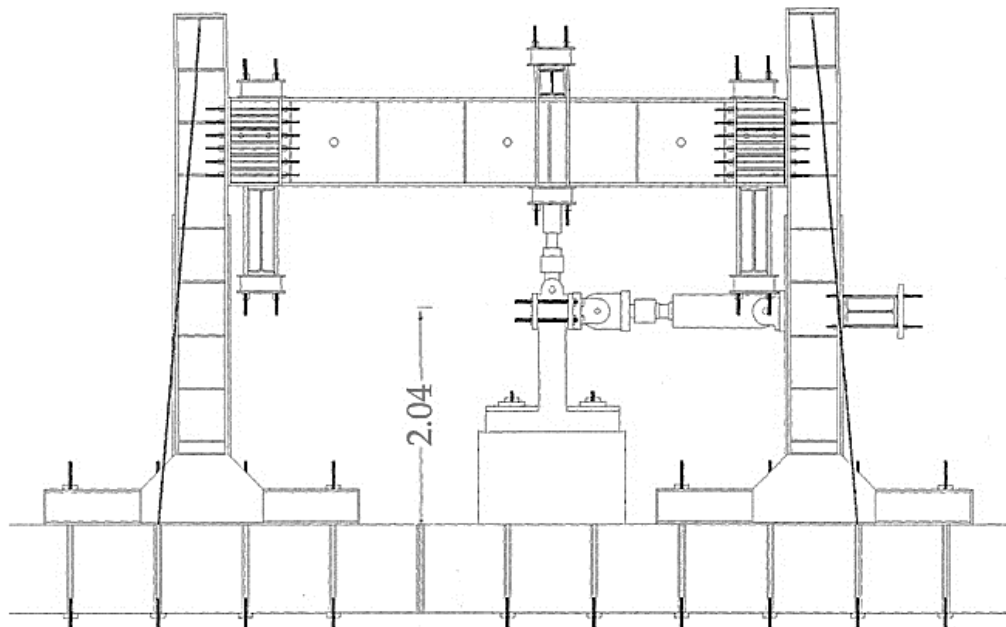


Figure 6-4: Experimental set-up shown schematically.

The double-hinged vertical actuator (Figure 6-5) operates in force-control mode, dwelling at a given axial load. This load is increased by 50% shortly before or soon after the onset of shear failure, with a view to investigating the impact on the overall deformability and energy dissipation capacity of the columns. A reference specimen for each set is tested with a constant axial load. The initial vertical load is set to 180 kN, i.e. an axial load ratio of  $\nu = 0.10$ , increasing to 270 kN, i.e.  $\nu = 0.15$ ; these are typical values for low-rise R/C buildings.

Both actuators' loading histories are shown in Figure 6-6 for all specimens, with the dark blue line corresponding to the horizontal actuator (left vertical axis) and the grey line to the vertical one (right vertical axis). The displacement histories are applied with a constant displacement

rate, hence having much higher duration at latter stages; this rate is 0.4 mm/s, which is adequately slow so that no noteworthy strain rate and inertial effects are exhibited (e.g. ASTM-E2126, 2011). In the histories where the axial load is increased, there is a pause of 9 s, during which the load is ramped up from 180 kN to 270 kN, resulting in a load rate of 10 kN/s. This is done before the first cycle of  $\pm 12$  mm in FSC\_2 and SC\_2 and before the first cycle of  $\pm 15$  mm in FSC\_3 and SC\_3, because the onset of shear failure was found to occur at a displacement of 12 mm based on FSC\_1 and SC\_1, as will be shown in the next chapter.



(a)



(b)



(c)



(d)

Figure 6-5: (a,b) Experimental set-up, and (c,d) vertical and horizontal actuators.

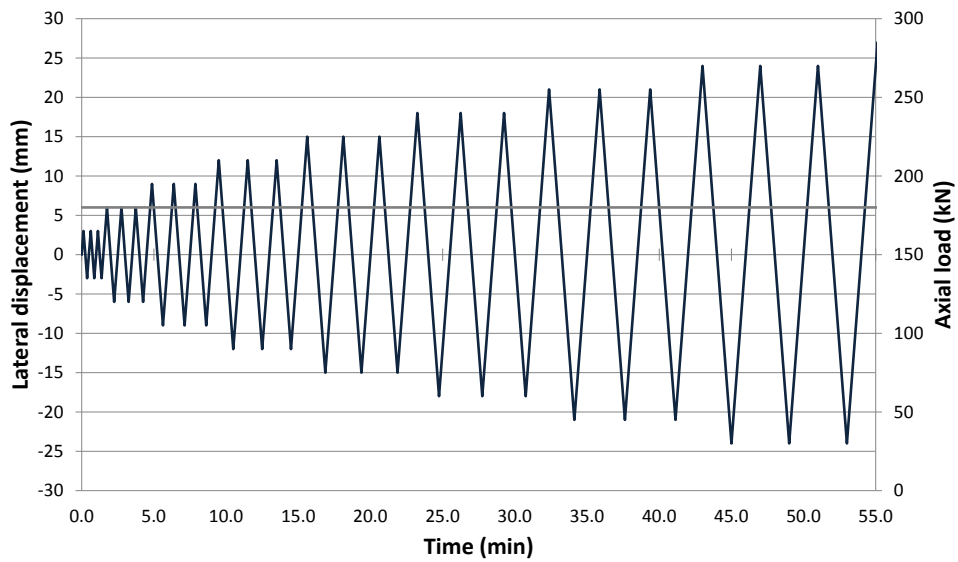
The instrumentation of the experiment comprises of load cells, LVDTs, draw-wire sensors and strain gauges (Figure 6-7). The load cells are embedded into the two actuators, measuring the resisting force from the specimens. Draw-wire sensors are used to measure the top lateral displacement (Figure 6-7d), the displacements needed to calculate the shear deformations (Figure 6-7e) for deformation decomposition, and the potential base uplift (Figure 6-7f), in order to ensure that no significant base deformations develop. As mentioned before, the internal LVDT

of the horizontal actuator is not used to get the actual top lateral displacement, as it incorporates considerable lash in its output. Nevertheless, this lash was measured, by calculating the difference between the displacements recorded by the external draw-wire sensor and the internal LVDT. In the vertical direction, there is no draw-wire sensor installed, thus axial deformation is directly measured only from the vertical actuator's LVDT; this means that some minor lash is inevitably included in these particular results.

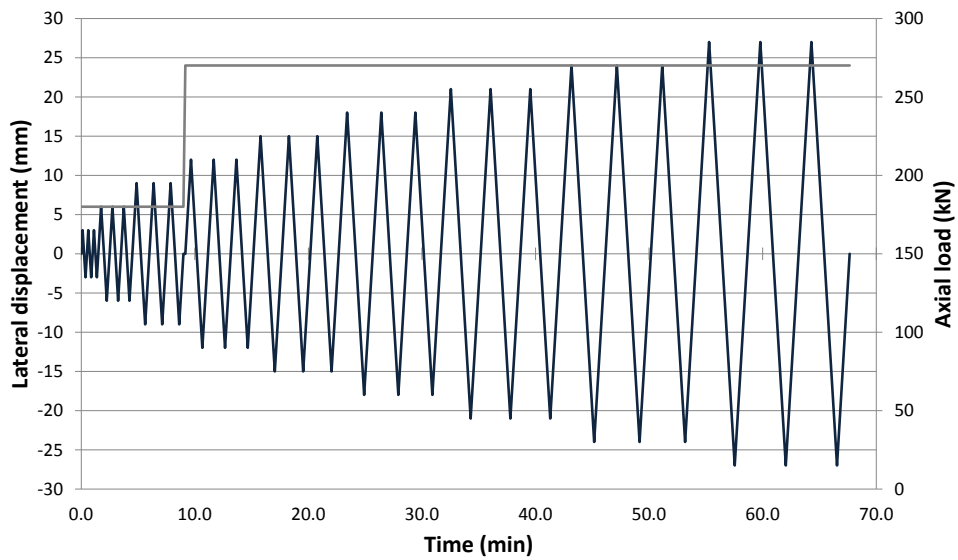
Strain gauges were installed on longitudinal and transverse bars of one shear critical column only (Figure 6-7a,b,c), namely SC\_3; the positions selected were near the base of the column. In Figure 6-8, one can see the exact arrangement of the instrumentation in detail.

In addition to instrumental measurements, digital image correlation was used in order to measure all the necessary deformations of the columns (Figure 6-9). Random speckle patterns were drawn on the front surface of each specimen (Figure 6-9b). Using a high-resolution camera (Figure 6-9a) from a constant position, images were collected at every zero displacement and maximum positive or negative excursion point of every cycle. Using this, the distance between the initial and the displaced positions of each individual point on the front face of the column can be measured at each cycle, thus providing the displacement field along the front surface of the column throughout the duration of the test.

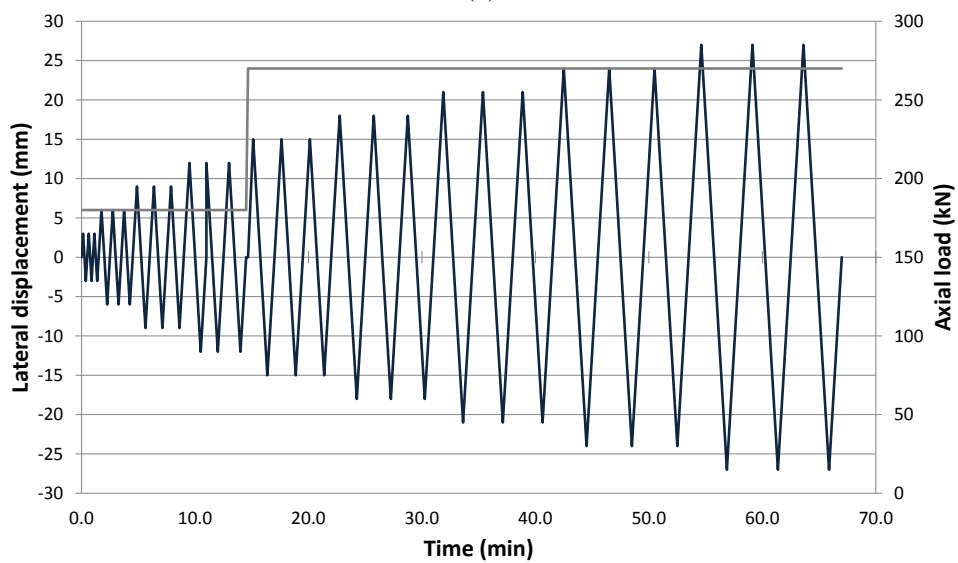
All of the recorded data are collected by the controller at a frequency of 10 Hz, presenting all the pre-defined diagrams and values in real-time, giving a sense of the specimen's status and response. The results are saved and exported at the end of each test for further processing. Simultaneously, the controlling system gathers more status data from various sensors and sends commands to the actuators (closed-loop control), being responsible for successfully applying the prescribed loading histories and controlling the overall experiment. Safety limits were imposed to automatically terminate the experiment, in case of any structural imbalance; 10 mm of vertical displacement (associated with axial failure) and 50 mm of lateral displacement were the limits to shut down the system; additionally, upper limits on the applied forces from the actuators and the temperature of the oil in the pump were set.



(a)



(b)



(c)

Figure 6-6: Lateral displacement (left vertical axis) and vertical force (right vertical axis) histories of (a) reference specimens FSC-1 and SC-1, (b) specimens FSC-2 and SC-2, and (c) specimens FSC-3 and SC-3.



(a)



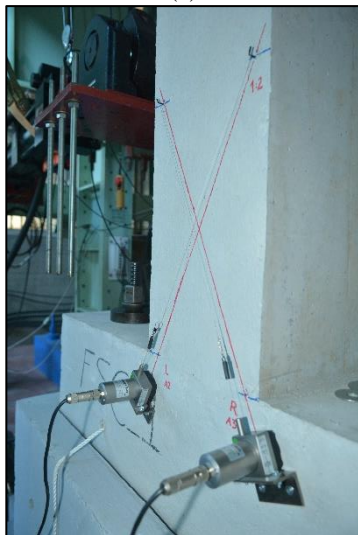
(b)



(c)



(d)



(e)



(f)

*Figure 6-7: (a) Installation of strain gauges on the reinforcing bars, (b) their final arrangement, and (c) connecting them to the corresponding sensors. Draw-wire sensors measuring: (d) lateral displacement at the top of the column, (e) shear displacement, and (f) potential base uplift.*

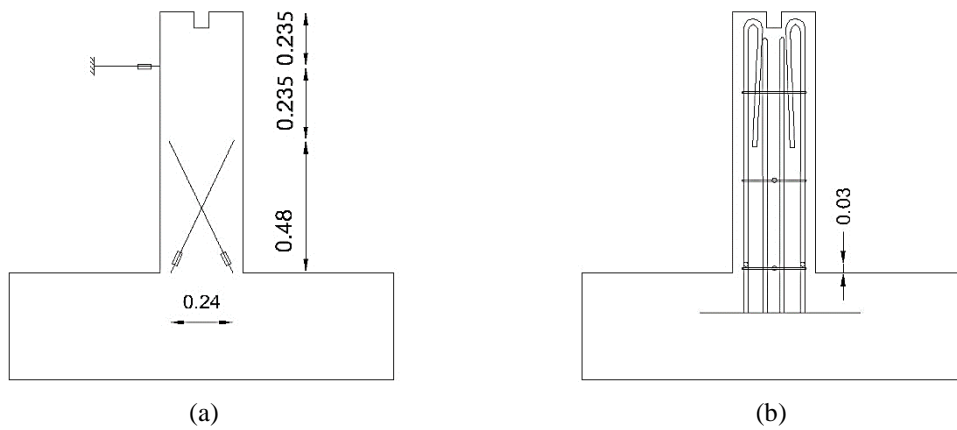


Figure 6-8: Instrumentation of the specimens: (a) draw-wire sensors and (b) strain gauges (drawn as circles on the respective rebars).

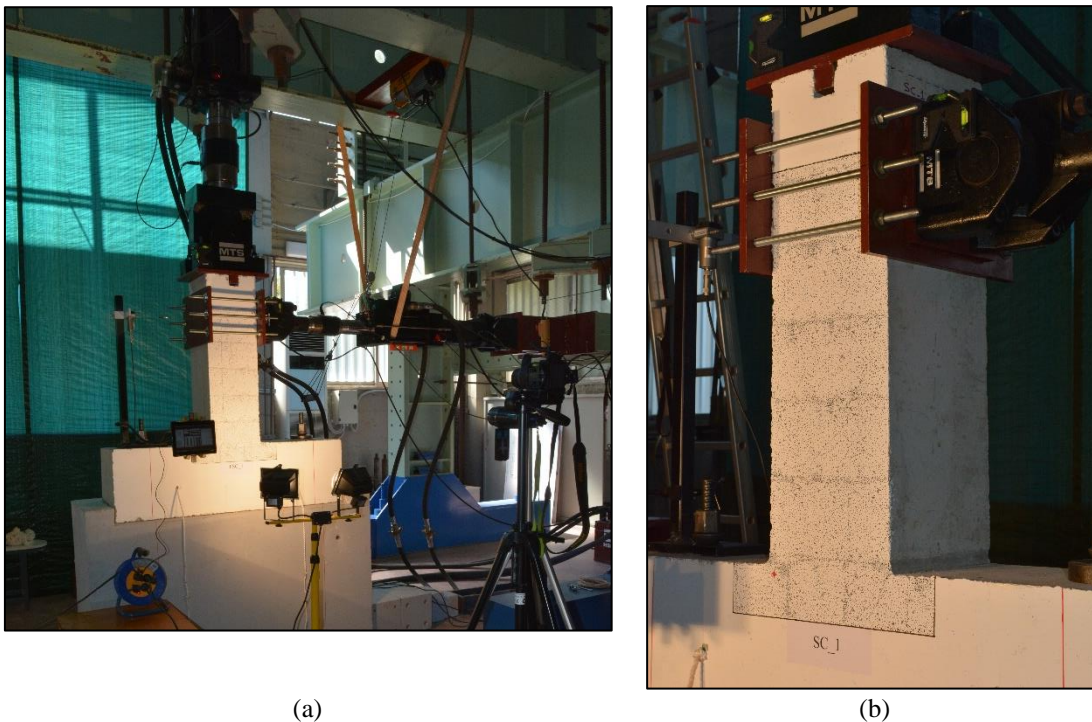


Figure 6-9: (a) Set-up for digital image correlation measurements, and (b) speckle pattern area on the front face of a specimen.

## 6.4 NUMERICAL BLIND PREDICTIONS

To supplement the design of the experiments that has been laid out in the previous sections, comparative blind predictive analyses were performed (Zimos *et al.*, 2016). One of them has been carried out using a distributed inelasticity element previously proposed by Mergos & Kappos (2012) and Zimos *et al.* (2015) – the most updated version of which is presented in Part III of this thesis – using the software [IDARC2D](#) (Reinhorn *et al.*, 2009). The other is a 3D finite element analysis performed using the software [ATENA v.5.3.4](#) (Cervenka *et al.*, 2016). These analyses are expected to offer a quantitative as well as qualitative indication of the expected strength, deformability and failure mode of the specimens. It is generally considered most useful to perform such analyses before conducting experimental work, not only to verify the integrity

of the experimental set-up, but also to prevent unwanted failure modes, especially regarding the physical implementation of the boundary conditions and the applied loading.

The ATENA 3D finite element simulation was realised with cubic solid elements in two distinct zones:

- a) a dense zone with 30 mm long elements (approximately double the size of the maximum aggregate size) that models the column itself as well as the area near the base of the column, wherein cracking is expected. In this zone, a fracture-plasticity constitutive law for concrete with the default values corresponding to the mean strength of concrete grade C12/15 according to EN 1992-1-1 (CEN, 2004) was used.
- b) a sparse zone with 60 mm long elements that models the rest of the base, wherein cracking is not expected. For the purpose of reducing computational cost, an elastic constitutive model with the elastic modulus of the concrete (27.0 GPa) was assigned to this area.

The reinforcement was introduced in the models using linear rebar elements with the characteristics of B500C steel according to EN 1992-1-1 (CEN, 2004), which are integrated within the concrete elements without the need for common nodes (embedded reinforcement). The sparse and dense zones, due to different meshing, were joined by constraining the corresponding degrees of freedom (surface fixed contact). Figure 6-10 shows the common concrete meshing characteristics of SC and FSC columns (due to having the same geometry), as well as their reinforcement, separately for each one of them.

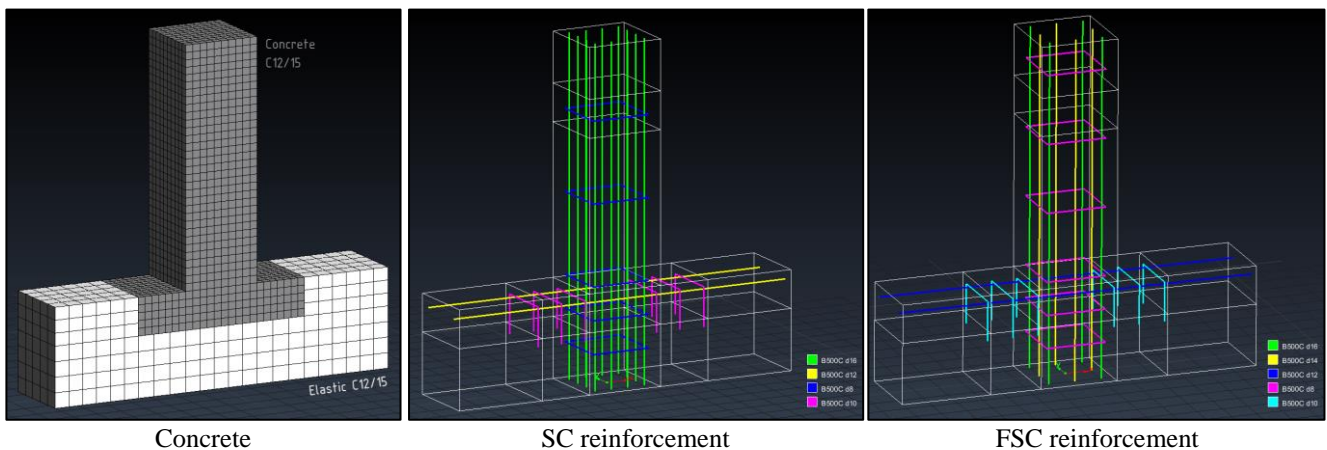
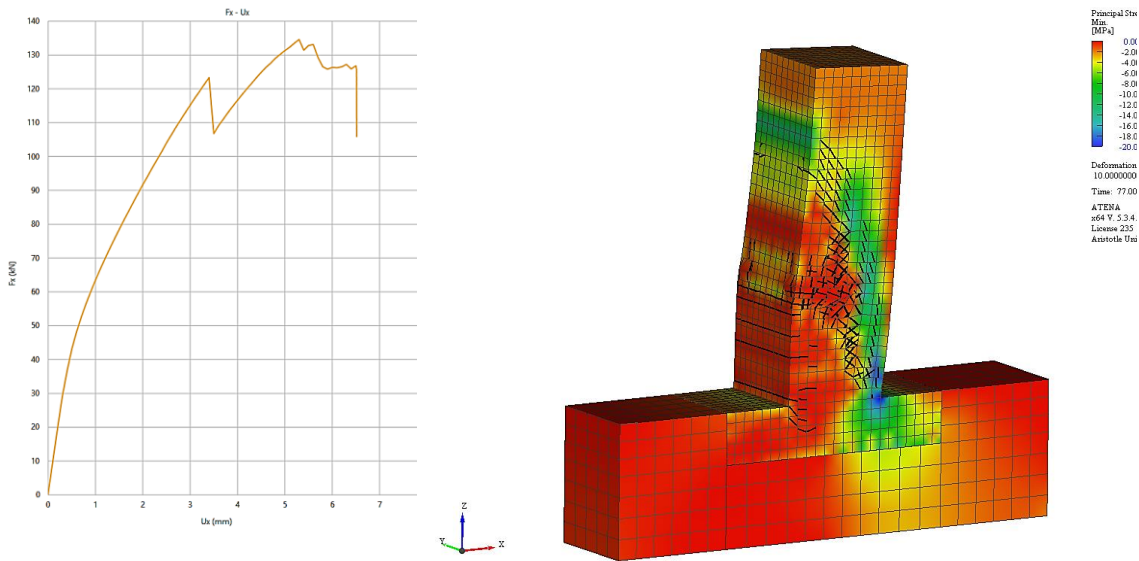


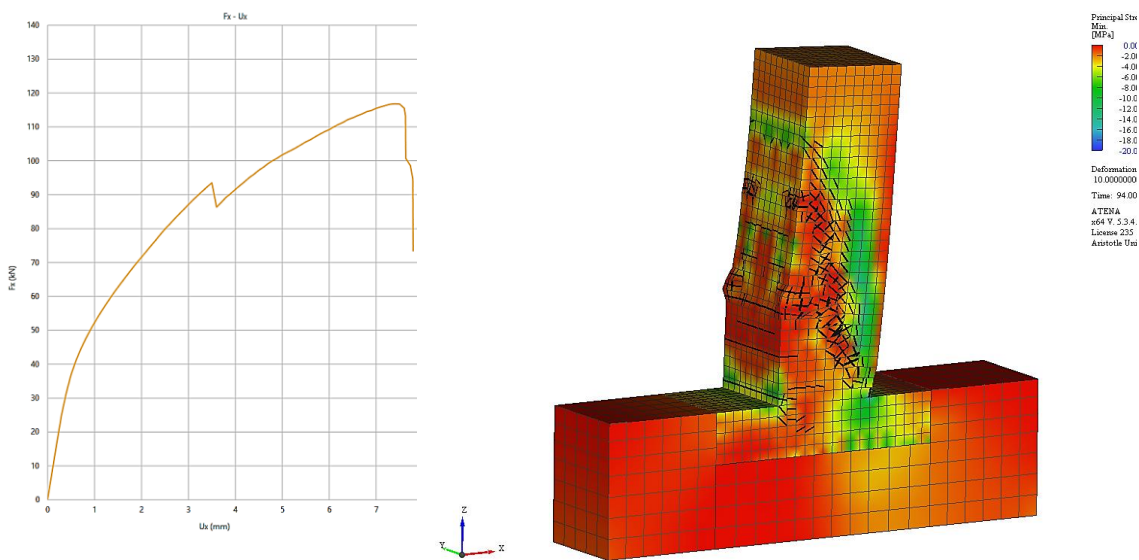
Figure 6-10: Numerical 3D finite element model (concrete / reinforcement).

The boundary conditions were modelled by fully restraining the column base nodes (fixed support) and the loading was initially applied as an axial compressive load on the top surface of the column ( $\nu = 0.1$  hence an axial load of 180 kN) and subsequently as a horizontal displacement at the level of +0.715 m from the base of the column with a displacement step of 0.1 mm. The analysis was performed for an adequate number of loading steps up to the appearance of a

descending branch in the response (of brittle nature due to the effect of shear), whereupon it was terminated due to the expected non-convergence of the numerical solution.



(a)



(b)

Figure 6-11: Response and failure modes (from ATENA analysis) of the (a) SC, and (b) FSC reference specimens.

The results of the two ATENA analyses in terms of horizontal reaction against displacement are presented in Figure 6-11. Furthermore, the cracking patterns predicted by the analysis can be seen (crack width  $\geq 0.1$  mm) as well as the principal compressive stress contours of the columns after the termination of the analysis. The strength of the SC column reaches 134.6 kN at a displacement of 5.3 mm, while the failure that occurs at a horizontal displacement of 6.5 mm is brittle and clearly of shear type – the few horizontal cracks do not seem to penetrate beyond the concrete cover. Moreover, the formation of the compressive strut starts at the point of

action of the horizontal loading and ends at the opposite side of the base of the column. On the contrary, the FSC column's strength is slightly lower (116.8 kN), but develops at a significantly larger displacement (7.4 mm), which practically coincides with the failure displacement (7.6 mm). With regard to failure mode, the specimen eventually fails in shear similarly to SC, but the extended horizontal flexural cracks which penetrate beyond the concrete cover – especially near the base of the column – attest to its flexure-shear nature.

In Figure 6-12, the history of the maximum tensile stress of the longitudinal rebar located on the loading column side can be seen, as well as that of the second hoop from the bottom of the column. It is observed that the hoop of both specimens yields relatively early (yield stress of  $f_y = 500$  MPa at a horizontal displacement of 3.5 mm), which results in the initial sudden loss of strength observed in both response curves, marking the onset of shear cracking along the web of the column. On the contrary, the longitudinal reinforcement bars do not reach the yield point, albeit approaching it much more in the FSC specimen (443 MPa as compared to 206 MPa of the SC), due to the lower longitudinal reinforcement ratio ( $4\emptyset 16+4\emptyset 14$  instead of  $12\emptyset 16$ ) and the higher contribution of flexure, as noted earlier.

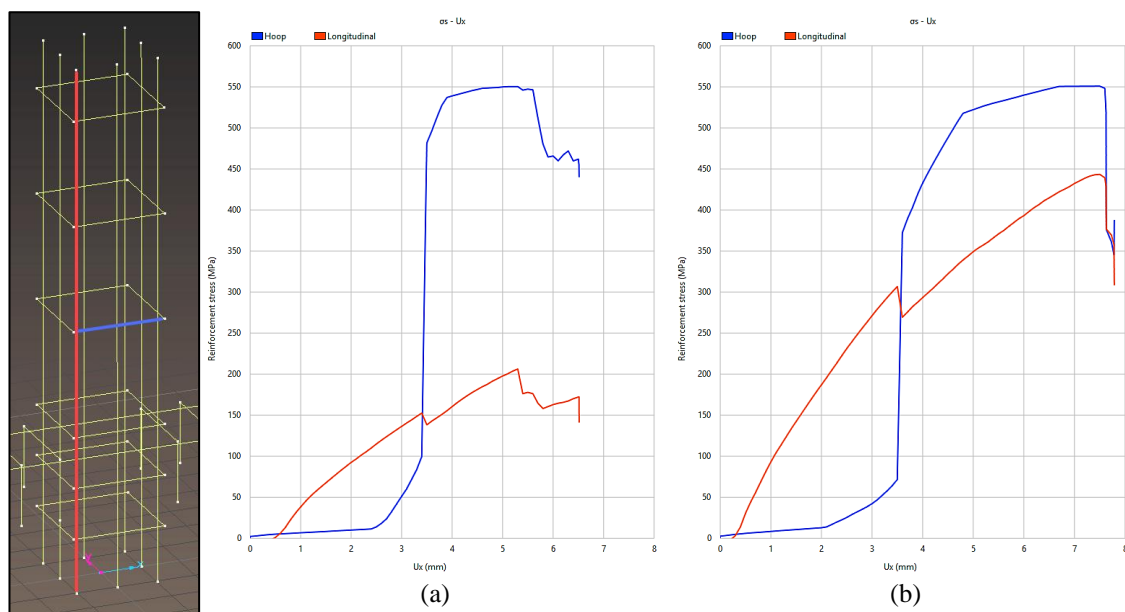
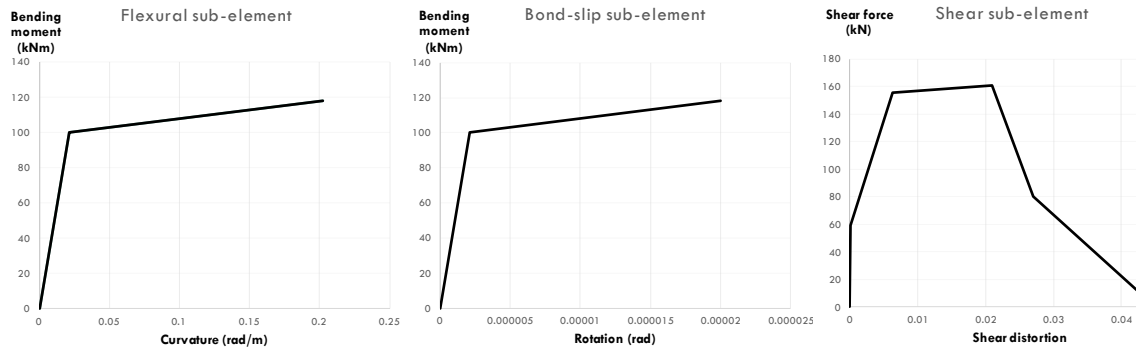


Figure 6-12: History of maximum tensile stress of longitudinal (red line) and transverse (blue line) reinforcement of the (a) SC, and (b) FSC reference specimens.

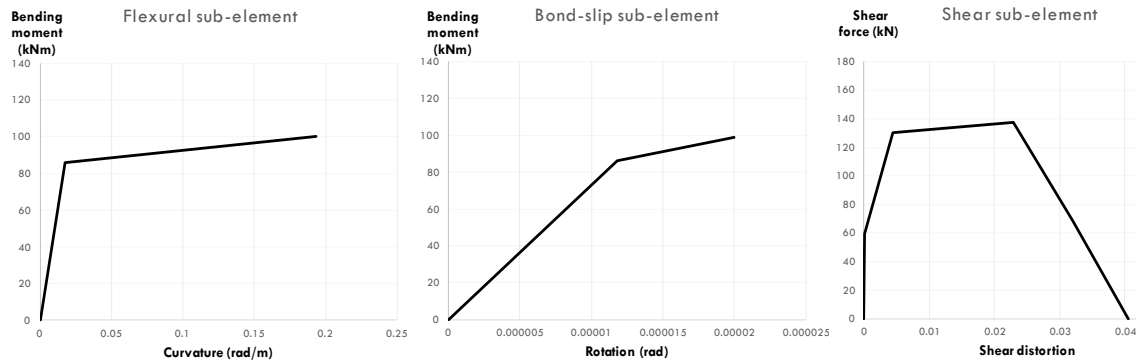
The beam-column element comprises three sub-elements accounting for flexural, shear and bond-slip deformations connected in series. The envelope used for each one is shown in Figure 6-13, both for shear (SC) and flexure-shear critical (FSC) specimens. They were generated following the models described in the respective publications (Mergos & Kappos, 2012; Zimos *et al.*, 2015) for the design, material and loading characteristics of these specimens. Based on these envelopes, both specimen sets are expected to yield in flexure and then fail in shear, the

SC ones reaching however lower curvature ductility compared to the FSC ones that almost reach their ultimate flexural deformation.

The shear critical lengths are calculated as 630 mm (SC) and 500 mm (FSC). This means that the critical shear crack angle and the subsequent shear damage are expected to concentrate in a region of such length in each respective element.



(a)



(b)

Figure 6-13: Envelopes of flexural, bond-slip and shear sub-elements for the (a) SC, and (b) FSC specimens.

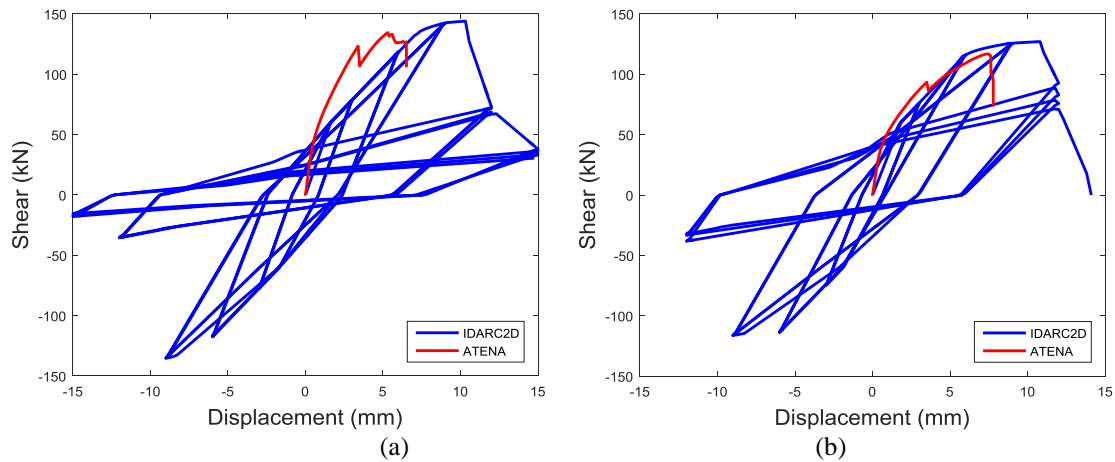


Figure 6-14: Comparison of obtained response for (a) SC, and (b) FSC reference specimens, according to the beam-column element (blue) and the 3D finite element analysis (red).

The results of the IDARC2D analysis for constant axial load can be seen in Figure 6-14. The envelope predicted from the ATENA 3D finite element analysis is included for comparison. The response of the FSC specimen as predicted by IDARC seems to match the monotonic envelope predicted by ATENA up to about 7.5 mm. However, its strength slightly increases further thereafter to 127 kN instead of immediately descending. Its deformability is considerably higher, reaching 10.8 mm at the onset of shear failure (as opposed to 7.6 mm from the finite element analysis) and eventually reaching the onset of axial failure at 14 mm. The SC, on the other hand, is predicted to be considerably less stiff than expected from the monotonic envelope. Its strength is also slightly larger, at 144 kN, and it is predicted to reach 10.3 mm at the onset of shear failure and 15 mm at the onset of axial failure.

Inelastic cyclic analysis was not attempted with the 3D finite element model as this is a very complicated and time-consuming procedure, generally with great difficulties in the convergence of the solution. On the contrary, the 2D analysis with the aforementioned beam-column model is extremely efficient and is shown to produce results relatively close to the ones produced by the 3D finite element analysis, while also capturing the post-peak response of the columns.

The axial load increase and its effect on the response is a more complex matter that cannot be modelled using existing procedures. This will be attempted in Part III, after the experimental results are obtained and the axial load increase effect on the response can be further understood and modelled. Moreover, analyses will be performed again in Part III, with the actual material values of the specimens, in order to validate the analytical beam-column model's performance.

## 6.5 FABRICATION OF SPECIMENS

The formwork used for the specimens can be seen in Figure 6-15b,c. Three units were constructed, casting first the FSC specimens and then re-using them for the SC. The inner surfaces were lubricated with oil, so that the wood plates would not stick on the hardening concrete and that the specimen could easily be extracted. Steel cages were fabricated for each specimen (Figure 6-15a) and then placed inside the formwork (Figure 6-15c).

Three specimens were cast per day, firstly the FSC and one week later the SC; the detailed schedule of casting, as well as testing, of the specimens can be seen in Table 6-2. Slightly more than two concrete batches were required per specimen. The quantities of materials used per concrete batch as well as the quantities per cubic metre can be seen in Table 6-3. Variations were used to get greater or lower volumes of concrete, maintaining however the same proportions between the materials. The concrete was compacted using vibration as soon as it

was poured into the formwork (Figure 6-15d), so as to achieve a uniform distribution and avoid air voids. Pipes were placed in the formwork, in order to leave open holes during the casting of concrete (Figure 6-16a), wherefrom to be able to lift and move the specimens inside the lab with the aid of cranes (Figure 6-16c,d), as well as to anchor them to the strong floor for testing.

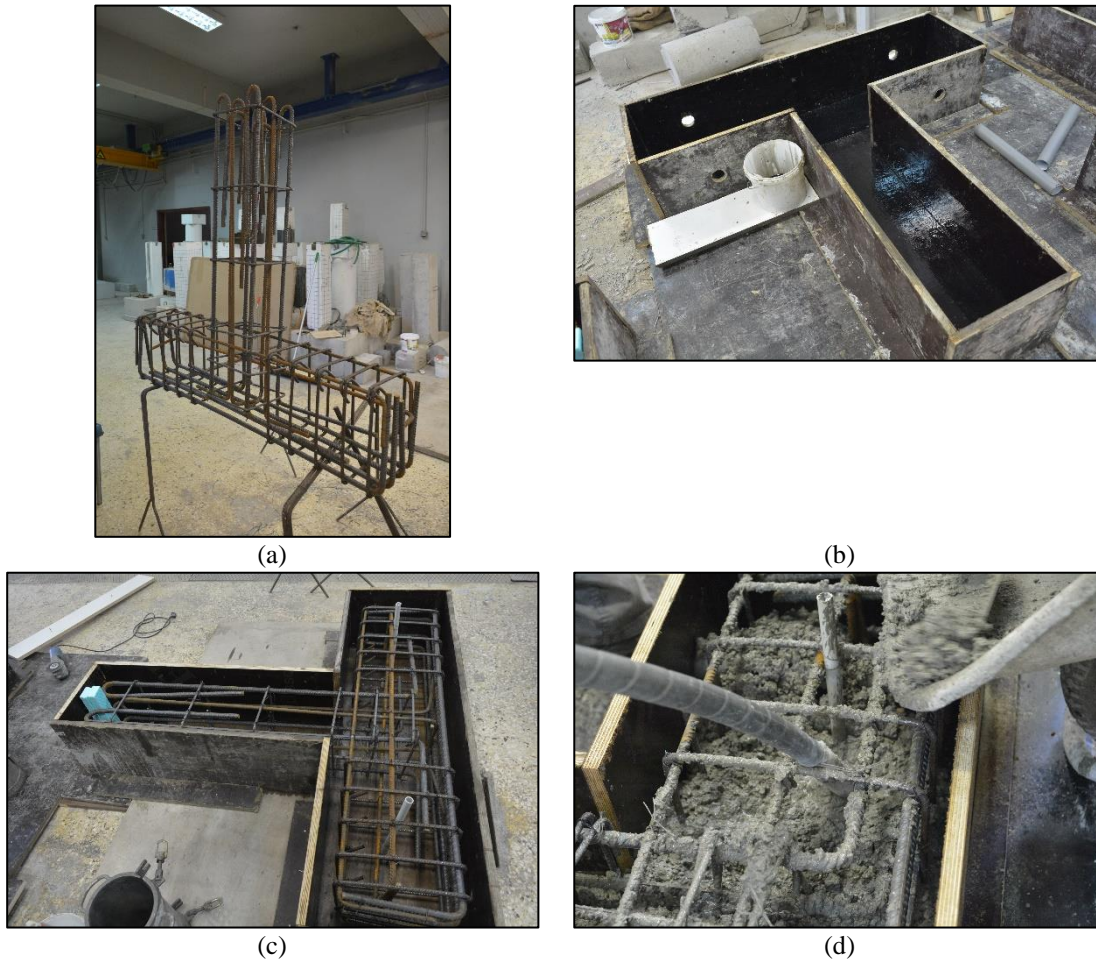


Figure 6-15: (a) Steel cage of FSC specimen, (b) completed, lubricated formwork, (c) steel cage placed inside the formwork prior to casting, and (d) casting and compaction of concrete.

Table 6-2: Schedule of specimen casting and testing.

Specimen	Time of casting	Time of testing
FSC_1	17/06/2016 10:00	26/09/2016 09:30
FSC_2	17/06/2016 11:00	29/09/2016 09:00
FSC_3	17/06/2016 12:00	29/09/2016 12:30
SC_1	24/06/2016 09:30	27/09/2016 09:30
SC_2	24/06/2016 10:30	28/09/2016 10:30
SC_3	24/06/2016 15:30	30/09/2016 14:00

Curing of the specimens included keeping them under constant temperature (with occasionally higher temperatures) and humidity inside the laboratory and using wet cloth (kept wet throughout a big part of the curing time, but not the entire duration) while in the formwork (Figure 6-16b), in order to ensure no shrinkage cracks would appear during the first days after

casting. In Figure 6-17, one can see the six specimens resting on the laboratory floor after construction and initial curing.



(a)



(b)



(c)



(d)

Figure 6-16: (a) Cast specimens just after concrete pouring, (b) curing of specimens inside formwork covered with wet cloth, (c,d) lifting and moving specimens inside the laboratory.

Table 6-3: Concrete mix materials per batch (kg) and per cubic metre (kg/m<sup>3</sup>).

Material	Quantity (kg)	Quantity (kg/m <sup>3</sup> )
Cement IV35.5	38	300
Water	26.5	210
Fine Sand (≤ 4 mm)	102	803.3
Coarse Sand (≤ 8 mm)	56.5	446.3
Gravel (≤ 16 mm)	68	535.6
<b>Total:</b>	<b>291</b>	<b>2295.2</b>



Figure 6-17: Shear critical (SC) and flexure-shear critical (FSC) specimens after construction.

## 6.6 MATERIAL PROPERTIES

A concrete sample was retained from each specimen, which can be seen both in Figure 6-17 and Figure 6-18a. It included concrete from all batches (about two per specimen), in order to get a representative average strength. Compression tests (Figure 6-18b) were performed simultaneously with the column tests, so as to get a reliable value of the concrete compressive strength. The recorded strengths are included in Table 6-4; their mean and median are calculated as well as their 16.7% truncated mean, i.e. the mean excluding the top and bottom 16.7% values of the sample, in other words the average of the central four values in this particular sample. Their strength is on average 27.5 MPa, much closer to C20/25, rather than C12/15, as initially designed for. This might be attributed to the long period (slightly above three months, Table 6-2) between casting and testing with the consequent increase in strength, good curing conditions resulting in avoidance of early shrinkage cracks (Figure 6-16) or the retainment of a small volume of water by the mixer in each mix, especially the first ones of each day.

Samples of the ribbed B500C steel bars used for reinforcement were tested to verify their behaviour. The tests showed a yielding stress of 565 MPa, ultimate stress of about 675 MPa and ultimate strain around 16-17%, on average. Stress-strain curves are included for the ribbed

B500C Ø16 and Ø10 bars (Figure 6-19); strength properties are similar for both diameters, but the smaller bars (Ø10) have a somewhat longer yield plateau and higher ultimate strain.

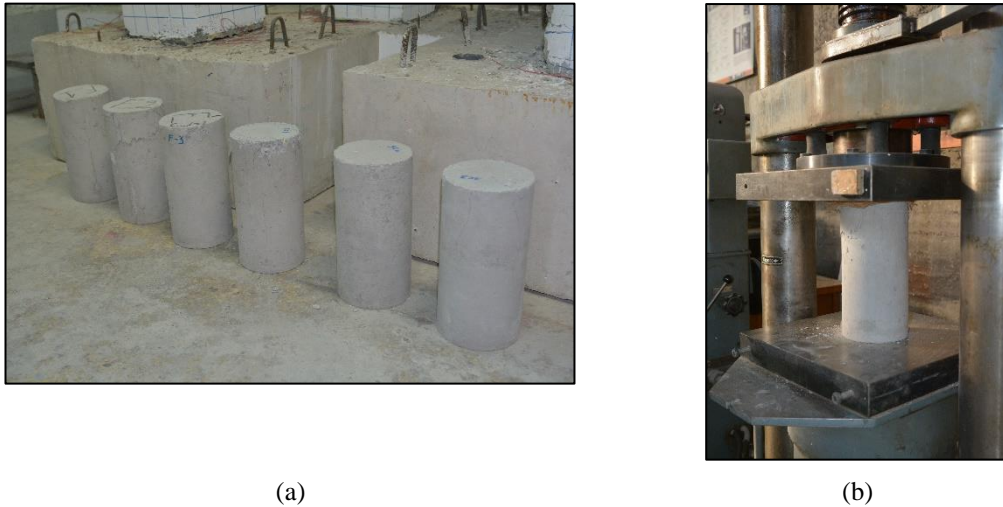


Figure 6-18: (a) Concrete samples of all six specimens, and (b) a concrete sample under compression test.

Table 6-4: Compressive strength of concrete samples for each specimen.

Specimen	Strength (MPa)
FSC_1	26.0
FSC_2	28.3
FSC_3	27.7
SC_1	32.8
SC_2	27.2
SC_3	24.3
<b>Mean:</b>	27.7
<b>Median:</b>	27.4
<b>16.7% Truncated Mean:</b>	27.3

Table 6-5: Flexure- and shear-controlled resistance (kN) predicted for each specimen set, based on  $M-\phi$  analysis and various shear strength expressions.

Specimen series	Flexural strength ( $M-\phi$ analysis)		Shear strength				
			Priestley <i>et al.</i>		Biskinis <i>et al.</i> / EC8-3	Sezen & Moehle	MC2010
	Yield	Ultimate	30°	45°			
SC	157	182	196	169	198	134	144
FSC	136	156	210	178	141	142	140

Accounting for the actual values of the material strengths, the shear resistance is calculated again using the same procedures as in Table 6-1. The results based on measured material strengths are shown in Table 6-5; the FSC specimens are still expected to fail in shear after yielding in flexure, although there is again very high variability. The SC ones are shown to have a high difference between flexural ultimate and shear strength (with most models), thus being almost certain to fail in shear, while potentially failing before even yielding. As for the classification criterion, the ratios  $V_p/V_n$  have changed to 1.36 and 1.09, thus leading to

conclusions in line with those drawn from Table 6-5, with SC specimens also likely to undergo flexure-shear failure.

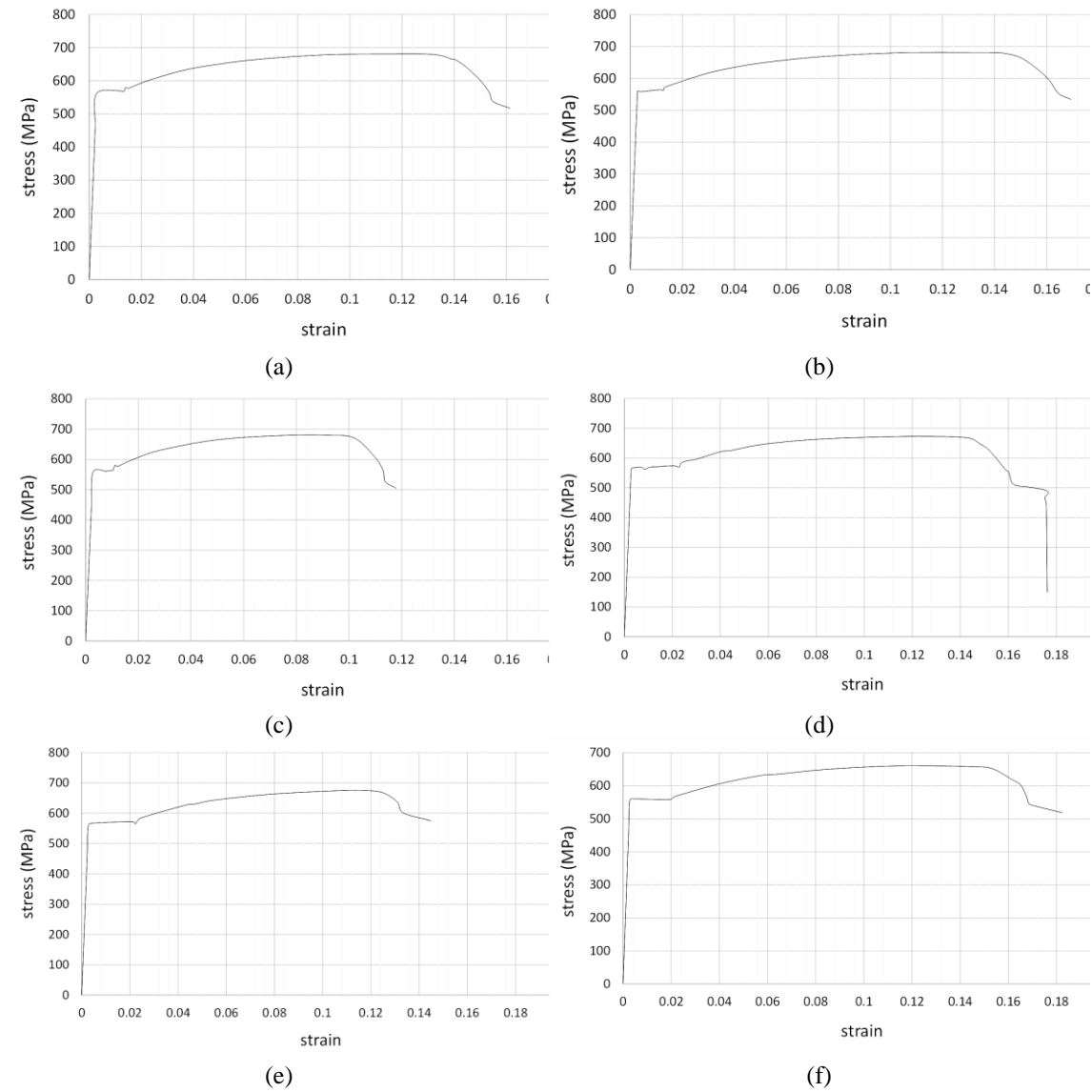


Figure 6-19: Tensile response of ribbed B500C (a-c) Ø16 bars, and (d-f) Ø10 bars.

## Chapter 7: EXPERIMENTAL RESULTS

---

### 7.1 DAMAGE PROPAGATION

The initiation and propagation of cracks along the specimens are described in detail in Table 7-1 to Table 7-6. Crack widths were measured using digital image correlation, i.e. comparing the original image of the specimen with the axial load applied and zero lateral displacement, with every subsequent given picture. As shown in Figure 7-1, two 'points' across the crack are defined and the distance between them is measured in every image; the length obtained from each image minus the length from the reference image gives the opening of the crack, assuming the points are on or very close to the side of the crack. As is shown in Figure 7-1, these 'points' are actually areas in micro-scale, enclosing a sufficient number of pixels, so as to be able to identify said areas during image processing, in order to track the varying coordinates of their centres (i.e. the 'points'). Of course, the points cannot lie exactly on the side of the crack, due to the aforementioned limitation of the area of pixels that has to surround them. Furthermore, in order for the areas to be tracked even in higher damage states, where the cracks open further and the areas around them start exhibiting some concrete spalling, points slightly farther away from the actual crack sides have to be taken into account. As a result, the widths recorded might be slightly greater than the actual crack widths, however this difference is believed to be negligible. An issue particular to shear cracks in higher damage states (after the onset of shear failure) is that there is also slip along the crack, not just opening (more details in section 7.5 below), which does lead to a somewhat higher ostensible recorded crack width.

Only the "pull" direction was taken into account in compiling these tables being considered generally representative of both loading directions, albeit not identical at every loading step. Some entries are "N/A", because those displacement levels were not reached during the experiment, or because no photographic evidence was captured at those displacement levels, or because there was extensive spalling around a given crack at a given displacement level preventing the proper measurement of its width, due to inability to correlate the image with the reference one. A blank cell implies that although the photograph was taken at a given displacement level and correlation was possible, the particular crack had not yet appeared.

The "interface crack" is a horizontal crack exactly at the column-base interface in most cases, while in a couple of specimens it formed about 10-20 mm above the interface. The positions of the other flexural cracks along the vertical axis are provided in parentheses for each specimen. If more than one cracks are included in an entry, the widths are given as a range, corresponding to the lowest and highest of the crack widths. The average inclination of each shear crack is provided in parentheses, measured with respect to the longitudinal axis of the specimen.

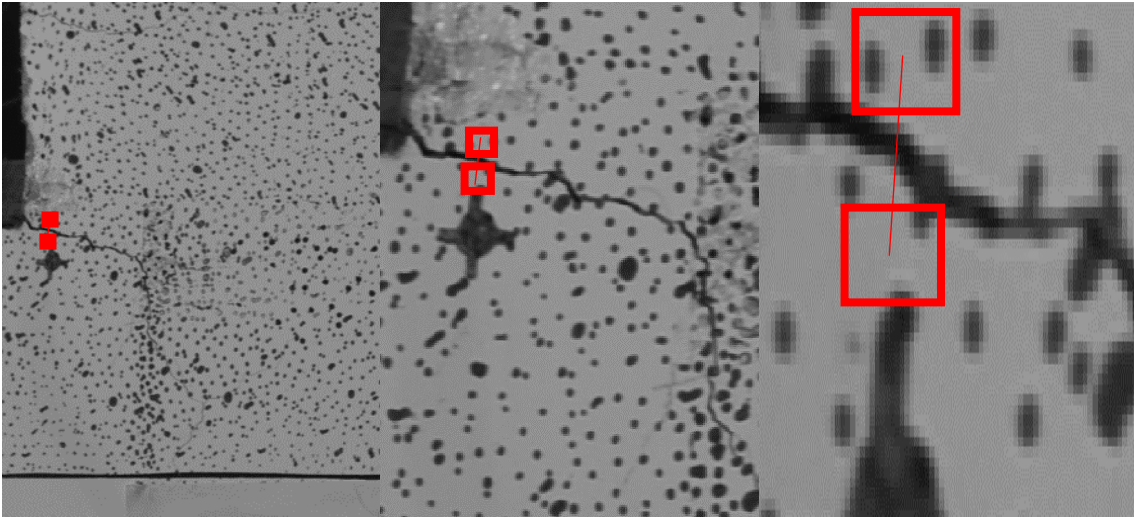


Figure 7-1: Example of crack width measurement (snapshot of SC3 at displacement level of +12 mm).

Table 7-1: Evolution of crack widths in specimen FSC\_1.

displacement level [mm]	+3	+6	+9	+12	+15	+18	+21
interface crack	N/A	0.7 mm	0.85 mm	1.2 mm	1.55 mm	N/A	N/A
3 flexural cracks (90 mm, 220 mm, 440 mm)	N/A	0.3 - 0.4 mm	0.4 - 0.6 mm	0.45 - 0.75 mm	0.5 - 0.8 mm	0.3 - 1.15 mm	N/A
shear crack (28°)	N/A	hairline	0.4 - 0.5 mm	0.65 - 0.9 mm	0.9 - 1.15 mm	3.3 - 3.6 mm	N/A

Table 7-2: Evolution of crack widths in specimen FSC\_2.

displacement level [mm]	+3	+6	+9	+12	+15	+18	+21
interface crack	hairline	N/A	N/A	1.35 mm	2.45 mm	N/A	N/A
2 flexural cracks (110 mm, 240 mm)	hairline	N/A	N/A	0.55 - 0.6 mm	0.55 - 0.65 mm	1.0 mm	N/A
1 flexural crack (430 mm)		N/A	N/A	0.5 mm	0.3 mm	hairline	N/A
shear crack (28°)		N/A	N/A	0.55 - 0.7 mm	1.55 - 2.3 mm	3.0 - 3.2 mm	N/A

The state of the specimens at a displacement level of +12 mm is also visually presented in Figure 7-2, at which level shear cracks have formed on all specimens and the initiation of minor damage can be observed. Subsequently, the state of the specimens at the displacement level of +18 mm is shown in Figure 7-3, except for FSC\_3, for which the second peak of +15 mm is included, right before its axial collapse. The cracks presented in Tables 7-1 to 7-6 can be seen in these figures; all the cracks have been highlighted in red, the thickness of the lines corresponding to the crack widths.

Table 7-3: Evolution of crack widths in specimen FSC\_3.

displacement level [mm]	+3	+6	+9	+12	+15	+18	+21
interface crack		hairline	0.3 mm	0.55 mm	0.8 mm	N/A	N/A
3 flexural cracks (30 mm, 105 mm, 275 mm)	0.35 - 0.45 mm	0.4 - 0.45 mm	0.45 - 0.6 mm	0.55 - 0.7 mm	0.35 - 0.7 mm	N/A	N/A
1 flexural crack (420 mm)		hairline	0.3 mm	0.45 mm	0.3 mm	N/A	N/A
shear crack (28°)		hairline	0.3 mm	0.6 - 0.7 mm	3.75 mm	N/A	N/A

Table 7-4: Evolution of crack widths in specimen SC\_1.

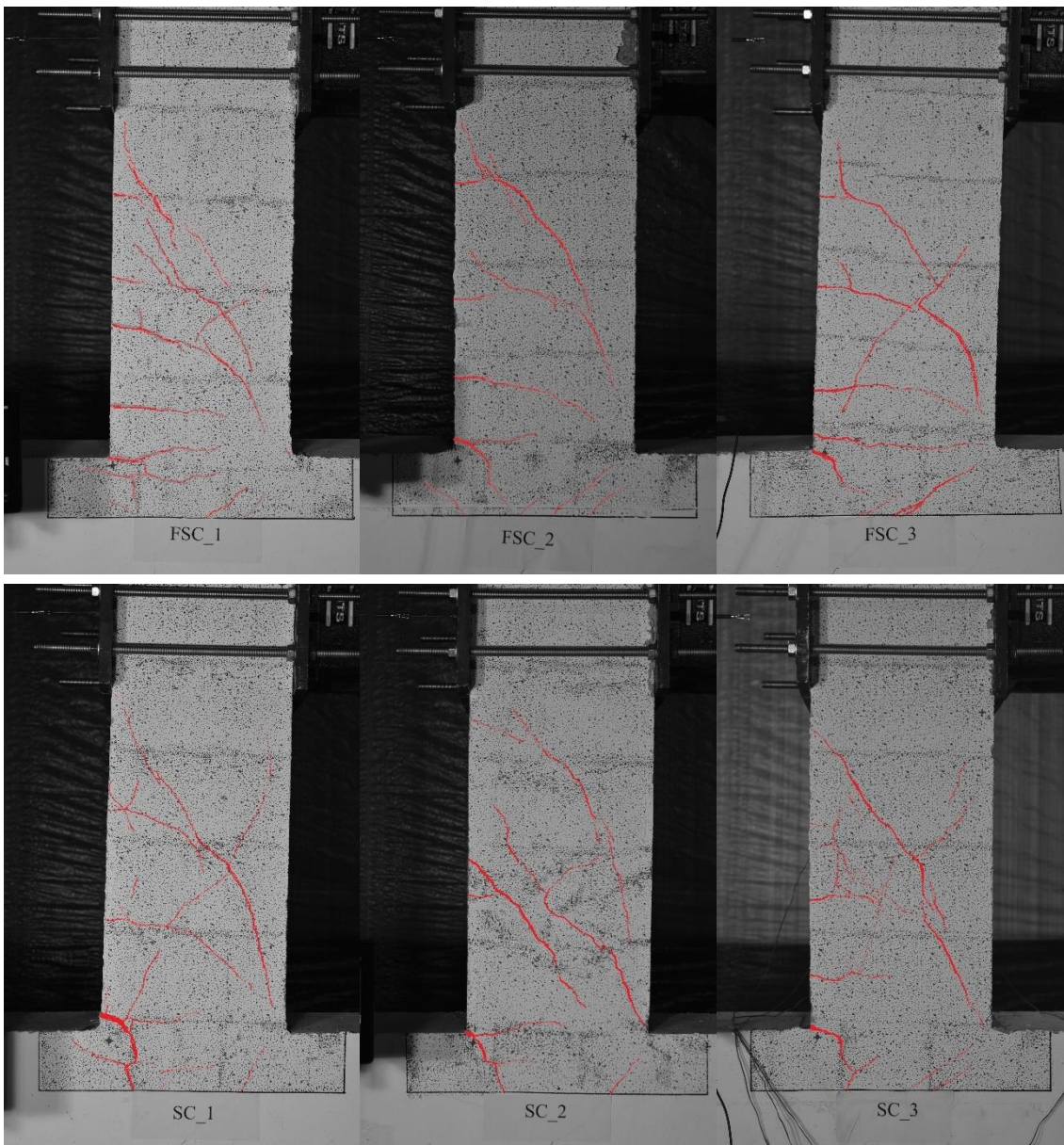
displacement level [mm]	+3	+6	+9	+12	+15	+18	+21
interface crack	hairline	0.7 mm	1.15 mm	1.45 mm	0.85 mm	N/A	N/A
2 flexural cracks (160 mm, 340 mm)	hairline	0.3 - 0.4 mm	0.45 mm	0.45 - 0.65 mm	0.5 - 0.9 mm	0.3 - 0.65 mm	N/A
shear crack (28°)			hairline	0.6 - 0.8 mm	1.3 - 1.85 mm	3.0 - 4.0 mm	6.0 mm

Table 7-5: Evolution of crack widths in specimen SC\_2.

displacement level [mm]	+3	+6	+9	+12	+15	+18	+21
interface crack	hairline	1.0 mm	1.4 mm	1.7 mm	0.2 mm	N/A	N/A
1 flexural crack (225 mm)	hairline	0.5 mm	0.5 mm	0.7 mm	0.1 mm	N/A	N/A
shear crack (35-37°)	hairline	hairline	0.55 - 1.4 mm	0.8 - 1.6 mm	8.0 - 9.0 mm	N/A	N/A

Table 7-6: Evolution of crack widths in specimen SC\_3.

displacement level [mm]	+3	+6	+9	+12	+15	+18	+21
interface crack	hairline	0.65 mm	0.9 mm	1.0 mm	N/A	N/A	N/A
2 flexural cracks (90 mm, 220 mm)	hairline	0.35 - 0.55 mm	0.4 - 0.65 mm	0.55 - 0.7 mm	0.7 - 1.15 mm	N/A	N/A
shear crack (33°)		hairline	0.6 mm	0.7 - 0.9 mm	1.25 - 1.6 mm	N/A	N/A



*Figure 7-2: Damage state of specimens at displacement level of +12 mm.*

It is noted that the general pattern of damage propagation involves a horizontal crack forming at or very close to the column-base interface, where the highest bending moment and curvature is expected. Further horizontal cracks form higher up along the specimen at some distance from the interface crack and from each other, since a certain distance is required between cracks for the tensile strength to build up again through bond, as is well-known (Figure 7-2). These cracks cross the concrete cover and the position of the longitudinal bars, not extending much deeper towards the middle of the specimen, and initiate quite early on, mostly at the displacement level of +3 mm. The former crack is usually wider than the latter cracks, as would be expected; all of them tend to increase in width with increasing lateral displacement, while generally remaining constant or decreasing towards the last displacement steps of the test (the reason for which will be explained in section 7.5). FSC specimens exhibit more flexural cracks in total along the height of the specimen - four to five - being affected more by flexure, while the SC ones exhibit 2 to 3.

However, SC\_3's corner longitudinal bars are also shown to reach yield strains (around 0.002) in Figure 7-4 around the displacement levels of +/- 9 to +/- 12 mm and exceed them at +/- 15 mm.

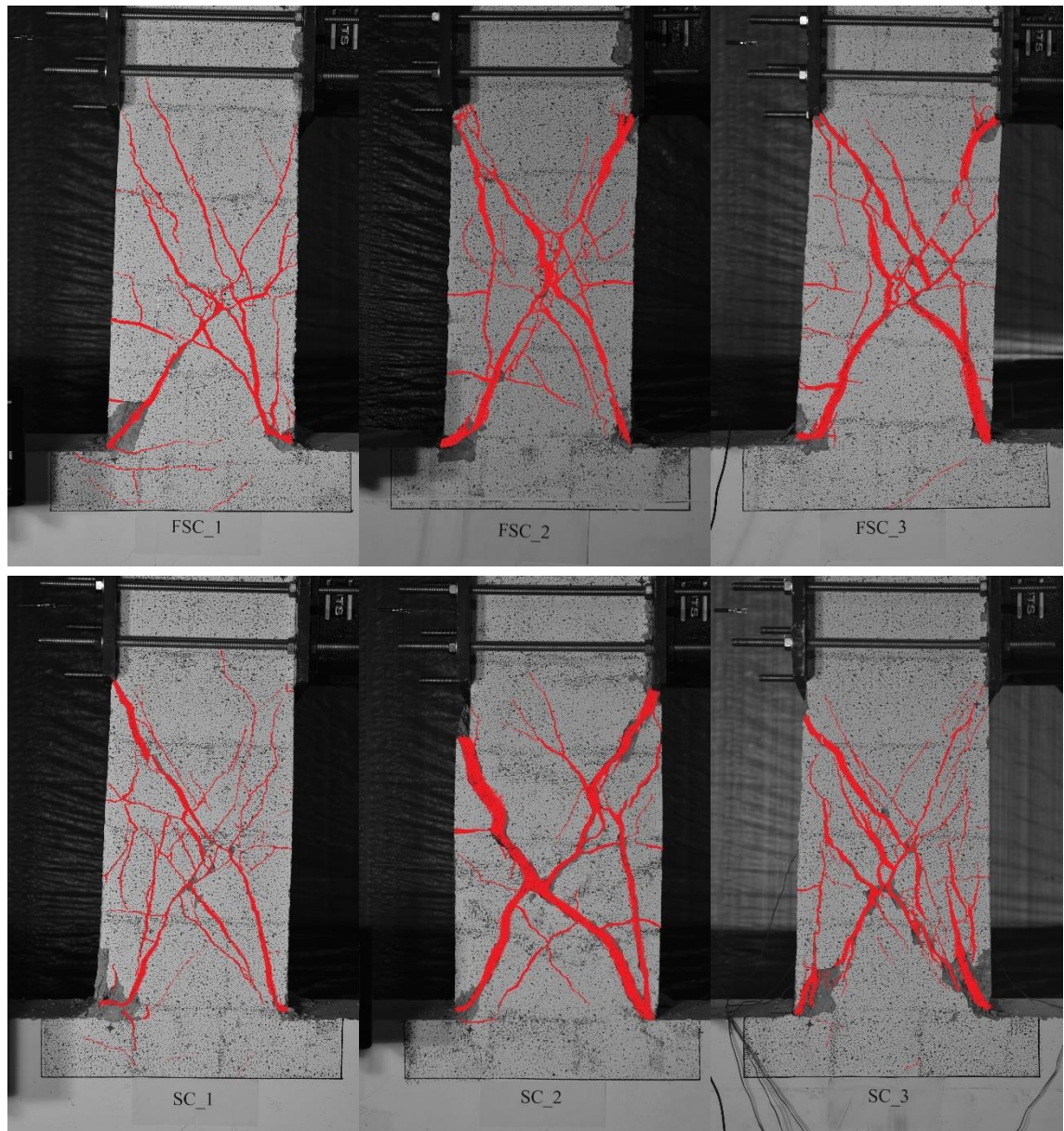


*Figure 7-3: Damage state of specimens at displacement level of +18 mm (besides FSC\_3, for which the second peak of +15 mm is included, right before its axial collapse).*

In almost every specimen, the crack at the interface initiated horizontally at the corner of the specimen and branched downwards into the base, due to base deformations, and was partially or completely closed at later stages of the response. Moreover, other thin diagonal and horizontal cracks appeared at the column-base joint at displacement levels of +6 mm and +9 mm, their width peaking at +12 mm (Figure 7-2) and thenceafter retracting (Figure 7-3), for reasons explained in section 7.5. As a matter of fact, the widest of these cracks reached a peak width of about 0.35 - 0.45 mm.

Cross-inclined (X-patterned) shear cracks appear at a displacement level of approximately +6 mm or +9 mm and start opening considerably from about +12 mm (Figure 7-2), reaching very large widths of approximately 4.0 to 10.0 mm near the last steps of testing (Figure 7-3). Their bottom end is always at the column-base interface and their inclinations are usually around 28°-33° on average, with local linear segments of lower and higher angles. It was observed that no shear crack could achieve an inclination lower than 28°, which corresponds to the length of the region between the column-base interface and the lower end of the horizontal actuator's steel plates (Figure 7-3). This is because of the much higher stiffness of the base and the fact that the actuator's plates connected with tightened bolts offer extra confinement to the top region of the column. Unexpectedly, the SC specimens seem to have higher average shear crack angles than the FSC ones, which all exhibit 28° angles on average, contrary to the general trend presented in section 4.2. Spalling of concrete cover is observed close to the bottom ends of the inclined cracks; this is due to the local decrease of the compression zone depths at those sections, because of the existence of the shear cracks. Despite substantial opening of these diagonal cracks, no fracture of transverse bar seems to have occurred. This is evidenced by the fact that there was no sound of fracture in any of the experiments, as well as by removing loose concrete at the end of the tests, which revealed that there was no fracture. Instead, the insufficient 90°-anchorage of the ties led to their slippage at latter displacement levels. The strain gauges mounted on transverse bars in SC\_3 (Figure 7-4) show that tie #1 (at about 350 mm from the interface) reached its strain-hardening branch - which was shown to be reached at a strain of about 0.002 – at the displacement level of +/- 15 mm, reaching very high strains after that. This is due to the opening of the full-depth crack at that point of the test, with the consequent widening of the gap, which will be commented further in section 7.5. Tie #2 did not yield, because it was placed about 30 mm above the interface and, consequently, was not crossed by any shear crack.

Minor vertical cracks appeared in some of the specimens at the positions of the main reinforcement, caused by bond-split of the longitudinal bars. In all cases, these were very narrow and deemed to be of minor importance.

The specimens FSC\_2, FSC\_3 and SC\_2 exhibited limited out-of-plane displacements at the onset of axial failure (Figure 7-5), unlike the other specimens. It is recalled (see chapter 6) that no lateral support was provided at the top of the specimen.

Photographic documentation of the specimens after the end of testing shows a residual curvature of the longitudinal bars of almost all specimens (Figure 7-6), due to buckling, initiated towards the end of the experiment. Their buckling length is hardly confined between two consecutive ties, owing to their 90°-anchorage and low anchorage length that do not provide

adequate restraint. Moreover, the disintegration of the concrete core is obvious, with parts of it having shattered during cycling, particularly near the final cycles.

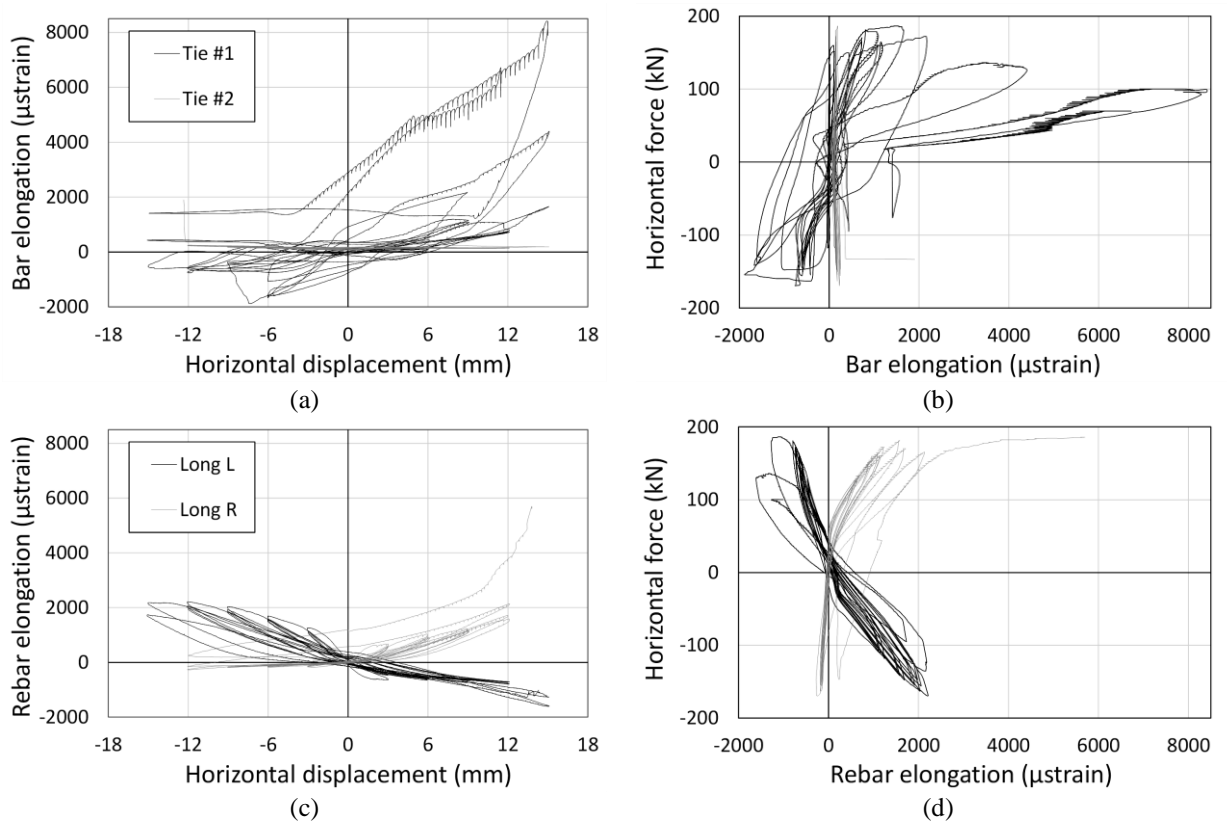


Figure 7-4: Hysteretic response of bar elongation of (a, b) transverse and (c, d) longitudinal reinforcement against (a, c) lateral displacement and (b, d) force of specimen SC\_3.

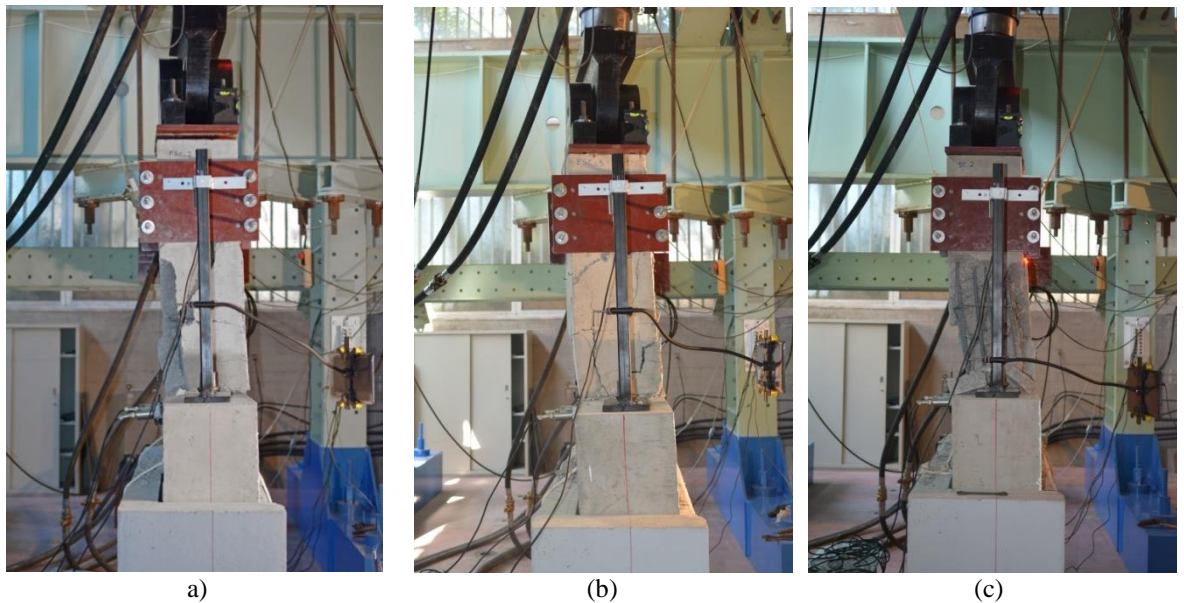


Figure 7-5: Side view at the onset of axial collapse of (a) FSC\_2, (b) FSC\_3 and (c) SC\_2.

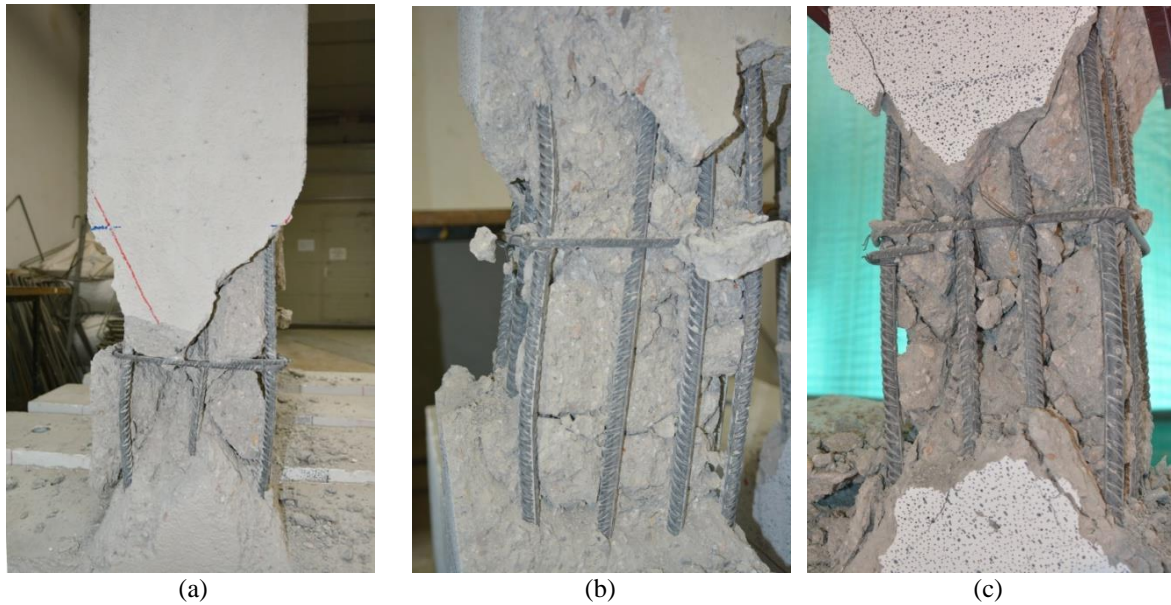


Figure 7-6: State after the end of testing of specimens (a) FSC\_2, (b) SC\_2 and (c) SC\_3.

## 7.2 LATERAL RESPONSE

All the diagrams in this section are produced for the externally recorded horizontal displacement. The internal one, recorded by the actuator's LVDT, is used solely for the purpose of calculating the lash in section 7.8.

Smoothing has been applied to all the hysteretic responses reported herein. The original responses without smoothing are presented in Appendix D. The method used to smooth them out is also explained therein. The full hysteretic responses of all specimens in terms of horizontal force (kN) and lateral displacement (mm) or lateral drift (%) are included in Figure 7-7.

Testing of specimen SC\_3 was interrupted near the final cycles. The corrected data are included herein, where this disruption was eliminated (original data included in Appendix D, Figure D-6).

The responses of the FSC specimens are quite similar. Overall, they seem to have a 'stiff' response up to a load of about 120 kN, which is reached at the first displacement level, subsequently following a branch of lower tangent stiffness and reaching a strength of about 150-160 kN at the peak of +/- 12 mm. They exhibit very limited cyclic strength degradation in the pre-peak domain, which increases significantly from the peak onwards. Furthermore, their reloading stiffness deterioration is also much higher than in the pre-peak domain.

The SC specimens are quite different from FSC, albeit rather similar to each other. They have a 'stiff' response up to a strength of around 130 kN at the peak of the first displacement level, after which they follow a rather stiff strain-hardening branch, reaching almost 200 kN of strength at the peak of +/- 12 mm; there is one exception, namely SC\_3, which did not reach its peak strength at a displacement of +/- 12 mm, but at +/- 15 mm. This led to the increase of axial load

happening before the onset of shear failure, instead of just after it, as initially planned. The SC specimens also exhibit much higher cyclic strength degradation in the post-peak domain, in contrast to pre-peak.

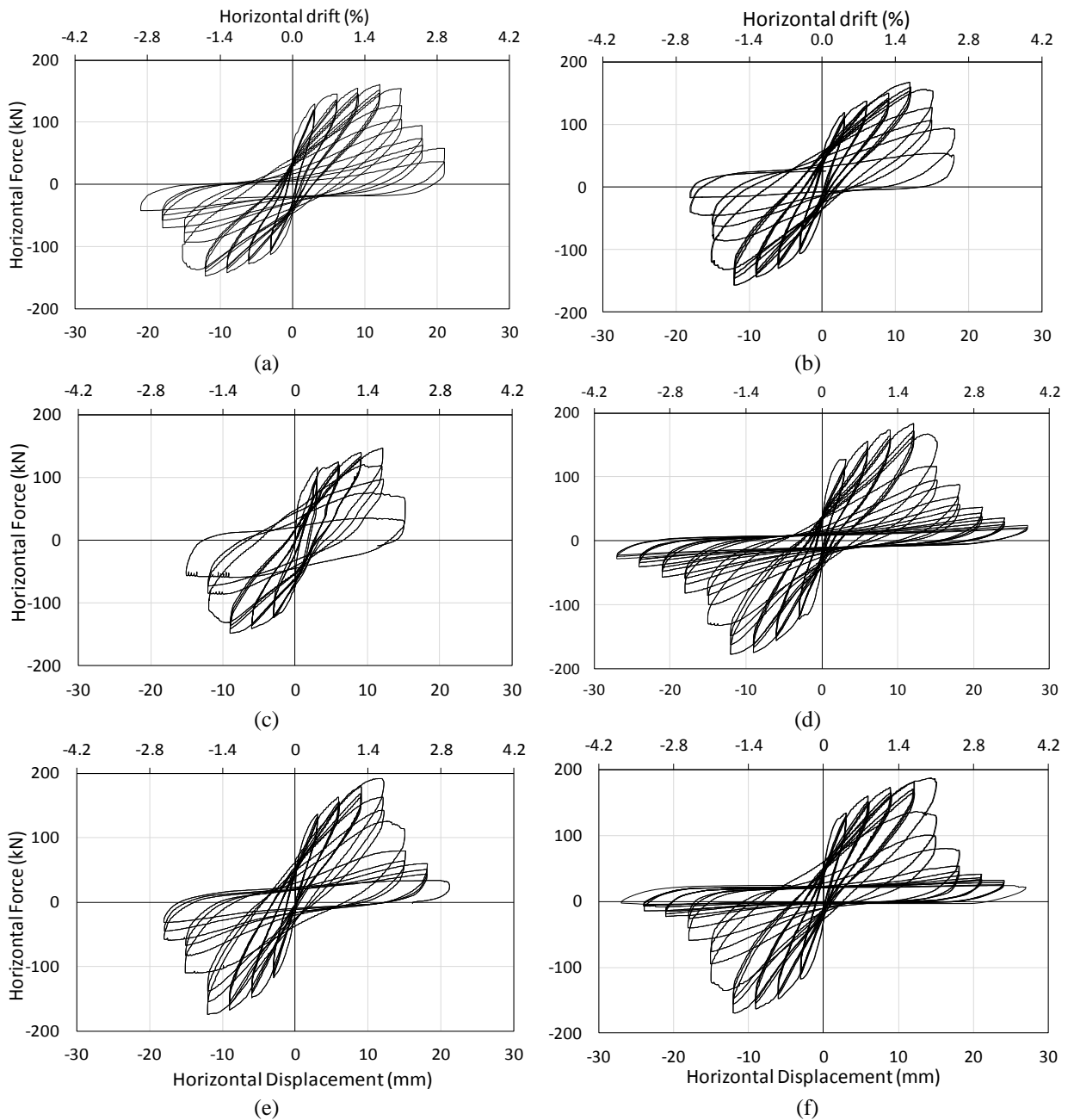


Figure 7-7: Hysteretic response of specimens (a) FSC\_1, (b) FSC\_2, (c) FSC\_3, (d) SC\_1, (e) SC\_2 and (f) SC\_3.

It is observed that the highest cyclic strength degradation in each specimen (both FSC and SC) takes place at the displacement level where the peak is reached, i.e. at the onset of shear failure. This coincides with the formation of a full-depth diagonal shear crack on each specimen (e.g. Figure 7-2) in each loading direction and happened in most specimens at +/- 12 mm. In-cycle strength degradation (which in general did not occur often due to the 3-cycles-per-

displacement-level protocol used and the small displacement step) is also observed around the onset of shear failure in all specimens.

While the cycles of both FSC and SC specimens are quite full in the first displacement levels, i.e. the specimens dissipate a large amount of energy, they become much narrower in the post-peak range of their response.

Pinching is observed in most responses, albeit lower than expected given that the specimens are not well-designed and they failed in shear. Of course, closing of shear cracks of one side and reopening of the other side's cracks upon reversal and the corresponding 'low-stiffness' response is observed. However, perhaps owing to the 90°-anchorage ties and the consequent slippage of the transverse reinforcement, the reloading stiffness deterioration rate is rather high, thus visually reducing the effect of pinching.

*Table 7-7: Displacement ductilities of specimens at various levels.*

<b>Specimen</b>	$\mu_{peak}$	$\mu_{max}$	$\mu_{ax,f}$
<b>FSC_1</b>	6.00	10.51	N/A
<b>FSC_2</b>	4.26	6.42	6.42
<b>FSC_3</b>	5.53	7.00	7.00
<b>SC_1</b>	4.62	10.43	N/A
<b>SC_2</b>	4.27	7.54	7.54
<b>SC_3</b>	5.73	10.34	N/A

The displacement capacities of the specimens in absolute terms are quite variable. FSC\_1 reaches 21 mm, while the rest of the FSC fail earlier owing to the increased axial load. SC specimens reach higher displacements, reaching even the displacement level of +/- 27 mm (both SC\_1 and SC\_3). This is due to the high longitudinal reinforcement percentage that can lead shear-deficient columns under cyclic loading to higher displacement capacities, as shown through the proposed empirical relationships of chapter 4.

The displacement ductility of the specimens is compared in Table 7-7 at peak (i.e. at the onset of shear failure where the peak strength is reached), at the maximum attained displacement and (wherever applicable) at the onset of axial failure (see further below, section 7.3). The yield displacement is defined as the displacement on the cyclic envelope curve corresponding to a strength equal to 70% of the peak strength. The displacement ductility achieved by most specimens is remarkable given their poor design and their shear-dominated - usually called 'non-ductile' or even 'brittle' - response. All of them reach their peak resistance at a ductility between 4 and 6. The specimens that do fail axially reach a ductility of 6.5 to 7.5, while the specimens that do not fail axially are shown to exceed a ductility of 10.

Most specimens exhibit a slight strength asymmetry between the 'positive' and 'negative' directions of the response, the positive ('pulling') side force being consistently 10-20 kN higher. Of course, it is well-known that the cyclic response of nonlinearly responding members is never fully symmetric, even when their geometry is. It is herein deemed that this is caused (at least to some extent) by the following:

- The negative side is the push-side. In order to displace the specimen to this side, the force acts as a compressive force on the steel plate, being transferred through that to the top of the specimen (Figure 7-8b). From this, the other steel plate is displaced via compression and the draw-wire sensor records the displacement.
- The positive side is the pull-side. In order to displace the specimen in this direction, the force acts as a force through the steel plates, nuts and bolts (Figure 7-8b), to the nuts on the other side and through the steel plate to the top of the specimen (Figure 7-8a); simultaneously, the draw-wire sensor measures the displacement of the steel plate. Therefore, there are eccentricities in the force path from the actuator to the column, unlike in the push-side.
- Bending of the steel plates on either side due to these eccentricities can result in a given force being applied without causing the corresponding displacement to the draw-wire sensor. This would eventually cause no asymmetry in the displacements, but indeed an asymmetry in the forces acting upon the column, since the force is measured internally in the actuator; more particularly, it would cause a higher force in the pull direction for the same displacement, as is the case herein.
- The previous statement is corroborated by the fact that the steel plates were visibly bent after the first few tests, which means that a different horizontal displacement would be measured at their centre (where the external draw-wire sensor is connected) and near the edges, where the bolts and nuts are connected and where contact with the top of the column would be made.
- Furthermore, through image correlations, it is observed that the top of the specimen is displaced slightly more in the pull-direction, in order to achieve the same recorded displacement. For instance, SC\_3 is displaced to about +4.7 mm to achieve a +3 mm displacement, but only to about -3.8 mm for the corresponding displacement on the other direction. A further example is SC\_2, which is displaced to about +8.4 mm to achieve a +6 mm displacement, but only to about -6.3 mm for the corresponding displacement on the other direction.

The maximum horizontal strength of each specimen is compared in Figure 7-9. As expected on the basis of blind predictions, shear critical specimens have attained higher strengths than

flexure-shear critical ones. It is obvious in both experimental series that specimens with an axial load increase before attaining the peak strength (namely FSC\_2, SC\_2 and SC\_3) reach a higher strength than the one with constant axial load. This was expected, as higher axial loads act favourably on the shear strength (so long as failure is due to diagonal tension) as well as on the flexural strength when being below the 'balanced' failure point. This increase is about 4%, in line with the predictions of the herein used shear models (Priestley *et al.*, 1994; Biskinis *et al.*, 2004; Sezen & Moehle, 2004) for an axial load increase of 50%.

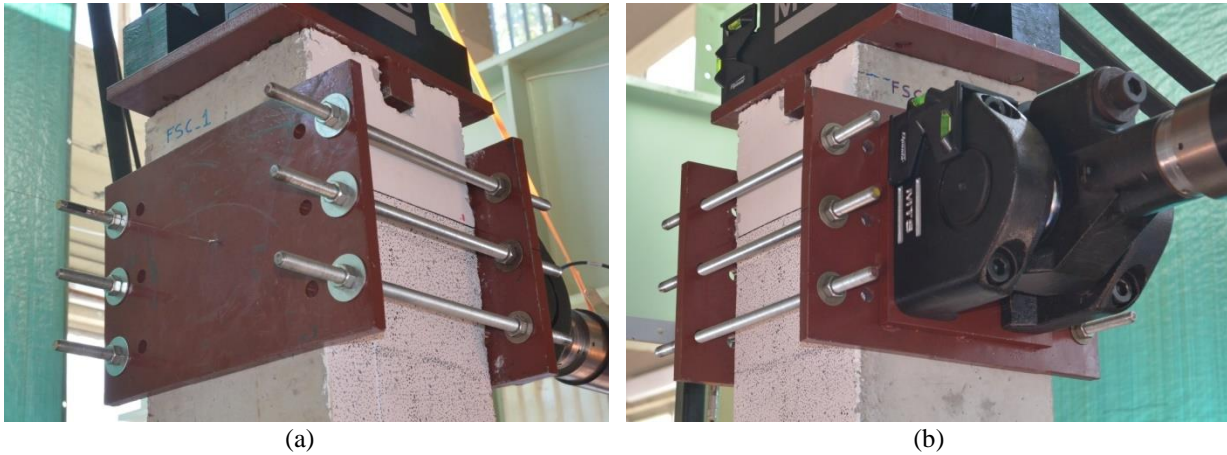


Figure 7-8: Side views of system of steel plates and bolts transferring the forces from the double-action horizontal actuator to the top of the specimen.

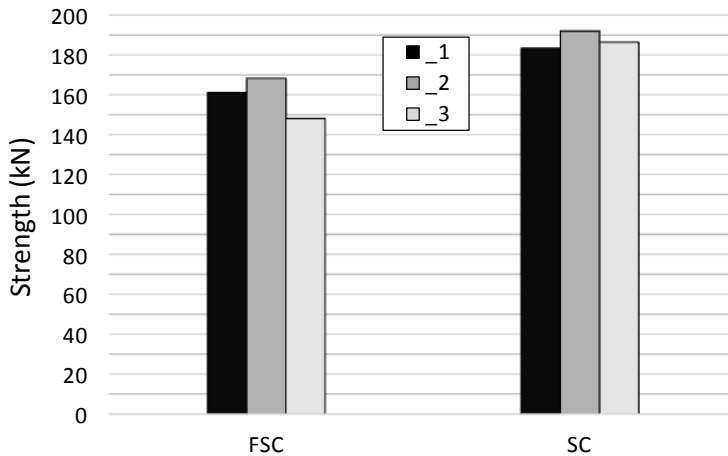
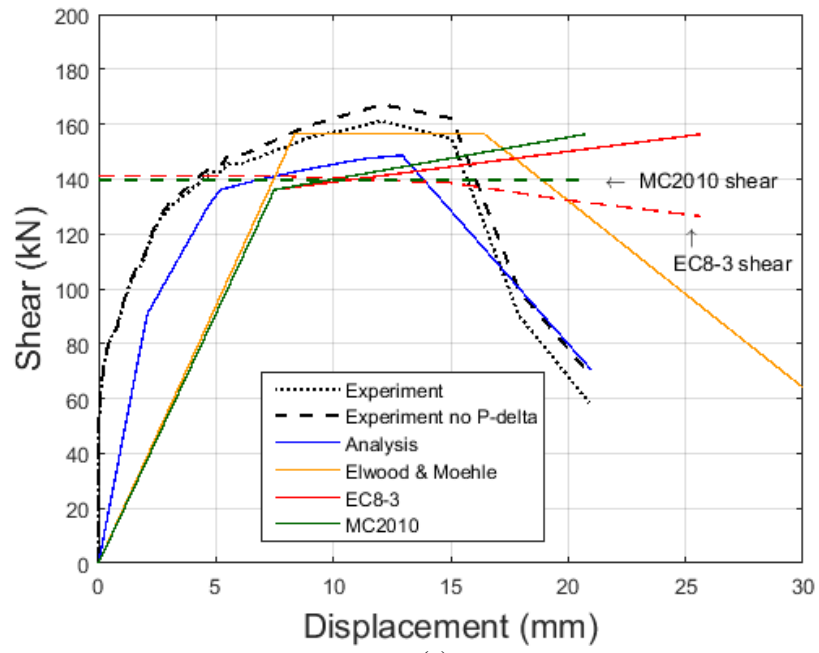
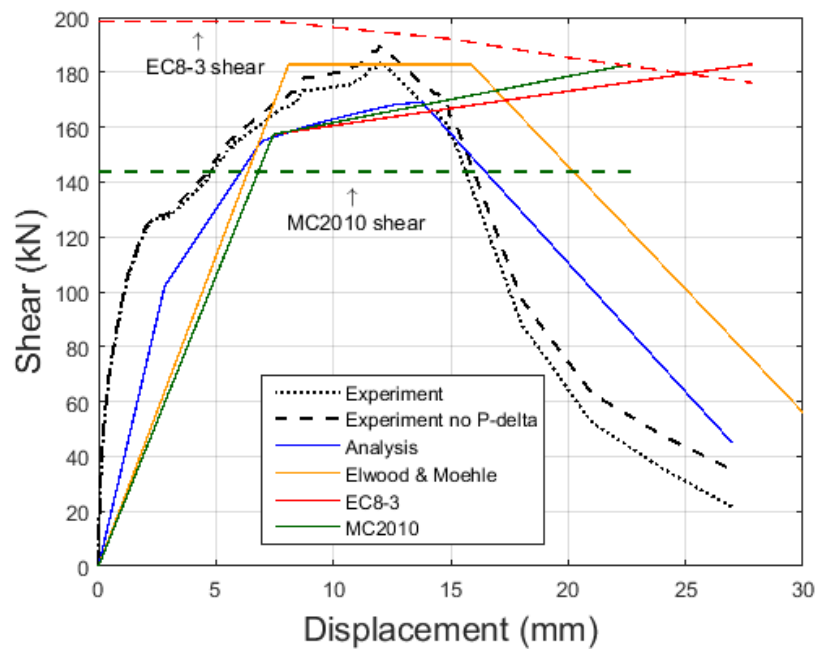


Figure 7-9 : Comparison of the maximum horizontal strength, for FSC and SC specimens.

However, this was not the case for specimen FSC\_3, i.e. the one with axial load increase after the peak. In this case, the ultimate strength was already reached before the increase took place, so it had no effect on this parameter. In theory, the strength should be exactly the same as FSC\_1, however there is some deviation, which will be addressed in section 7.9.



(a)



(b)

Figure 7-10 : Comparison of experimental cyclic envelope with the ones predicted by codes as well as the proposed beam-column model (section 8), for (a) FSC\_1 and (b) SC\_1.

The cyclic envelopes of reference specimens (FSC\_1 and SC\_1) are plotted in Figure 7-10. Both original envelopes and P- $\delta$ -free curves have been added (of course, the effect is not very substantial, due to the low axial load and the low drifts reached). The analytical cyclic envelope predicted by the model proposed in the next section is shown in blue. The envelope predicted by the model proposed by Elwood & Moehle (2006) is shown in orange. The capacities predicted by EC 8-3 (CEN, 2005) and MC 2010 (fib, 2010) are included with continuous red and green lines, respectively; the actual mechanical properties of the materials were used, also accounting for

strain-hardening of the reinforcement. The limiting shear capacity of each code is included in dashed line of the same colour.

FSC\_1 is shown to be very well predicted by the proposed analytical model, although with some underestimation of its strength and its post-peak strength degradation. The codes, on the other hand, predict it to be considerably more flexible in the pre-yield branch. Also, they underpredict its ultimate deformation capacity, both of them estimating it to be around 10 mm, while the specimen loses 20% of its strength at about 16 mm, which is most accurately predicted by the proposed model. Its strength is underestimated even more than by the analytical model, both codes predicting a shear strength limit of 140 kN. The backbone proposed by Elwood & Moehle (2006) produces the same stiffness as the codes, overestimating the specimen's flexibility. It predicts very well the 20% strength degradation point (at 16.5 mm), but it overpredicts by large the strength post-peak.

As for SC\_1, the analytical model's prediction is very good. Again, there is minor underestimation of its strength as well as its strength degradation post-peak. The codes are found to predict adequately the secant stiffness at yield, roughly agreeing with the analytical model, which however accounts for shear stiffness pre- and post-concrete-shear-cracking. The discrepancy between the two codes is immense in this case. MC2010 (fib, 2010) predicts a shear failure before flexural yielding at 144 kN and 7 mm. On the other hand, EC8-3 predicts flexural yielding and subsequent tension shear failure at a very high deformation, namely 25 mm, at a strength of 180 kN. Nonetheless, the specimen reaches 20% strength degradation at about 16 mm. The analytical model is much better in this respect, predicting a 20% strength degradation at about 17 mm. The backbone proposed by Elwood & Moehle (2006) produces slightly greater stiffness than the codes, agreeing with the analytical model. It predicts very well the 20% strength degradation point (at 16 mm), but it overpredicts by large the strength post-peak, although the descending branch's slope is roughly equal to the herein proposed analytical model's.

### 7.3 AXIAL RESPONSE

The hysteretic response in terms of average vertical displacements at the top of the specimen (mm) vs. lateral displacements (mm) and horizontal force (kN) are presented in Figure 7-11 (FSC specimens) and Figure 7-12 (SC specimens). The vertical displacements are recorded by the vertical actuator's LVDT, so they are bound to include a small percentage of lash, which cannot be eliminated. Since the recording system was zeroed *after* the axial load was applied, the vertical displacement at the initial position is 0.0 mm; in reality, it is lower and it can readily be estimated as it is elastic: with  $E = 30 \text{ GPa}$  for C20/25,  $A = 0.09 \text{ m}^2$  and  $L = 0.715 \text{ m}$ ,  $EA/L$  equals

3,776 kN/mm, hence 180 kN axial load (compression) result in 0.048 mm vertical displacement (shortening).

Vertical displacements of all specimens follow the typical U-shaped pattern up to the onset of shear failure, i.e. having a specific negative displacement at the 'resting' position (zero lateral displacement) with increasing displacements towards the peaks of each cycle. The increased vertical displacements at the extremes of each cycle come from the well-known phenomenon of member elongation; the curvatures applied on the specimen lead to high positive strains of the longitudinal reinforcement bars (accompanied by opening of cracks), which lead to an elongation of the member. With consecutive cycles at increasing lateral displacements, plastic strains accumulate leading to further elongation.

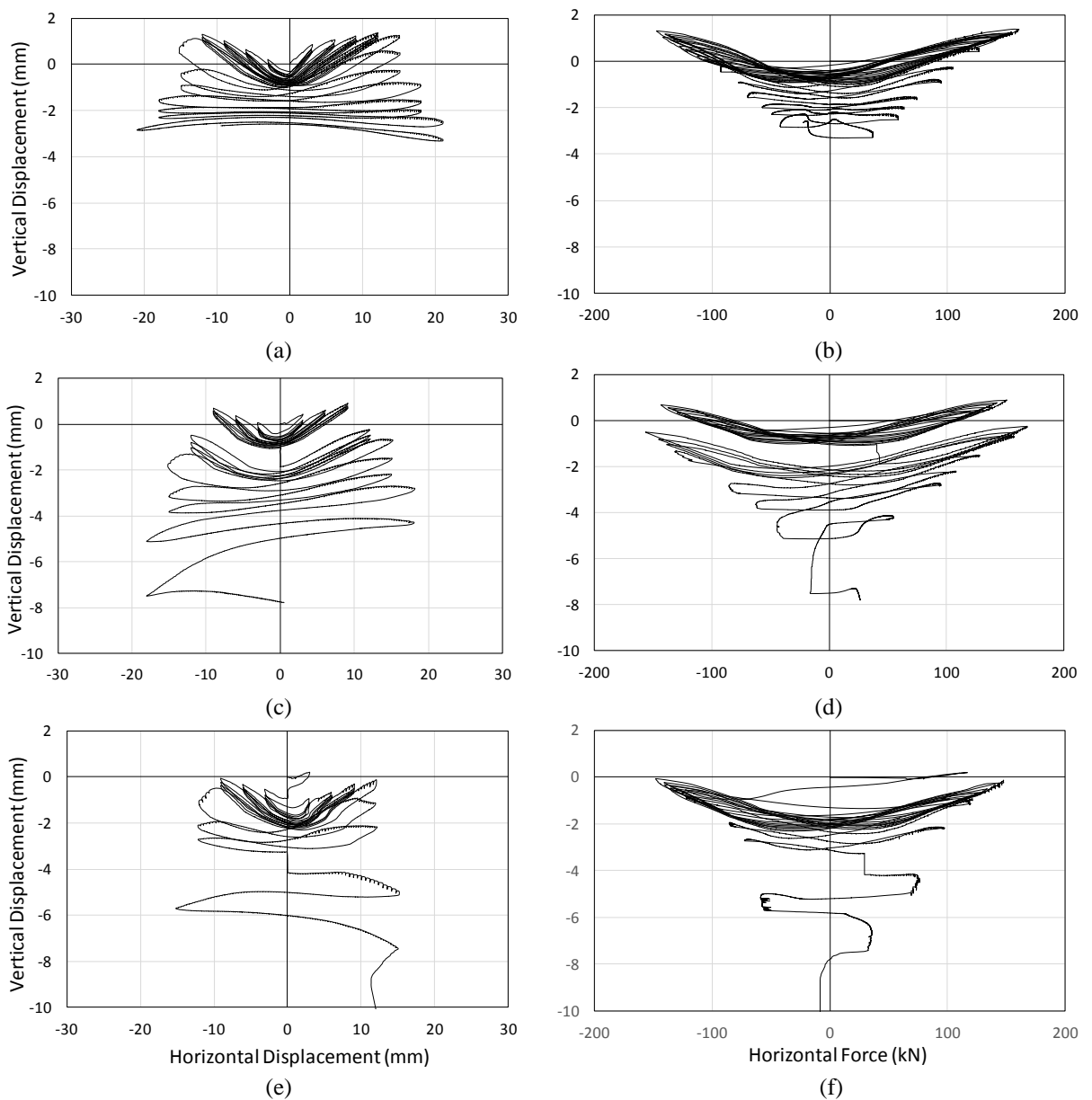


Figure 7-11: Axial hysteretic response of specimens (a, b) FSC\_1, (c, d) FSC\_2, (e, f) FSC\_3 .

This is better illustrated in Figure 7-13, where the vertical displacements of the top column cross-section (at the loading level) are shown for various displacement level peaks for specimen SC\_2, considered representative of the rest of the specimens. These were obtained from digital image correlation; the horizontal and vertical displacement of any point can be calculated by comparing its initial position on the reference image and the position in any given image. To get this, every point is tracked using a given area of pixels around it, as described in section 7.1. Doing this for a dense grid of points, the horizontal and vertical displacement profiles can be obtained for each specimen at each displacement level.

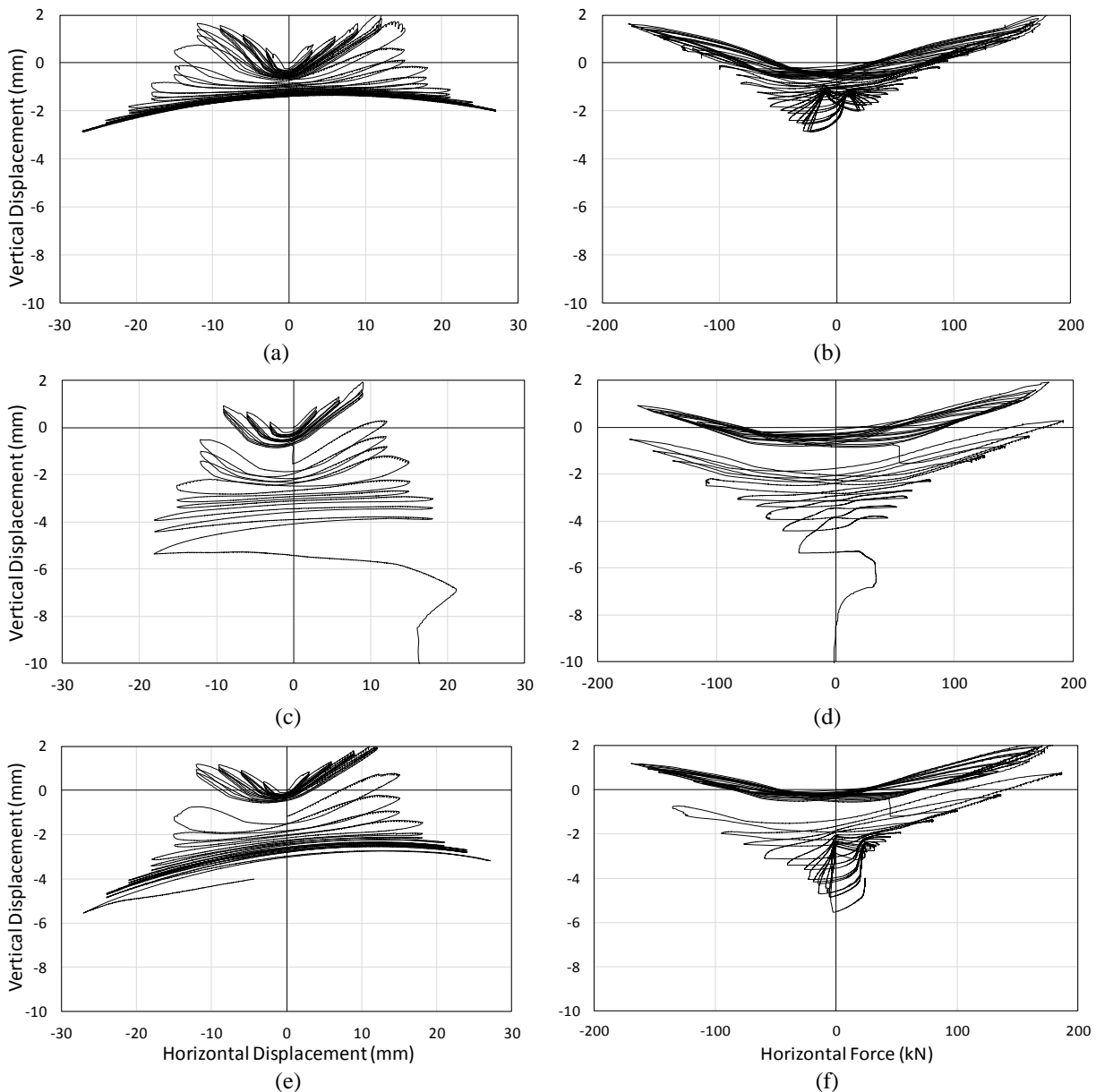


Figure 7-12: Axial hysteretic response of specimens (a, b) SC\_1, (c, d) SC\_2, (e, f) SC\_3 .

Figure 7-13 illustrates the behaviour (vertical displacements) of the entire section, in contrast to an average vertical displacement, which is measured by the vertical actuator's LVDT. Vertical displacements increase with further lateral displacement owing to the accumulation of steel bar

elongation and the associated higher curvatures; displacements as high as +5 mm are reached at the peaks of the displacement levels of +9 mm and +12 mm.

Nonetheless, the aforementioned patterns change from the onset of shear failure onwards, as a result of shear failure influencing the axial deformations of the specimen. In Figure 7-13, the vertical displacements of the top section are shown to retract after this point, ever so slightly at the peak of +12 mm, but much more significantly in the subsequent displacement levels. At the displacement of 12 mm shear cracks are just forming, not having achieved a full depth diagonal crack at the first cycle (for which this diagram is plotted). However, when +15 mm is reached, a full depth diagonal crack has formed and has widened considerably. In general, as soon as this happens in each test, increased ostensible axial shortening is recorded; in reality, there is no actual shortening of the entire column, but the axial load pushes the upper discrete part of the column relatively to the lower one, causing these negative vertical displacements.

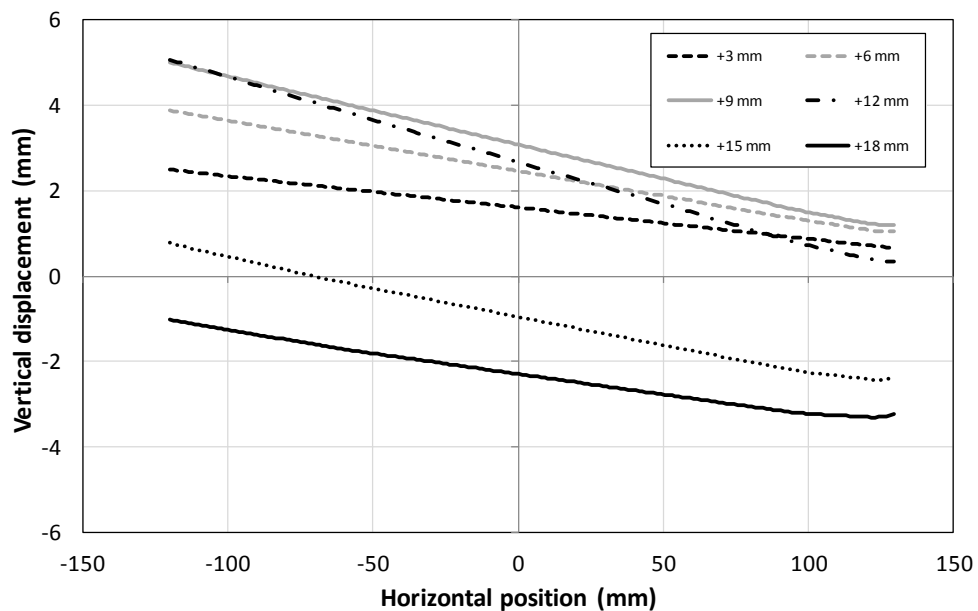


Figure 7-13: Vertical displacement of top of SC\_2 at various displacement level peaks.

In Figure 7-11 and Figure 7-12, the previously described phenomenon is manifested in two ways. Firstly, vertical displacements decrease after the onset of shear failure and keep decreasing further with each cycle. Secondly, the shape of the observed pattern (in terms of vertical displacement vs. lateral displacement) changes at this defining point of the response; from a U-shape, it turns flat and eventually into an inverted-U-shape. This corresponds to a change in the physical behaviour of the member. Initially, the lateral displacements cause high curvatures near the peaks of cycles that cause elongations of the bars, which also accumulate over the cycles. Of course, this elongation has not disappeared in latter stages and it is certainly not turned into shortening of the main bars; what happens is that as the peak of each cycle is reached after this full depth diagonal crack has formed, the lateral displacement increases are translated into

widening of the shear crack instead of further curvature increases - this process will be better explained in section 7.5. As the cracks open, it is easier for the upper discrete parts of the column to move downwards under the influence of the constant axial load. Of course, as the displacement reverses, the cracks partly close and a part of this downward displacement is recovered (hence the inverted-U-shape); after a given point, the accumulation of downward displacements becomes very significant with vertical displacements decreasing to even less than -5 mm (which corresponds to an average normal strain of -0.7%).

The safety limit for the system to shut down was set at a vertical displacement of -10 mm. Indeed the sudden increase of axial deformations accompanying the onset of axial failure is shown to start at a higher value in the cases of axial failure, as shown in Figure 7-11 and Figure 7-12, namely around -7 mm. Of course, in columns with different design or axial loads, it might well be below -10 mm. Specimen FSC\_2, FSC\_3 and SC\_2 can be seen to exhibit this sudden increase of downward displacements, while FSC\_1, SC\_1 and SC\_3 were stopped before the onset of axial failure was reached either for the safety of the equipment or because the specimen was visually judged to have been damaged extensively and its resistance had fallen to a really small fraction of the maximum strength.

## 7.4 DEFORMATION ANALYSIS

The deformations of the specimens were calculated based on images taken during the tests and post-processing using the technique of digital image correlation (see section 7.3 above). Comparing vertical and horizontal displacements at the top of the specimens obtained from the external draw-wire sensor (DWS) and the vertical actuator's internal LVDT, with displacements estimated from digital image correlation (DIC), there seems to be adequately good agreement so as to use DIC for the deformation decomposition of the elements.

A second comparison is conducted between shear displacements recorded for each specimen with DWS (Figure 7-15) and estimated from DIC. The former was based on two cross-inclined DWSs with 24 cm horizontal and 48 cm vertical dimensions (see Figure 6-8a). One set of cross-inclined diagonals with the same geometry (24 cm horizontal and 48 cm vertical lengths) as well as an extra set (24 cm horizontal and 24 cm vertical lengths) are used in DIC, starting off slightly below the column-base interface and ending up roughly at the loading level; thus, the latter are expected to capture a slightly larger shear displacement. The same formula is used to extract the shear displacement in both cases, (e.g. Beyer *et al.*, 2011):

$$\delta_{sh} = \frac{1}{4b} \left( (d + \delta_2)^2 - (d + \delta_1)^2 \right) \quad (7-1)$$

where  $b$  is the width of the instrumented area (i.e. 24 cm),  $d$  is the initial length of the diagonals, and  $\delta_i, i=1,2$  is the change in length of each diagonal.

The results from the two techniques are very close in some cases (e.g. Figure 7-14a) and close to some extent for others (e.g. Figure 7-14b), giving matching results overall with respect to the increase of shear displacements with increasing lateral top displacement as well as their higher-rate increase after the onset of shear failure. It has to be noted that some variation is to be expected, due to the slight differences of deformation between the front and back face of the column, since both techniques are based on surface measurements; it was repeatedly observed during the tests that the cracking pattern of the two sides was not always on a par. Therefore, an average of the two measurement techniques will be used herein, except if there is reason to use only one, as explained further below.

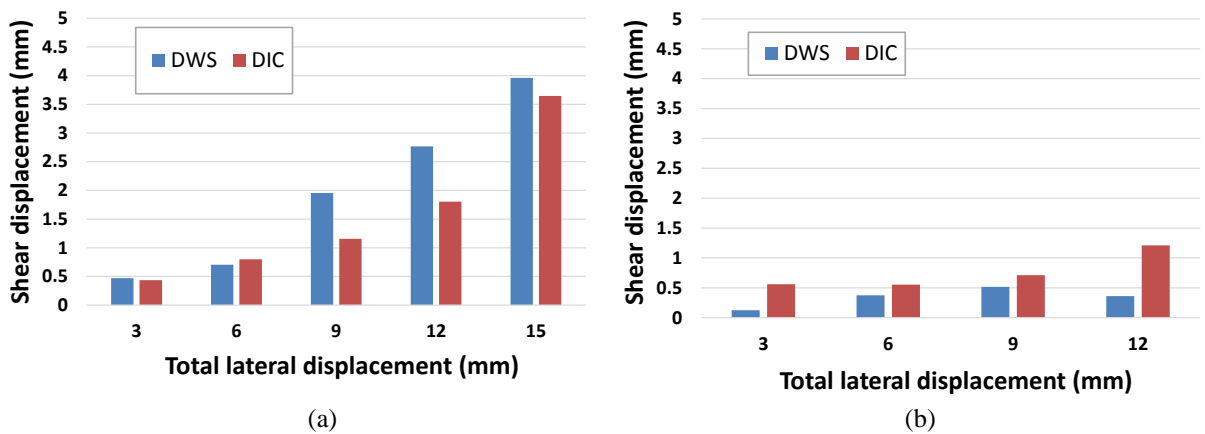


Figure 7-14: Comparison between shear displacement recorded by the Draw-Wire Sensors (DWS) and calculated via Digital Image Correlation (DIC) for specimens (a) SC\_1, and (b) FSC\_3.

Regarding the calculation of flexural displacements, the strains along the vertical direction,  $\epsilon_{zz}$ , were calculated based on the images along the positions of the longitudinal corner reinforcement. To extract strains, nine different vertical segments were defined along the column and their initial (based on reference image with zero lateral displacement) and changed lengths were obtained. The segments' starting points were below the base-column interface and their ending points were just above the interface crack, at  $h/4$  (75 mm),  $h/2$ ,  $3h/4$ ,  $h$ ,  $5h/4$ ,  $3h/2$ ,  $2h$ , and at the loading level (715 mm), all distances measured from the interface. Displacements caused by slippage of the anchorage of the reinforcement bars are lumped together with the flexural ones, since attributing the deflection caused by the interface crack to bond-slip would overestimate its contribution, as some flexural deformation would be inevitably included.

Dividing the strain difference by their horizontal distance, the distribution of curvature along the element was obtained. Integrating the product of this distribution with its vertical distance from the top of the specimen (loading level), the flexural displacement at the top was obtained:

$$\delta_{fl} = \int \varphi(y) y dy \quad (7-2)$$

$$\varphi(y) = \frac{\varepsilon_{zz,1}(y) - \varepsilon_{zz,2}(y)}{\Delta x_{1-2}} \quad (7-3)$$

where  $y$  is the distance from the loading level,  $\varphi(y)$  is the curvature of the element at any given position along the element,  $\varepsilon_{zz,1}(y)$  and  $\varepsilon_{zz,2}(y)$  are the strains obtained along the positions of the longitudinal corner bars and  $\Delta x_{1-2}$  the horizontal distance between these bars.

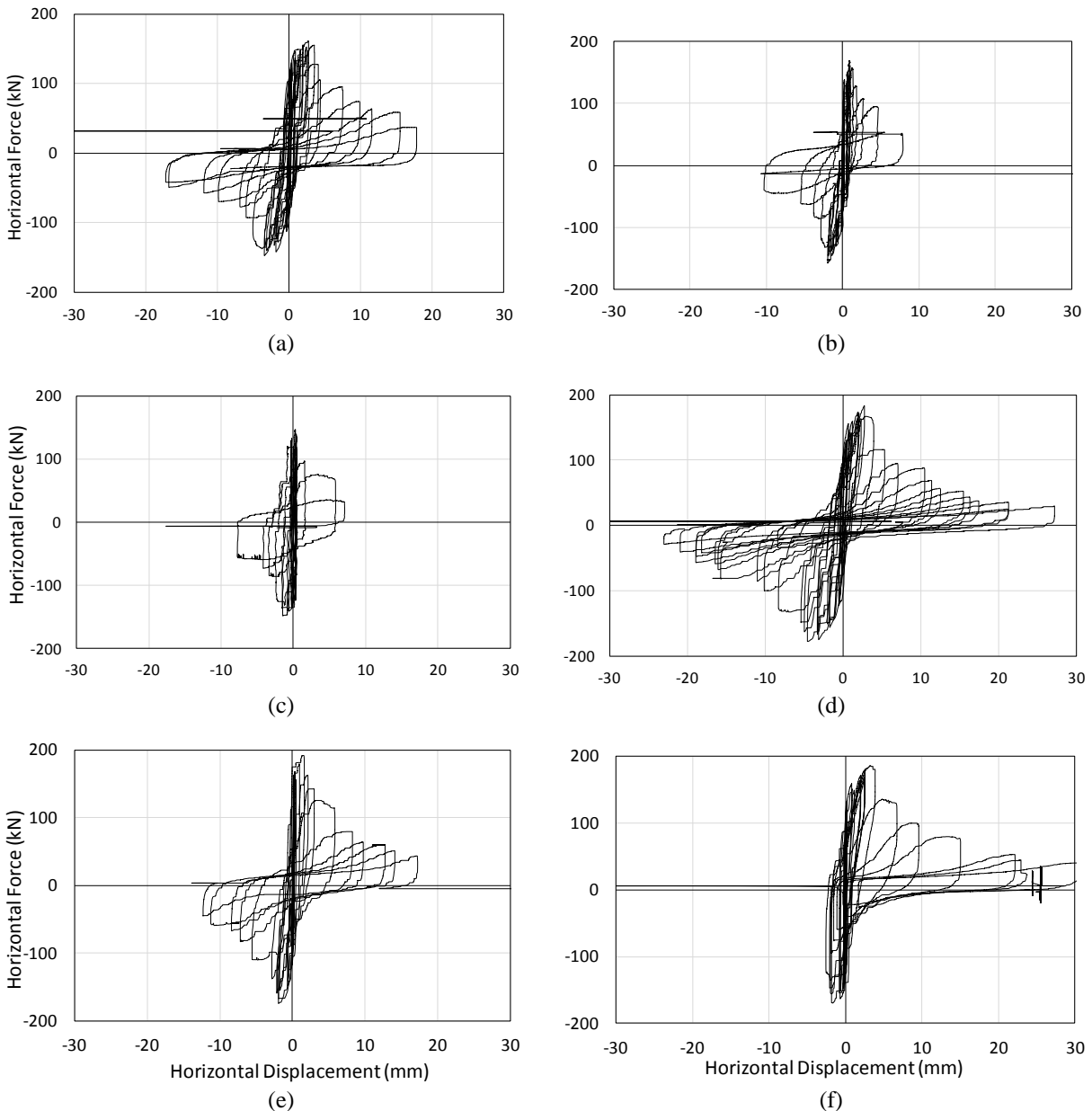


Figure 7-15: Hysteretic response in terms of shear displacement of specimens (a) FSC\_1, (b) FSC\_2, (c) FSC\_3, (d) SC\_1, (e) SC\_2 and (f) SC\_3.

The metal post, wherefrom the top lateral displacements were measured via a draw-wire sensor, was mounted on the base of the specimen. As a consequence, horizontal displacements induced by sliding of the base that are found to reach up to 4.0 mm are already implicitly taken

into account. Had this not been done, the measured response would be completely different from the actual one recorded herein. That is why such a component of lateral displacement is not included in this deformation analysis.

Because of limitations of both techniques (DIC or DWS), the following approach was followed:

- In the final steps of each test, due to extensive concrete spalling, there was not enough speckled surface to obtain DIC measurements. In that case, the DWS measurements of shear displacement were used as basis and the rest were calculated by subtracting them from the total lateral displacement.
- For two tests (FSC\_1 and FSC\_2), some images are missing (e.g. Table 7-1 and Table 7-2). For these, again, the DWS were used as basis.

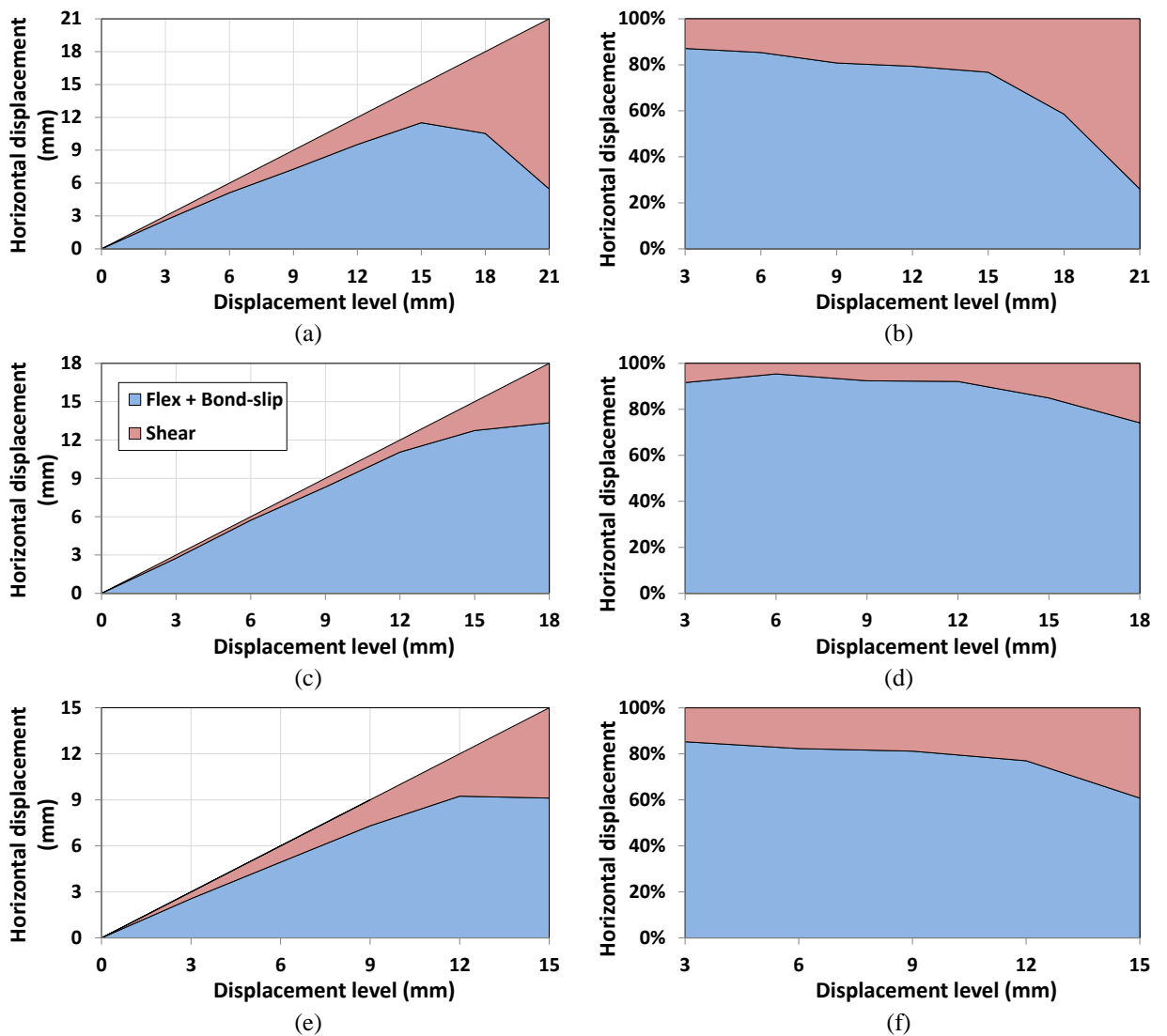


Figure 7-16: Lateral displacement decomposition for (a, b) FSC\_1, (c, d) FSC\_2, and (e, f) FSC\_3 in (left) absolute and (right) relative terms.

- In general, the initiation of shear failure with the consequent widening of and slipping along the full depth shear cracks affects the measurements of flexural displacement

with DIC. Therefore, DIC measurements were not taken into account beyond the onset of shear failure. For those displacement levels, again, the DWS were used as basis.

- The DWS results were not accurate in specific displacement levels of some tests after the onset of shear failure, as debris from the back of the column would get entangled in the measuring wires, causing significant distortion in the measured displacements. This can be seen as an extreme value, much higher/lower than would be expected (e.g. last step in Figure 7-15d as well as Figure 7-15f). SC\_3 exhibited an extremely asymmetrical response, which implies that debris got stuck in one of the two wires, hence increasing the displacement calculated for one direction and decreasing the other. For this specific case, the average of the two directions was used for the last displacement levels, with the error assumed to cancel out. Besides this, each such displacement level was discarded altogether, i.e. the last steps of SC\_1 and SC\_2. This does not imply that DWS measurements' accuracy is only influenced by falling debris, of course.

Based on the above assumptions and calculations, the displacement decomposition for the push direction can be seen in Figure 7-16 and Figure 7-17 for FSC and SC specimens, respectively. Of course, there was some 'unaccounted for' part of the displacements, which was mostly ranging between 0% and 20%, with some higher or lower values. This was redistributed in the two displacement components ('flexural and bond-slip', 'shear') proportionally. As examples, two specimens without redistribution of the 'unaccounted for' part are shown in Figure 7-18. FSC\_3 is actually the only one exhibiting also negative 'unaccounted for' part, meaning that the calculated components are higher than the total displacement. SC\_3 is a specimen exhibiting some of the highest unaccounted for components of all the tests.

It was observed that there was a higher unaccounted for part in the other direction (pull). This might be attributed to slight rotations of the base during reversals, which cause the metal post – upon which the DWS that measures top lateral displacements was mounted – to move closer to or away from the specimen, thus adding or subtracting some displacement. This is just a speculation based on visual inspection of videos of the tests and could not be verified or quantified.

A decomposition with the flexural and bond-slip parts separated is shown in Figure 7-19, as an indicative example only. As mentioned above, this component certainly contains some flexural deformation, which results in it being so high – in fact, even higher than the flexural deformations in the first couple of displacement levels. The reader is also cautioned of the difference in scale between Figure 7-19 and Figure 7-17(c, d), with respect to comparison of the decomposition in each case; naturally, in both figures the shear component is exactly the same.

It is observed in Figure 7-16 and Figure 7-17 that shear displacements always start off low, as expected, usually around 10% to 15% of the total displacement at a displacement level of +3 mm. They increase steadily as damage propagates and much more sharply from the onset of shear failure onwards. They reach percentages of 40% to 70% at the final displacement levels, a clear indication of the dominance of shear response after the peak strength is reached.

On the other hand, the flexural (including bond-slip) displacements start as a high proportion of the total lateral displacement, around 85% to 90%. Although they increase considerably in subsequent cycles, they decrease as a percentage of the total displacements up to the onset of shear failure, falling with a much higher rate after that, in line with the previous comments about shear displacements. These findings verify the intended initial design of the specimens.

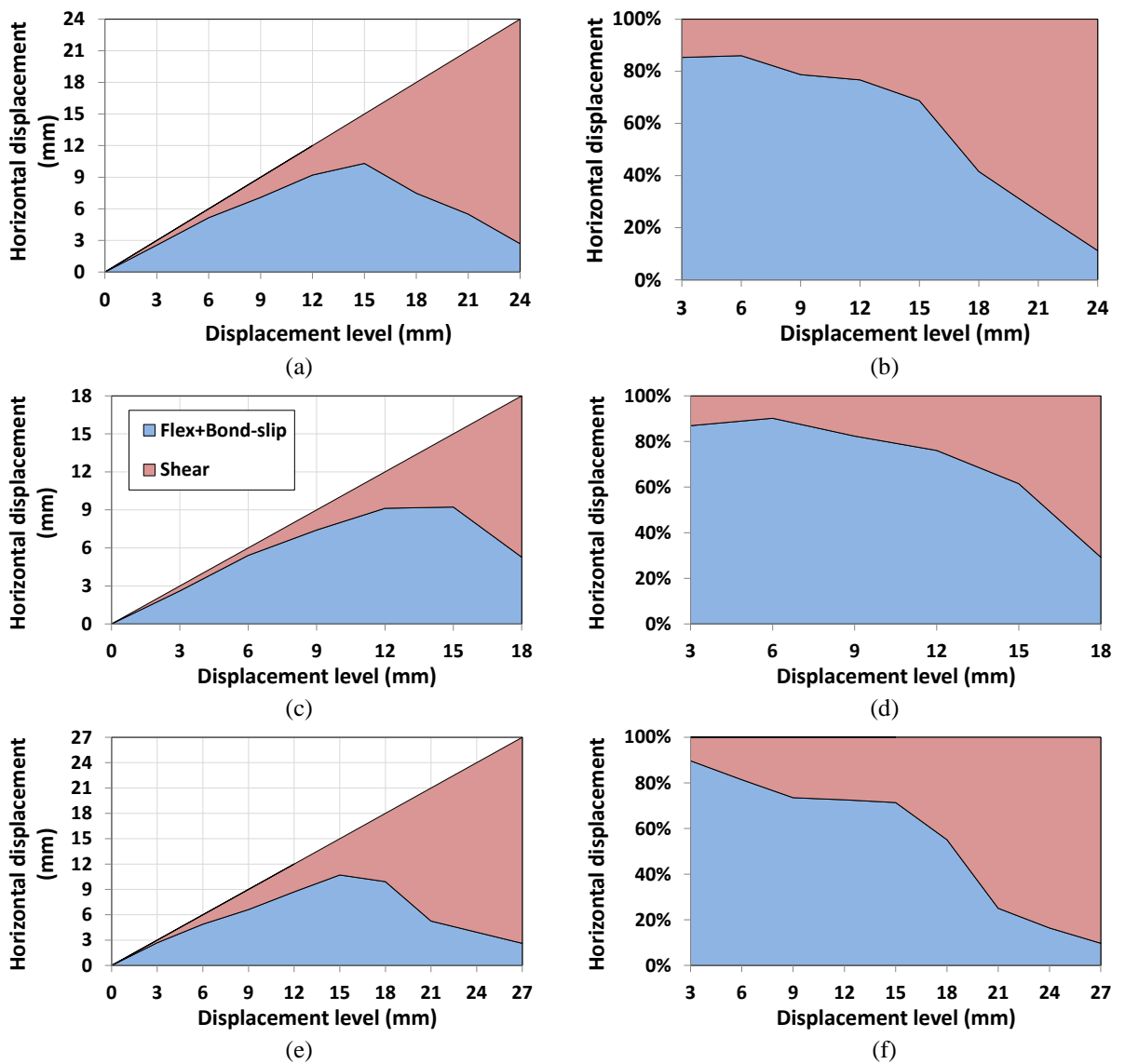


Figure 7-17: Lateral displacement decomposition for (a, b) SC<sub>1</sub>, (c, d) SC<sub>2</sub>, and (e, f) SC<sub>3</sub> in (left) absolute and (right) relative terms.

More importantly, these observations are completely in line with the theoretical model basis outlined in section 4.1. It is shown that after the onset of shear failure, the flexural and bond-

slip parts of the response do not increase any further, staying constant or in some cases even decreasing.

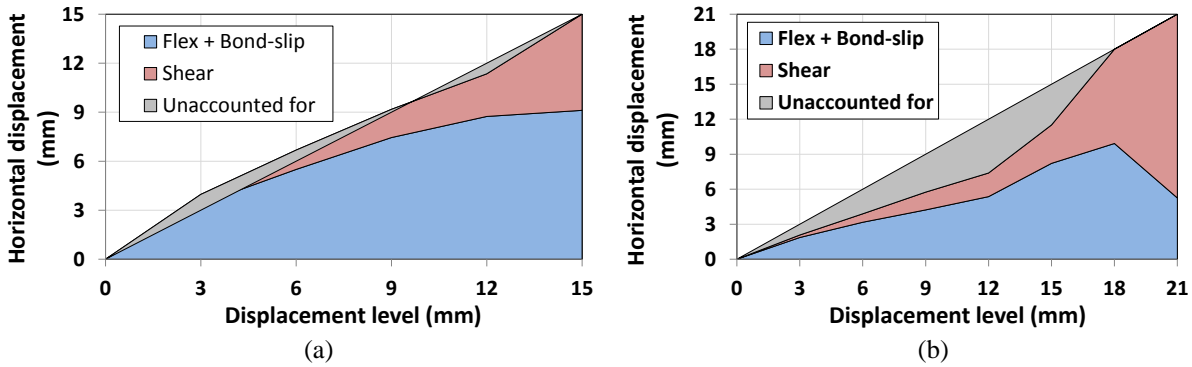


Figure 7-18: Lateral displacement decomposition for (a) FSC\_3, and (b) SC\_3, including the 'unaccounted for' component.

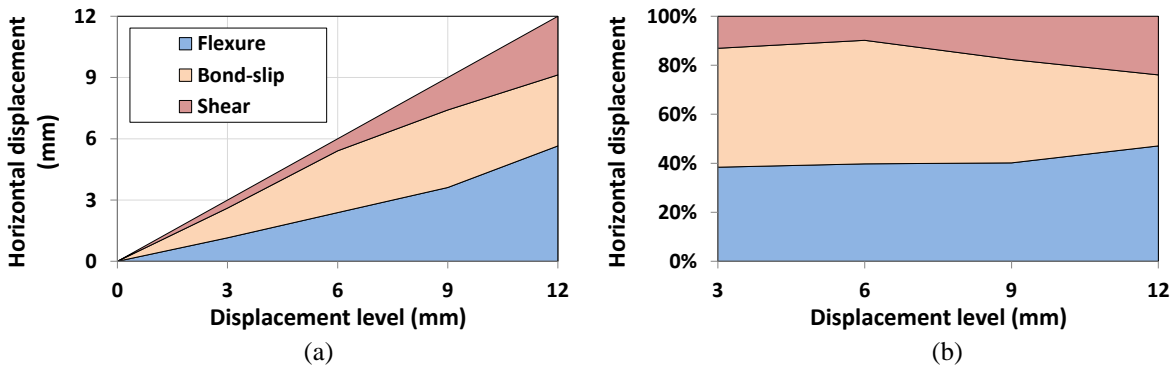


Figure 7-19: Lateral displacement decomposition for SC\_2, including the bond-slip component, in (a) absolute and (b) relative terms.

It is observed that FSC specimens have in general higher percentages of flexural displacements than the SC specimens. This observation, in combination with the fact that in FSC specimens many more flexural cracks form, as noted in section 7.1, are clear indications of the higher influence of flexure on the response of FSC specimens and a response of SC specimens closer to pure shear at the later stages of response. Of course, flexural deformations still play an important role in the overall response of SC specimens and, as mentioned in section 7.1, yielding of their longitudinal reinforcement was recorded.

## 7.5 SHEAR FAILURE LOCALISATION

The phenomenon of shear failure localisation is central to this research work and one of the cardinal bases as well as innovation points of the proposed model in the next chapters. It is demonstrated herein using experimental evidence first of all that it does indeed exist in shear and flexure-shear critical specimens and, secondly, how it physically manifests.

All the images and diagrams in this section refer to the positive direction (pull-side).

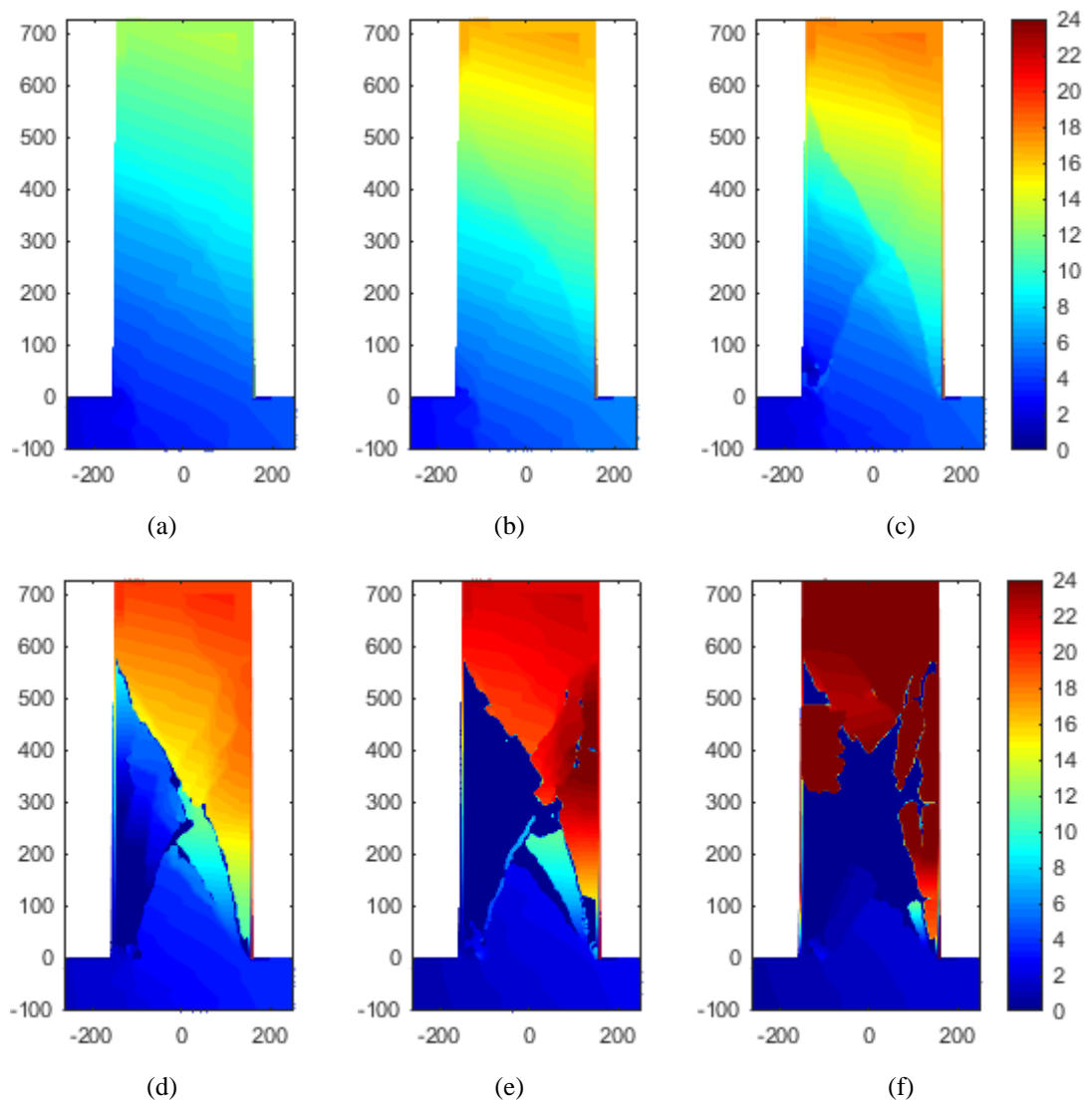


Figure 7-20: Lateral displacement (in mm) profiles along the surface of specimen SC\_1 from a displacement level of (a) 9 mm until (f) 24 mm.

In Figure 7-20, the lateral displacement profiles (estimated as explained in section 7.3) along the surface of SC\_1 at various displacement levels are shown. Note that at the final displacement steps, part of the surface has spalled off, thus appearing as having zero displacement (i.e. dark blue in Figure 7-20). Before the onset of shear failure, they appear continuous along the surface, while they start showing "jumps" at a displacement of 12 mm. This is due to shear cracks, where horizontal displacement is localised, so the two crack sides have a non-negligible difference in horizontal position, which is shown to be around 1-3 mm at the displacement levels of 12 mm and 15 mm. Especially from 21 mm, this difference becomes very pronounced, reaching values of 10 mm, and the difference between the top and bottom discrete parts of the column is very obvious. A similar response can also be seen in Figure 7-21 for specimen SC\_3. It also separates

into two discrete parts after the displacement level of 18 mm and behaves in much the same way as SC\_1.

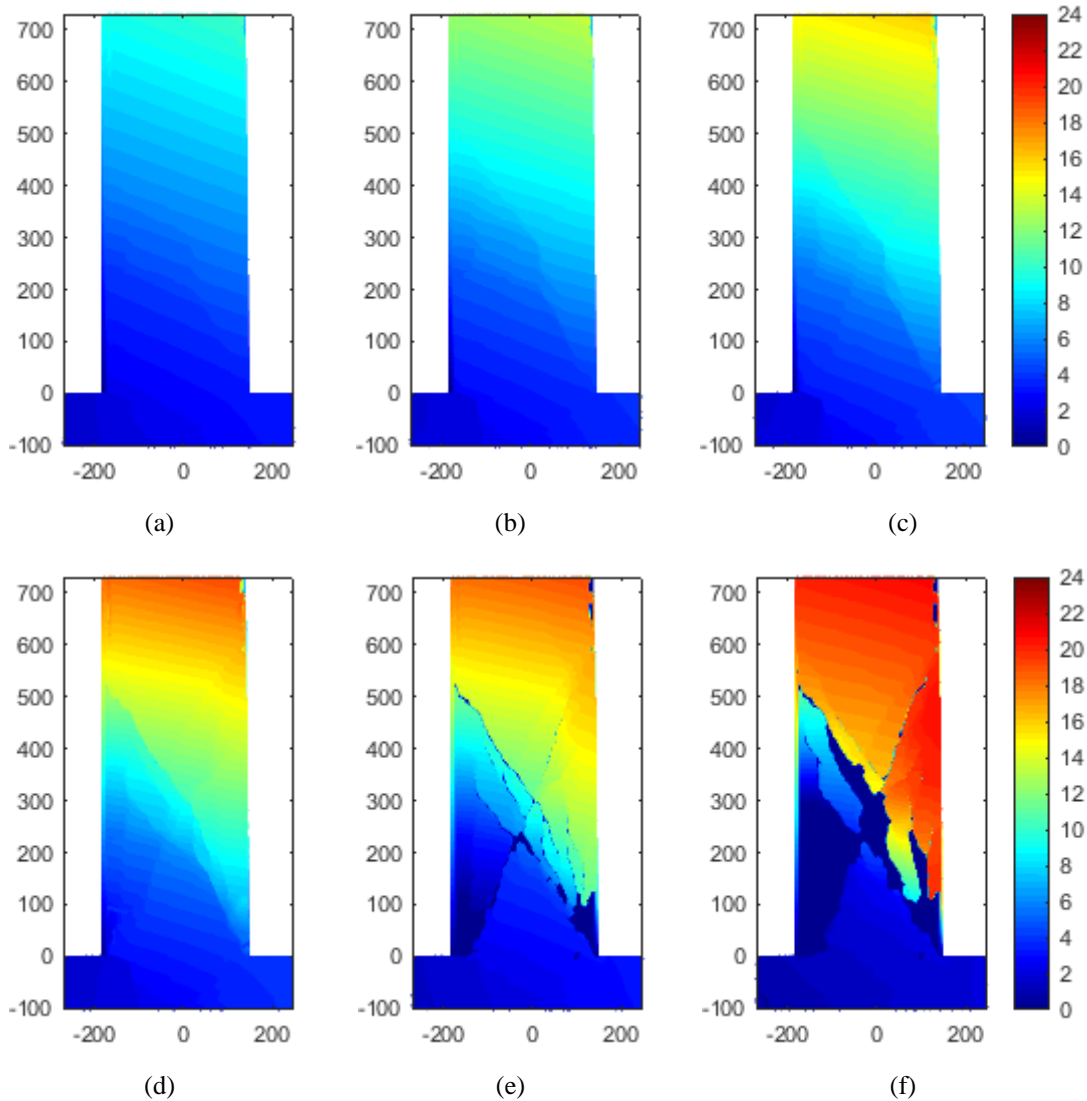


Figure 7-21: Lateral displacement (in mm) profiles along the surface of specimen SC\_3 from a displacement level of (a) 9 mm until (f) 24 mm.

This is further investigated in Figure 7-22, where the lateral displacement profiles (subtracting the non-zero base displacement, as the metal post is mounted on the base, so it is disregarded in the measurement) of the centroidal axis of the front surface of two specimens are provided for displacement levels from 3 mm up to 15 mm and 18 mm, respectively. One can clearly see the smooth continuous displacement lines produced in the initial stages of the response. This changes to a continuous line with smooth parts and some jumps after shear cracks start appearing on the specimen. Well into the post-peak domain with a formed clear full-depth diagonal crack, the displacements become discontinuous, being broken up by the existence of one or more wide shear cracks; the displacement reached is quite low below the cracks (similar

to levels of 3 mm or 6 mm), jumping to a much higher value above them and increasing gradually until the top from that point onward.

What happens is that the column is effectively turned into two discrete parts from the onset of shear failure onwards, divided along the side-to-side shear crack; in reality it comprises of four discrete parts, however they can be lumped into two parts in each loading direction. When applying a load to the top part, it is deformed to some extent and simultaneously the gap opens further, while the bottom part stays almost still, which can be clearly seen in Figure 7-20. In effect, it is 'easier' to further open the crack than to deform each discrete part of the column, like a weak link in a chain. In other words, imagining the column as a set of deformation components connected in series, the crack component (part of the shear deformations in the post-peak regime) requires less energy than the other components to achieve a given displacement – in other words, it is 'less stiff' – hence it is the preferred mode of deformation over the others. That is why it was observed in most specimens that the flexural as well as bond-slip (located at the column-base interface) cracks tended to partly close from the onset of shear failure onwards (section 7.1).

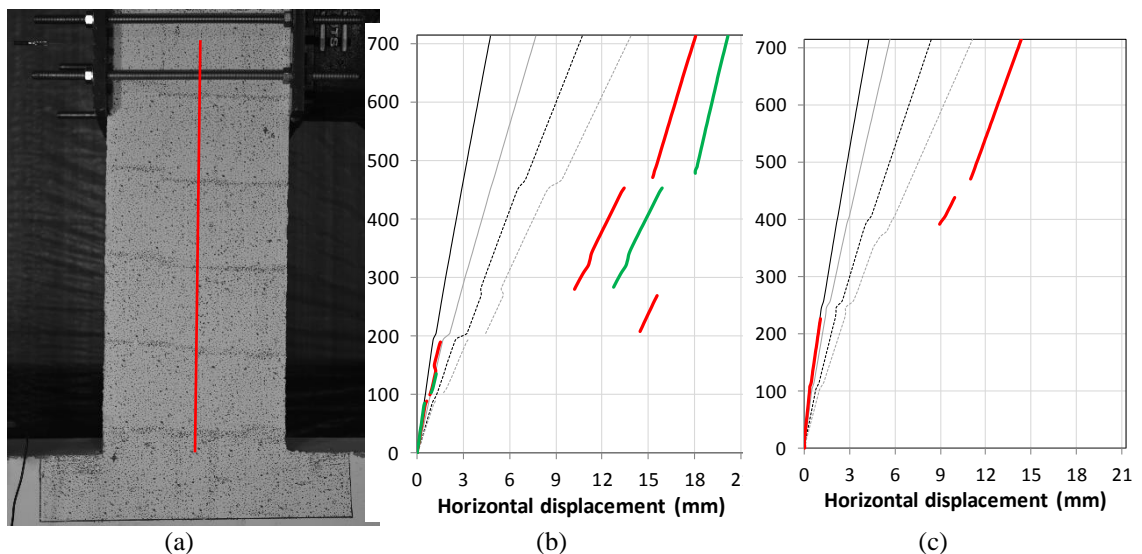


Figure 7-22: Lateral displacement profiles along the centroidal axis of specimen (b) SC\_2 (displacement levels +3 mm until +18 mm from left to right), and (c) FSC\_3 (+3 mm until +15 mm from left to right).

The area wherein these "jumps" take place is defined by the geometry of the shear cracks and has been herein termed critical shear length; this is where the majority of post-peak displacement concentrates, as seen in Figure 7-20, Figure 7-21 and mainly in Figure 7-22.

Simultaneously, this phenomenon also influences the longitudinal direction. The upper discrete part of the column moves downwards relatively to the bottom one when displaced laterally under the influence of the constant axial load, resulting in decreased vertical displacements as shown in Figure 7-13.

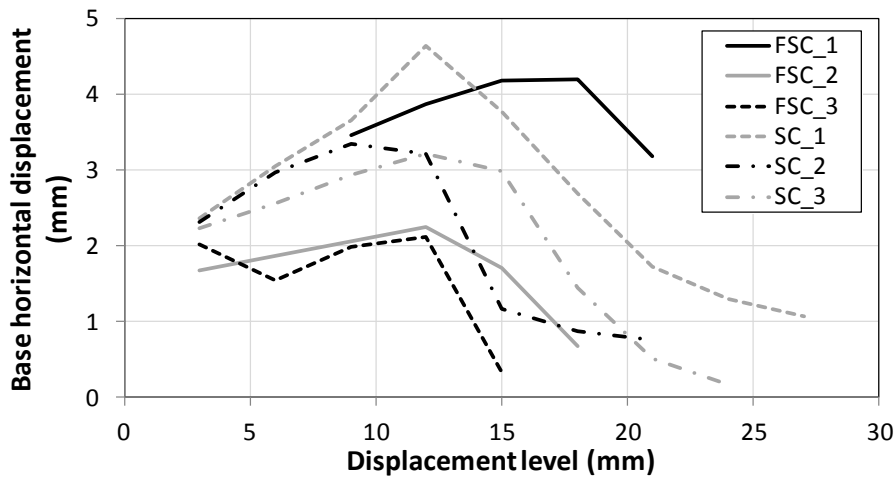


Figure 7-23 : Horizontal displacement of the base of the specimens at each displacement level.

These observations are corroborated by the fact that the base generally has a significant horizontal displacement before the onset of shear failure, while this decreases down to almost zero at the final displacement levels. This can be seen in Figure 7-20 and Figure 7-21 for SC\_1 and SC\_3, respectively. It is much more clearly displayed in Figure 7-23, wherein the horizontal displacement of the base of each specimen is plotted for successive displacement levels. The displacement of a point along the centroidal axis at a vertical position of -50 mm is used for this plot. A trend is evident in the plots: a base displacement of 1.5-2.5 mm is reached at 3 mm, which keeps increasing until about 12 mm and then decreases sharply in the next displacement levels. Thus, the claim is reinforced that after the column is discretised into 'two' bodies, the horizontal loading causes displacement mainly through opening of the full-depth diagonal crack, while the lower body remains almost unaffected, having little to no displacement.

In conclusion, it has been shown that the lateral displacement is largely localised at the critical shear length defined by the shear cracks, after the initiation of shear failure. These displacements mainly represent the relative rigid body displacement between the discrete upper and lower parts of the column, separated along the diagonal shear crack(s).

## 7.6 STIFFNESS

The secant stiffness at the peaks of the lateral hysteretic response is calculated with a view to examining how it degrades with increasing cycles and ductility. It is presented in absolute and relative terms in Figure 7-24 and Figure 7-25, taking into account the average of both the positive and negative direction, in order to have a more representative quantity. The elastic stiffness ( $K_{el}$ ) used to compare the stiffness is derived assuming a cantilever of 715 mm length, C20/25 concrete and  $300 \times 300$  (mm) cross-section, hence  $K_{el} = 166.2$  kN/mm.

Overall, the stiffness deterioration is rather similar in all specimens with few discrepancies. There is a very significant decrease in stiffness with increasing ductility, falling to about half the stiffness of the +3 mm displacement level by the displacement level of +6 mm or +9 mm. Subsequently, it keeps decreasing, reaching zero stiffness asymptotically after +18 mm.

The second and third cycles have only slightly lower stiffness than the first cycles at the initial displacement levels. From +9 mm or +12 mm, the gap becomes greater, due to the higher cyclic strength degradation and reloading stiffness deterioration that was observed in section 7.2.

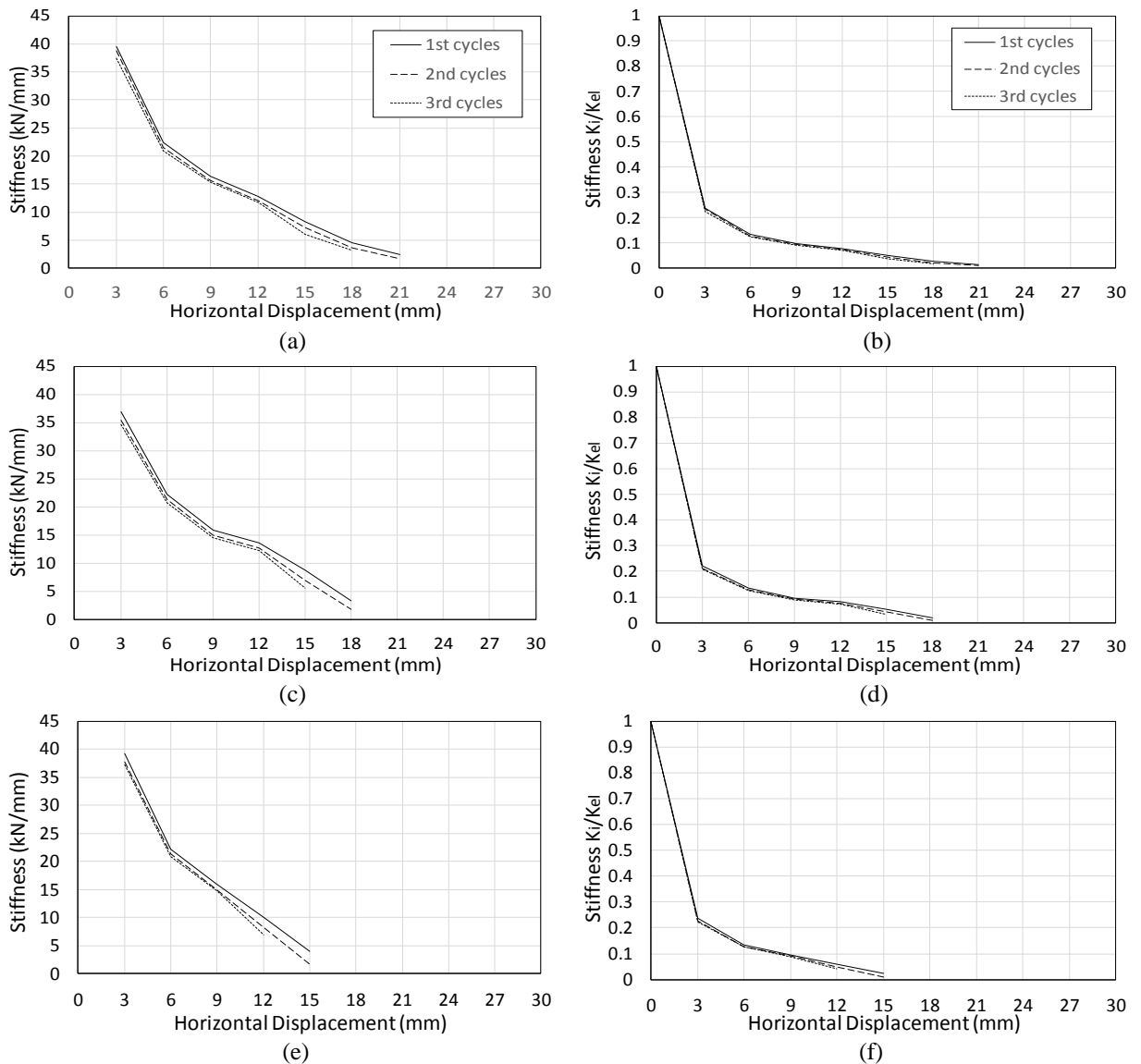


Figure 7-24: Lateral displacement secant stiffness for (a, b) FSC\_1, (c, d) FSC\_2, and (e, f) FSC\_3 in (left) absolute and (right) relative terms.

Comparing the relative stiffness diagrams, the stiffness at the first peak of the first displacement level is found to be much lower than the predicted elastic stiffness, with a value roughly 20-25% of  $K_{el}$ . An important source of this discrepancy with the estimated elastic stiffness is that at the peak of +/- 3 mm, there is already flexural cracking in all the specimens (see section 7.1), which adds a lot to the flexibility of the members; as seen in section 7.2, the first cycle by no means

corresponds to a linear elastic response. At the same time, shear deformations, which are not taken into account in the calculation of the elastic stiffness, are a considerable part of the total displacement at this stage of the response – about 10% to 15% as shown in section 7.4 –, commensurately decreasing the resulting stiffness. Other minor sources might be shrinkage cracks, the aforementioned bending of the plates connecting the actuator to the column as well as some added flexibility from the deforming base of the specimen. It cannot be known exactly to what extent each factor actually influences the recorded value, but flexural cracking and shear deformations can be considered the main sources.

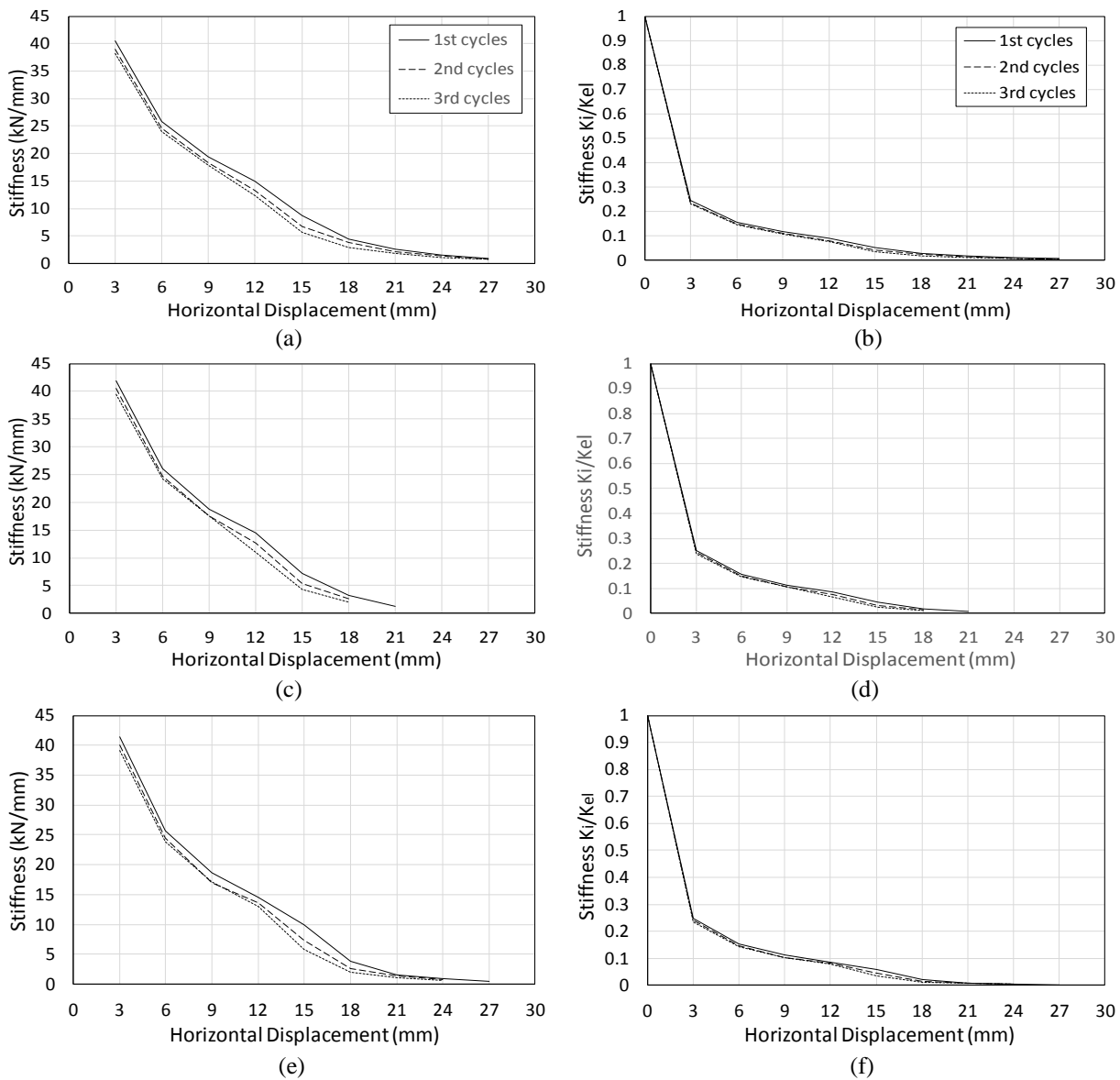


Figure 7-25: Lateral displacement secant stiffness for (a, b) SC\_1, (c, d) SC\_2, and (e, f) SC\_3 in (left) absolute and (right) relative terms.

Therefore, it becomes clear that if an element is to be deformed into its post-peak range (or even at moderate displacements in the pre-peak range), a conventional elastic stiffness – even 50% – could not represent its actual response adequately; it would greatly overestimate its resistance for any given displacement.

## 7.7 ENERGY DISSIPATION

Energy dissipation is an attribute of paramount importance for the seismic response of structures. Herein the energy dissipated throughout each test is calculated and compared to each other. It is calculated as the area of the hysteretic loops and it is presented in Figure 7-26 for every specimen.

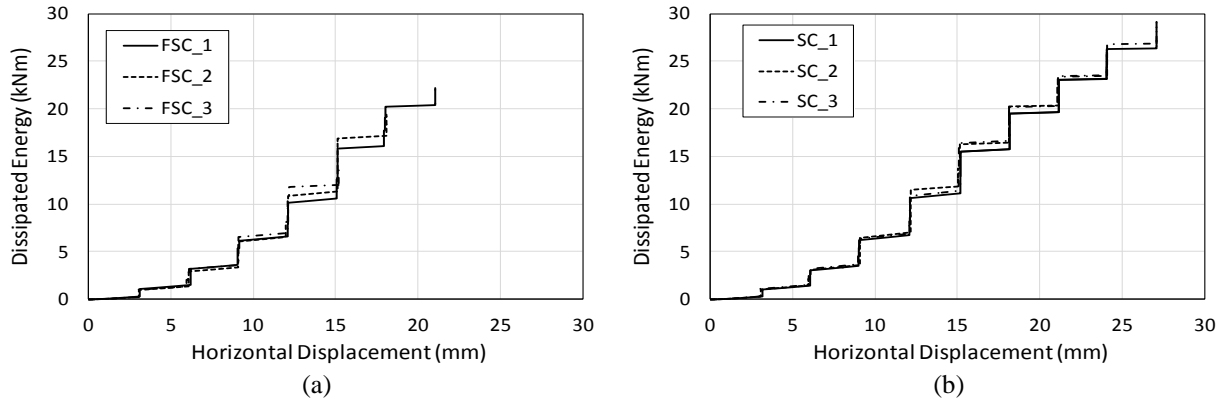


Figure 7-26: Cumulative dissipated energy against displacement level for (a) FSC, and (b) SC specimens.

SC specimens are found to dissipate more energy than the FSC ones, cumulatively. This is not a surprise, as they were found to have higher displacement capacity as well as higher resistance. The difference is caused by the significant increase of longitudinal reinforcement, counteracting the slight decrease of transverse reinforcement.

Nonetheless, all the specimens seem to be on a par with each other throughout the loading history, so they are found to dissipate roughly the same amount of energy up to any given point. For example, they all attain the same dissipated energy at the onset of shear failure (i.e. about 7kNm), except for SC\_3 that fails at 15 mm, reaching just above 11 kNm. The energy at the onset of axial failure, however, is quite different for each specimen, largely depending on the displacement at which failure took place.

Last but not least, the rate of energy dissipation is found to increase after +6 mm, when more plastic deformations start concentrating, dissipating more hysteretic energy. They tend to slightly decrease again after +21 mm, due to the extreme strength degradation, leading to very narrow loops.

## 7.8 LASH

Lash comprises the sum of all horizontal displacements that are not due to the column deformation itself. These have often been recorded as part of the column deformations, leading to an ostensibly more flexible element. Typical examples of such displacements are the sliding

of the base on the strong floor (or sub-base in this particular case), elastic bending of the reaction frame or displacement of the bolts due to inadequate tightening onto the plates.

Attempts were made to preclude lash as much as possible from measurements, thus it is defined as the difference between what the internal LVDT of the actuator and the external draw-wire sensor record. Of course, it is possible that there are more sources that have not been eliminated, e.g. the differential application of force resulting in a slight force asymmetry (see section 7.2) or base rotations (see section 7.4).

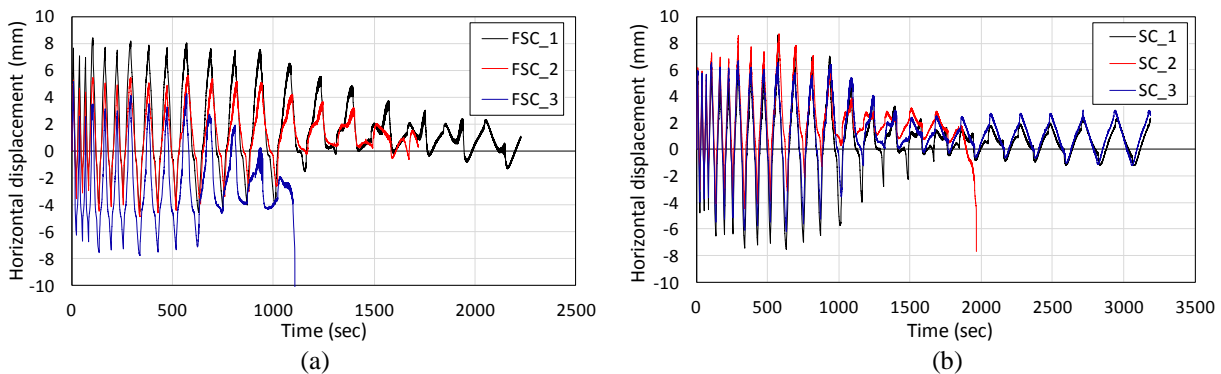


Figure 7-27: Recorded lash throughout experiments of (a) FSC, and (b) SC specimens.

Based on Figure 7-27, it is observed that the lash is very significant in all specimens, reaching values of more than  $\pm 8$  mm in the first 9-12 cycles, i.e. up to horizontal displacement levels of  $\pm 9$  mm to  $\pm 12$  mm. This means that during many cycles lash is even higher than the actual recorded horizontal displacement. For instance, at a peak of  $+3$  mm, the lash can be  $+6$  mm, meaning that if the internal LVDT was taken into account, the force actually recorded for the first peak would be recorded for the first peak of the displacement level of  $+9$  mm, i.e. the elements would reach 120-130 kN resistance and yield at the latter displacement level, giving an unrealistic picture of the element's response.

A really interesting trend observed in all experiments is that the lash decreases considerably after about 1000 sec, i.e. at a horizontal displacement level of about  $\pm 15$  mm. This can be explained taking into account the nature of lash. A big part of it comes from elastic deformation of other parts of the system besides the column, e.g. the reaction frame whereupon the actuators are supported. Around  $\pm 15$  mm of horizontal displacement, the specimens have already entered the post-peak domain and their stiffness has degraded so much that the acting force is much lower than in the cycles of the first displacement level. Therefore, the elastic deformations produced by other parts of the system do decrease proportionally.

Another interesting pattern is the asymmetrical distribution of lash after a specific point. In the overwhelming majority of specimens (i.e. all of them, except FSC\_3 that has a negative-skewed lash from the beginning of the test), the lash tends to concentrate invariably on the positive side

towards the end of the experiment. The positive side corresponds to pulling of the actuator. This might be due to slight untightening of the bolts during the test due to very high forces acting upon them, which leads to some lash produced when pulling the column. Of course, no bolt is involved when pushing, and since the acting force is so low, the lash on the negative side is negligible.

It is observed that in the end of the lash time-series of FSC\_3 and SC\_2 (two out of the three specimens that failed axially), a sudden drop to the negative side occurs. This corresponds to the onset of axial failure and the sudden increase of vertical deformations.

## 7.9 REPEATABILITY

The issue of repeatability is well-established and widely discussed in many science and engineering disciplines, including structural engineering. However, performing multiple tests is not the norm, particularly in large-scale experiments like the ones herein presented, where restrictions pertinent to time and other resources can be prohibitive.

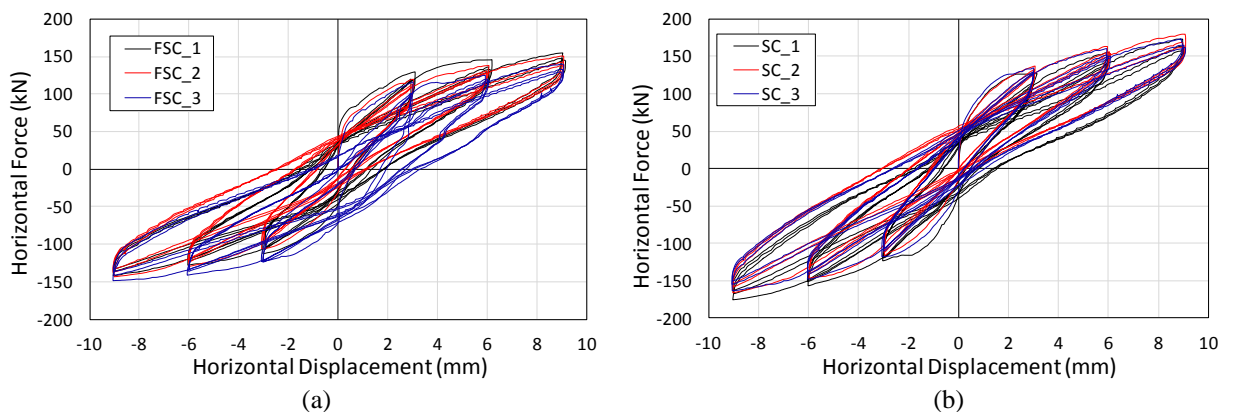


Figure 7-28: Comparison of the first 9 cycles of the (a) FSC, and (b) SC specimens.

In this series, although not having replicated the experiments per se, the first 9 cycles of each set of specimens are in effect “identical” in all respects. They are shown in Figure 7-28. As expected, the overall responses are quite similar. However, there are many slight differences in the curves produced. For example, the strength reached at each cycle is almost always different in the three specimens. A pronounced discrepancy is observed at the unloading stiffness on the positive side (pull) as well as the reloading stiffness on the negative side (push) of the FSC specimens, wherein FSC\_3 has a much stiffer response than the other two. These can be attributed to different concrete strength, as discussed previously (section 6.6), slight geometric deviations in the way the concrete cage was constructed or how it was positioned in the formwork and perhaps differences in the lash included in the results, due to different tightening of the bolts of each specimen.

Furthermore, the actual member-level response is the result of a plethora of events taking place at micro-level, the random nature of which would lead even the most “identical” specimens to have differences when inspected at a macro-level. Therefore, the common reference to specimens as “identical” when they belong to the same experimental series and have been identically designed is actually a fallacy. An appropriate way to refer to them could be “nominally identical” (e.g. Henkhaus *et al.*, 2013), as in reality they can only be similar in their behaviour, but not identical.

### 7.10 EFFECT OF VERTICAL LOAD VARIATION

Figure 7-29a shows the experimentally obtained descending branch slope values of each specimen, for both experimental series. Figure 7-29b shows the former compared to the ones calculated using Eq. 4-7 and the design and material characteristics of each specimen; in the case of variable axial load, the slope values have been calculated both with the initial axial load (‘predicted – low’) and with the latter one (‘predicted – high’).

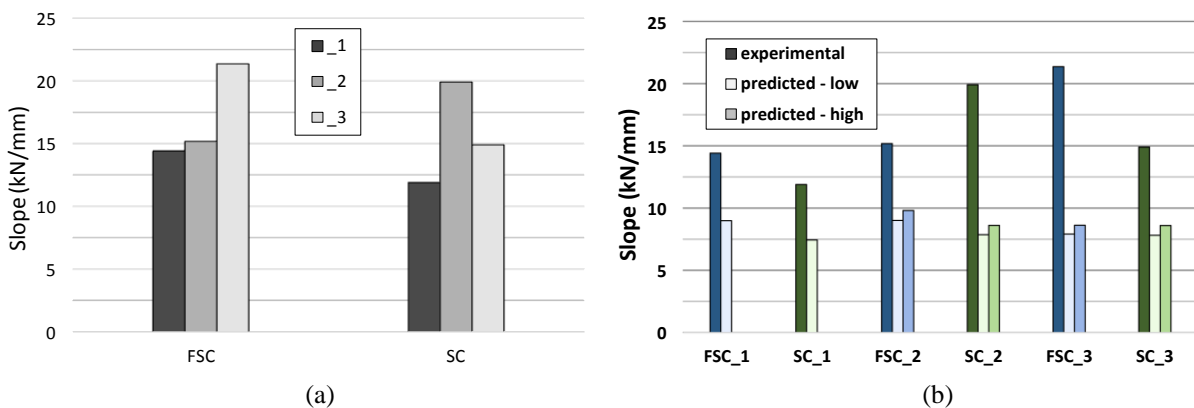


Figure 7-29: (a) Experimentally obtained descending branch slopes of FSC and SC specimens. (b) Comparison of experimentally obtained against analytically predicted descending branch slopes of each specimen.

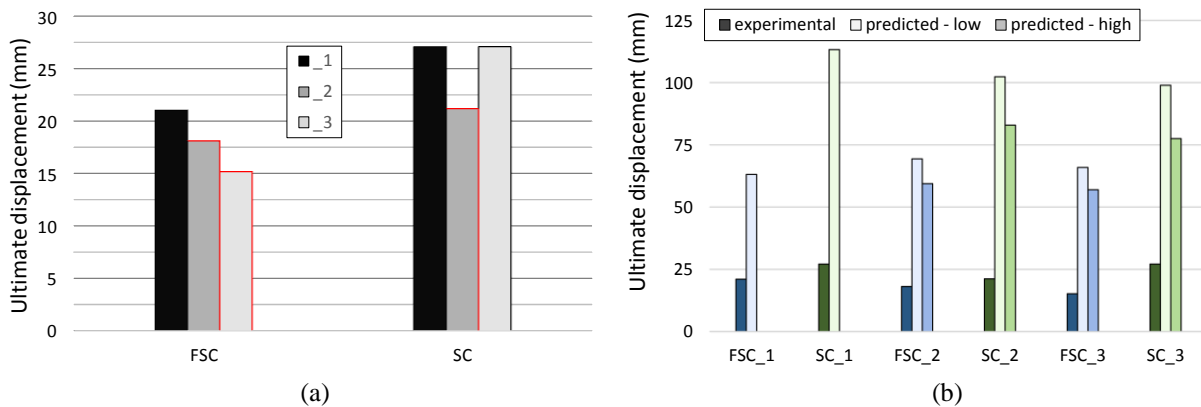


Figure 7-30: (a) Ultimate horizontal displacement reached by each specimen. (b) Comparison of experimentally obtained and predicted values of ultimate horizontal displacement.

It is clear that increasing the axial load leads to higher degradation rate in the post-peak range. All specimens' descending slopes are steeper than the reference ones (Figure 7-29a). In Figure 7-29b, evidently all of the slopes are slightly underestimated by Eq. 4-10, with the reference specimens, FSC\_2 and SC\_3 (taking into account the prediction with higher axial load) not being very far off the prediction. However, the other two are way higher than expected. It is interesting that the difference between the low- and high-axial-load-predictions seems to be quite low, while the actual difference between the reference specimens and the ones with increased axial load is much higher. It would suggest that either (1) the effect of the axial load has been underestimated in the proposed relationships, or (2) the application of higher axial load in or just before the post-peak range has a more detrimental effect on the strength degradation rate than the application of constant axial load from the beginning of the test.

The only exception is FSC\_2 that is almost equal to FSC\_1, partly due to having a higher strength concrete than FSC\_1, compensating for the increase of the slope owing to the increased applied axial load.

The ultimate horizontal displacement achieved by each specimen is presented in Figure 7-30a. The specimens that failed axially are outlined in red. This means that the ones that didn't were stopped because their lateral force had declined significantly, but did not lose their axial load-bearing capacity. So, this is a lower limit on their deformability with regard to axial load-bearing capacity; in other words they might actually be able to support their axial load for even larger lateral displacements.

FSC\_1 with low constant axial load is cycled up to +/- 21 mm without losing its vertical load-bearing capacity. FSC\_2 and FSC\_3 with the increased axial load lose it way before that, reaching an ultimate displacement at the onset of axial failure of +/- 18 mm and +/- 15 mm, respectively. In this series, increasing the load after the peak is reached led to the axial capacity being lost sooner than increasing it before the peak.

In the SC series, the axial load in both specimens (SC\_2 and SC\_3) was increased before the peak; as commented in section 7.2, this was not the initial intention and it was caused by SC\_3's increased displacement at the onset of shear failure (compared with all the other specimens), which was not expected, as explained in section 7.2. SC\_2 was led to much lower deformability than SC\_1, i.e. +/- 21 mm instead of +/- 27 mm, while SC\_3 achieved the same displacement as SC\_1 whose axial load was kept constant; however, it was much closer to axial failure than the reference specimen, reaching a vertical displacement of - 5.6 mm as contrasted to the - 2.8 mm of SC\_1. Judging from the trend of the vertical responses, SC\_3 would fail axially before completing the three cycles at +/- 27 mm, while SC\_1 managed to complete all of them with

very low axial displacement, thus not nearing the onset of axial failure. The comparison of SC\_2's and SC\_3's deformability leads to unexpected results, since the latter has a lower concrete strength and would in theory be expected to fail axially sooner than the former.

In Figure 7-30b, Eq. 4-16 was used to predict the displacement at the onset of axial failure, using both the initial and the increased axial load. All specimens' displacement capacity is overpredicted, in line with the aforementioned underprediction of the descending branch slope. This is because these are specimens with rather high longitudinal reinforcement index and low axial load ratio (see Eq. 4-16 and Figure 4-16), thus expected to reach much higher deformations based on the database. This highlights the importance of supplementing the existing experimental literature on post-peak response with tests on specimens with design characteristics not existing in the current literature, so as to obtain even more reliable empirical relationships.

In conclusion, the clear conclusion is that the increase of axial load before or just after the onset of shear failure is reached leads to higher strength degradation rate and lower ultimate displacement. No difference between the application of the load before or after the onset has been detected, however there were only three and one such specimens, respectively. More similar experiments would be required to get a bigger sample and a clearer idea as to how exactly these quantities are affected.

## PART III: BEAM-COLUMN ANALYTICAL MODEL



# Chapter 8: DESCRIPTION AND IMPLEMENTATION OF ANALYTICAL MODEL

## 8.1 HYSTERETIC SHEAR MODEL

The hysteretic shear model is based on the one proposed by Mergos & Kappos (2012), which is an extension of the originally proposed model by Ozcebe & Saatcioglu (1989) and has been shown to fare satisfactorily as to the shear response of sub-standard R/C members. It is formulated in terms of shear force,  $V$ , against shear distortion,  $\gamma$ , at section level and comprises of the  $V$ - $\gamma$  backbone curve and the hysteresis rules determining the response under cyclic loading. Its primary  $V$ - $\gamma$  backbone curve is defined disregarding interaction with flexure and can be used for elements that have not yielded in flexure, as well as for the elastic regions of members that have developed flexural yielding (Figure 8-1). The ascending part of this curve is defined by the shear cracking point where the nominal tensile principal stress exceeds the tensile concrete strength ( $\gamma_{cr}$ ,  $V_{cr}$ ), the onset of yielding of the transverse reinforcement, where the maximum shear strength is attained ( $\gamma_{st}$ ,  $V_{max}$ ), and a plateau, where shear strains increase up to the onset of initiation of lateral strength degradation, i.e. the onset of shear failure ( $\gamma_{sh,f}$ ,  $V_{max}$ ). Expressions for each of the above quantities have been proposed by Mergos & Kappos (2012); the shear strength is based on the Priestley *et al.* (1994) model with conservative assumptions, as it was found to be unconservative in the specimens examined herein, which have insufficient transverse reinforcement.

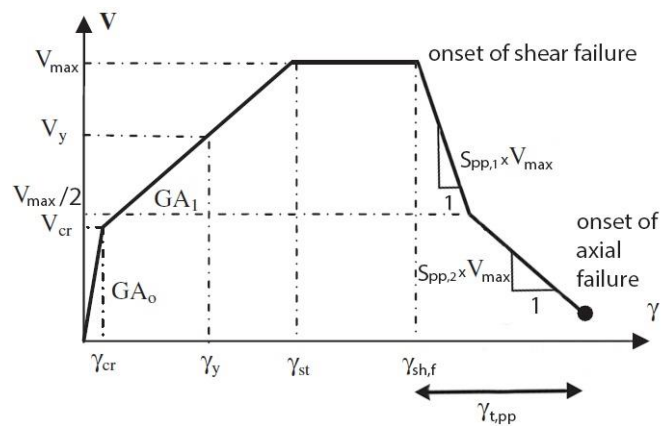


Figure 8-1:  $V$ - $\gamma$  primary curve of the proposed shear model (without shear-flexure interaction).

The ascending primary  $V$ - $\gamma$  curve is modified in plastic hinge regions of flexure-shear critical elements to account for shear-flexure interaction, resulting in a decrease of the shear capacity simultaneously with significant increase of the shear flexibility (Figure 8-2C). This is based on the curvature ductility demand and the ensuing degradation of the “concrete contribution” to shear strength, based on the Priestley *et al.* (1994) model (Figure 8-2a), resulting in an increase of the shear reinforcement contribution (Figure 8-2b) (Mergos & Kappos, 2008; 2012). The parts of the

backbone curve between the shear force corresponding to flexural yielding ( $\gamma_y, V_y$  in Figure 8-1) and the onset of shear failure ( $\gamma_{sh,f}, V_{max}$ ) are affected as Figure 8-2c shows, when shear-flexure interaction is considered.

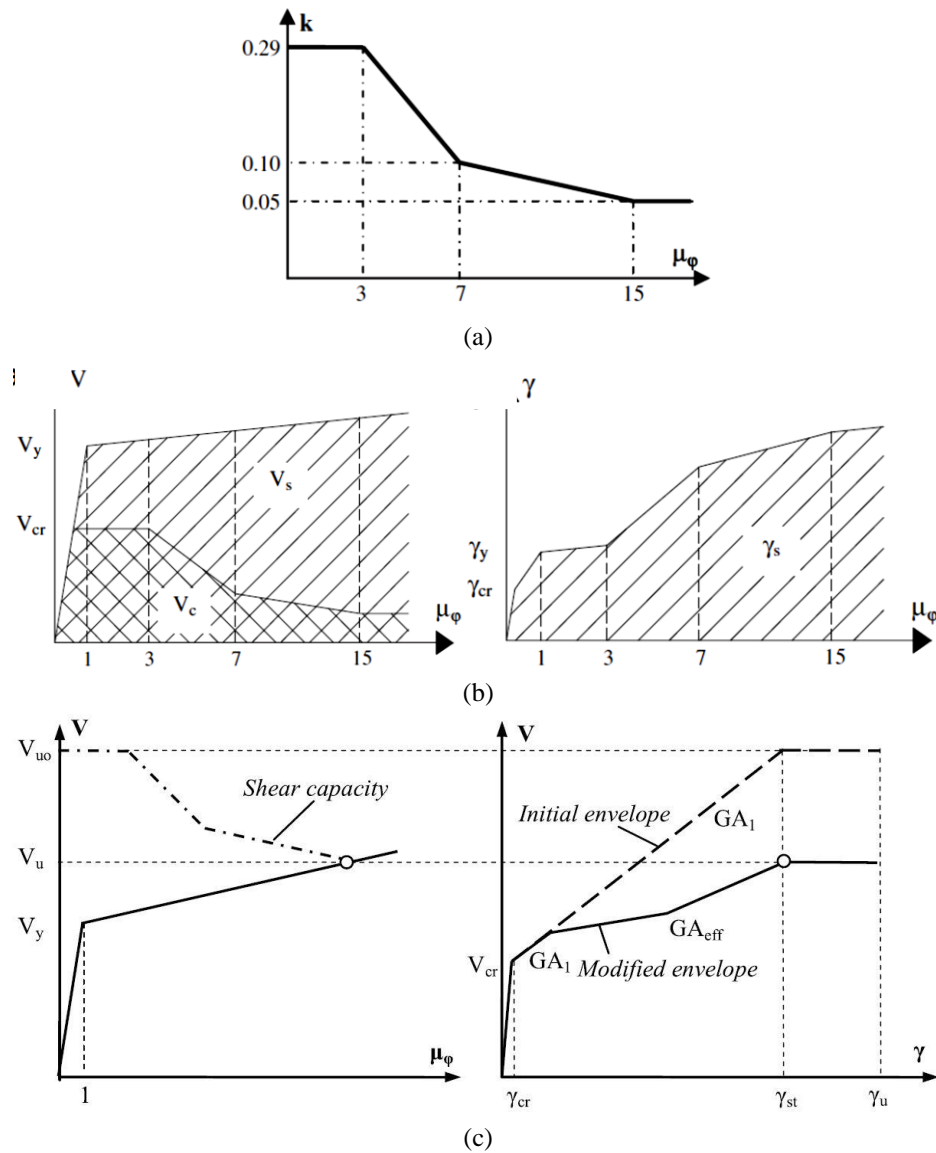


Figure 8-2: (a) Relationship between curvature ductility demand and strength of concrete shear resisting mechanisms (Mergos & Kappos, 2012). (b) Variation of shear resisting mechanisms (strut mechanism lumped with concrete mechanism); shear strain after shear cracking with curvature ductility demand in plastic hinge regions of R/C members (Mergos & Kappos, 2012). (c) Flexural primary curve and shear capacity in terms of member shear force and curvature ductility demand of the critical cross-section (left); shear ( $V$ - $\gamma$ ) primary curve before and after modelling shear-flexure (right) (Mergos & Kappos, 2013b).

After the onset of shear failure is reached, a bi-linear descending branch is followed. It includes a breaking point at half the maximum strength and is defined by the slopes of the two linear segments  $S_{pp,1} \times V_{max}$  (Eq. 4-9 to 4-11) and  $S_{pp,2} \times V_{max}$  (Eq. 4-12 to 4-14), respectively (Figure 8-1). This shape is chosen herein due to its simplicity and satisfactory correlation with the recorded experimental post-peak responses, as already demonstrated in section 4. Using two independent branches in the descending part, the resulting response can approximate linear,

concave or convex responses, encompassing different potential descending branch shapes, hence making the model more versatile and powerful. Furthermore, it can readily accommodate a linear descending branch (Eq. 4-6 to 4-8) by setting the slope of the second branch equal to the slope of the first.

The descending branch is terminated at the point of onset of axial failure, where physical collapse of the member initiates. The definition of the onset of axial failure in this study is both deformation-based and force-based. Specifically, a column is considered to have failed axially (i.e. lost its bearing capacity), if the shear deformation limit corresponding to the onset of axial failure has been reached (Figure 8-1). This deformation limit is equal to  $\gamma_{sh,f}$  plus the post-peak shear distortion up to the onset of axial failure,  $\gamma_{t,pp}$  (Eq. 4-16). However, if the shear resistance degrades to zero before this critical deformation is reached, the onset of axial failure is the point where the descending branch meets the axis of shear deformations (point on the descending branch with zero shear strength), i.e. the shear resistance is not allowed to assume negative values.

As described in chapter 6, when a column reaches the onset of axial failure, a fraction of the vertical load previously carried by it is subsequently redistributed to neighbouring vertical elements through adjacent horizontal members. During this vertical load redistribution, the axial load of the failing member is greatly reduced, while that in the neighbouring members is substantially increased. Axial load increase just before or after the onset of shear failure was found to lead to higher post-peak strength degradation rate and lower displacement at the onset of axial failure (see section 7.11). Axial load decrease in the post-peak domain, on the other hand, seems to lead to a lower strength degradation rate and a higher displacement at the onset of axial failure. Moreover, the greater the decrease and the sooner it takes place, the higher the ultimate displacement, while no significant effect on the descending branch slope was detected (Nakamura & Yoshimura, 2014).

Based on the limited existing experimental evidence, the proposed model is developed so as to take into account the effect of axial load variation on the lateral post-peak hysteretic response. The post-peak part of the response can take into account variable axial load during the analysis, using Eq. 4-6 to 4-16 as a basis to estimate the variation on the post-peak shear strength degradation rate and the shear deformation at the onset of axial failure. Hence, when an axial load variation is detected during the analysis, the aforementioned post-peak parameters change, reflecting the effect of axial load variation on the response.

As for the point of axial load change, it is herein appreciated that it does lead to different response, depending on how soon or late into the post-peak response the change happens,

according to Nakamura & Yoshimura's (2014) work. Nonetheless, it is not possible to reliably take this effect into account at this stage. Further investigations would be required to define exactly how this point influences the post-peak response.

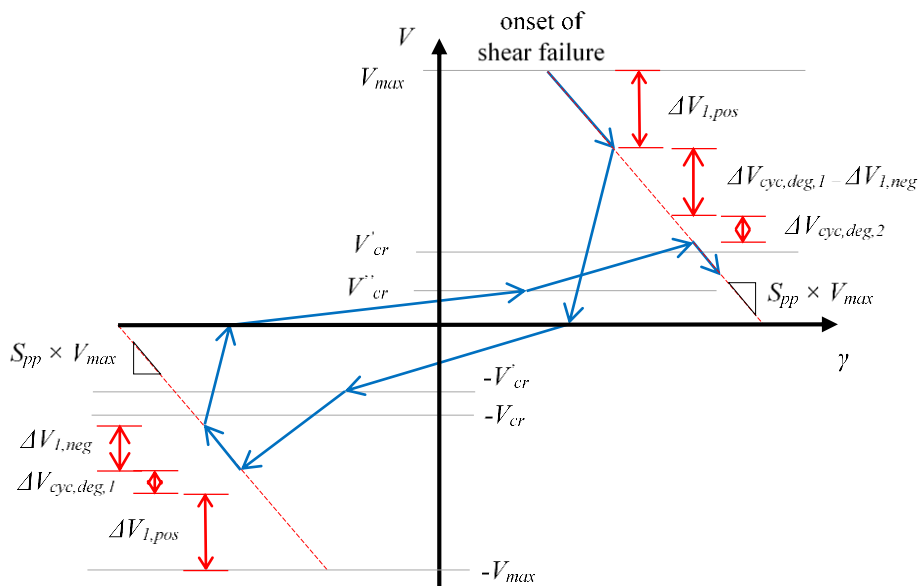


Figure 8-3: Hysteresis rules after the onset of shear failure.

The hysteresis rules adopted in the pre-peak domain of the shear model are based on those proposed by Ozcebe & Saatcioglu (1989), with several improvements introduced by Mergos & Kappos (2008; 2012) for numerical stability in dynamic analysis, as these rules were not originally developed explicitly for use in dynamic analysis for seismic loading. Pinching, unloading and reloading stiffness deterioration, as well as cyclic strength degradation, are accounted for.

In the post-peak domain, the same hysteretic model is adopted as a starting point. However, it was not developed explicitly for the post-peak response, but rather for the pre-peak. Therefore, some modifications are herein proposed, to make the hysteretic rules compatible with the response of specimens after the onset of shear failure. A calibration of the post-peak hysteretic rules based on experimental post-peak response data would be a worthwhile future endeavour, in order to further improve the prediction accuracy of the proposed model.

The hysteretic rules are shown in Figure 8-3, showing only the linear descending branch case, for the sake of simplicity;  $\Delta V_{1,pos}$  and  $\Delta V_{1,neg}$  denote in-cycle strength degradation in the positive or negative direction, respectively;  $\Delta V_{cyc,deg,i}$  ( $i=1,2$ ) denotes cyclic strength degradation. In-cycle strength degradation follows the aforementioned backbone descending branch(es), for instance  $S_{pp} \times V_{max}$  in Figure 8-3. Post-peak cyclic degradation is accounted for as in Ozcebe & Saatcioglu (1989), in line with the calibration of the post-peak descending branch (section 4), i.e. the end

reloading point lies on at the intersection with the descending branch (Figure 8-3) and, subsequently, the response follows the descending branch.

Pinching and reloading stiffness deterioration are accounted for using a bilinear reloading curve as in the pre-peak domain (Ozcebe & Saatcioglu, 1989; Mergos & Kappos, 2008). Nonetheless, the shear cracking strength,  $V_{cr}$ , which is the ordinate of the end point of the first reloading branch, degrades, unlike in the pre-peak domain. Its degradation is proportional to the degradation of the end point of the second reloading branch (e.g.  $V_{cr}$  and  $V'_{cr}$  in proportion to  $V_{max}$  and  $V_{max} - \Delta V_{1,pos} - \Delta V_{cyc,deg,1}$  in Figure 8-3). Were it not degrading, an end point of the second reloading branch with strength lower than the shear cracking strength would inevitably appear, leading to a negative stiffness of the second reloading branch, hence numerical instability. Unloading follows a linear branch with the same stiffness deterioration rules as in the pre-peak domain (Mergos & Kappos, 2008).

Shear strength degradation mirroring is also taken into account; this effectively means that once a certain amount of strength is lost in one loading direction, a higher strength cannot be reached in the other. For example, in Figure 8-3, the descent starts from the onset of shear failure with  $V_{max}$  on the positive side, followed by  $\Delta V_{1,pos}$  in-cycle degradation. The strength of the vertex point on the negative direction becomes  $-(V_{max} - \Delta V_{1,pos} - \Delta V_{cyc,deg,1})$ . Similarly, the in-cycle degradation on the negative side ( $\Delta V_{1,neg}$ ) is subtracted from the positive vertex point strength upon reloading on the positive side for the first time, and so forth. This assumption has been adopted in other similar models (e.g. LeBorgne & Ghannoum, 2013) and is supported by experimental evidence, for instance, specimens B1 and B4 (Henkhaus *et al.*, 2013) as well as Specimen-1 (Sezen & Moehle, 2006). One has to bear in mind the difference between the actual loss of strength, be it from cyclic or in-cycle degradation, and the ostensible loss of strength that arises from reloading stiffness deterioration and is sometimes confused with actual strength degradation; the latter is not included in shear strength degradation mirroring.

## 8.2 BEAM-COLUMN MODEL FORMULATION

A beam-column that can explicitly capture flexure, shear, and bond-slip deformations, while accounting for the interaction between flexural and shear deformations in the potential plastic hinges of substandard R/C members is herein needed. The spread of inelasticity of flexural deformations has to be taken into account, of course, but more importantly the shear inelasticity spread has to be accounted for, so as to align with the underlying assumptions of the afore-developed local shear hysteresis model. The phenomenological, force-based, spread inelasticity beam-column model by Mergos & Kappos (2012) is herein selected as the basis to model the response of shear deficient R/C members; it combines the aforementioned features with

computational efficiency – much needed in cases of dynamic non-linear analysis of entire R/C structures including the post-peak domain.

It is composed of three sub-elements accounting for flexural, shear and anchorage-slip deformations (Figure 8-4). The sub-elements are connected in series, hence the element flexibility matrix ( $F$ ) is produced by the summation of the flexibility matrices of the flexural ( $F^f$ ), shear ( $F^{sh}$ ) and anchorage-slip ( $F^{sl}$ ) sub-elements and its inversion results in the element stiffness matrix  $K$ , which in turn relates the bending moment increments at the ends of the flexible part of the element to its incremental rotations (Figure 8-4):

$$K = F^{-1} = (F^f + F^{sh} + F^{sl})^{-1} \quad (8-1)$$

$$\begin{bmatrix} \Delta M_A \\ \Delta M_B \end{bmatrix} = K \times \begin{bmatrix} \Delta \theta_A \\ \Delta \theta_B \end{bmatrix} \quad (8-2)$$

The flexural sub-element (Figure 8-4c) is divided into an ‘elastic’ intermediate region with stiffness equal to the stiffness of the first branch (secant stiffness at yield) of the flexural bilinear primary curve (Figure 8-5a) and two end regions, where flexural yielding takes place. A spread inelasticity model is employed to follow the gradual inward penetration of flexural yielding from the ends of each sub-element, based on the distribution of bending moments and the loading history; regarding the latter, the length of each plastic hinge cannot become shorter than its previously reached maximum value, in other words this length can never decrease from one analysis step to the next. This model distinguishes between loading and unloading or reloading states, leading to a uniform stiffness distribution in the plastic hinge in the former and a linearly varying stiffness distribution in the latter, with the minimum value at the end section and the maximum being equal to the elastic stiffness at the end neighbouring the elastic region. Both linearly varying bending moment distribution as well as parabolic, e.g. due to the presence of gravity loads on beams, can be taken into account when calculating the plastic hinge lengths (Mergos & Kappos, 2013a).

The flexural sub-element’s primary curve in terms of bending moment against curvature ( $M-\varphi$ ) is based on standard flexural analysis with appropriate bilinearisation of the resulting curve, so that the stiffness of the first branch of the bilinear curve is equal to the secant stiffness at first yield of the longitudinal reinforcement, the area enclosed by the bilinear curve is equal to the area enclosed by the initial  $M-\varphi$  curve, and the stiffness of the second branch is positive. The rules followed for unloading are based on the model proposed by Sivaselvan & Reinhorn (1999) adjusted for mild stiffness degradation, setting the unloading parameter equal to 15 (Mergos & Kappos, 2012), as shown in Figure 8-5a. Reloading is vertex-point oriented, i.e. the end-point of

the reloading branch is the point of maximum excursion in the opposite side of the response. Stiffness degradation during unloading and reloading as well as non-symmetric response are accounted for in this flexural hysteretic model, hence making it also suitable for R/C T-beams.

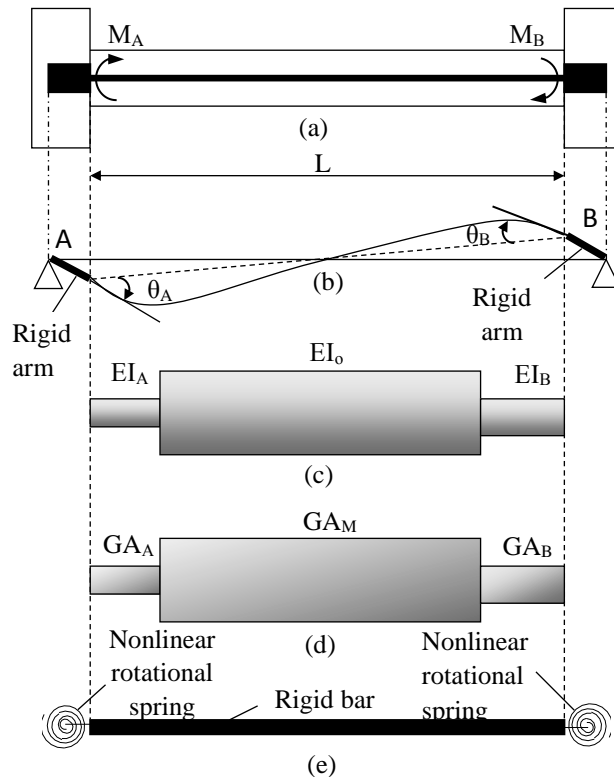


Figure 8-4: Finite element model: (a) geometry of R/C member; (b) beam–column finite element with rigid offsets; (c) flexural sub-element; (d) shear sub-element; (e) anchorage slip sub-element. (Mergos & Kappos 2012)

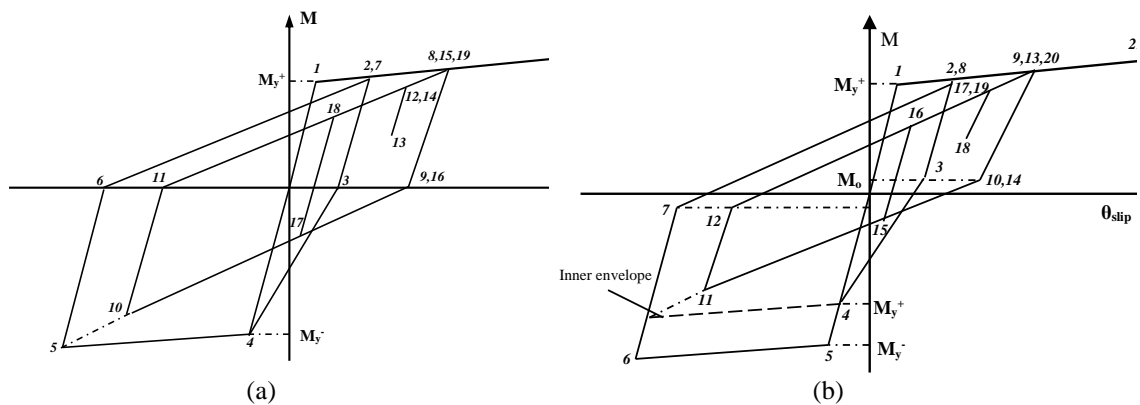


Figure 8-5: (a) Flexural ( $M-\phi$ ) hysteretic model and (b) anchorage slip ( $M-\theta_{slip}$ ) hysteretic model. (Mergos & Kappos 2013b)

The anchorage slip sub-element represents the rotations arising at the interfaces of adjacent R/C members, due to slippage of the reinforcement anchorage in the joints, resulting from bond deterioration. The anchorage slip sub-element (Figure 8-4e) consists of two concentrated springs at the ends of the element, connected by a rigid bar, hence adding flexibility in the respective end, with its off-diagonal terms being zero (Mergos & Kappos, 2012). Its primary

curve in terms of bending moment vs. end rotations ( $M-\vartheta_{slip}$ ) is derived for each level of bending moment acting at the element end assuming uniform bond stress along the various segments of the anchored bar – elastic, strain-hardening and pull-out cone regions –, calculating the steel stress and strain distributions along the anchorage length (Figure 8-6), hence computing the slippage via integration of the strains and the subsequent fixed-end rotation (Mergos & Kappos 2012); the resulting curve is subsequently appropriately bilinearised, so that the stiffness of the first branch of the bilinear curve is equal to the secant stiffness at first yield of the longitudinal reinforcement, the area enclosed by the bilinear curve is equal to the area enclosed by the initial  $M-\vartheta_{slip}$  curve, the ultimate point ( $M_u, \vartheta_{u,slip}$ ) is placed so that the correct failure mode dominates (depending on whether flexural or bond-slip failure is expected from the preceding analyses) and the stiffness of the second branch is positive. The various symbols used in Figure 8-6 can be found in Mergos and Kappos, 2012. The hysteretic rules used are based on the model proposed by Saatcioglu *et al.* (1992), as shown in Figure 8-5b.

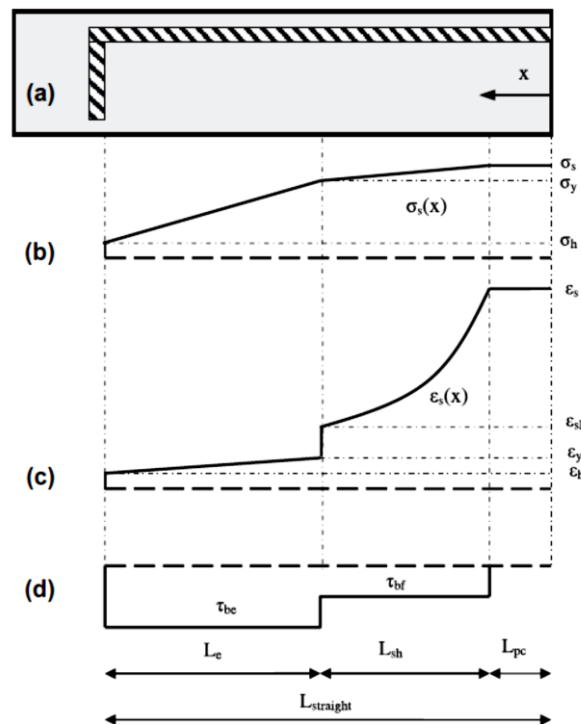


Figure 8-6: (a) Reinforcing bar with 90° hook embedded in concrete; (b) steel stress distribution; (c) strain distribution; (d) bond stress distribution. (Mergos & Kappos 2012)

Prior to the onset of shear failure, the shear sub-element has a flexibility distribution similar to the flexural sub-element (Figure 8-4d). Shear-flexure interaction is considered in its inelastic end regions, the lengths of which are set equal to the lengths of the respective regions of the flexural sub-element, so long as the shear demand is constant along the element length; otherwise, they may be different, dependent upon the shear force distribution. The shear flexibility matrix coefficients in the case of uniform stiffness distributions at the inelastic regions are as follows, applying the principle of virtual work (Mergos & Kappos, 2012):

$$f_{ij}^{sh} = \frac{a_{As}}{GA_A \times L} + \frac{1 - a_{As} - a_{Bs}}{GA_M \times L} + \frac{a_{Bs}}{GA_B \times L} \quad (8-3)$$

where  $i, j = A, B$ , i.e. the two ends of the element;  $a_{As}$  and  $a_{Bs}$  are defined as the yield penetration coefficients (Figure 8-7), which monitor the penetration of flexural yielding from the end  $A$  or  $B$ , respectively, towards the middle of the element;  $GA_A$ ,  $GA_B$  and  $GA_M$  are the corresponding shear rigidities of end  $A$ , end  $B$ , and the middle segment sections of the element;  $L$  is the element clear length.

Upon initiation of shear failure, localisation of shear strains is captured by setting the length of the region, wherein shear failure is detected, equal to the shear critical length  $L_{cr}$ . In line with experimental evidence that the shear failure plane in a given R/C member is practically always unique, the model invariably results in only one segment failing. For members where flexural yielding has developed prior to the onset of shear failure, the latter is expected to develop at either member end owing to the degradation of shear strength with inelastic flexural deformations, provided that the shear demand is constant along the length of the member. For members failing in shear without yielding in flexure, it is assumed that shear failure occurs in the middle region of the element, based on experimental evidence (e.g. Yoshimura *et al.*, 2003, see chapter 2). In Figure 8-7, the transition from pre-peak to post-peak regime for the generic cases of a flexure-shear and a shear critical specimen can be seen. The post-peak shear flexibility matrix coefficients – again, for the case of uniform stiffness distribution at both ends – with failure at the end  $A$ , in the middle of the element and at the end  $B$ , respectively, are as follows:

$$f_{ij}^{sh} = \frac{L_{cr}}{GA_A \times L^2} + \frac{1 - L_{cr}/L - a_{Bs}}{GA_M \times L} + \frac{a_{Bs}}{GA_B \times L} \quad (8-4)$$

$$f_{ij}^{sh} = \frac{1 - L_{cr}/L}{2 \times GA_A \times L} + \frac{L_{cr}}{GA_M \times L^2} + \frac{1 - L_{cr}/L}{2 \times GA_B \times L} \quad (8-5)$$

$$f_{ij}^{sh} = \frac{a_{As}}{GA_A \times L} + \frac{1 - a_{As} - L_{cr}/L}{GA_M \times L} + \frac{L_{cr}}{GA_B \times L^2} \quad (8-6)$$

Outside the critical shear length, only the pre-peak part of the previously described shear hysteretic model is applied. The pre-peak backbone curve modified for shear-flexure interaction is used in the regions that have yielded in flexure, and the primary backbone curve for the rest of the element. Inside the critical shear length, the local, post-peak shear hysteretic model (section 8.1) is applied. It is noted that this hysteretic model has been calibrated in terms of

average post-peak shear strains within  $L_{cr}$ . Therefore, following this approach, the distribution of shear deformations along the member before and after the onset of shear failure, as well as the location and extent of post-peak shear damage are predicted in an accurate and objective manner. Furthermore, by considering the interaction of inelastic flexural and shear deformations at a local level, the proposed approach does not rely on assumptions regarding the bending moment distribution, hence the actual phenomenon is more objectively captured.

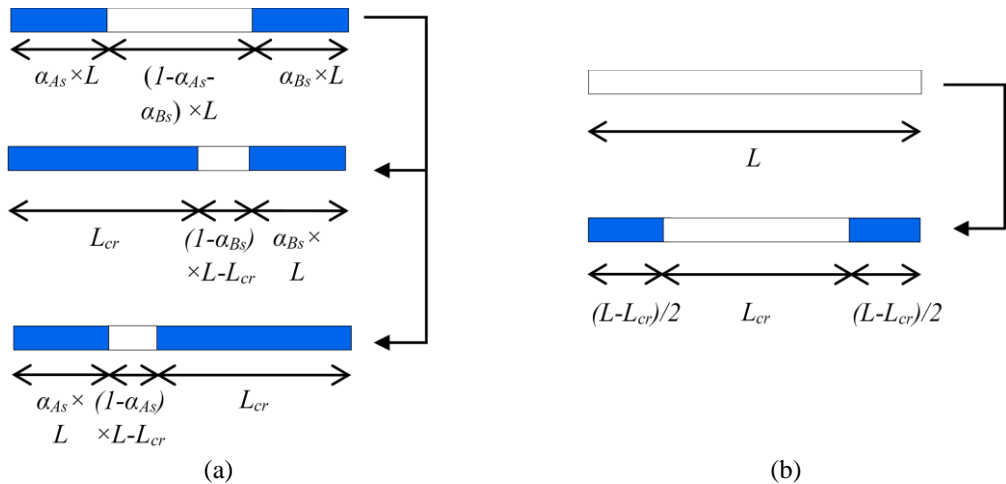


Figure 8-7: Spread inelasticity transition upon initiation of shear failure for: (a) a flexure-shear critical specimen, and (b) a shear critical specimen.

The beam-column element can model flexural failure, if the ultimate curvature limit is reached, anchorage failure, if the ultimate longitudinal bar slippage is reached, and shear failure followed by axial failure, which is both deformation-based and force-based as explained in section 8.1.

### 8.3 SOFTWARE IMPLEMENTATION

The beam-column model has been implemented in the general finite element program for inelastic dynamic analysis of structures [IDARC 2D v. 7.0](#) (Reinhorn *et al.* 2009; Valles *et al.* 1996). All the procedures described in the following paragraphs aim at numerically implementing the above proposed hysteretic beam-column model – more importantly, the shear sub-component – in [IDARC 2D v. 7.0](#).

The prescribed post-peak  $V$ - $\gamma$  descending branches (Eq. 4-6 to Eq. 4-14) are followed subsequent to the onset of shear failure in the failed segment of the shear sub-element. This is realised by a commensurate drop in the current force, the yield strength, as well as the entire post-yield branch of the shear backbone, as shown schematically in Figure 8-8 with a linear descending branch, for the sake of clarity (the program can also handle bilinear descending branches, in line with the hysteretic model presented in section 8.1). This way, the stiffness is always positive, hence no negative term can end up in the stiffness matrix, hence no instability occurs in the solution (note that IDARC cannot handle negative values of stiffness). The amount of strength

degradation ( $\Delta V_i$  with  $i=1,2\dots$ ) at each solution step equals the ‘over-shooting’ of strength at the same step with respect to the strength of the target post-peak backbone branch with the same shear strain (see Figure 8-8). The strength degradation of each step is then applied in the next loading step as part of the “unbalanced forces”. Figure 8-9 details the algorithmic procedure followed to apply said shear force degradation at each analysis step.

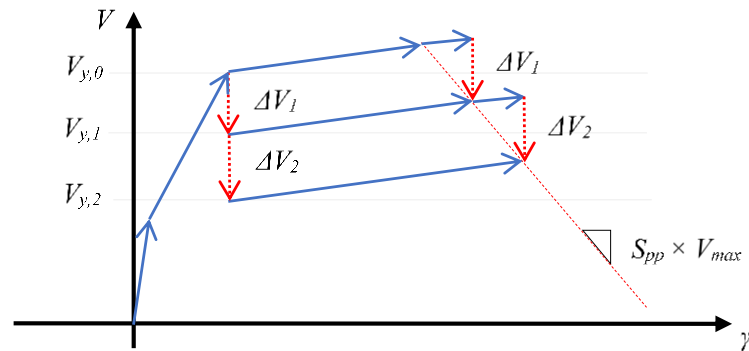


Figure 8-8: Schematic representation of the implementation of in-cycle degradation.

The model is ‘flexure-controlled’ before shear failure initiates. In other words, in each step, the flexural sub-element produces a specific force increment/decrement, which is subsequently used in the shear and bond-slip sub-elements. This results in the deformations coming from each separate sub-component, whose combination leads to the desired displacement step, as well as the stiffness of each sub-component, which is necessary to calculate their flexibility matrices and eventually the stiffness matrix of the element (Eq. 8-1). After the onset of shear failure, however, the element changes to ‘shear-controlled’. In other words, it switches from having the flexural sub-element lead the analysis to the shear one. The shear response is calculated first and the other sub-elements follow, using the force increment/decrement that has been calculated by the shear sub-element. This is essential for the strength degradation to function properly in the current formulation.

Cyclic strength degradation in the post-peak domain should not create a shift of the resulting response towards the origin, i.e. a permanent loss of strength, which would distort the produced descending branch and lead to a slightly premature onset of axial failure in the case of shear strength reaching zero (Figure 8-10a). A compensation algorithm has been introduced to avoid this shift; instead of the second reloading branch merely aiming at the previous maximum point with a reduced strength, it extends to the intersection of the second reloading branch and the target backbone descending branch, similarly to what was originally proposed for the pre-peak response (Ozcebe & Saatcioglu, 1989); hence, the resulting behaviour is as intended (Figure 8-10b) and in line with the calibration of the post-peak degrading response.



ascribed to the shear response, a very high unloading stiffness is assigned to the other sub-elements and the other segments of the shear sub-element, while the failed shear section is in contact with the descending branch (Figure 8-11). This ensures that the intended lateral displacement response is achieved.

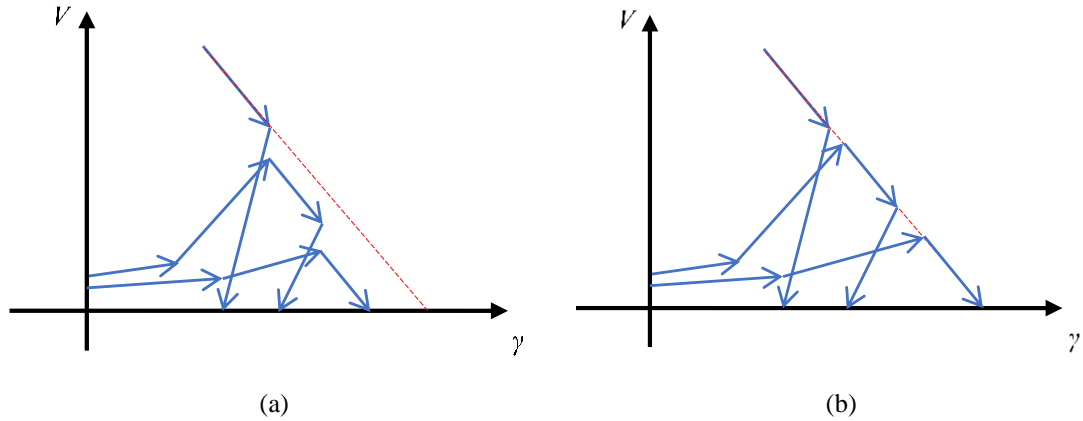


Figure 8-10: Schematic representation of (a) the shear response with descending branch offset due to cyclic degradation and (b) the response with compensation for this offset.

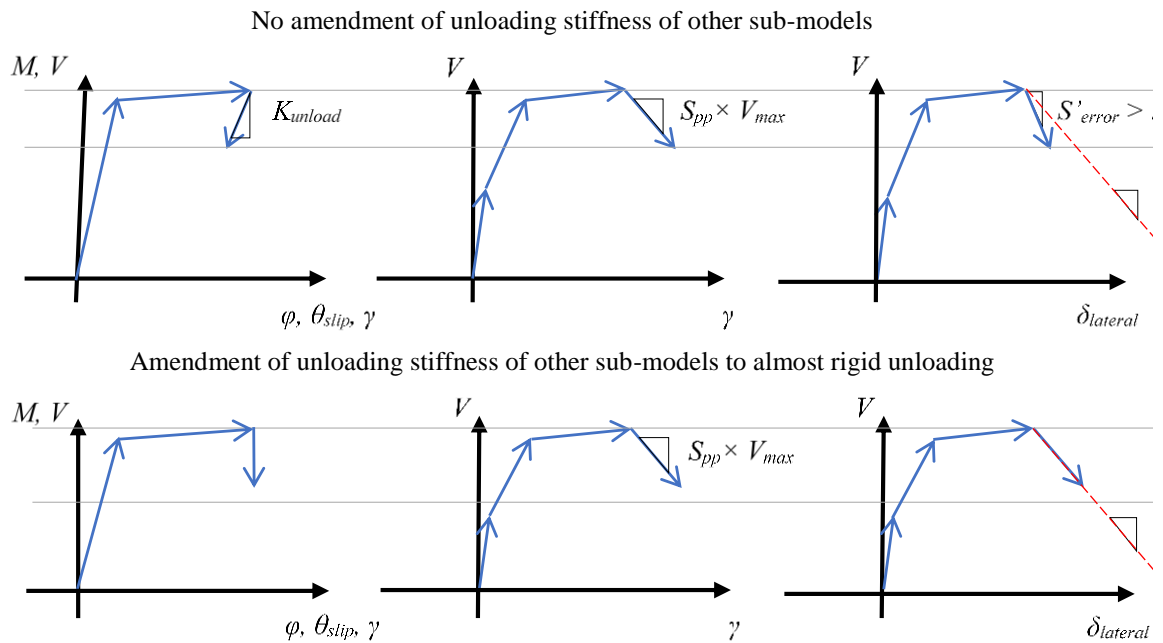


Figure 8-11: Schematic representation of the influence of unloading stiffness of the other sub-models (left) simultaneously with in-cycle strength degradation of failed section (middle) on the shear force vs lateral displacement response (right).

Another issue of similar nature is the shift of the response which occurs in reloading, due to the other sub-elements connected in series aiming at their previous vertex points, while the failed section aims at a degraded strength (Figure 8-12). This has been reported elsewhere in the past and was dealt with using a compensation algorithm that adjusts the shear reloading stiffness and backbone, so that the desired response is produced (LeBorgne & Ghannoum, 2013). A

simpler and more intuitive solution was preferred herein, which also represents more reliably the local deformation quantities in addition to global displacements. The strength degrades uniformly in the whole system; in other words, the strength degradation of the failed shear section (both in-cycle and cyclic) is also inflicted on the rest of the sub-elements and sections of the shear sub-element. Thus, they target their degraded vertex point in reloading, hence not producing this shift in response in the first place (Figure 8-12).

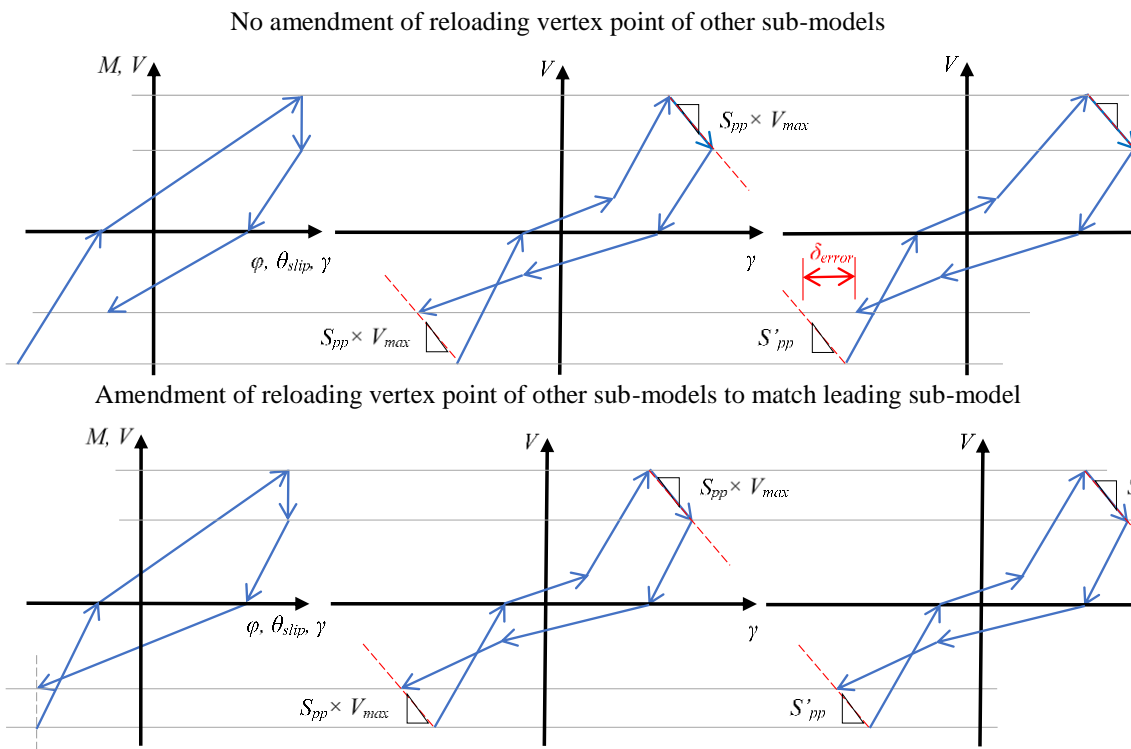


Figure 8-12: Schematic representation of influence of reloading of the other sub-models (left) simultaneously with reloading of the failed section (middle) on the shear force - lateral displacement response (right).

When there is an axial load change, as mentioned in section 8.1, the post-peak values change so as to reflect the level of the new axial load. In order for this to happen, the quantities are inserted into the program as a function of the axial load ratio,  $\nu$ . When the axial load changes by a substantial amount, the values are re-calculated. A lower limit of axial load change has to be placed for the case of dynamic analysis, where slight differences of axial load might come up during cycling even without any actual axial failure. This threshold was herein arbitrarily chosen to be 5%, as a very small change would cause negligible difference to the post-peak values and if it is very high, some important axial load changes might be missed.

The way this change of post-peak values occurs is that in effect the point of onset of shear failure changes to the point where the axial load change occurred. Thus, the calculation of the post-peak descending branch(es) uses the strength at that point and the new slope(s) as the basis.

For the deformation at the onset of axial failure, however, this could lead to overestimation. Therefore, the original deformation at the onset of shear failure,  $\gamma_{sh,f}$ , is summed up with the newly calculated post-peak deformation,  $\gamma_{t,pp}$ .

The beam-column model was originally developed with flexure-shear critical elements in mind. Therefore, in an earlier publication (Mergos & Kappos 2008), it was suggested that the second branch of the backbone curve of shear critical ones be removed, hence ensuring maximum pinching, stiffness and strength degradation. However, this methodology causes computational problems in the post-peak domain, i.e. the onset of axial failure is detected much earlier than it should. It is herein proposed that in these cases the third branch of the backbone curve be 'removed', instead, by setting the start of this branch slightly greater than the point of stirrup yielding. This results in the post-peak as well as pre-peak response working properly, albeit slightly decreasing the potential pinching, strength and stiffness degradation, which might somewhat overestimate the energy dissipation capacity.



## Chapter 9: VERIFICATION OF THE MODEL

---

In this chapter, the beam-column finite element model presented in chapter 8 will be applied to predict the response of a number of individual components as well as entire frames, in order to verify its prediction capabilities. Most cases are quasi-static analyses of R/C columns, with the exception of the frame specimens, which are subjected to dynamic shake-table excitations. The specimens with increasing axial load (presented in Part II) are also evaluated in the last section.

### 9.1 ANALYTICAL PREDICTION ACCURACY

The accuracy of analytical predictions is often presented and judged on a visual basis, i.e. through comparison of resulting diagrams. While this is reasonable, it provides by no means an objective metric so as to compare the performance among different models.

Therefore, herein inspired by a recent study (Huang & Kwon 2015), objective accuracy measures, i.e. ratios of numerical over experimental values, are used. The following are deemed important, hence are computed and presented:

- Energy Dissipation Ratio ( $R_E$ ).
- Shear Failure Displacement Ratio ( $R_{SFD}$ ), i.e. the displacement at the onset of shear failure.
- Axial Failure Displacement Ratio ( $R_{AFD}$ ), wherever applicable, i.e. wherever axial failure initiation was recorded in the experiment.

The ratio of initial stiffness is not considered important in the context of this thesis, since the full non-linear behaviour including the post-peak domain is taken into account. The authors (Huang & Kwon, 2015) have also commented that this is not an influential parameter for non-linear analysis with high intensity seismic loads.

### 9.2 FLEXURE-SHEAR CRITICAL SPECIMENS

#### 9.2.1 Specimen-1

Sezen & Moehle (2006) tested four double-curvature column specimens with different axial loads under quasi-static cyclic loading (Figure 2-3). They were lightly reinforced, representative of old-type construction, designed to yield in flexure and subsequently fail in shear. Column Specimen-1, tested under an axial load of 667 kN ( $\nu = 0.15$ ), is selected for verification of the proposed analytical model. Its clear height was 2946 mm, with a 457 mm square cross-section and a longitudinal reinforcement ratio of 2.5%. The transverse reinforcement comprised

rectangular and diamond-shaped ties at 305 mm spacing, with 90° anchorage hooks (Figure 2-3a). The concrete compressive strength was 21 MPa and the longitudinal and transverse reinforcement yield strengths were 434 MPa and 476 MPa, respectively.

The proposed model seems to be capturing the pre- and post-peak hysteretic response fairly well (Figure 9-1a). It matches very well the overall behaviour, with unloading and reloading stiffnesses of the analysis representing well the average stiffnesses observed experimentally, capturing very well the high strength degradation at the displacement level of  $\pm 82$  mm. Of course, there is some discrepancy at a few points.

Comparing the predicted values with the experimental ones (Table 9-1), the displacement at the onset of shear failure is predicted quite well, with some overestimation. The onset of axial failure is predicted at the last displacement level; the  $R_{AFD}$  (Table 9-1) shows about 20% underestimation of the expected deformation at zero shear strength, however. This is due to the fact that the strength in the last cycles seems to be unreasonably reaching negative values in the experimental response; of course, as explained in chapter 8, this is a failure criterion for the analytical model, thus not being able to capture the final displacement level. On the other hand, the energy dissipation is found to be overestimated by about 10% compared to the actual energy dissipated by the member during the cyclic test, largely due to the underestimation of pinching in the analytical model.

The lateral displacement components are captured very well both in the pre- and post-peak domains (Figure 9-1b-d), given the challenge of predicting individual displacement components in lieu of total displacements in displacement-controlled experiments. There is a negligible underestimation of shear deformations before the peak; subsequent to the onset of shear failure the shear displacement increases considerably in the positive direction, a tendency which the model captures adequately. There is slight underestimation of shear displacements on the subsequent negative side. Not all shear response history is provided by the researchers (Sezen & Moehle, 2006), possibly due to failure of the recording instruments, therefore only one full experimental post-peak cycle is presented in Figure 9-1b, while the entire analytical response is included. The anchorage slip displacement (Figure 9-1d) is predicted with very high accuracy, with the sole exception of the first negative post-peak half-cycle, where there is slight overestimation in the analytical prediction. The model shows good agreement with the experiment in the pre-peak flexural response (Figure 9-1c), with deviation in the post-peak range. The experimental post-peak flexural displacement seems to be biased towards the negative side, increasing substantially in the latter post-peak cycles; this asymmetry might be due to measurement errors in this advanced damage stage or due to the effect of widening shear cracks on flexural deformations.

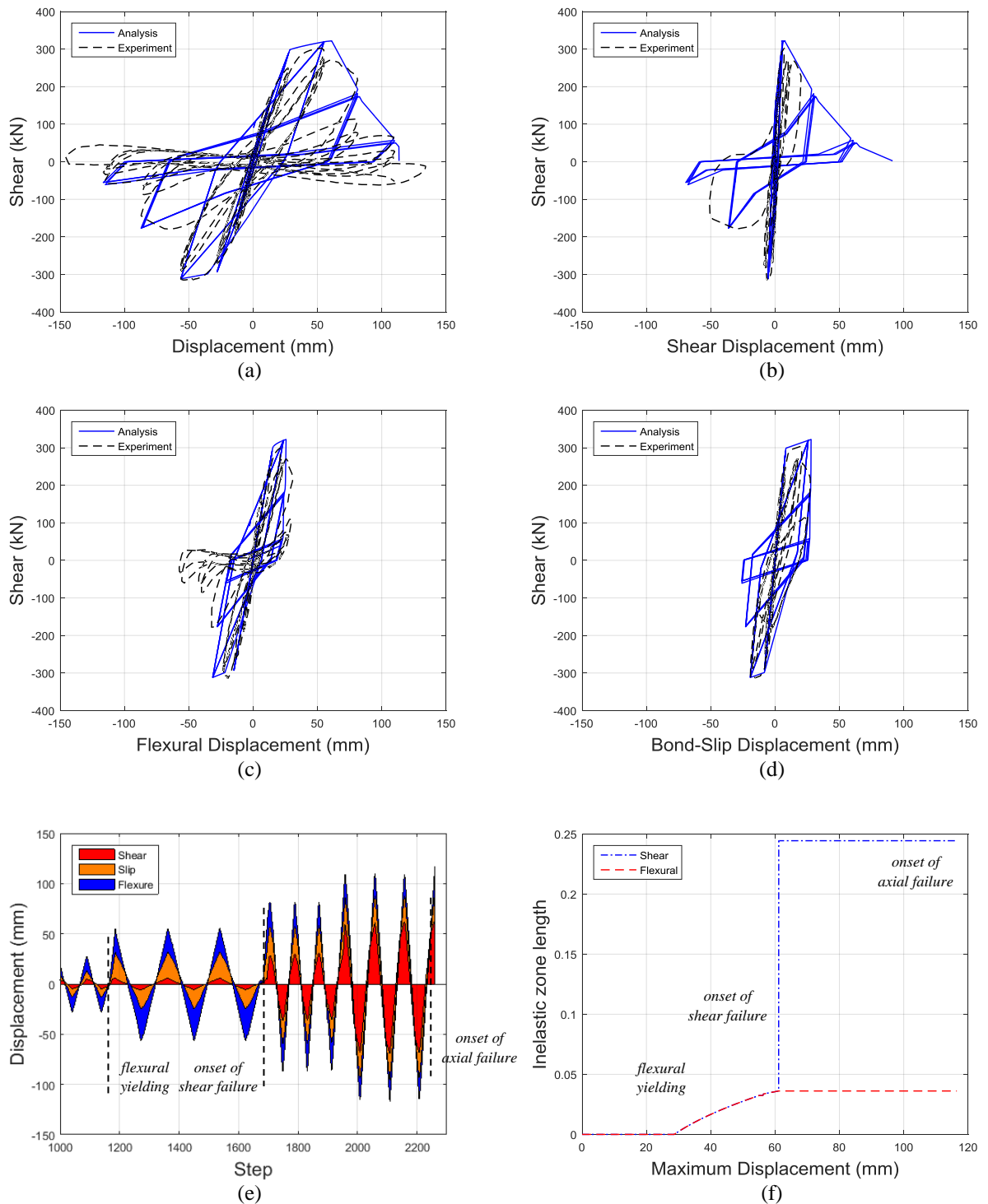


Figure 9-1: Comparison between the predicted response of Specimen-1 by the proposed model and the experimental one in terms of (a) shear force against lateral displacement, (b) shear displacement, (c) flexural displacement, and (d) anchorage slip displacement. (e) Displacement decomposition of the element's lateral displacement components, and (f) flexural and shear inelastic zone lengths normalised to the clear member length, throughout the analysis.

As has been reported (Sezen & Chowdhury, 2009), a hysteretic macro-model's objective should be to capture each individual component as accurately as possible, rather than merely predicting the total response. However, this has rarely been reported in previous studies, possibly due to scarcity of experimental programmes reporting separate deformation components, the

reliability of measured recordings that can be highly dependent on setup, methodology and instrumentation, or due to inability of some models to predict them accurately, relying on aggregation of overestimated and underestimated components to provide a reasonable total response. Achieving such level of agreement with individual components of experimental displacement can be considered a very positive indication for an analytical model.

For reasons of comparison with predictions from other analytical models, the response prediction both in terms of total and shear displacement is shown in Figure 9-2 by the model proposed by Baradaran-Shoraka & Elwood, 2013. Comparing these with Figure 9-1, the superior performance of the present model can be seen, especially in terms of energy dissipation that is judged to be much higher in the model of Figure 9-2. Furthermore, the shear displacement are predicted well pre-peak, but deviate substantially post-peak. This is a mostly theoretical (semi-empirical) model and this shows the difficulty of capturing the post-peak response with theory-based approaches, as opposed to empirical ones. As reiterated, uncertainties in this part of the response are very high, not least because of the very advanced state of damage of the specimens.

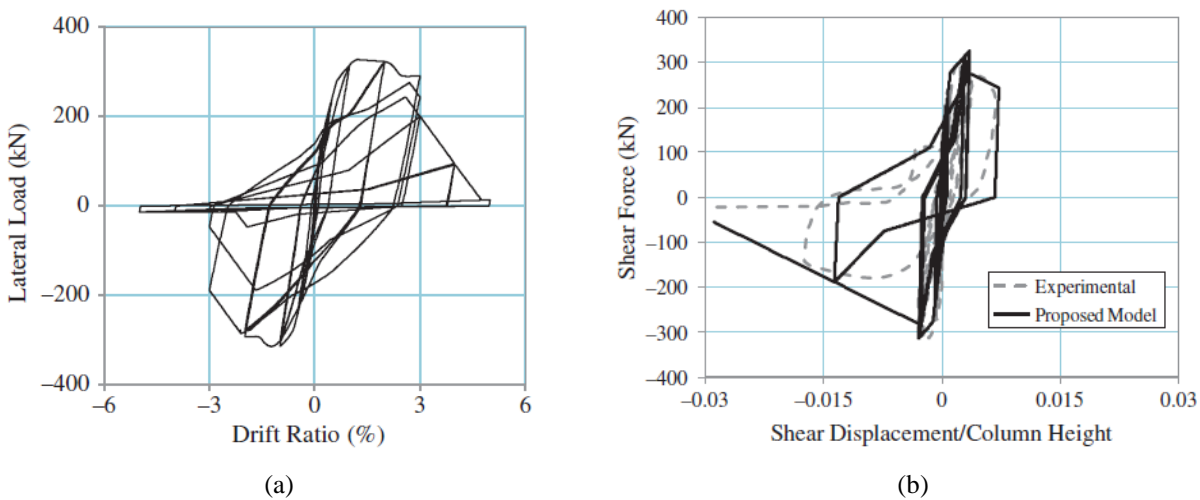


Figure 9-2: Comparison between the predicted response of Specimen-1 by the model proposed by Baradaran-Shoraka and Elwood (2013) and the experimental one in terms of (a) shear force against lateral drift ratio, (b) shear displacement over column height.

Figure 9-1e shows the analysis of the lateral displacement components of the specimen (only the second half of the response is shown, for the sake of clarity). Shear displacements are naturally very low at the first stages of the response, increasing after the element yields, due to shear-flexure interaction at the ends of the member. Furthermore, they increase drastically after the onset of shear failure, as all post-peak displacements are attributed to the shear sub-element; the flexural and bond-slip displacements, on the other hand, do not exceed their maximum pre-peak values at any point in the post-peak domain.

Figure 9-1f demonstrates the spread of inelasticity during the analysis for the flexural and shear sub-elements. After flexural yielding, the inelastic zones increase following the bending moment increase at the member ends, always being equal. As soon as the onset of shear failure is reached just after the maximum displacement of 60 mm, the inelastic zone of the shear sub-element instantly assumes a value corresponding to the shear critical length, where the diagonal shear failure plane forms, and maintains it for the remainder of the analysis. Simultaneously, the inelastic zone of the flexural sub-element remains equal to the maximum value it has reached up to the onset of shear failure.

Table 9-1: Accuracy measures of the analyses of Specimen-1, FSC\_1 and C-2.

	$R_E$	$R_{SFD}$	$R_{AFD}$
<b>Specimen-1</b>	1.362	1.086	0.797
<b>FSC_1</b>	1.106	0.970	N/A
<b>C-2</b>	0.858	0.571	N/A

### 9.2.2 FSC\_1

The reference specimen FSC\_1 of the flexure-shear-critical-specimens experimental series tested herein, is analysed to further validate the beam-column model's predictive ability with regard to flexure-shear critical R/C elements. It is emphasised that the verification against this test provides an opportunity for an independent examination of the model's predictive capabilities, as it was not included in the initial database, upon which the model was based. The characteristics of this specimen have been presented in detail in Chapter 6.

The proposed model seems to be capturing the pre- and post-peak hysteretic response fairly well (Figure 9-3a). It matches the overall behaviour, with unloading and reloading stiffnesses of the analysis representing reasonably well the average stiffnesses observed experimentally, capturing very well the significant strength degradation in the post-peak domain. The onset of shear failure is predicted very well ( $R_{SFD} = 0.97$  in Table 9-1). No axial failure is predicted analytically, in line with the specimen's experimentally obtained response.

The energy dissipation, which is a key characteristic with regard to the seismic response of R/C members, is shown to be overestimated only by about 10% compared to the actual energy dissipated by the member during the cyclic test (Table 9-1). Figure 9-3d demonstrates the cumulative dissipated energy throughout the experimental test and the analysis. The energies are on a par until the displacement level of  $\pm 12$  mm, while they deviate after that. This is by large attributed to the higher experimentally observed pinching that is not captured adequately in the analysis.

Figure 9-3b shows the shear hysteretic response. The shear displacements are relatively low in the first stages of the response, increasing drastically after the onset of shear failure; this is

something that the analysis captures very well, predicting correctly the pre-peak displacement, and the considerable increase upon initiation of shear failure. There are few deviations in the positive direction of the last post-peak cycles. Some jumps observed in the experimental response are due to debris falling on the draw-wire sensors, as explained in chapter 7.

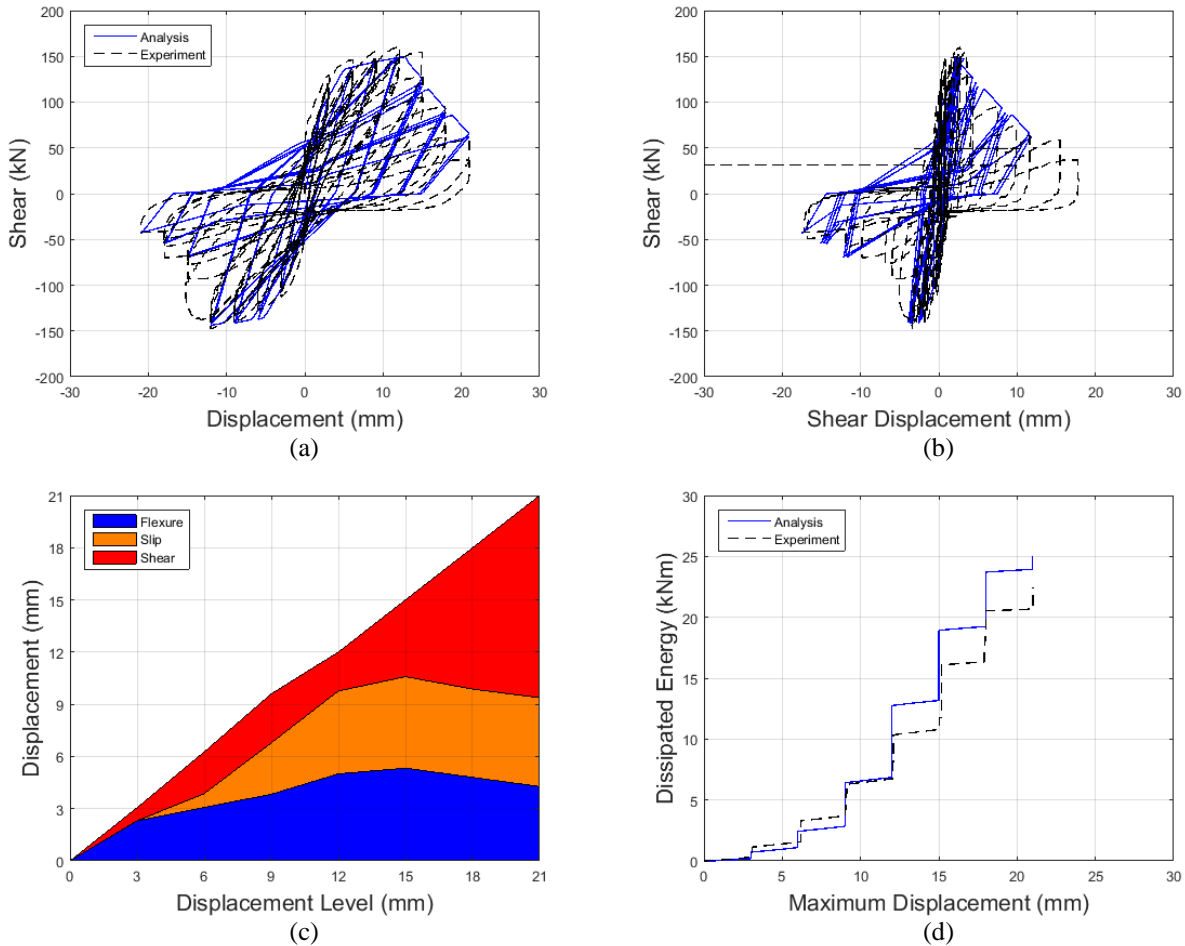


Figure 9-3: Comparison between the predicted response of FSC\_1 by the proposed model and the experimental one in terms of (a) shear force against lateral displacement, and (b) shear displacement. (c) Decomposition of the element's lateral displacement components throughout the analysis. (d) Comparison between predicted and experimentally obtained cumulative dissipated energy.

Figure 9-3c shows the break-down of the lateral displacement components, which compares very well with Figure 7-16a. Flexural and bond-slip displacements seem to steadily increase up to the onset of shear failure, while they decrease to some extent in the post-peak domain, on a par with the experimentally obtained decomposition. Achieving such agreement with individual components of an independent test (not included in the database) highlights the analytical model's performance.

Figure 9-4 shows comparisons of selected individual hysteretic cycles of the analytical response against the experimental one, in the post-peak domain of the response. The total displacement analytical cycles are found to agree very well with the experimental ones, with the unloading and reloading stiffness matching the experimentally recorded ones on average. Pinching is also

shown to be well-captured, being little in the first post-peak cycles (e.g. Figure 9-4a), but increasing significantly towards the end (e.g. Figure 9-4e), in line with the experimental response. Overall, the energy dissipated along each analytical cycle can be seen to be roughly equal to the corresponding experimental ones.

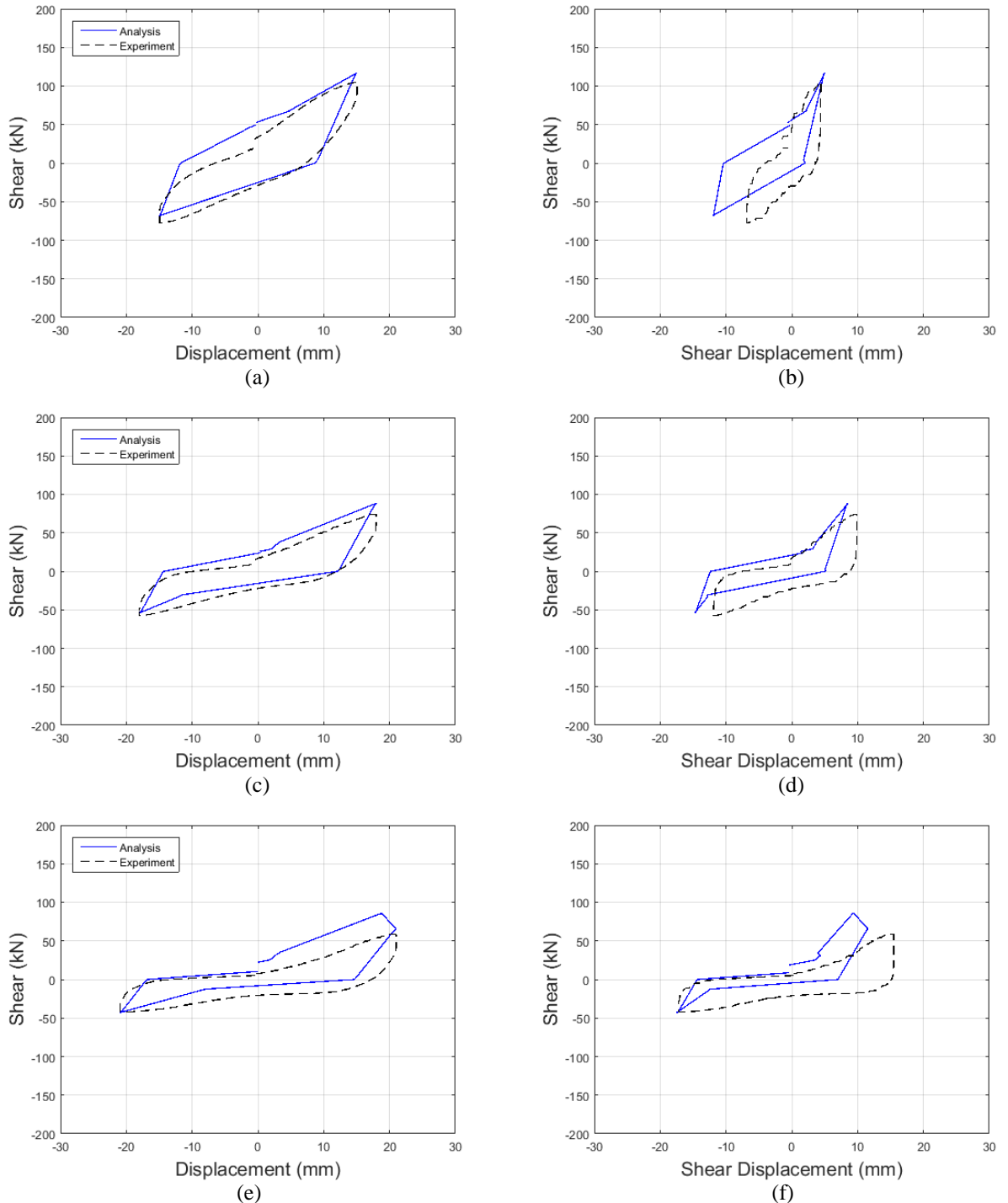


Figure 9-4: Comparison between individual cycles of the predicted response of FSC\_1 by the proposed model and the experimental one: (a, b) 3<sup>rd</sup> cycle at +/- 15 mm, (c, d) 2<sup>nd</sup> cycle at +/- 18 mm, and (e, f) 1<sup>st</sup> cycle at +/- 21 mm. (left) Total displacements and (right) shear displacements.

The shear displacement ones do not show such good agreement. The analytical response is similar on average, but there are discrepancies in several points. Nonetheless, taking into

account the difficulty for a model to capture individual displacement components correctly, the match can be considered adequate.

### 9.2.3 C-2

Lejano *et al.* (1995) conducted an experimental programme to study the deformation characteristics of short double-curvature R/C columns with high-strength concrete under quasi-static cyclic loading as well as high or fluctuating axial load. The specimen C-2 is herein selected for analysis, having a 278 mm square cross-section and a length of 646 mm, which results in a very low aspect ratio close to 1, with high longitudinal and transverse reinforcement ratios of almost 4% and 1%, respectively (Figure 2-1). The steels used had a yield strength of 496.2 and 414.0 MPa, respectively, while the strength concrete compressive strength was 39.6 MPa. It is subjected to unusually high compressive axial load, i.e. an axial load ratio ( $\nu = N / A_g \times f_c$ ) of approximately 0.80.

The proposed model captures the pre- and post-peak hysteretic response very accurately (Figure 9-5a). The overall behaviour is matched very well, with unloading and reloading stiffnesses of the analysis closely capturing the average stiffnesses observed experimentally. The onset of shear failure is predicted slightly earlier, mainly due to the ductility of the specimen after yielding, which is more limited in the analytical prediction; this can also be seen in Figure 9-5c, where the overall flexural and bond-slip analytical response exhibits very limited inelasticity, while the experimental one exhibits a relatively larger – yet still low – inelastic deformation component. The strength degradation follows very closely the apparent descending branch of the response, deviating slightly only in the last positive half-cycle; in addition, the cyclic strength degradation of the analytical prediction is accurately captured, particularly in the post-peak domain.

Comparing the predicted values with the experimental ones (Table 9-1), the displacement at the onset of shear failure seems to be underestimated considerably based on  $R_{SFD}$ , although in absolute terms it has no such a great difference, hence not influencing adversely the descending branch and the subsequent response. The maximum displacement reached is predicted to be lower than the actual one, i.e. about 13 mm, while the experimental test reaches 20 mm without axial failure. This is, of course, attributed to the extremely high axial load ratio value, which leads to a prediction of very low deformability. Probably the high longitudinal and transverse reinforcement contributed to reaching such displacement capacity during the experiment and this was not reflected by the empirical relationship's prediction.

The energy dissipation is underestimated compared to the actual energy dissipated by the member during the cycling (Table 9-1). Nevertheless, Figure 9-5d shows that the analytically

predicted energy dissipation is on a par with the experimental one at all stages of the analysis, generally being underestimated more in the pre-peak domain, due to the aforementioned underestimation of ductility in the first cycles and some dissipation of the experiment during the initial cycles which is considered completely elastic behaviour by the analytical model. Once the post-peak domain is entered, the energy is slightly overestimated, mainly due to the underprediction of pinching, making up for the pre-peak deficit and reaching practically the same total dissipated energy by the displacement of 13 mm. The experimental energy keeps rising after that, leading to the aforementioned discrepancy owing to the higher displacement capacity of the member.

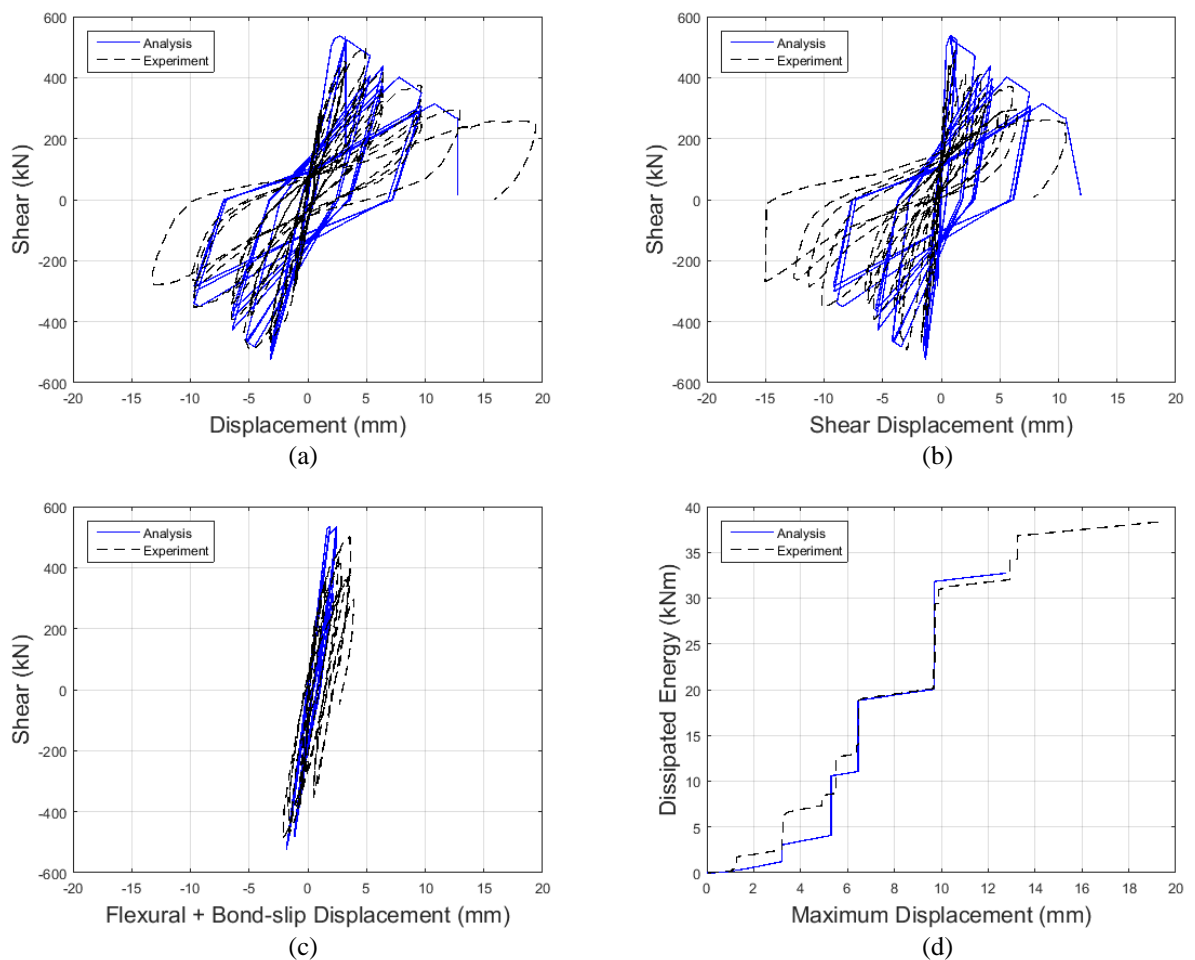


Figure 9-5: Comparison between the predicted response of C-2 by the proposed model and the experimental one in terms of (a) shear force against lateral displacement, (b) shear displacement and (c) flexural and bond-slip displacement; (d) cumulative dissipated energy throughout the experiment.

Figure 9-5b-c show separately the shear as well as flexural and bond-slip responses. It can be seen that both of them are very well predicted. The drastic increase of shear displacements with simultaneous limiting of the other components is very clear, confirming once again the fact that shear displacements increase drastically after the onset of shear failure, while the other components are essentially capped. The flexural and bond-slip response seems to have a

ratcheting asymmetric behaviour beyond shear failure skewed towards the positive side, which is not captured by the analytical model; in turn, this leads to an asymmetry in the shear response towards the negative side, leading to the symmetric analytical prediction overestimating the positive side shear deformations while underestimating the negative.

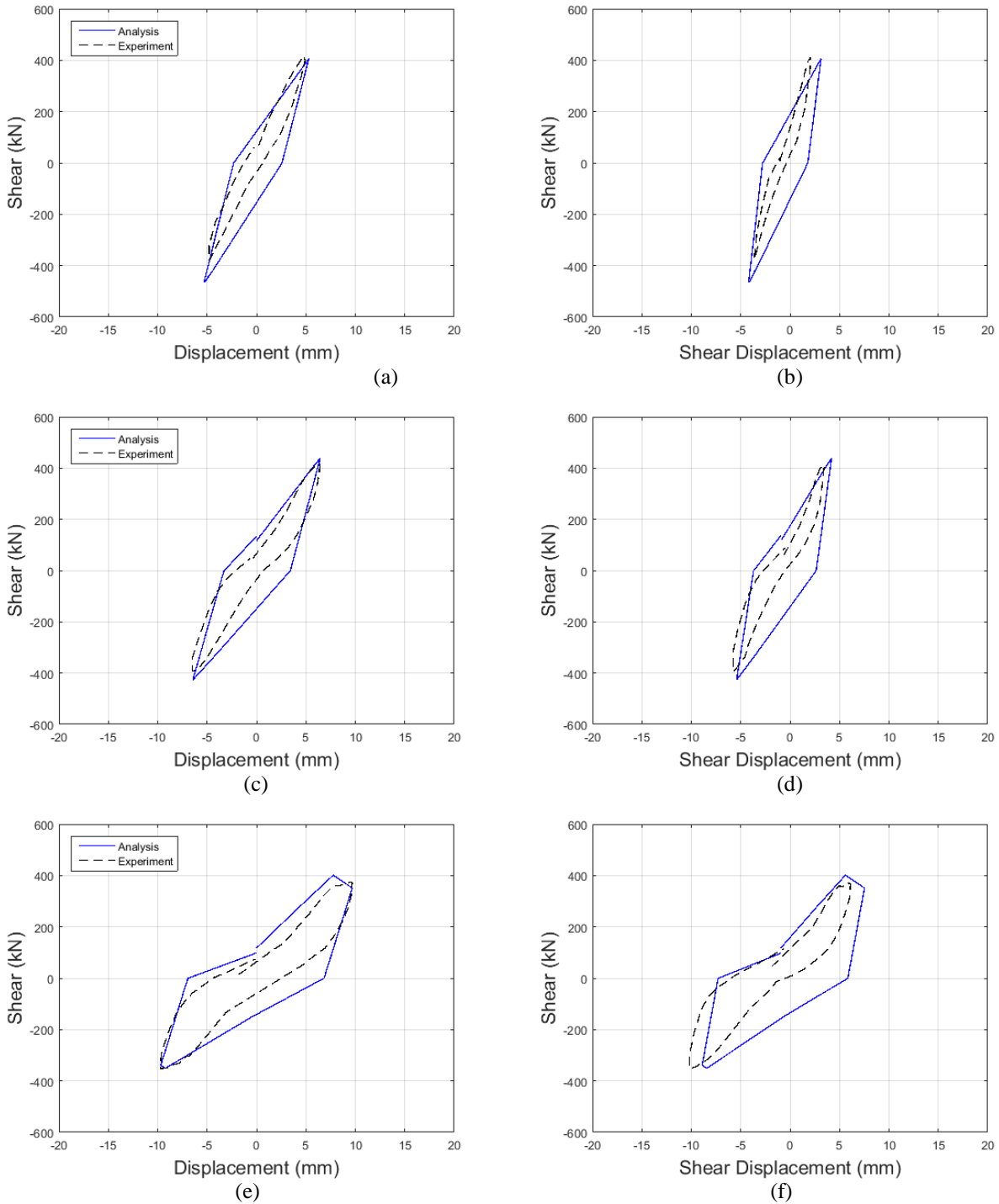


Figure 9-6: Comparison between individual cycles of the predicted response of C-2 by the proposed model and the experimental one: (a, b) 2<sup>nd</sup> cycle at +/- 5 mm, (c, d) 1<sup>st</sup> cycle at +/- 6.5 mm, and (e, f) 1<sup>st</sup> cycle at +/- 10 mm. (left) Total displacements and (right) shear displacements.

The inelastic lengths' behaviour is similar to Specimen-1, hence not included herein. The flexural inelastic zone, however, is very limited (less than 1% of the column length), owing to the very limited curvature ductility of the specimen.

Figure 9-6 shows comparisons of selected individual hysteretic cycles of the analytical response against the experimental one, in the post-peak domain of the response. The total displacement analytical cycles are found to agree very well with the experimental ones. The unloading and reloading stiffness in each cycle match the experimentally recorded ones on average. The strength degradation inflicted upon the specimen with increasing displacement and cycles seems to be followed very well. Pinching is observed in the advanced displacement levels of the experimental response (e.g. Figure 9-6c, e), which however is underestimated in the analytical prediction and is only slightly captured in the very last analytical cycles not show here. The energy dissipated along each analytical cycle can be seen to be greater than the corresponding experimental ones, largely due to the aforementioned underprediction of pinching, leading to thicker loops. The shear displacement cycles of the analysis also show good agreement, once more being thicker than the experimental ones, though.

It is noteworthy that disregarding the post-peak response of this specimen, e.g. using an analytical model considering 15% or 20% strength degradation as failure, the deformability of the specimen would be gravely underestimated, predicting a maximum displacement of about 5 mm, whilst the column is shown to be able to reach 20 mm, a fourfold displacement, barely losing half its lateral strength. This highlights once more the importance of modelling the full-range response of substandard R/C elements in cases where the collapse limit state has to be considered.

## 9.3 SHEAR CRITICAL SPECIMENS

### 9.3.1 SC3

Aboutaha *et al.* (1999) tested 11 large-scale short columns, investigating the effect of various rectangular steel jacket types on strength and ductility of columns with inadequate shear strength. Three of them were tested before retrofit as reference response. Herein the unretrofitted cantilever specimen SC3 is examined, which failed in shear before yielding in flexure. Its clear height was 1219 mm, with a section 914×457 (mm) and a longitudinal reinforcement ratio of 1.9%. It was subjected to uniaxial cyclic loading in its weak direction. Its transverse reinforcement comprised rectangular perimeter ties combined with cross ties, spaced at 406 mm. The concrete compressive strength was 21.9 MPa and the yield strengths of longitudinal and transverse reinforcement were 434 and 400 MPa, respectively.

The proposed model captures the pre- and post-peak hysteretic response well (Figure 9-7a). The plateau from  $\pm 10$  mm to approximately  $\pm 23$  mm is very well captured and unloading and reloading stiffnesses are on a par with the experimental ones. The onset of shear failure is predicted slightly later than the experimental one and the predicted post-peak descending branch underestimates the experimental strength degradation to some extent, especially on the positive side.

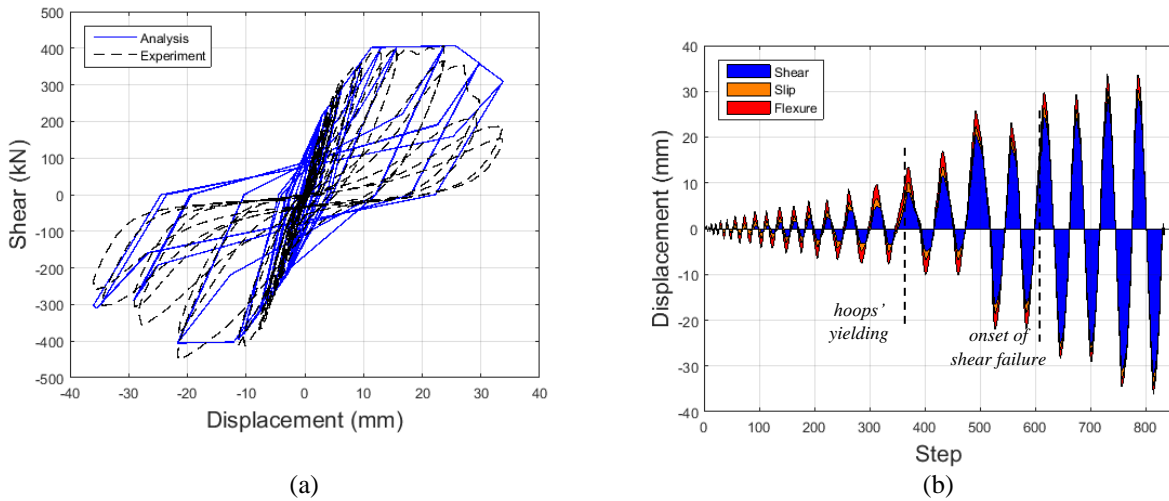


Figure 9-7: (a) Comparison between the predicted response of SC3 by the proposed model and the experimental one in terms of shear force against lateral displacement. (b) Decomposition of the element's lateral displacement components throughout the analysis.

Comparing the predicted values with the experimental ones (Table 9-2), the displacement at the onset of shear failure is overestimated by about 10%. The maximum displacement reached is correctly predicted, as the model did not underestimate the onset of axial failure neither overestimated the in-cycle strength degradation of the test, hence reaching the final step of the displacement history and correctly predicting that the specimen does not fail axially during the test. The energy dissipation is also predicted with about 24% overestimation compared to the actual energy dissipated by the member during the test. This discrepancy is mainly attributed to the aforementioned delayed onset of shear failure and low predicted strength degradation, as well as the extreme pinching behaviour observed in the post-peak experimental response. Although the model also predicts substantial pinching, it does not capture its actual extent.

Figure 9-7b shows the decomposition of lateral displacement components throughout the analysis. The member being shear critical, shear-induced displacements are a non-negligible part of the total displacement from the early stages of the response. Nonetheless, they increase drastically as a percentage of the total after the onset of shear failure, as all post-peak displacements are localised at the shear sub-component; the flexural and bond-slip displacements, on the other hand, do not exceed their maximum pre-peak values at any point

in the post-peak domain, thus decreasing significantly as a percentage of the total lateral displacement.

Table 9-2: Accuracy measures of the analyses of SC3 and SC\_1.

	$R_E$	$R_{SFD}$	$R_{AFD}$
SC3	1.241	1.103	N/A
SC_1	1.174	1.225	N/A

### 9.3.2 SC\_1

The reference specimen of the shear-critical-specimens experimental series, SC\_1, is analysed to further validate the beam-column model's predictive ability in the case of shear critical R/C elements. Although it is mostly dominated by shear, especially post-peak, flexure was found to play a significant role in its response, so it is not a purely shear critical element.

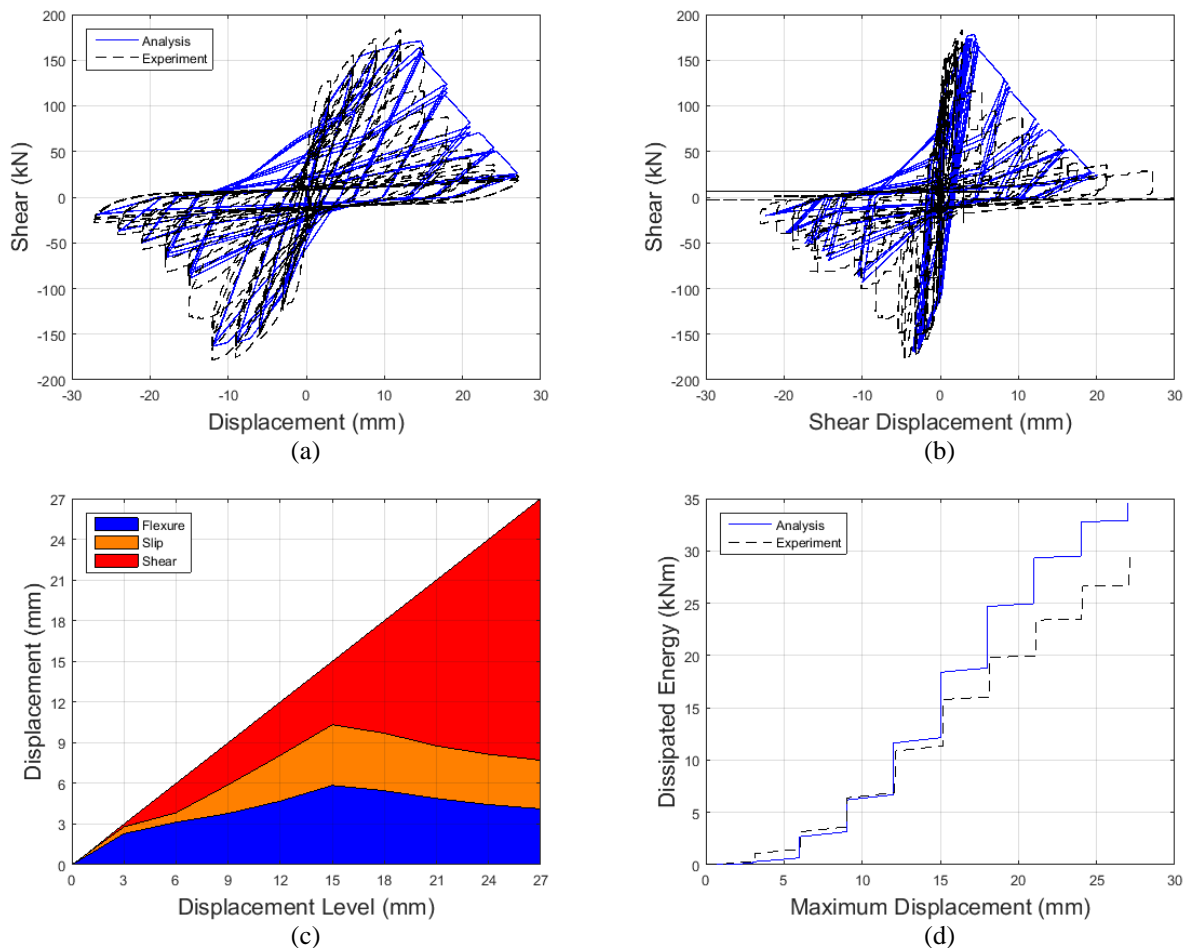


Figure 9-8: Comparison between the predicted response of SC\_1 by the proposed model and the experimental one in terms of (a) shear force against lateral displacement, and (b) shear displacement. (c) Decomposition of the element's lateral displacement components throughout the analysis. (d) Comparison between predicted and experimental cumulative dissipated energy.

It is emphasised again that the verification against this test provides an opportunity for a better examination of the model's predictive capabilities, as it was not included in the initial database, upon which the model was based. The characteristics of this as well as all the other specimens of the experimental programme are shown in detail in section 6.

The proposed model captures the pre- and post-peak hysteretic response well (Figure 9-8a). It matches the overall behaviour, with unloading and reloading stiffnesses derived from the analysis representing reasonably well the average stiffnesses observed experimentally. The strength and stiffness are slightly underestimated in the pre-peak domain, while being slightly overestimated in the post-peak domain. The post-peak strength degradation in the negative direction is predicted very well, unlike in the positive one. Significant pinching is observed in the experimental response after the initiation of strength loss; this is captured very well in the last post-peak cycles, although not so well in the first ones, producing visibly thicker loops.

Contrasting the predicted values with the experimental ones (Table 9-2), the displacement at the onset of shear failure is found to be overestimated; this can also be seen in Figure 9-8a. The specimen did not fail axially during the experiment, although reaching a very low lateral – almost negligible – strength by the end of cycling. This is captured by the model, which is thus shown not to overestimate the strength degradation, nor underestimate the deformation at the onset of axial failure.

The energy dissipation is shown to be overestimated by about 17% compared to the actual energy dissipated by the member during the cyclic test. In Figure 9-8d, it can be seen that this is mainly attributed to the aforementioned underestimation of pinching, which results in the dissipation of more energy in the cycles immediately subsequent to the onset of shear failure, i.e. at the displacement levels of  $\pm 15$  mm and  $\pm 18$  mm. Furthermore, underestimation of the shear strength degradation leads to higher energy dissipation post-peak.

Figure 9-8b shows the shear response and Figure 9-8c shows the decomposition of lateral displacement components throughout the analysis. The shear displacements are relatively low in the first stages of the analytical response, gradually increasing after shear cracking and flexural yielding; they increase drastically after the onset of shear failure, as all the additional post-peak displacements are attributed to shear deformations. Overall, the analytical response seems to be in agreement with the experimental response of Figure 9-8b, besides some underestimation of the shear displacements in the last couple of post-peak cycles. Flexural and bond-slip displacements, on the other hand, increase up to the onset of shear failure, but decrease considerably as a percentage of the total lateral displacement in the post-peak domain, as shown in Figure 9-8c. The decomposition matches well the experimental one shown in Figure

7-17a; the shear component increases drastically post-peak as in the analysis and the other components peak at the onset of shear failure and thenceafter retract to some extent.

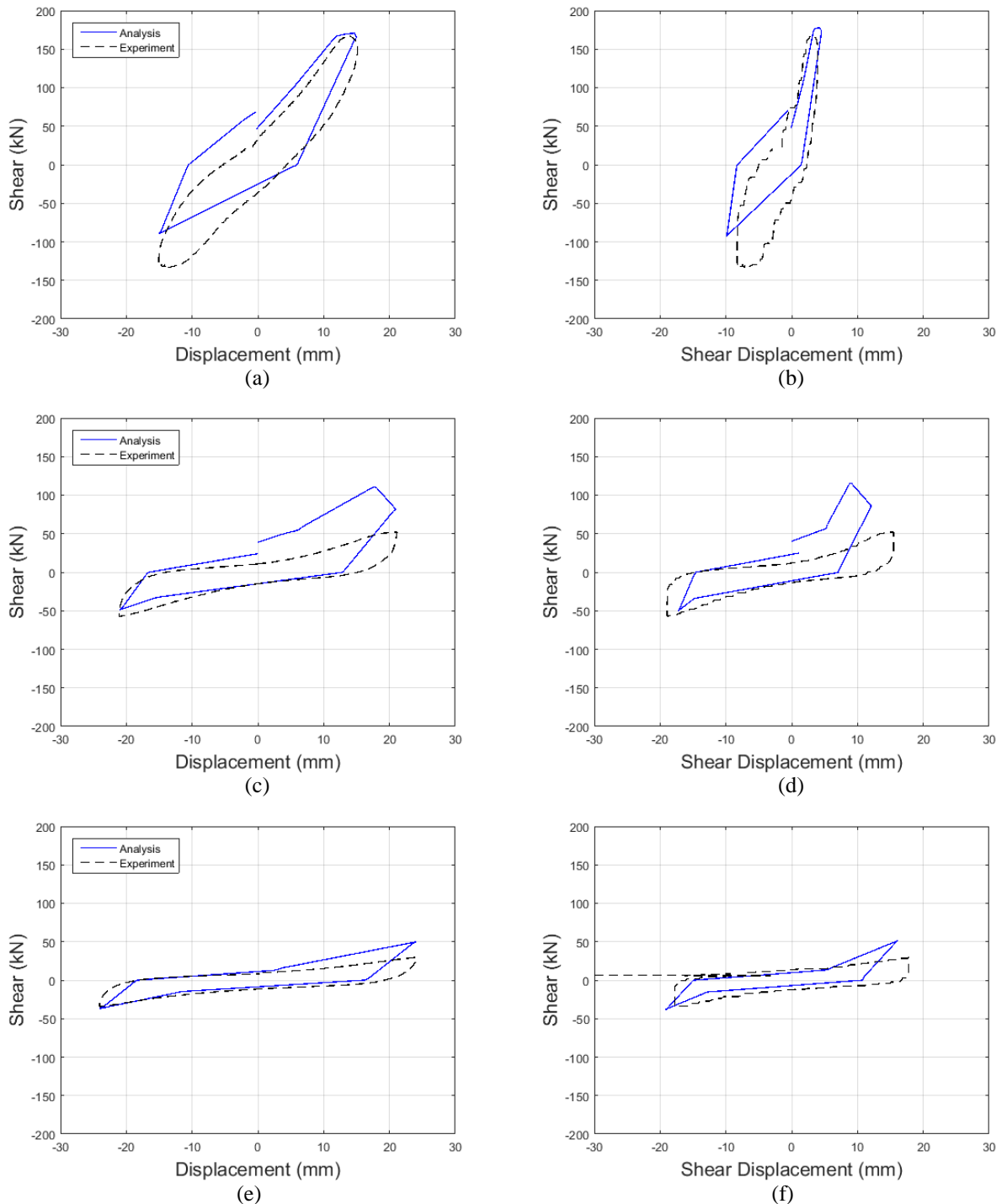


Figure 9-9: Comparison between individual cycles of the predicted response of SC\_1 by the proposed model and the experimental one: (a, b) 1<sup>st</sup> cycle at +/- 15 mm, (c, d) 1<sup>st</sup> cycle at +/- 21 mm, and (e, f) 2<sup>nd</sup> cycle at +/- 24 mm. (left) Total displacements and (right) shear displacements.

Figure 9-9 shows comparisons of selected individual hysteretic cycles of the analytical response against the experimental one, in the post-peak domain of the response. Due to debris, the last shear displacement cycle (Figure 9-9f) was translated to the positive direction (spanning from

-8.4 mm to +27.2 mm). In order to have a fair comparison, it was recentred at zero (adding the average of the two extremes).

The total displacement analytical cycles are found to moderately agree with the experimental ones, their discrepancies chiefly arising from the aforementioned underestimation of the descending branch slope. In the loop where the onset of shear failure is detected (Figure 9-9a), the positive side of the response is predicted very well, but there is significant deviation in the negative one. The subsequent cycle (Figure 9-9c) is better overall, while the last one (Figure 9-9e) is found to be most accurate. Pinching is shown to be well-captured, being little in the first post-peak cycles (e.g. Figure 9-9a), but increasing significantly towards the end (e.g. Figure 9-9c, e), in line with the experimental response. The analytical shear displacement cycles are similar to the experimental ones on average, but there are discrepancies in several points, largely due to the aforementioned underestimation of the descending branch slope. However, pinching, unloading and reloading stiffness degradation are predicted very well. Taking into account the difficulty for a model to capture individual displacement components correctly, the match can be considered adequate.

## 9.4 FRAME SPECIMENS

### 9.4.1 Frame 1

Elwood & Moehle (2008b) carried out shake-table tests on two R/C frames to study shear followed by axial failure and the redistribution of vertical loads in an R/C sub-assembly. They were both three-column one-storey frames, with two well-designed circular columns at the edges and a rectangular shear-deficient column in the middle, supported on large footings at the bottom and connected at the top via a 1.5 m wide 'beam' (Figure 9-10). The specimen Frame 1 is examined herein, which supported a total mass of 31 t, resulting in a weight of 128 kN carried by the central column. The latter had a 230 mm square section, being a ½-scale mock-up of the column analysed above (Specimen-1). It had a longitudinal reinforcement ratio of 2.5% and a transverse reinforcement ratio of 0.18% consisting of rectangular and diamond-shaped ties with 90° anchorage hooks. The concrete compressive strength was 24.5 MPa and the longitudinal and transverse reinforcement yield strengths were 479 and 718 MPa, respectively. The outside columns were detailed with closely-spaced spiral hoops leading to very high confinement, ensuring that when the axial support of the mid-column is lost, these columns will be capable of supporting the redistributed gravity loads. The specimen was subjected to a horizontal component of a scaled ground motion of the 1985 Chile earthquake recorded at Viña del Mar. Before the main shaking, it was subjected to an accelerogram scaled to 13% of this one, the frame remaining elastic throughout, thus this has not been modelled herein.

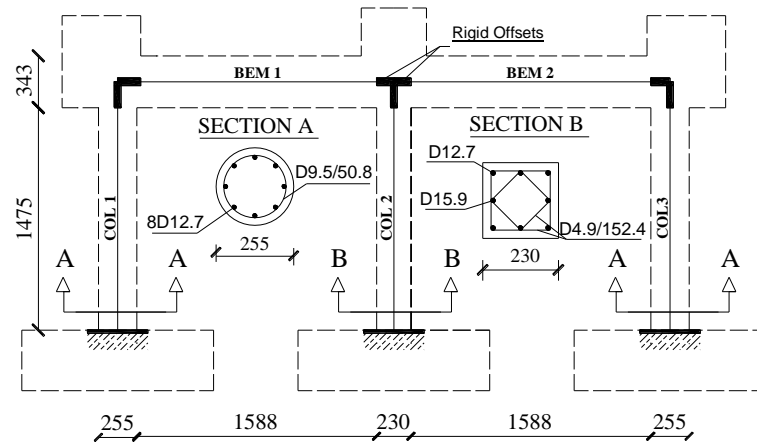


Figure 9-10: Frame 1 layout (dimensions in mm) and applied finite element model (Mergos & Kappos, 2012).

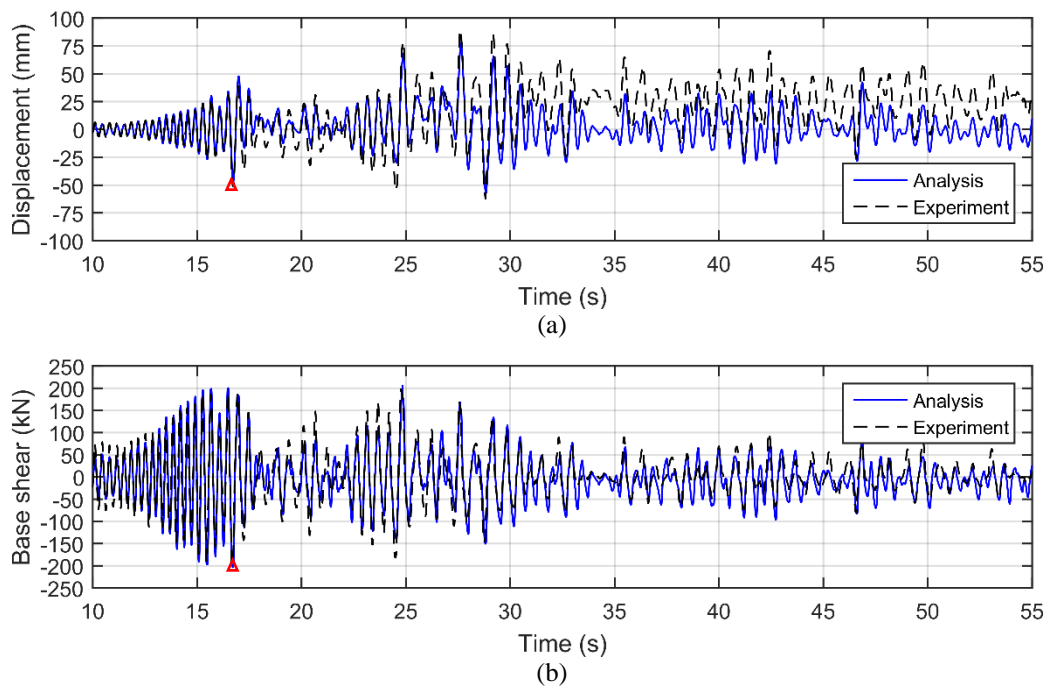


Figure 9-11: Comparison between response history of Frame 1 predicted by the proposed model and the experimental test in terms of (a) lateral displacement of the frame's first storey as well as (b) its base shear.

This case puts the model's capabilities to the test, as it is both an R/C sub-assembly instead of an individual member and an actual dynamic analysis instead of a quasi-static one. The finite element model applied herein for the inelastic response-history analysis of the R/C frame is shown in Figure 9-10a. It consists of three column elements and two beam elements, keeping the minimal number of finite elements required, ensuring low computational cost (Mergos & Kappos, 2012). The columns are assumed to be fixed at the bottom. Rigid offsets are employed to model the joint regions of the frame. Viscous damping is modelled using the Rayleigh model with an equivalent viscous damping equal to 2% of critical for the fundamental vibration mode, as suggested by free-vibration tests conducted before the test (Elwood & Moehle, 2008b). The

mass has been assumed lumped at the top of the frame. The values used for the descending branch slopes are an average of Eq. 4-10 and 4-11 (1<sup>st</sup> segment) and Eq. 4-13 and 4-14 (2<sup>nd</sup> segment), to reflect the expected combination of cyclic and in-cycle strength degradation.

The response histories of the lateral displacement of the first storey as well as the base shear of the frame are shown in Figure 9-11. The hysteretic response of the entire R/C frame and the middle column, the cumulative energy dissipation of the frame, as well as hysteretic local shear deformations of the mid-column, are presented in Figure 9-12. A triangular marker is inserted in every diagram of Figure 9-11 and Figure 9-12 to signal the onset of shear failure of the middle column. Part of the response is omitted in Figure 9-11 for the sake of clarity, i.e. before 10 s, as it has also been reported in detail in Mergos & Kappos (2012), and after 55 s, as it consists of very low amplitude cycles, fading out to the eventual resting position of the frame. In Figure 9-12a,b and d, the more critical part of the response is shown, i.e. between 15 s and 35 s, for the sake of clarity.

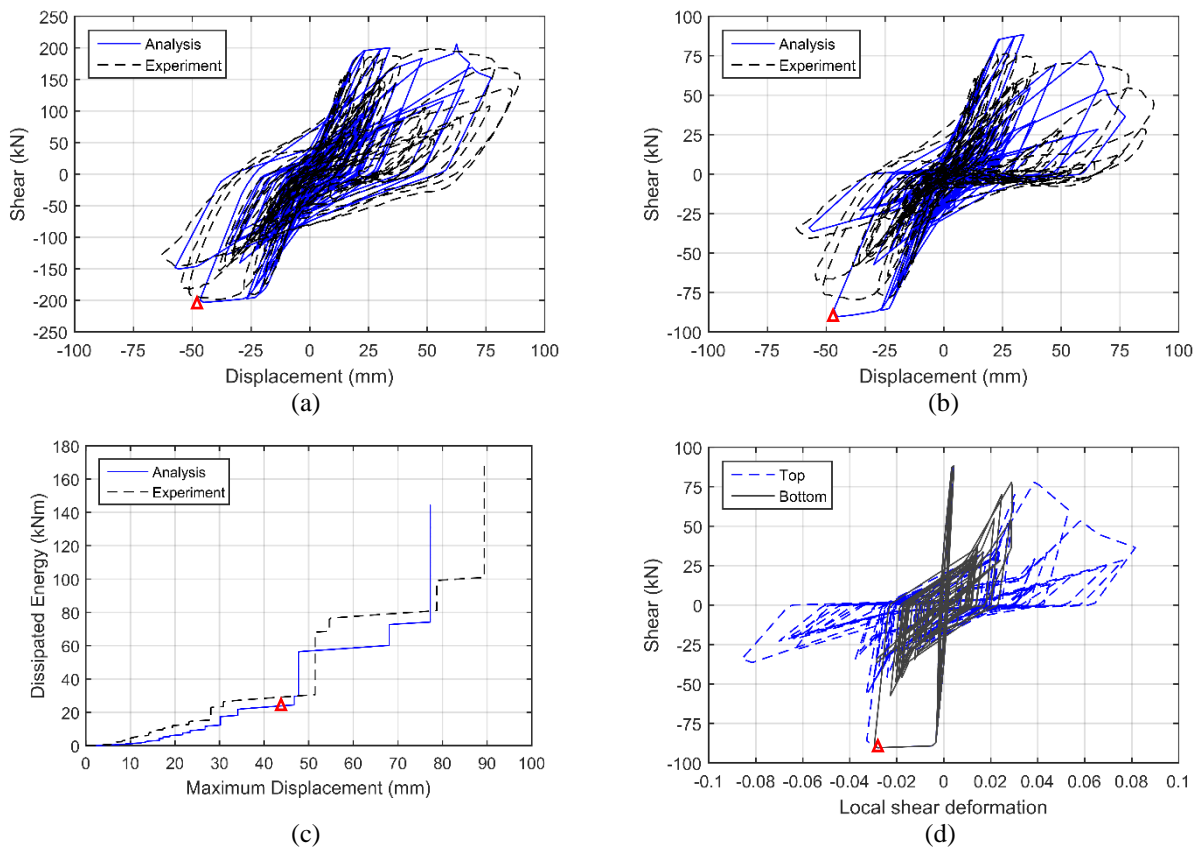


Figure 9-12: Comparison between predicted response of Frame 1 by the proposed model and the experimental test in terms of (a) base shear against lateral displacement of the first storey of the frame and (b) shear force against lateral displacement of the middle column; (c) cumulative dissipated energy throughout the experiment. (d) Analytical prediction of shear force against local shear deformation,  $\gamma$ , of top and bottom plastic hinges of the mid-column.

Shear failure took place at the top of the middle column during the analysis, in line with photographic evidence of the damage (Figure 9-13a), subsequent to flexural yielding of the

column. The predicted shear-damaged zone and bottom plastic hinge are shown in an illustration of the damage, based on the analytical results, in Figure 9-13b; the entire length of the column was predicted to have shear cracking. The other two columns yielded slightly sooner than the middle column as in the experimental test. The key point of shear failure initiation of the mid-column is predicted very accurately at 16.7 s.

As can be seen in Figure 9-11, the experimentally obtained and analytically predicted lateral displacements are on a par up to about 30 s, achieving very good agreement. Thenceafter, there is a shift of the experimental displacements to +30 mm that remains even after the end of the test as a residual lateral displacement, which the analysis does not capture; this discrepancy is in agreement with analytical results published by the same research team that conducted the experiments (Elwood & Moehle, 2008a). This highlights the open challenges in correctly predicting the residual displacements of such R/C sub-assemblages and the complexity of non-linear dynamic analyses. Except for this discrepancy, the analytical response matches very closely the experimental one. The shear failure (Table 9-3) and maximum lateral displacement predictions are fairly good with over- and under-estimation of about 15%, respectively. With regard to base shear, the predicted response seems to be even more accurate, closely observing the experimentally obtained one before and after the initiation of shear failure.

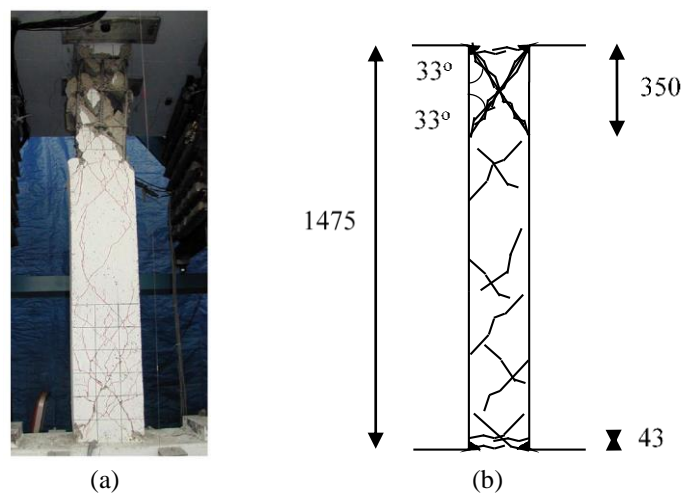


Figure 9-13: (a) Photographic documentation of the damage sustained by Frame 1 (Elwood & Moehle, 2008b); (b) predicted damage by the proposed model.

The analytical and experimental hysteretic responses (Figure 9-12a) show very close agreement, the onset of shear failure and the ensuing shear strength degradation are predicted very well and the resulting analytical cyclic envelope coincides fairly well with the experimental one. This good match can also be seen in Figure 9-12b in the hysteretic response of the middle column. Its maximum strength is overestimated; however, a fairly good prediction of the expected overall behaviour is attained. Despite the fact that the displacements of some large-amplitude

cycles are somewhat underestimated, the post-peak strength degradation follows closely the experimentally measured shear resistance.

Figure 9-12c demonstrates the cumulative energy dissipation throughout the shake-table test. Overall, it is predicted very well, albeit maintaining a small underestimation of about 6 kNm since the very first cycles, wherein limited energy is dissipated at the experimental test that is considered completely elastic behaviour by the analytical model. At the end of the test, there is a 15% difference between the two values (Table 9-3).

Table 9-3: Accuracy measures of the analyses of Frame 1 and Frame 2.

	$R_E$	$R_{SFD}$	$R_{AFD}$
<b>Frame 1</b>	0.852	1.152	N/A
<b>Frame 2 mean</b>	0.262	0.622	0.617
<b>Frame 2 low</b>	0.927	0.622	0.762

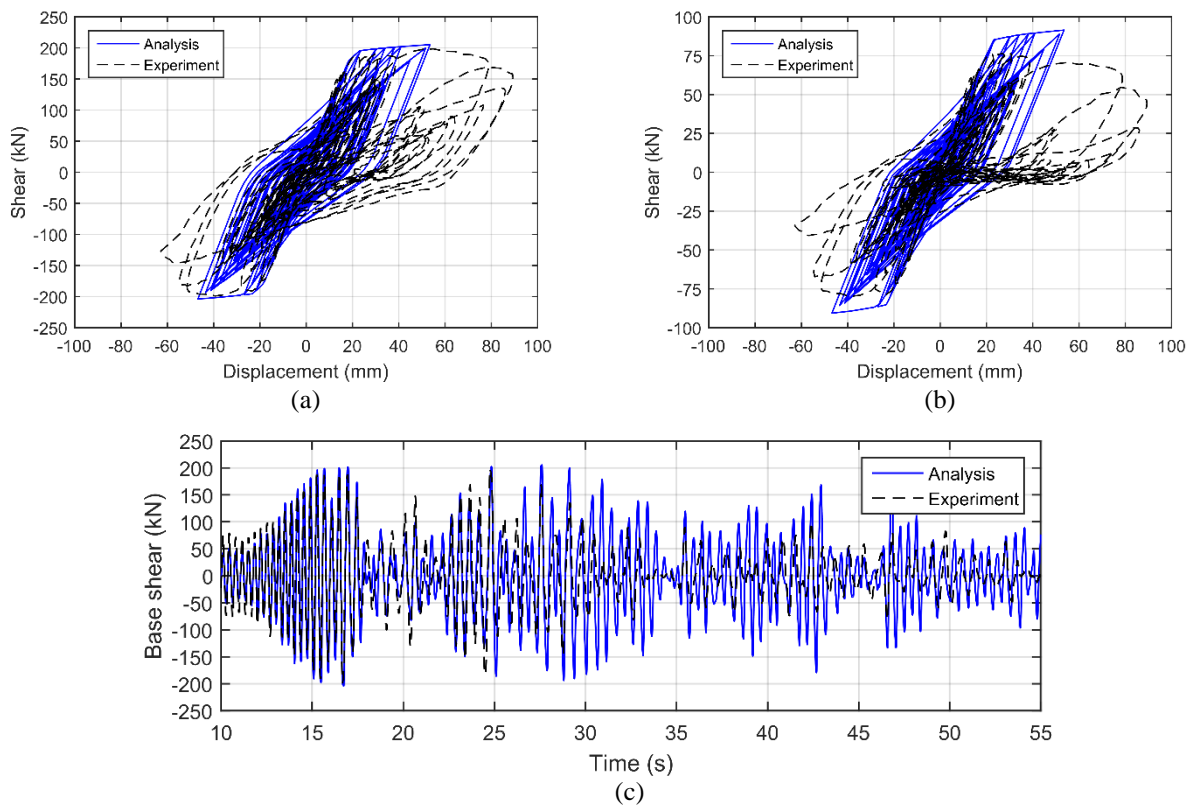


Figure 9-14: Comparison between the analytically predicted response of Frame 1 without considering shear failure and the experimental test in terms of (a) base shear against lateral displacement of the first storey of the frame, (b) shear force against lateral displacement of the middle column and (c) base shear history.

Figure 9-12d shows the local  $V - \gamma$  relationships at the top and bottom plastic hinges of the mid-column. The local shear deformations at the top are way larger than the others, as expected due to shear failure, reaching values of almost 0.10. Simultaneously, the bottom segment also reaches significant shear deformations of up to 0.03, due to shear-flexure interaction inside the plastic hinge length. However, the bottom shear deformation is capped by its value at the onset

of shear failure, in line with the finite element model formulation, whilst the top follows the prescribed post-peak descending branch.

Analytical results precluding the effect of shear failure are presented in Figure 9-14 for comparison. The response is identical up to the onset of shear failure, deviating substantially after that, though. There is no strength degradation in the hysteretic response depicted in Figure 9-14a and b, which the experimental response exhibits, hence the strength and the energy dissipation are grossly overestimated at the latter stages of the response; it is reminded that this being a dynamic analysis, the predicted and actual displacements at each step are generally different, i.e. an accelerogram rather than a displacement history is applied in the experimental test as well as the analysis. The strength overestimation can be much more clearly seen in Figure 9-14c, particularly after about 27 s. Simultaneously, the analytical model is rendered much stiffer, resulting in far lower lateral displacements of the R/C frame. This can be more clearly observed in Figure 9-14a, with the frame's lateral displacements being significantly underestimated, barely exceeding 50 mm, while the experimental response reaches 90 mm. This is in line with comments made by the research team that conducted the experiments, who also investigated analytically identical, non-degrading frames (Elwood & Moehle, 2008b), and underlines the significance of appropriately modelling the post-peak response in shear deficient R/C sub-assembly.

#### 9.4.2 Frame 2

One more frame specimen, namely Frame 2, was tested by the aforementioned research team (Elwood & Moehle, 2008b). The design and loading history are exactly the same, the only difference being the axial load applied on the middle column, which is 303 kN instead of 128 kN, resulting in an axial load ratio of 0.24 instead of 0.10. This was applied with hydraulic jacks directly on the column, hence not changing the distributed vertical load applied upon the beams nor the axial load carried by the exterior columns. The finite element model of the structure (Figure 9-10) and the applied accelerogram are the same as in Frame 1 above.

The response histories of the lateral displacement of the first storey as well as the base shear of the frame are shown in Figure 9-15. The hysteretic response of the entire R/C frame and the middle column, the cumulative energy dissipation of the frame, as well as hysteretic local shear deformations of the mid-column, are presented in Figure 9-16. A triangular and a square marker are inserted in every diagram of Figure 9-15 and Figure 9-16 to signal the onset of shear and axial failure of the middle column, respectively; these markers refer to the analytical response. Part of the response history is omitted in Figure 9-15 for the sake of clarity, i.e. before 10 s, as it consists of very low-amplitude elastic cycles. The entire hysteretic response is included in Figure

9-16. In Table 9-3, this analysis is annotated as “Frame 2 mean”, as it is based on mean values of the calculated post-peak parameters.

Shear failure took place at the top of the middle column during the analysis, in line with photographic evidence of the damage (Figure 9-17a), subsequent to flexural yielding of the column. The predicted shear-damaged zone and bottom plastic hinge are shown in an illustration of the damage, based on the analytical results, in Figure 9-17b; the entire length of the column was predicted to have shear cracking. The other two columns yielded slightly sooner than the middle column, as in the experimental test. The key point of the onset of shear failure of the mid-column is predicted very accurately at 16.7 s, while the onset of axial failure is analytically predicted soon after that owing to the high values of shear strength degradation calculated from Eq. 4-10 and Eq. 4-13.

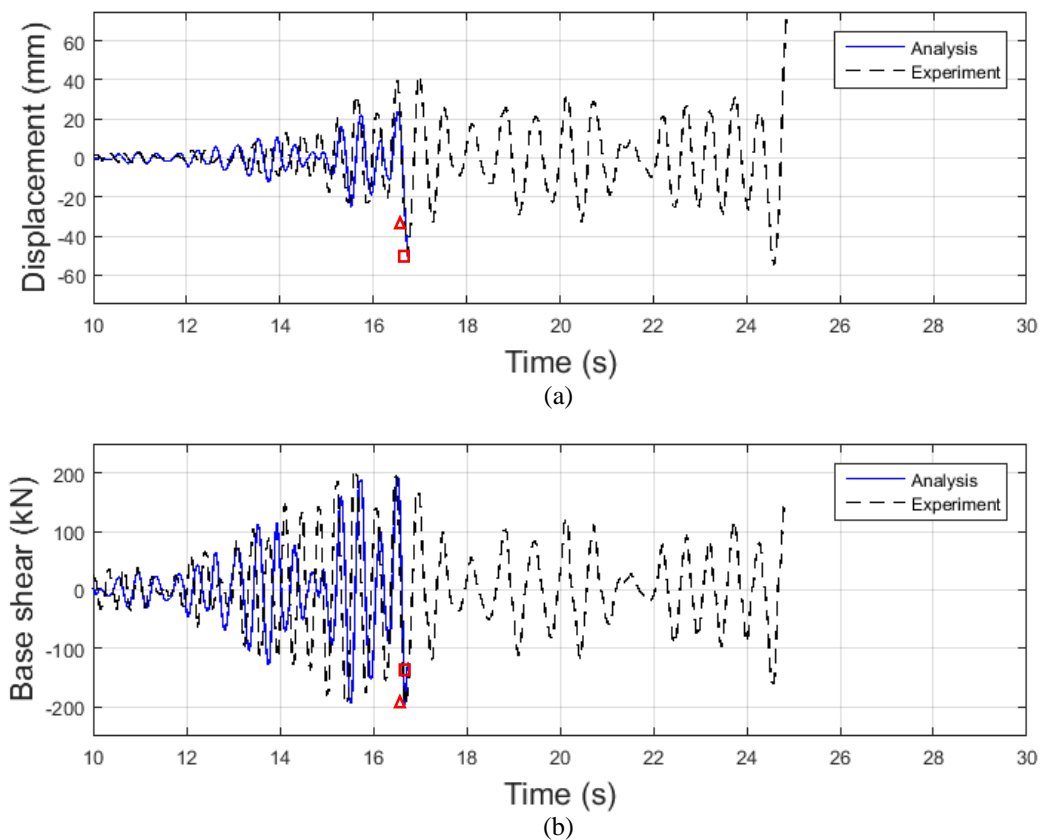


Figure 9-15: Comparison between response history of Frame 2 predicted by the proposed model and the experimental test in terms of (a) lateral displacement of the frame’s first storey as well as (b) its base shear.

As can be seen in Figure 9-15, the experimentally obtained and analytically predicted lateral displacements are on a par for the better part of the first 17 s, when the analytical model prematurely predicts the onset of axial failure. There are only a couple of cycles where discrepancies can be seen at around 14-15 s, but besides this a good overall agreement is achieved. With regard to base shear, the predicted response seems to be even more accurate,

closely observing the experimentally obtained before the initiation of shear failure. Again, only a couple of discrepancies can be observed, mainly at 15 s.

The analytical and experimental hysteretic responses (Figure 9-16a) agree in the pre-peak response. Nevertheless, the onset of shear and axial failure displacement predictions are both significantly lower than the test values (Table 9-3), almost by 40%. The post-peak degradation is predicted to be far more severe than experimentally recorded. Similarly, in Figure 9-16b, the hysteretic response of the middle column is shown where the same trends can be seen.

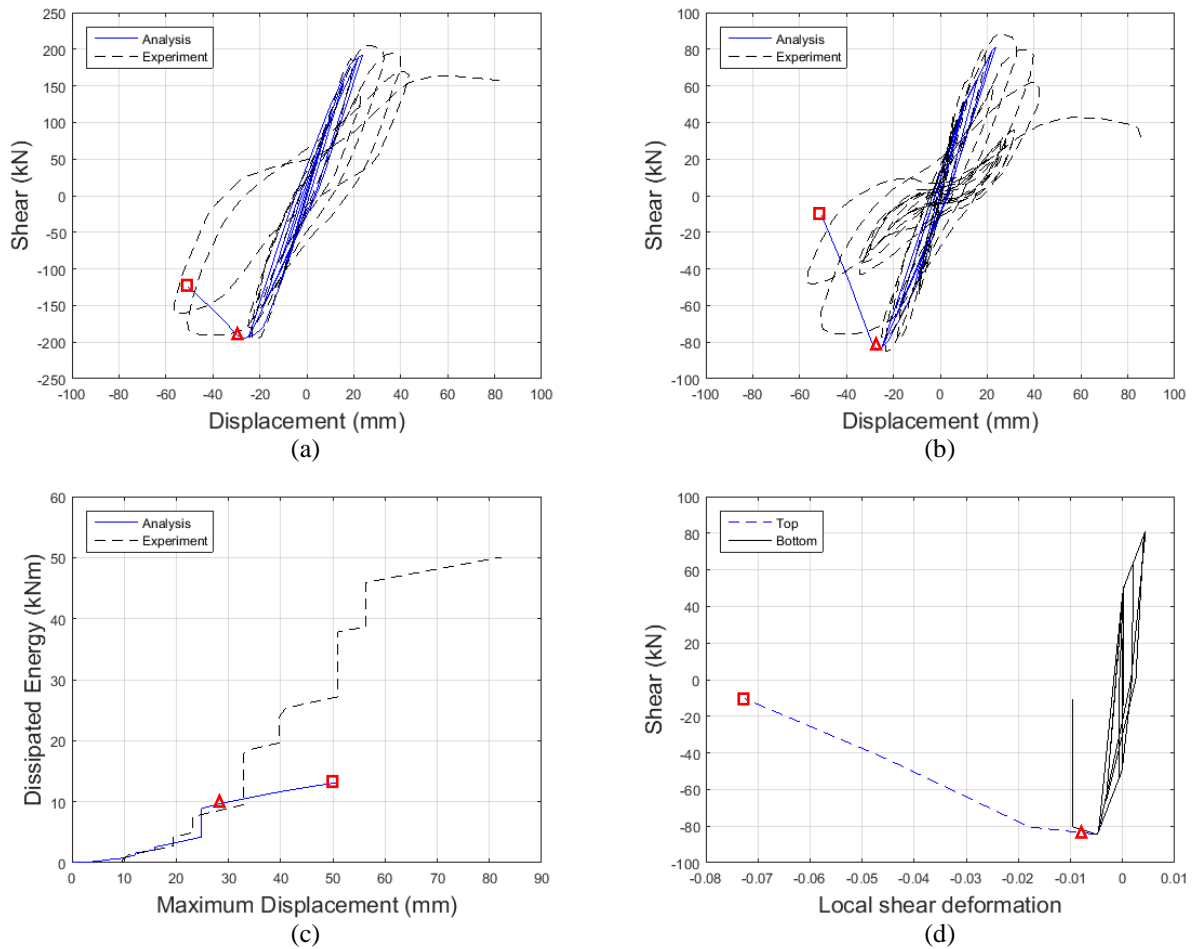


Figure 9-16: Comparison between predicted response of Frame 2 by the proposed model and the experimental test in terms of (a) base shear against lateral displacement of the first storey of the frame, (b) shear force against lateral displacement of the middle column, and (c) cumulative dissipated energy throughout the experiment. (d) Analytical prediction of shear force against local shear deformation,  $\gamma$ , of top and bottom plastic hinges of the mid-column.

Figure 9-16c demonstrates the cumulative energy dissipation throughout the shake-table test. It is found to be predicted most accurately up to a maximum lateral displacement of about 33 mm. Nonetheless, the experimental one keeps rising significantly after that, leading to an  $R_E$  of only 0.262 at the end of the test (Table 9-3). Figure 9-16d shows the local  $V - \gamma$  relations at the top and bottom plastic hinges of the mid-column. The local shear deformation at the top is way larger than the bottom, increasing sharply after the onset of shear failure in a pulse-type

manner, leading to zero shear resistance of the middle column and the consequent onset of axial failure. The bottom shear deformation, although reaching significant deformations due to shear-flexure interaction inside the plastic hinge length, is capped by its value at the onset of shear failure, in line with the finite element model formulation.

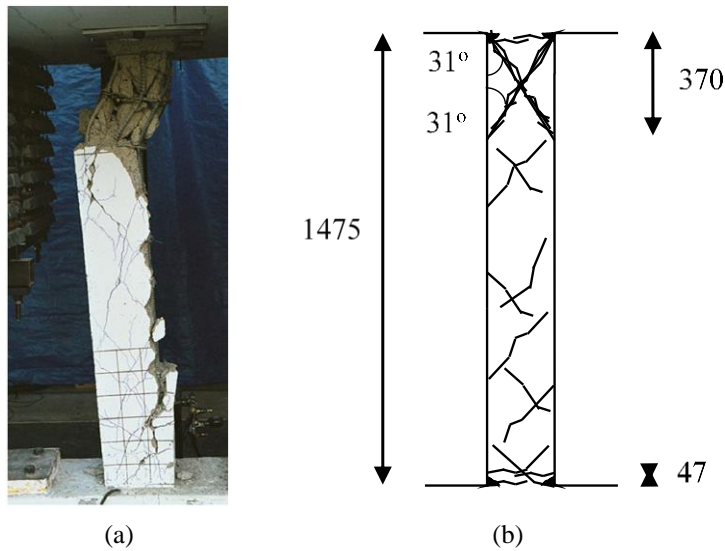


Figure 9-17: (a) Photographic documentation of the damage sustained by Frame 2 (Elwood & Moehle, 2008b); (b) predicted damage by the proposed model.

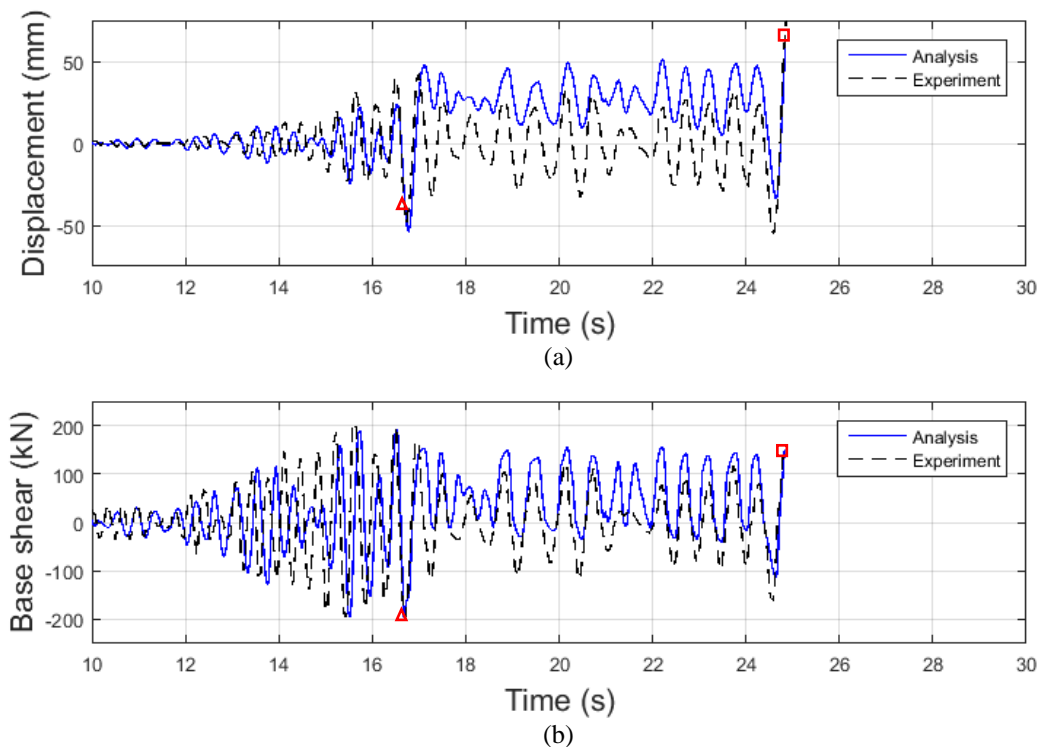


Figure 9-18: Comparison between response history predicted by the proposed model (Frame 2 low) and the experimental test in terms of (a) lateral displacement of the frame's first storey as well as (b) its base shear.

Comparing the experimental response of Frame 1 and Frame 2 (Figure 9-12 and Figure 9-16), it is noteworthy that the sole change of axial load carried by one of the three frame columns leads

to very high decrease of the energy dissipated during cycling, namely a decrease of more than two thirds, as well as to much more significant shear strength degradation once shear failure initiates. At the same time, however, there is no significant difference in the maximum base shear or lateral displacement reached.

Given the already discussed high uncertainty in post-peak response (see chapter 4), the frame was analysed once more, this time using lower values for the descending branch slope, equal to the mean predicted value minus one standard deviation ( $\mu - 1\sigma$ ) for each equation (see chapter 4). The new diagrams are plotted in Figure 9-18 and Figure 9-19. Triangular and square markers are used similarly in every diagram of Figure 9-18 and Figure 9-19. In Table 9-3, this analysis is annotated as “Frame 2 low”.

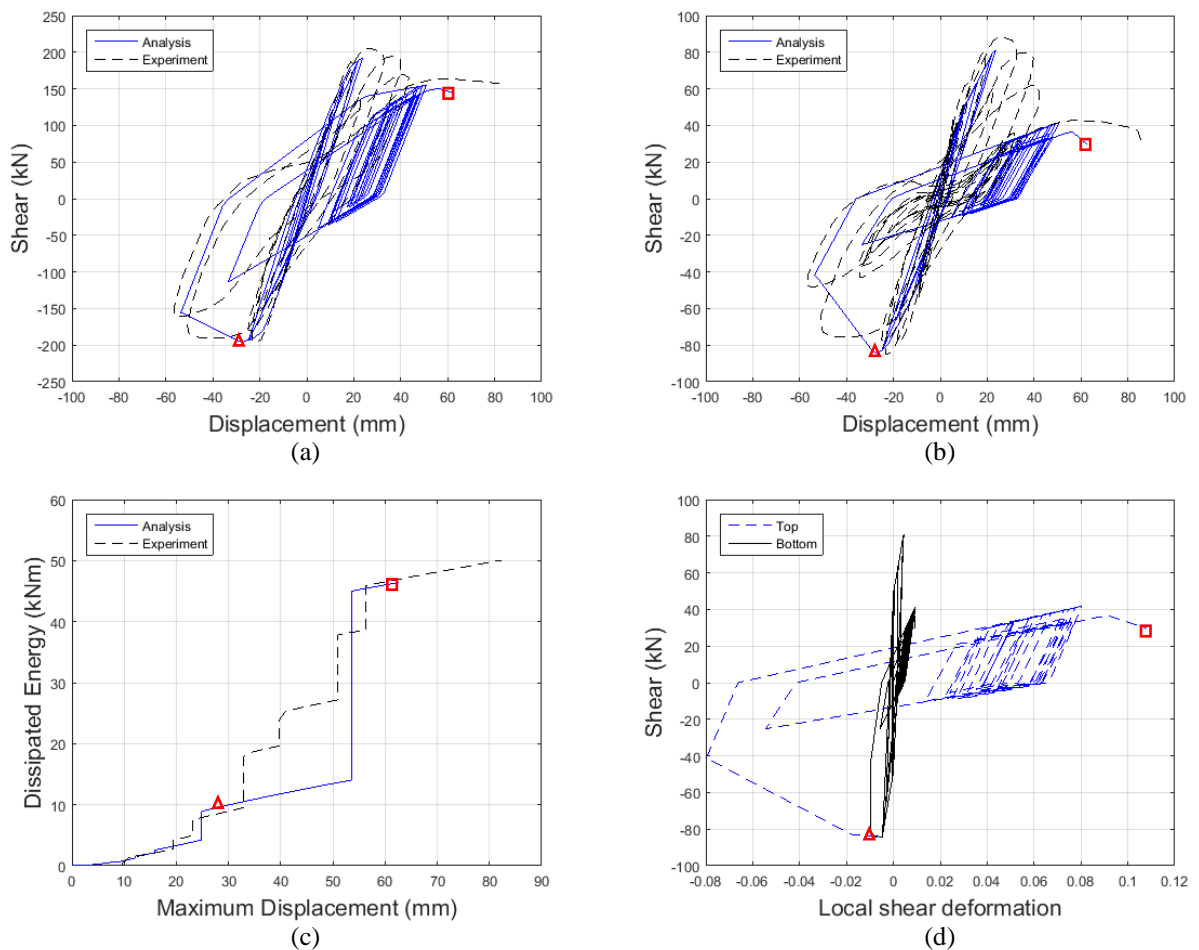


Figure 9-19: Comparison between predicted response by the proposed model (Frame 2 low) and the experimental test in terms of (a) base shear against lateral displacement of the first storey of the frame and (b) shear force against lateral displacement of the middle column; (c) cumulative dissipated energy throughout the experiment. (d) Analytical prediction of shear force against local shear deformation,  $\gamma$ , of top and bottom plastic hinges of the mid-column.

As can be seen in Figure 9-18 and Figure 9-19, the analytically predicted response is way closer to the experimental one than in the previous analysis, a. Both displacements and base shear closely match the experimental results, exhibiting only a small shift of base-line to the positive

direction just after the onset of shear failure, which is not recorded experimentally. The key stages of initiation of shear and axial failure are most accurately predicted at 16.7 and 24.9 s, respectively, the difference in the corresponding lateral displacements being slightly less than 40% and 30%, respectively (Table 9-3).

Both hysteretic responses (Figure 9-19a,b) show very close agreement both in the pre-peak as well as post-peak range of the response. Despite the reported difference in lateral displacement at the onset of shear and axial failure, the overall behaviour seems to be well-predicted and the rate of shear strength degradation is modelled very well. Furthermore, Figure 9-19c demonstrates the cumulative energy dissipation, which is deemed to be very accurate; as a matter of fact, the only discrepancy arises at the very last millimetres of the shake-table test, which multiplied by the base shear add another 5 kNm to the energy dissipated thus far. This difference eventually produces an  $R_E$  of 0.914 at the end of the test (Table 9-3). There is also some ostensible deviation between 33 mm and 53 mm, which arises due to the pulse-type response of the cycle where shear failure initiation is detected; in other words, the displacement of about 53 mm is directly attained in this cycle, hence skipping the scale-like increase of maximum displacement that the experimental response exhibits (Figure 9-19c).

## 9.5 SPECIMENS WITH INCREASING AXIAL LOAD

The only experiments, wherein the applied axial load was increased just after or before the onset of shear failure are the ones presented herein (chapters 6 and 7). These will be analysed in this section and their characteristics can be found in chapter 6. It is reiterated that the verification against these tests provides an excellent opportunity for an independent evaluation of the model's predictive capabilities, as they were not included in the initial database, upon which the model was based.

Specimen FSC\_2 was tested under cyclic lateral loading and an axial load increase just before the onset of shear failure. The analytically predicted response is compared with the experimental one in Figure 9-20. The steep strength degradation rate after the onset of shear failure seems to be captured in the analytical response with some underestimation, while the onset of shear failure is very accurately predicted (Table 9-4). The energy dissipation closely matches the experimental one, except for a jump at the displacement level of  $\pm 12$  mm, mostly owing to thinner loops produced experimentally than in the predicted response; this eventually led to an approximately 13% overestimation at the end of the test (Table 9-4). The analysis was stopped at the second cycle of  $\pm 18$  mm, however the displacement at the onset of axial failure would be detected at 21.12 mm, leading to a 17% overestimation compared to the experimental one (Table 9-4).

Shear response seems to be also captured quite well, with some overestimation of the displacements in the positive direction pre-peak and slight overestimation in the negative direction post-peak (Figure 9-20b). The analytical deformation decomposition (Figure 9-20c) seems similar to the experimental one (Figure 7-16c) overall, albeit systematically overestimating the shear component.

Specimen FSC\_3 was tested under cyclic lateral loading and an axial load increase just after the onset of shear failure. The analytically predicted response is compared with the experimental one in Figure 9-21. The very high strength degradation rate after the onset of shear failure and subsequent sudden loss of the biggest part of the lateral load resistance from  $\pm 12$  mm to  $\pm 15$  mm is well-captured in the negative direction of the predicted hysteretic response, but not as well in the positive direction. The displacement at the onset of axial failure would be overestimated by about 47% (Table 9-4). Nevertheless, the predicted energy dissipation is on a par with the experimental one all along the test, eventually having a very small underestimation of about 5%.

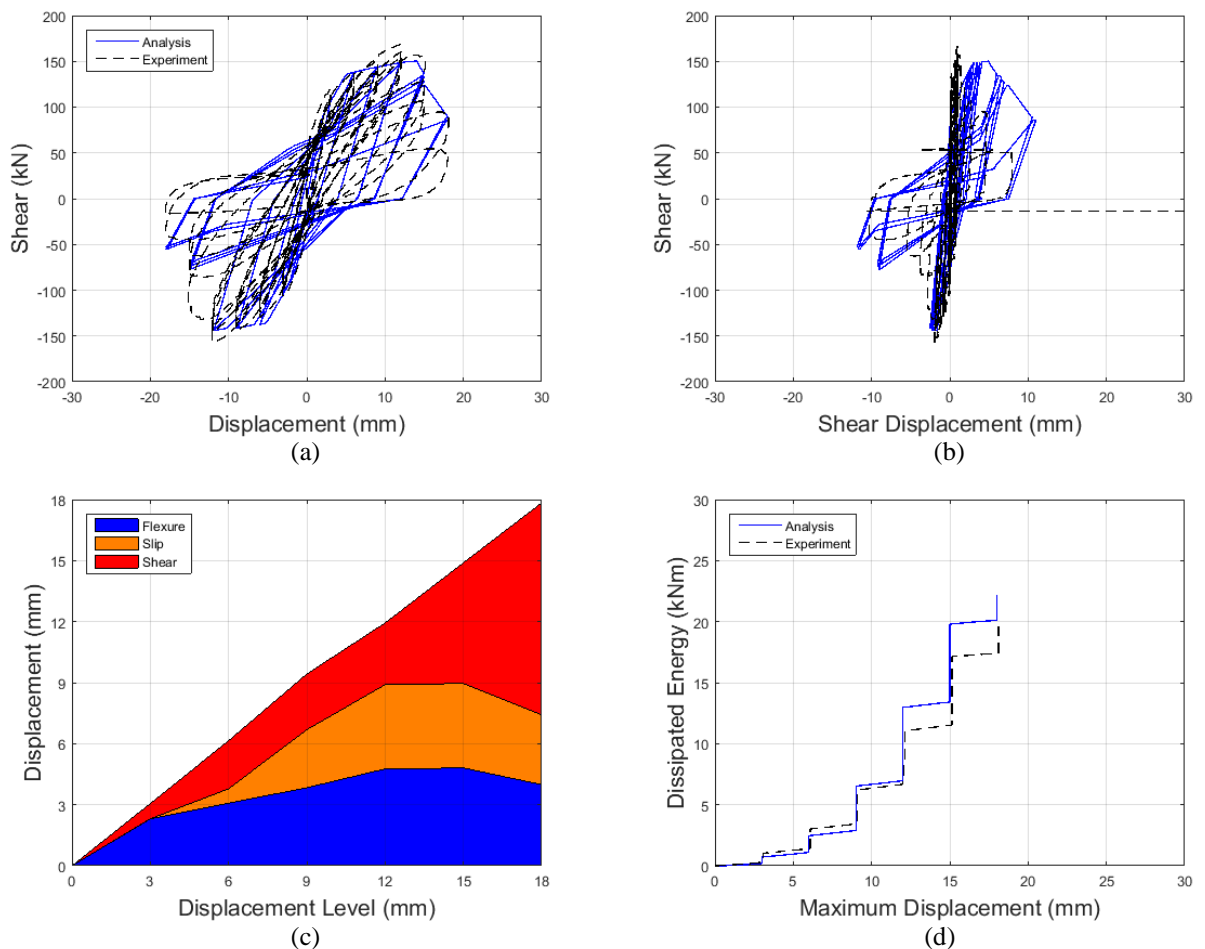


Figure 9-20: Comparison between the predicted response of FSC\_2 by the proposed model and the experimental one in terms of (a) shear force against lateral displacement, and (b) shear displacement. (c) Decomposition of the element's lateral displacement components throughout the analysis. (d) Comparison between predicted and experimental cumulative dissipated energy.

Table 9-4: Accuracy measures of the analyses of specimens SC\_2, SC\_3, FSC\_2 and FSC\_3.

	$R_E$	$R_{SFD}$	$R_{AFD}$
FSC_2	1.130	0.993	1.173
FSC_3	0.952	0.992	1.472
SC_2	1.311	1.075	1.209
SC_3	1.430	0.998	N/A

The shear displacement seems to be captured quite well, with considerable overestimation pre-peak, but only some overestimation in the negative direction post-peak (Figure 9-21b). The analytical deformation decomposition (Figure 9-21c) is very similar to the experimental one (Figure 7-16e), with some overestimation of the shear component in the two displacement steps preceding the onset of shear failure.

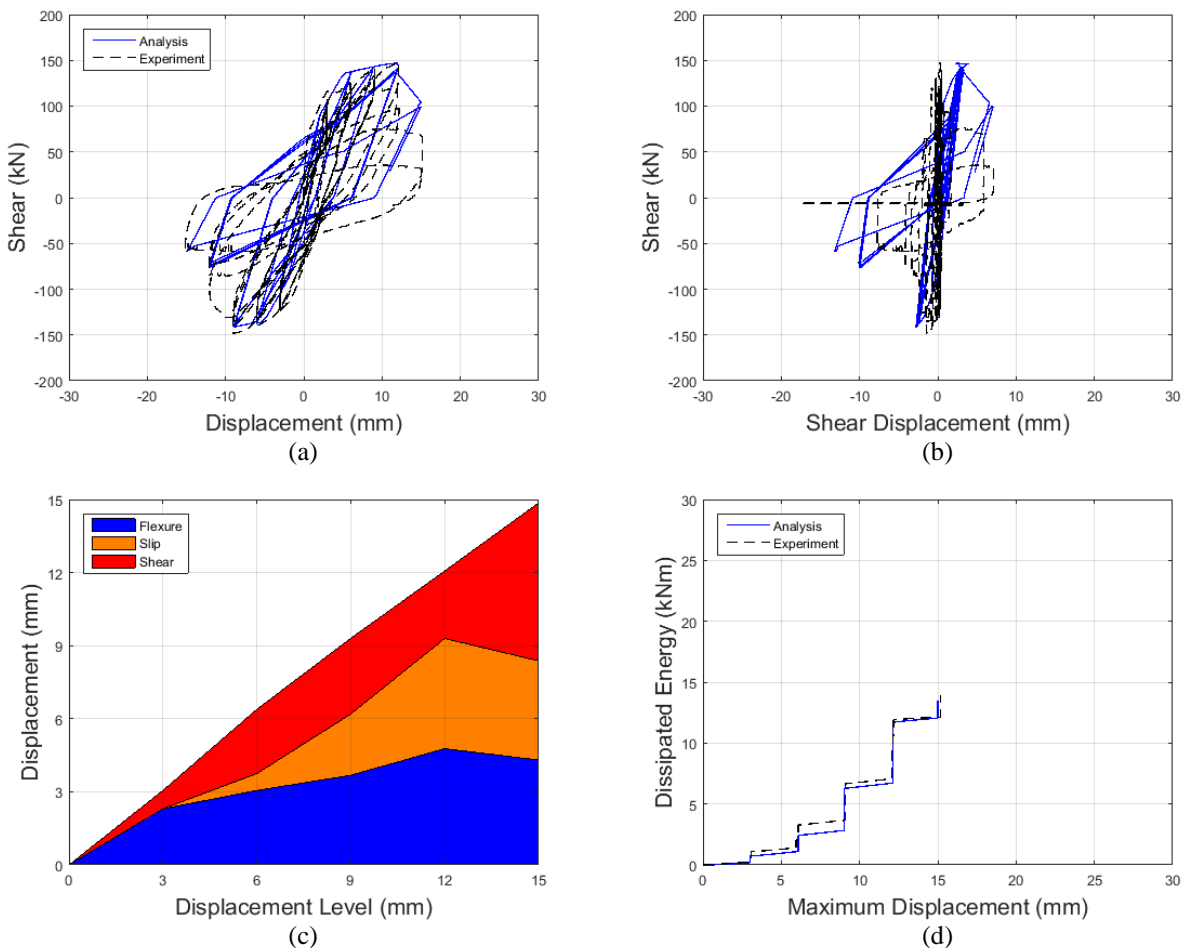


Figure 9-21: Comparison between the predicted response of FSC\_3 by the proposed model and the experimental one in terms of (a) shear force against lateral displacement, and (b) shear displacement. (c) Decomposition of the element's lateral displacement components throughout the analysis. (d) Comparison between predicted and experimental cumulative dissipated energy.

Specimen SC\_2 was tested under cyclic lateral loading and an axial load increase just before the onset of shear failure. The analytically predicted response is compared with the experimental one in Figure 9-22. The pre-peak and post-peak response seem to be captured well; the descending branch slope after the onset of shear failure seems to be captured with some

underestimation in the hysteretic response, partly due to having a parallel shift owing to the overestimation of 7.5% of the displacement at the onset of shear failure (Table 9-4). The onset of axial failure would be predicted with approximately 21% overestimation of the corresponding experimentally observed displacement (Table 9-4). The energy dissipation matches well the experimental one pre-peak, however deviating post-peak, owing to narrower loops produced experimentally than in the predicted response; this eventually led to a considerable overestimation of the cumulatively dissipated energy at the end of the test (Table 9-4).

The shear hysteretic response (Figure 9-22b) includes some overestimation both before and after the peak, being overall similar to the experimental one. Comparing the deformation decomposition (Figure 9-22b) with the experimental one (Figure 7-17c), there seems to be slight overestimation of the shear component pre-peak, however the agreement is good in the post-peak domain, with the flexural and bond-slip components retracting on a par with the experimentally estimated ones.

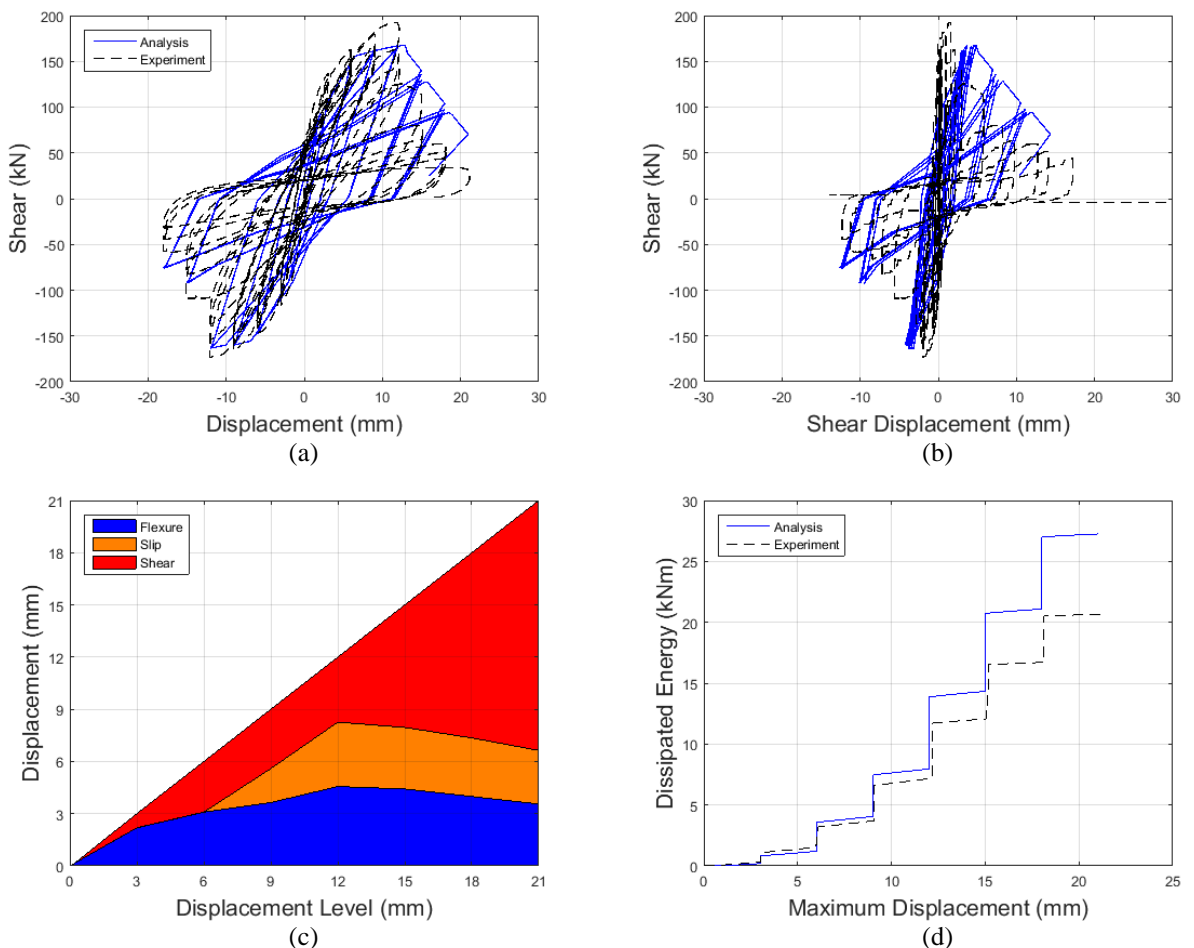


Figure 9-22: Comparison between the predicted response of SC\_2 by the proposed model and the experimental one in terms of (a) shear force against lateral displacement, and (b) shear displacement. (c) Decomposition of the element's lateral displacement components throughout the analysis. (d) Comparison between predicted and experimental cumulative dissipated energy.

Specimen SC\_3 was tested under cyclic lateral loading and an axial load increase just before the onset of shear failure (initially planned to increase after the onset of shear failure, as explained in section 7.2). The analytically predicted response is compared with the experimental one in Figure 9-23. The hysteretic response match is very good overall. The strength degradation rate after the onset of shear failure is underestimated to some extent. The displacement at the onset of shear failure is predicted accurately (Table 9-4). On the other hand, the onset of axial failure is predicted at the last displacement level, while no axial failure was experimentally observed even when the specimen reached a displacement of 27 mm. The predicted cumulative energy dissipation is overestimated systematically in the post-peak response, owing to narrower loops produced experimentally than in the predicted response. The dissipated energy at the end of the test was overestimated by about 43% (Table 9-4).

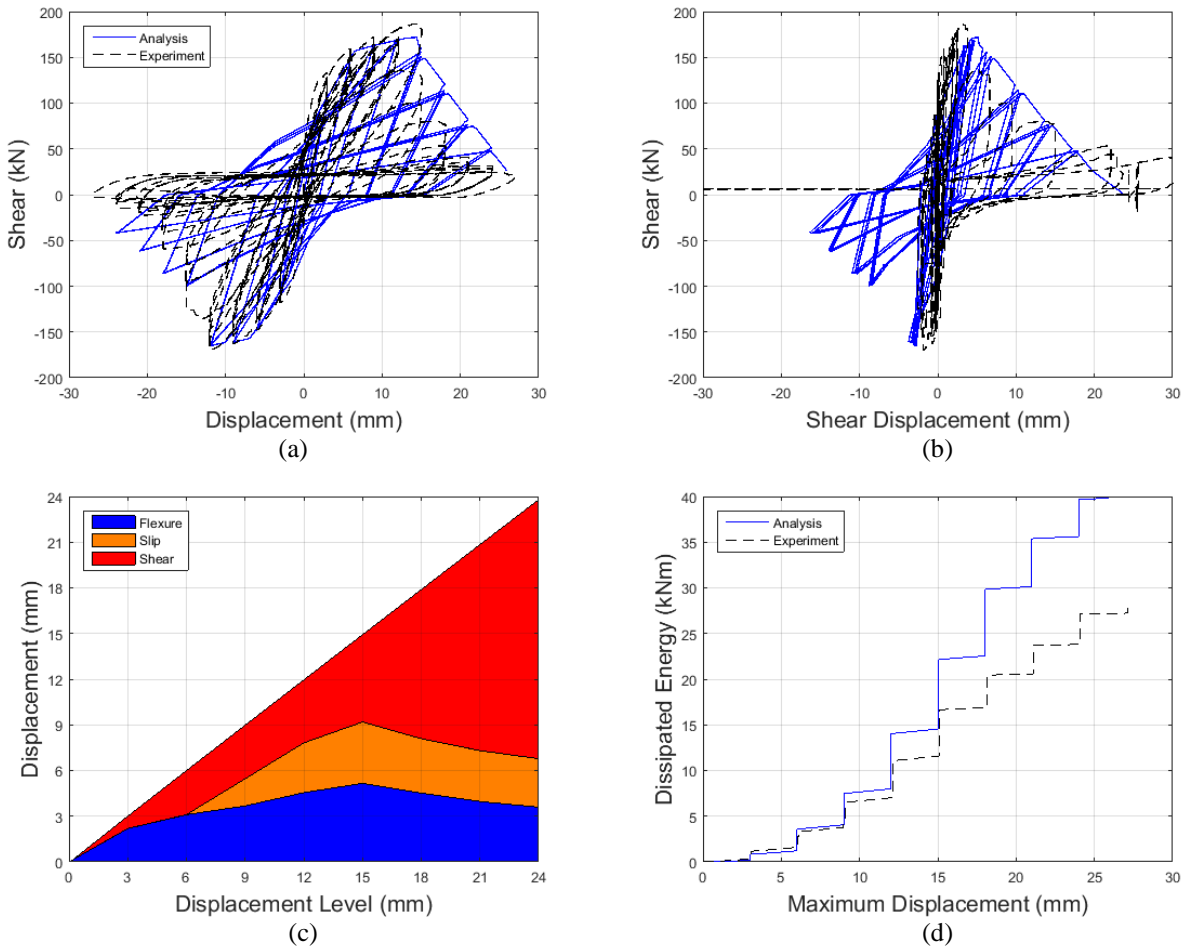


Figure 9-23: Comparison between the predicted response of SC\_3 by the proposed model and the experimental one in terms of (a) shear force against lateral displacement, and (b) shear displacement. (c) Decomposition of the element's lateral displacement components throughout the analysis. (d) Comparison between predicted and experimental cumulative dissipated energy.

The experimental shear response exhibits an asymmetry (Figure 9-23b), as explained in section 7.4. The analytical prediction, of course, does not capture this, producing a symmetrical 'average' response in both directions, which is believed to be close to the actual response of the

column. The deformation decomposition (Figure 9-23c) is in very good agreement with the experimental one (Figure 7-17e), having some discrepancies at some points.

Of course, as explained in chapter 8, the increase in lateral load resistance observed at the displacement levels of  $\pm 12$  mm in FSC\_2, SC\_2 and of  $\pm 15$  mm in SC\_3 is not captured by the analytical beam-column model, since the pre-peak parameters are not axial-load-dependent.

In conclusion, the beam-column model is found to fare more than satisfactorily in these four cases of specimens with an axial load increase just before or after the onset of shear failure. The predictions of post-peak strength degradation rate and displacement at the onset of axial failure are adequately close to the experimentally observed ones. Moreover, the shear component – as well as the rest of the deformation components – of the response, which are the major focus of this study, are predicted very well overall in cases of independent tests, which is very positive for the predictive abilities of the finite element model.

Verifications against specimens with decreasing axial load (Nakamura & Yoshimura, 2014) are not included, as it is not clear how such displacement capacities (drifts of the order of 20%) were obtained. It is reminded that the slope of the descending branch is not a physical property of a member, but always depends on the way the test is carried out (among other factors).



## Chapter 10: CONCLUSIONS AND FUTURE WORK

---

### 10.1 SUMMARY AND CONCLUSIONS

The contributions of this research project will be herein summarised and the conclusions highlighted, following the structure of the thesis, i.e. in three parts addressing the respective aspects of this project.

#### ***Part I: Investigation of the Post-Peak Response of Shear-deficient R/C Members***

The largest database of shear and flexure-shear critical R/C columns cycled well beyond the onset of shear failure and/or up to the onset of axial failure was compiled. This formed the basis for the development of empirical relationships and criteria pertinent to shear failure, post-peak response, and axial failure and can form a solid foundation for future endeavours to shed further light on other aspects of the post-peak response of shear-deficient R/C columns.

Empirical relationships were developed for key parameters defining the response after initiation of shear failure. These parameters are:

- The critical shear crack angle, hence the critical shear length, wherein damage concentrates after the onset of shear failure. The proposed relationship differentiates between shear and flexure-shear critical specimens and is found to be more accurate than existing models.
- The descending branch slope(s) of the shear response curve after the onset of shear failure. Separate expressions were proposed for a bilinear curve with breaking point at 50% shear strength degradation with independent slopes and a linear one. Moreover, there are different relationships for monotonic loading, cyclic loading, or a mix of both, hence attempting to separate in-cycle and cyclic strength degradation as much as feasible based on the available data.
- The average local post-peak shear deformation at the onset of axial failure.

It is reiterated that the scatter associated with these parameters is significant (CoV of 20% - 70%), as it is influenced by the very high uncertainty inherent in post-peak phenomena, arising among other factors from the difference in the history of demands and experimental set-up used in each case, as well as the randomness of the succession of degradation phenomena taking place at a lower level.

These relationships are used in the beam-column model proposed herein, but could also be useful in other finite element models. Additionally to the expressions per se, noteworthy

findings, which can be useful for analytically modelling shear-deficient R/C components or future experimental investigations on such elements, are the following:

- Lower axial load, higher transverse reinforcement content and the occurrence of prior flexural yielding – as opposed to pure shear failure – were shown to result in the formation of a higher critical shear crack angle, with respect to the longitudinal axis of the specimen. On the other hand, the angle was shown to be independent of the longitudinal reinforcement content.
- Initiation of shear failure in one direction was shown to only have a minor effect on the degradation rate in the other direction, i.e. their descending branch slopes tend to be equal no matter which side – positive or negative – shear failure first appeared in.
- The data suggests either that practically no residual strength is developed in shear-deficient R/C columns – at least those with the characteristics of this database – or that axial failure occurs in most specimens before they reach their residual resistance.
- Shear critical specimens tend to exhibit mostly convex post-peak descending branch shapes, possibly influenced by shear failure leap (a loss of a potentially substantial part of the shear strength as soon as shear failure initiates), which was observed in some cases; however, this phenomenon could not be modelled at this stage. Flexure-shear critical specimens mostly exhibit approximately linear curves with some convex and some concave ones.
- Defining a descending branch by a line connecting the onsets of shear and axial failure, as done in some previous works, instead of fitting a least-squares line starting from the onset of shear failure could significantly under- or overestimate the resulting dissipated energy. In the case of a convex curve, there would be overestimation of the energy dissipation; the opposite would happen in a concave curve. The deviation would generally be larger the farther away from a linear descending branch a specimen's post-peak strength degradation curve shape is.
- The post-peak response is generally subject to very high uncertainty. However, relationships for monotonic tests have considerably lower variation compared to the cyclic ones. This is due to the fact that only in-cycle degradation is captured in the former, while cyclically loaded specimens are substantially affected by the displacement history leading to potentially low or high cyclic strength degradation, thus producing extra uncertainty.
- Higher transverse and longitudinal reinforcement content, as well as lower axial load are shown to reduce the post-peak shear strength degradation rate, i.e. resulting in a

milder descending branch slope, and lead to higher deformability, i.e. greater local shear deformation at the onset of axial failure.

- Shear strength has been typically considered zero at the onset of axial failure. It was shown herein that this is not a valid assumption; its adoption could lead to high discrepancies by producing much steeper descending branches and great underestimation of the energy dissipation capacity, especially in cases where axial failure initiates before significant shear strength degradation.

Regarding the inclination of the critical shear crack angle, a specific procedure including geometrical corrections has been presented, in order to acquire it from a photograph of a shear-damaged specimen taken at or after the onset of shear failure. This procedure can be used for the addition of future specimens to the database or in future research endeavours to further study this parameter.

Criteria aiming to identify members susceptible to simultaneous shear and axial failure without the need for rigorous analysis of the entire structure or even individual components, are herein proposed for the first time:

- The main one represents the necessary conditions for the simultaneous failure of a column in the form of a two-parameter classification criterion. It requires knowledge of the axial load carried by the column, its longitudinal and transverse reinforcement characteristics.
- In case transverse reinforcement details are unknown or if a preliminary estimation is to be made, a simplified one-parameter criterion is proposed, which is inevitably associated with higher uncertainty.

Furthermore, more conservative criteria (“extra-safe zones”) have been proposed for use in case of higher safety requirements, e.g. in a code practice context.

In general, R/C columns having low longitudinal or transverse reinforcement content or carrying high axial loads are shown to be vulnerable to this mode of failure.

These are believed to be very useful tools for engineers working on the assessment and retrofit of existing R/C structures. Failure to identify such elements can lead to redistribution of vertical loads at a low lateral deformation level in the case of a ground motion, hence adversely affecting the collapse mode of the whole structure and severely increasing the structure’s collapse probability.

## ***Part II: Experimental Programme***

Vertical loads carried by an axially failing member are subsequently redistributed (though the beam-slab system) to neighbouring vertical elements, which leads to a significant increase of axial load acting on the neighbouring R/C columns. The non-linear lateral response of the latter will be altered as a result of this increase and this needs to be taken into account, in order for reliable progressive collapse analyses of existing R/C buildings to be performed. Nonetheless, this is a problem not addressed in previous studies; this study is the first to experimentally investigate how this axial load increase affects the post-peak response of shear and flexure-shear critical R/C columns, opening for the first time the discussion on this topic.

Six cantilever specimens have been herein designed, fabricated and tested. Three of them are flexure-shear and three shear critical (the latter are also affected significantly by flexure, but markedly less than the former), all of them being representative of older construction. They were tested under a quasi-static cyclic lateral loading based on external displacement control, having their axial load increase just before or after the onset of shear failure.

Axial load increase just before or after the onset of shear failure was found to unequivocally lead to a higher rate of post-peak shear strength degradation and a lower displacement at the onset of axial failure of shear-damaged R/C columns – accompanied by the respective reduction in the total dissipated energy. Nonetheless, a quantifiable pattern cannot be established with regard to the percentage of increase, as in all these tests the axial load was increased by 50%; nor with regards to the effect of the point of increase of the axial load, since in three of them it happened just before and in one just after the onset of shear failure.

Besides the afore-described phenomenon that was investigated, the design characteristics of the specimens are selected with a view to supplementing the existing experimental literature on post-peak response, particularly with respect to the aspect ratio.

Both sets of test specimens exhibit similar hysteretic response, with limited cyclic strength degradation in the pre-peak domain that increases significantly post-peak, limited pinching, remarkable ultimate displacement ductility and quite full loops before the onset of shear failure that afterwards turn into narrower ones with increasing lateral displacement. Shear critical specimens attain higher strength and displacement capacity. All of the specimens are found to have similar energy dissipation capacity, their cumulatively dissipated energy being on a par throughout all cycling stages. Nonetheless, the shear critical ones dissipate considerably more energy in total, due to the aforementioned higher ultimate displacement.

Two codes' capacity models (Eurocode 8-3 & Model Code 2010) were herein compared with the obtained responses. They both resulted in underestimation of the stiffness and strength of the elements. In most cases, the deformation capacity was also underestimated.

All specimens initially developed horizontal flexural cracks– flexure-shear critical specimens more than the shear critical ones –, followed by cross-inclined shear cracks. The former cracks kept increasing in width up to about the onset of shear failure, remaining constant or retracting thereafter, in line with the recorded flexural and bond-slip deformations, as shown through deformation decomposition. The cross-inclined cracks appeared before the onset of shear failure, they turned into full-depth cracks at the peak and kept increasing substantially with increasing lateral displacement post-peak, accompanied by slippage and opening of the insufficiently anchored ties; shear deformations followed a similar increasing trend with increasing ductility in all specimens.

Flexure-shear critical specimens exhibited higher percentages of flexural and bond-slip displacements than the shear critical specimens, as well as more moderate increase of shear deformations post-peak.

The secant stiffness decreases significantly with increasing ductility, falling to about a quarter of the predicted elastic stiffness at the peak of the first displacement level, chiefly affected by flexural cracking and shear deformations. It decreases further to hardly 10% of the elastic one by the onset of shear failure. Therefore, it is clear that if an element such as those herein tested is to be deformed up to the onset of shear failure or beyond, a conventional percentage of elastic stiffness – even 50% – would greatly overestimate its resistance at high displacements.

Vertical displacements follow the typical U-shaped pattern up to the onset of shear failure due to member elongation at high lateral displacements, while exhibiting the inverted pattern after that, owing to the effect of shear failure localisation in the post-peak domain. A sudden decrease in axial deformation – or increase in downward displacement – signals the onset of axial failure, accompanied by a corresponding drop of axial load resistance, as has been observed in other similar experimental studies.

The phenomenon of shear failure localisation is central to this research work and one of the cardinal bases, as well as innovation points, of the proposed hysteretic and beam-column models. These tests provided an opportunity to verify this underlying assumption, a task of paramount importance for the reliability of and the confidence in the predictions of the model. It has been shown here through solid experimental proof that deformations after the onset of shear failure tend to be largely attributed to shear. They mostly concentrate in the critical shear

length, a region defined by the diagonal failure planes, in cyclic tests of shear and flexure-shear critical specimens.

From the onset of shear failure onwards the column is effectively turned into two discrete parts, divided along the previously formed full-depth shear crack; in reality it comprises of four discrete parts defined by cross-inclined full-depth shear cracks, however they can be lumped into two parts in each loading direction. When applying load to the top part, it is deformed up to an extent and simultaneously the crack opens further, while the bottom part stays practically still; in effect, it seems to be 'easier' to further open the crack than to deform each discrete part of the column, like a weak link in a chain. This phenomenon manifests as a discontinuity or a 'jump' of horizontal displacements along the element, owing to the localisation of displacement along the shear cracks; simultaneously, the upper discrete part of the column moves downwards relatively to the bottom one when displaced laterally under the constant influence of the axial load, resulting in decreased vertical displacements. This is the first time that clear experimental evidence has been gathered about this phenomenon, which governs the post-peak response of shear-damaged R/C columns, and it can form the basis for analytically modelling post-peak response in the future.

Deformation decomposition was performed for each specimen. Flexural and bond-slip deformations were found to constitute a very high proportion of the total lateral displacement from the initiation of the test up to the onset of shear failure (about 80% on average), thereafter decreasing – in most cases, substantially. Shear deformations follow the inverse pattern, of course, exhibiting a remarkable increase post-peak, dominating the response of the columns.

Additionally, these tests provided an excellent opportunity for verification of the proposed analytical model. Not being included in the compiled database, they allow for an 'external' independent validation of the model's predictive capabilities (see Part III conclusions below). Of course, carrying out a limited experimental programme like this was not expected to furnish enough results to recalibrate a model that is based on such a large number of specimens.

Other pertinent issues explored are:

- A consistent force asymmetry was observed in the hysteretic responses; it was attributed to the experimental setup, more specifically it was caused by the different way of load transfer from the horizontal actuator to the top of the column in the push and pull directions – directly from the actuator or via bolts, nuts and plates, respectively.

- Lash is defined as the sum of all displacements that are not due to the column deformation itself. There have been previous studies where these have been recorded as part of the column deformations, leading to ostensibly more flexible elements. Typical examples of such displacements in the horizontal direction are the sliding of the base on the strong floor, elastic bending of the reaction frame or displacement of the bolts due to inadequate tightening onto the plates. Attempts were made to preclude them as much as feasible from the measurements, primarily using external displacement control instead of the actuator's internal LVDT as well as mounting the metal post, wherefrom the top lateral displacements were measured, on the base of the specimen; hence horizontal displacements induced by sliding of the base that are found to reach up to 4.0 mm were precluded. The lash was found to be very significant, occasionally reaching even 200% of the actual recorded horizontal displacement, particularly in the first displacement levels. Hence, having included it would have led to a completely unrealistic picture of the element's response – assessing it as much more flexible than it actually is. Therefore, one has to be very cautious of such components being included intentionally or not inside reported experimental results.
- The lash decreased considerably after the onset of shear failure, which is attributable to its nature. The specimens have entered the post-peak domain and their resistance is lower than in the first displacement levels. Therefore, the elastic deformations produced by other parts of the system do decrease proportionally. This means that the post-peak response can be much less affected by the inclusion of lash in the results than the pre-peak, therefore both internally and externally controlled experiments were included in the aforementioned compiled database and it is believed not to have a major impact on the uncertainty of the results.
- Simultaneously, this low lash tended to concentrate invariably on the pull side post-peak. This might be due to slight untightening of the bolts during the previous cycles, due to very high forces acting upon them; of course, no bolt is involved in the push direction, and since the specimens' resistance has decreased considerably, the lash on the negative side is negligible.
- In this series, although not having replicated the experiments per se, the first 9 cycles of each set of specimens are “nominally identical”. As expected, the overall responses are quite similar, but there are many slight and few pronounced discrepancies in the curves produced. Besides slight material, geometrical and set-up related differences, the actual member-level response is the result of a plethora of events taking place at micro-level, the random nature of which would lead even the most “identical” specimens to have differences when inspected at a macro-level.

### ***Part III: Beam-Column Analytical Model***

A novel shear hysteretic model was put forward herein, determining the pre- as well as post-peak range of the response of a shear-damaged R/C member up to the onset of axial failure. It is a local hysteretic shear model based on the above proven concept of shear failure localisation, i.e. accounting for the localisation of shear strains, after the onset of shear failure, in a critical length defined by the diagonal failure planes.

It comprises a penta-linear primary curve, accounting for shear cracking, yielding of transverse reinforcement, onset of shear failure, the subsequent post-peak strength degradation and the onset of axial failure. This curve is altered inside an element's plastic hinge to take into account the shear resistance decrease simultaneously with significant shear flexibility increase, owing to the increasing curvature ductility demand. Its pre-peak hysteretic rules – based on a previous model – are herein extended into the post-peak domain, with several improvements proposed for compatibility with the response of specimens after the onset of shear failure.

A beam-column finite element model for shear-deficient R/C elements has been put forward herein. It is a computationally efficient, flexibility-based, distributed inelasticity, phenomenological model predicting the hysteretic non-linear response of shear and flexure-shear critical R/C members up to the onset of axial failure. Being based on local deformation quantities – curvatures, shear deformations and anchorage slip rotations – in lieu of inter-storey displacements, it can account in an unbiased way for the interaction of inelastic flexural and shear deformations, including the gradual decrease of an element's shear resistance and increase of its shear flexibility, and more reliably predict the location and extent of shear deformations and shear damage subsequent to the onset of shear failure. Thus, the response of sub-standard R/C elements can be reliably predicted up to the onset of axial failure following shear failure with or without prior flexural yielding, while simultaneously accounting for potential flexural and anchorage failure modes.

Owing to its formulation, it can avoid shortcomings of previous models, for instance not relying on assumptions about the bending moment distribution, which generally changes during seismic loading, capturing the actual distribution of inelasticity, deformations and damage along the element throughout the analysis, as well as not suffering from numerical localisation issues pertinent to the softening response after the onset of shear failure.

The proposed model was implemented in a finite element structural analysis software. Issues pertinent to the numerical implementation have been described, among which the most salient have to do with the interaction between the model's sub-components. After a segment of the

shear sub-component enters the post-peak domain, the other sub-components' resistance degrades along with it. Simultaneously, the other sub-components unload with a very high stiffness while the shear segment sustains in-cycle strength degradation, the produced lateral displacements effectively being capped at their shear-failure values.

Subsequently, the predictive capabilities of the proposed beam-column model are verified against a multitude of experimental tests, including quasi-static cyclic tests of double-curvature shear and flexure-shear critical R/C columns and dynamic R/C frame shake-table tests. Especially the tests carried out as part of this study, provided an excellent opportunity for independent verification of the proposed analytical model, not being included in the compiled database upon which the model was based. The model is shown to be sufficiently accurate not only in terms of total lateral displacement, but more importantly in terms of individual displacement components, which is no simple feat for a finite element model.

The importance of modelling the post-peak response in shear-deficient R/C columns and sub-assemblages was highlighted time and time again, showing that not taking it into account could lead to gross underestimation of the capacity of individual members and sub-assemblages, particularly in terms of lateral displacement.

For the purpose of comparison, objective accuracy measures quantifying the performance of the analytical model with regard to the experimental response were proposed and used in the verifications, so that the results can be meaningfully compared with other analytical predictions.

Axial load change just before the peak or post-peak was found to unequivocally lead to a change in the rate of post-peak shear strength degradation and the axial failure displacement capacity of shear-damaged R/C columns. This effect was taken into account in the proposed beam-column model; no other beam-column model taking this effect into account has been proposed so far and the sample of relevant experiments is not considered sufficient for precisely quantifying these effects as of yet. Nevertheless, specimens with increasing axial load (tested in this study) were herein analysed. The analytical model was found to perform well in predicting the change in the aforementioned post-peak parameters as well as their overall response.

Overall, it can be said that the accuracy, versatility and simplicity of this beam-column finite element model make it a valuable tool in seismic analysis of complex R/C buildings with substandard structural elements.

## 10.2 RECOMMENDATIONS FOR FUTURE WORK

Although the aforementioned contributions are valuable for the field of earthquake engineering, future work is always necessary in the open-ended search for knowledge. Below are some recommendations, in order to build up on the present research and shed further light on the issues at hand.

First of all, the database that was compiled could be used in other investigations of various aspects of the post-peak response of shear-deficient R/C columns. Moreover, it would be worthwhile extending the database even further, including data from new experimental tests, in order to get more reliable correlations and hopefully reduce the associated dispersion. The post-peak domain is characterised by high variability in the response, hence a probabilistic approach would be strongly recommended as a future extension of the developed empirical relationships. Along the same lines, further experimental work pertaining to the onset of axial failure of sub-standard R/C columns would be desirable in order to improve the proposed empirical relationships as well as to validate or further refine the proposed criteria for simultaneous shear and axial failure. Shear failure leap was observed and discussed, but could not be modelled as this stage as a potential initial part of the post-peak descending branch at this stage. Further investigation into this phenomenon would be worthwhile.

The proposed empirical relationships, the shear hysteretic model as well as the more general conclusions regarding post-peak response of substandard R/C elements can be of use or even also be implemented in other analytical models, so long as the adopted basis and assumptions are similar.

The proposed analytical member-type model has been verified against individual components as well as two-bay one-storey R/C frames. Therefore, it could be used for analytical assessments of existing R/C sub-assemblages or entire structures in the context of vulnerability assessment for high damage states, namely significant damage or near-collapse; this would also further verify its capabilities. So long as the redistribution of vertical loads as well as the response of members beyond the onset of axial failure (e.g. degrading axial resistance with increased axial shortening and perhaps residual axial strength) can be correctly accounted for, the model can also be used for progressive collapse analyses of such structures.

A calibration of the post-peak shear hysteretic rules based on experimental shear response data would be another worthwhile future endeavour, in order to further improve the prediction accuracy of the proposed shear and member-type models.

With respect to axial load increase or decrease, a recent experimental investigation on columns with decreasing axial load and the herein presented experimental project with increasing axial

load pave the way for more analytical investigations with the aim to properly model this kind of response. However, definitive conclusions cannot be drawn yet; in other words, exact patterns cannot be extracted from such a small data sample. Advantage should be taken of the data produced by the aforementioned experimental studies and more similar experiments should be performed. Such experimental studies should comprise a greater variety of design characteristics, initial axial loads, increased axial loads and points of axial load increase, in order to advance into the direction of more precisely predicting the impact of axial load change on the non-linear hysteretic response of shear and flexure-shear critical specimens.



## APPENDIX A: DATABASE OF R/C COLUMN TESTS

The specimens of the compiled database are presented in detail in the following table (Table A-1), along with original publications, wherefrom the data were extracted (of course, some of them were obtained from the [SERIES database](#) (Perus *et al.*, 2014) as mentioned in section 3), and their main characteristics.

Table A-1: Specimens contained in the database, original publication and some of their most important characteristics.

Specimen Name	Publication	$b$ (mm)	X	$h$ (mm)	$L$ (mm)	Test Type	$f_c$ (MPa)	$f_{yl}$ (MPa)	$f_{yw}$ (MPa)	$L_s/d$	$\rho_l$ (%)	$\rho_{w,conf}$ (%)	$\tau_{max}/vf_c$	$\nu$	$s/d$
LamX8	Lam <i>et al.</i> (2003)	267.0	X	267.0	400.0	DC	47.0	433.0	270.0	1.53	3.03	0.10	0.51	0.40	0.38
LamX9		267.0	X	267.0	400.0	DC	47.0	433.0	270.0	1.53	3.03	0.10	0.63	0.40	0.38
WibowoS2	Wibowo (2013)	270.0	X	300.0	1200.0	C	21.0	536.0	362.0	4.29	0.99	0.08	0.25	0.20	1.07
Matchulat1	Matchulat (2009)	457.2	X	457.2	1473.2	DC	33.1	441.3	372.3	3.53	2.47	0.08	0.35	0.32	1.09
Matchulat2		457.2	X	457.2	1473.2	DC	33.6	441.3	372.3	3.53	2.47	0.08	0.34	0.22	1.09
CotofanaC6	Cotofana & Popa (2009)	300.0	X	300.0	475.0	DC	20.0	700.0	400.0	1.68	1.18	0.28	0.68	0.20	0.46
CotofanaC7		300.0	X	300.0	475.0	DC	20.0	700.0	400.0	1.68	1.18	0.09	0.68	0.20	0.88
MatsukawaF0101	Matsukawa <i>et al.</i> (2012)	400.0	X	400.0	400.0	DC	34.7	396.0	370.0	1.07	4.28	0.11	0.53	0.05	0.40
MatsukawaF0102	Matsukawa <i>et al.</i> (2013)	300.0	X	300.0	300.0	DC	29.2	382.0	365.0	1.05	3.78	0.09	0.59	0.10	0.35
MatsukawaF0103		300.0	X	300.0	300.0	DC	29.2	366.0	365.0	1.05	2.68	0.09	0.48	0.11	0.35
MatsukawaF0203		300.0	X	300.0	300.0	DC	29.2	366.0	365.0	1.05	2.68	0.23	0.65	0.11	0.14
UmeharaOUS	Umehara & Jirsa (1982)	230.0	X	410.0	455.0	DC	40.1	441.0	414.0	1.18	3.01	0.35	0.52	0.00	0.23
UmeharaOUW		410.0	X	230.0	455.0	DC	40.1	441.0	414.0	2.22	3.01	0.35	0.48	0.00	0.43
UmeharaCMS		230.0	X	410.0	455.0	DC	42.0	441.0	414.0	1.18	3.01	0.35	0.68	0.13	0.23
UmeharaCUS		230.0	X	410.0	455.0	DC	34.9	441.0	414.0	1.18	3.01	0.35	0.63	0.16	0.23
UmeharaCUW		410.0	X	230.0	455.0	DC	34.9	441.0	414.0	2.22	3.01	0.35	0.54	0.16	0.43
Umehara2CUS		230.0	X	410.0	455.0	DC	42.0	441.0	414.0	1.18	3.01	0.35	0.74	0.27	0.23

<b>UmemuraAN2</b>		250.0	X	250.0	600.0	C	31.6	360.0	456.0	2.50	2.57	0.27	0.30	0.00	0.17
<b>UmemuraAN4</b>		250.0	X	250.0	600.0	C	31.6	360.0	456.0	2.50	2.57	0.27	0.37	0.06	0.17
<b>UmemuraBN3</b>	Umemura &	250.0	X	250.0	600.0	C	31.2	360.0	531.0	2.50	2.57	0.27	0.41	0.12	0.17
<b>UmemuraBN5</b>	Ichinose (2004)	250.0	X	250.0	600.0	C	31.2	360.0	531.0	2.50	2.57	0.27	0.42	0.12	0.17
<b>UmemuraBS2</b>		250.0	X	250.0	600.0	C	31.2	360.0	530.0	2.50	2.57	0.27	0.42	0.12	0.14
<b>UmemuraBS3</b>		250.0	X	250.0	600.0	C	31.2	360.0	530.0	2.50	2.57	0.27	0.39	0.12	0.14
<b>SaatciogluU2</b>	Saatcioglu & Ozcebe (1989)	350.0	X	350.0	1000.0	C	30.2	453.0	470.0	3.05	3.21	0.34	0.45	0.16	0.46
<b>TagamiS3</b>	Tagami <i>et al.</i>	250.0	X	250.0	300.0	DC	31.3	391.0	400.0	1.28	1.70	0.51	0.74	0.26	0.21
<b>TagamiD3</b>	(2005)	250.0	X	250.0	300.0	DC	30.7	391.0	400.0	1.28	1.70	0.51	0.84	0.27	0.21
<b>OusalemC1</b>		300.0	X	300.0	450.0	DC	13.5	340.0	587.0	1.66	1.77	0.10	0.54	0.30	0.59
<b>OusalemC4</b>	Ousalem <i>et al.</i>	300.0	X	300.0	450.0	DC	13.5	340.0	384.0	1.65	1.77	0.31	0.57	0.30	0.28
<b>OusalemC8</b>	(2002)	300.0	X	300.0	450.0	DC	18.0	340.0	384.0	1.65	1.77	0.31	0.68	0.30	0.28
<b>OusalemC12</b>		300.0	X	300.0	450.0	DC	18.0	340.0	384.0	1.65	1.77	0.31	0.63	0.20	0.28
<b>OusalemD1</b>		300.0	X	300.0	300.0	DC	27.7	447.0	398.0	1.10	1.77	0.46	0.80	0.22	0.18
<b>OusalemD11</b>		300.0	X	300.0	450.0	DC	28.2	447.0	398.0	1.65	2.36	0.15	0.57	0.21	0.55
<b>OusalemD12</b>	Ousalem <i>et al.</i>	300.0	X	300.0	450.0	DC	28.2	447.0	398.0	1.65	2.36	0.15	0.58	0.21	0.55
<b>OusalemD13</b>	(2003)	300.0	X	300.0	450.0	DC	26.1	447.0	398.0	1.65	2.36	0.46	0.65	0.23	0.18
<b>OusalemD14</b>		300.0	X	300.0	450.0	DC	26.1	447.0	398.0	1.65	2.36	0.46	0.72	0.23	0.18
<b>OusalemD16</b>		300.0	X	300.0	300.0	DC	26.1	447.0	398.0	1.10	1.77	0.46	0.83	0.23	0.18
<b>YoshimuraFS0</b>		300.0	X	300.0	900.0	C	27.0	387.0	355.0	3.28	3.78	0.84	0.47	0.26	0.27
<b>YoshimuraFS1</b>	Yoshimura & Yamanaka (2000)	300.0	X	300.0	900.0	C	27.0	387.0	355.0	3.28	3.78	0.84	0.45	0.26	0.27
<b>YoshimuraS1</b>		400.0	X	400.0	900.0	C	25.1	547.0	355.0	2.43	3.80	0.26	0.53	0.20	0.49
<b>Yoshimura2C</b>		300.0	X	300.0	300.0	DC	25.2	396.0	392.0	1.12	2.68	0.24	0.55	0.19	0.37
<b>Yoshimura2M</b>		300.0	X	300.0	300.0	DC	25.2	396.0	392.0	1.12	2.68	0.24	0.58	0.19	0.37
<b>Yoshimura2C13</b>	Yoshimura &	300.0	X	300.0	300.0	DC	25.2	350.0	392.0	1.12	1.77	0.24	0.65	0.19	0.37
<b>Yoshimura2M13</b>	Nakamura (2002)	300.0	X	300.0	300.0	DC	25.2	350.0	392.0	1.12	1.77	0.24	0.63	0.19	0.37
<b>Yoshimura3C</b>		300.0	X	300.0	300.0	DC	25.2	396.0	392.0	1.12	2.68	0.24	0.66	0.29	0.37
<b>Yoshimura3M</b>		300.0	X	300.0	300.0	DC	25.2	396.0	392.0	1.12	2.68	0.24	0.62	0.29	0.37
<b>YoshimuraNo.1</b>	Yoshimura <i>et al.</i>	300.0	X	300.0	600.0	DC	30.7	402.0	392.0	2.23	2.68	0.24	0.52	0.20	0.37
<b>YoshimuraNo.3</b>	(2003)	300.0	X	300.0	600.0	DC	30.7	402.0	392.0	2.23	2.68	0.12	0.42	0.20	0.74

<b>YoshimuraNo.4</b>		300.0	X	300.0	600.0	DC	30.7	402.0	392.0	2.23	2.68	0.24	0.53	0.30	0.37
<b>YoshimuraNo.5</b>		300.0	X	300.0	600.0	DC	30.7	402.0	392.0	2.23	2.68	0.24	0.60	0.35	0.37
<b>YoshimuraNo.6</b>		300.0	X	300.0	600.0	DC	30.7	409.0	392.0	2.24	1.77	0.24	0.48	0.20	0.37
<b>YoshimuraNo.7</b>		300.0	X	300.0	600.0	DC	30.7	409.0	392.0	2.24	1.77	0.16	0.48	0.20	0.56
<b>NakamuraN18M</b>		300.0	X	300.0	450.0	DC	26.5	380.0	375.0	1.67	2.68	0.24	0.62	0.18	0.37
<b>NakamuraN18C</b>	Nakamura &	300.0	X	300.0	450.0	DC	26.5	380.0	375.0	1.67	2.68	0.24	0.64	0.18	0.37
<b>NakamuraN27M</b>	Yoshimura (2002)	300.0	X	300.0	450.0	DC	26.5	380.0	375.0	1.67	2.68	0.24	0.69	0.27	0.37
<b>NakamuraN27C</b>		300.0	X	300.0	450.0	DC	26.5	380.0	375.0	1.67	2.68	0.24	0.62	0.27	0.37
<b>NakamuraA1</b>		450.0	X	450.0	450.0	DC	28.0	383.0	399.0	1.10	1.12	0.14	0.59	0.16	0.73
<b>NakamuraB1</b>		450.0	X	450.0	450.0	DC	28.0	383.0	399.0	1.10	1.68	0.28	0.61	0.16	0.37
<b>NakamuraB4</b>	Nakamura &	450.0	X	450.0	450.0	DC	28.0	383.0	399.0	1.10	1.68	0.28	0.60	0.16	0.37
<b>NakamuraC1</b>	Yoshimura (2014)	450.0	X	450.0	450.0	DC	28.0	376.0	399.0	1.09	2.25	0.56	0.71	0.16	0.18
<b>NakamuraS100</b>		450.0	X	450.0	450.0	DC	25.0	383.0	399.0	1.10	1.68	0.28	0.57	0.18	0.37
<b>NakamuraL100</b>		450.0	X	450.0	700.0	DC	25.0	383.0	399.0	1.71	1.68	0.21	0.56	0.18	0.49
<b>TranRC-1.7-0.05</b>		250.0	X	490.0	850.0	DC	32.5	460.0	392.6	1.83	2.05	0.23	0.43	0.05	0.27
<b>TranRC-1.7-0.20</b>		250.0	X	490.0	850.0	DC	24.5	460.0	392.6	1.83	2.05	0.23	0.53	0.20	0.27
<b>TranRC-1.7-0.35</b>		250.0	X	490.0	850.0	DC	27.1	460.0	392.6	1.83	2.05	0.23	0.57	0.35	0.27
<b>TranRC-1.7-0.50</b>		250.0	X	490.0	850.0	DC	26.8	460.0	392.6	1.83	2.05	0.23	0.59	0.50	0.27
<b>TranSC-1.7-0.05</b>	Tran (2010)	350.0	X	350.0	600.0	DC	29.8	460.0	392.6	1.85	2.05	0.15	0.45	0.05	0.38
<b>TranSC-1.7-0.20</b>		350.0	X	350.0	600.0	DC	27.5	460.0	392.6	1.85	2.05	0.15	0.48	0.20	0.38
<b>TranSC-1.7-0.35</b>		350.0	X	350.0	600.0	DC	25.5	460.0	392.6	1.85	2.05	0.15	0.56	0.35	0.38
<b>TranSC-1.7-0.50</b>		350.0	X	350.0	600.0	DC	26.4	460.0	392.6	1.85	2.05	0.15	0.64	0.50	0.38
<b>TranSC-2.4-0.20</b>		350.0	X	350.0	850.0	DC	22.6	460.0	392.6	2.62	2.05	0.15	0.40	0.20	0.38
<b>TranSC-2.4-0.50</b>		350.0	X	350.0	850.0	DC	24.2	460.0	392.6	2.62	2.05	0.15	0.42	0.50	0.38
<b>KabeyasawaA-1</b>	Kabeyasawa <i>et al.</i> (2001)	150.0	X	420.0	630.0	DC	18.3	349.0	289.0	1.59	1.00	0.20	0.56	0.29	0.51
<b>KabeyasawaB-1</b>		300.0	X	300.0	450.0	DC	18.3	338.0	289.0	1.66	1.77	0.10	0.51	0.29	0.59
<b>KogomaCT1</b>	Kogoma <i>et al.</i> (1992)	130.0	X	130.0	425.0	DC	22.8	355.2	355.2	3.76	4.76	0.21	0.36	0.18	2.52
<b>HenkhausB1</b>	Henkhaus <i>et al.</i> (2013)	457.0	X	457.0	736.5	DC	20.0	455.0	490.0	1.75	1.49	0.08	0.67	0.37	1.08
<b>HenkhausB2</b>		457.0	X	457.0	736.5	DC	19.3	455.0	455.0	1.75	1.49	0.08	0.63	0.38	0.48
<b>HenkhausB4</b>		457.0	X	457.0	736.5	DC	24.1	441.0	490.0	1.75	2.47	0.08	0.77	0.43	1.08

<b>KatoD10SH-1</b>		180.0	X	180.0	180.0	DC	32.2	371.0	316.0	1.06	0.97	0.50	0.72	0.29	0.41
<b>KatoD10SH-2</b>		180.0	X	180.0	180.0	DC	32.2	371.0	316.0	1.06	0.97	0.50	0.81	0.48	0.41
<b>KatoD10SL-1</b>		180.0	X	180.0	180.0	DC	19.1	371.0	316.0	1.06	0.97	0.50	0.66	0.24	0.41
<b>KatoD10SL-2</b>		180.0	X	180.0	180.0	DC	19.1	371.0	316.0	1.06	0.97	0.50	0.73	0.48	0.41
<b>KatoD10WH-1</b>		180.0	X	180.0	180.0	DC	32.2	371.0	316.0	1.06	0.97	0.50	0.68	0.29	0.41
<b>KatoD10WH-2</b>		180.0	X	180.0	180.0	DC	32.2	371.0	316.0	1.06	0.97	0.50	0.79	0.48	0.41
<b>KatoD10WL-1</b>		180.0	X	180.0	180.0	DC	19.1	371.0	316.0	1.06	0.97	0.50	0.63	0.24	0.41
<b>KatoD10WL-2</b>		180.0	X	180.0	180.0	DC	19.1	371.0	316.0	1.06	0.97	0.50	0.66	0.48	0.41
<b>KatoD13S-2</b>		180.0	X	180.0	180.0	DC	26.7	335.0	335.0	1.06	1.64	0.50	0.81	0.58	0.41
<b>KatoD13W-1</b>		180.0	X	180.0	180.0	DC	26.7	335.0	335.0	1.06	1.64	0.50	0.76	0.35	0.41
<b>KatoD13W-2</b>	<i>Kato et al. (2006)</i>	180.0	X	180.0	180.0	DC	26.7	335.0	335.0	1.06	1.64	0.50	0.82	0.58	0.41
<b>KatoS-3</b>		180.0	X	180.0	180.0	DC	23.4	377.0	303.0	1.06	0.97	0.50	0.81	0.40	0.41
<b>KatoW-3</b>		180.0	X	180.0	180.0	DC	23.4	377.0	303.0	1.06	0.97	0.50	0.77	0.40	0.41
<b>KatoW-4</b>		180.0	X	180.0	180.0	DC	23.4	377.0	303.0	1.06	0.97	0.50	0.78	0.66	0.41
<b>KatoW52-1</b>		180.0	X	180.0	180.0	DC	28.2	382.0	341.0	1.06	0.97	0.68	0.96	0.55	0.31
<b>KatoD13S-1</b>		180.0	X	180.0	180.0	DC	26.7	335.0	335.0	1.06	1.64	0.50	0.73	0.35	0.41
<b>KatoW52-2</b>		180.0	X	180.0	180.0	DC	28.2	382.0	341.0	1.06	0.97	0.68	0.88	0.38	0.31
<b>KatoW90-1</b>		180.0	X	180.0	180.0	DC	28.2	382.0	341.0	1.06	0.97	0.39	0.72	0.38	0.53
<b>KatoW90-2</b>		180.0	X	180.0	180.0	DC	28.2	382.0	341.0	1.06	0.97	0.39	0.71	0.22	0.53
<b>Katoφ4W-1</b>		180.0	X	180.0	180.0	DC	26.7	502.0	335.0	1.06	0.16	0.50	0.77	0.35	0.41
<b>Katoφ4W-2</b>		180.0	X	180.0	180.0	DC	26.7	502.0	335.0	1.06	0.16	0.50	0.69	0.58	0.41
<b>Zhou204-08</b>	<i>Zhou et al. (1985)</i>	160.0	X	160.0	320.0	DC	21.1	341.0	559.0	2.17	2.22	0.73	0.61	0.80	0.27
<b>Zhou104-08</b>	<i>Zhou et al. (1987)</i>	160.0	X	160.0	160.0	DC	19.8	341.0	559.0	1.08	2.22	0.73	0.79	0.80	0.27
<b>Zhou114-08</b>		160.0	X	160.0	160.0	DC	19.8	341.0	559.0	1.08	2.22	0.73	0.87	0.80	0.27
<b>ArakawaOA2</b>	<i>Arakawa et al. (1989)</i>	180.0	X	180.0	225.0	DC	31.8	340.0	249.0	1.32	3.13	0.24	0.76	0.18	0.38
<b>ArakawaOA5</b>		180.0	X	180.0	225.0	DC	33.0	340.0	249.0	1.32	3.13	0.24	0.76	0.45	0.38
<b>Lynn3CLH18</b>		457.2	X	457.2	1473.2	DC	26.9	331.0	399.9	3.52	3.04	0.08	0.28	0.09	1.09
<b>Lynn3CMH18</b>	<i>Lynn (2001)</i>	457.2	X	457.2	1473.2	DC	27.6	331.0	399.9	3.52	3.04	0.08	0.34	0.26	1.09
<b>Lynn3CMD12</b>		457.2	X	457.2	1473.2	DC	27.6	331.0	399.9	3.52	3.04	0.21	0.37	0.26	0.73
<b>Lynn3SLH18</b>		457.2	X	457.2	1473.2	DC	26.9	331.0	399.9	3.52	3.04	0.08	0.28	0.09	1.09
<b>Lynn2SLH18</b>	<i>Lynn et al. (1996)</i>	457.2	X	457.2	1473.2	DC	33.1	331.0	399.9	3.52	1.94	0.08	0.22	0.07	1.09

<b>Lynn3SMD12</b>		457.2	X	457.2	1473.2	DC	25.5	331.0	399.9	3.52	3.04	0.21	0.40	0.28	0.73
<b>Lynn2CLH18</b>		457.2	X	457.2	1473.2	DC	33.1	331.0	399.9	3.52	1.94	0.08	0.23	0.07	1.09
<b>Lynn2CMH18</b>		457.2	X	457.2	1473.2	DC	25.5	331.0	399.9	3.52	1.94	0.08	0.33	0.28	1.09
<b>AboutahaSC3</b>	Aboutaha <i>et al.</i>	914.4	X	457.2	1219.2	C	21.9	434.0	400.0	2.91	1.88	0.10	0.25	0.00	0.97
<b>AboutahaSC9</b>	(1999)	457.2	X	914.4	1219.2	C	16.0	434.0	400.0	1.39	1.88	0.09	0.40	0.00	0.46
<b>NagasakaHPRC1 0-63</b>	Nagasaka (1982)	200.0	X	200.0	300.0	DC	21.6	371.0	344.0	1.60	1.27	0.77	0.51	0.17	0.19
<b>NagasakaHPRC1 9-32</b>		200.0	X	200.0	300.0	DC	22.1	371.0	344.0	1.60	1.27	1.35	0.66	0.35	0.11
<b>NagasakaHPRC1 9-62</b>	Nagasaka (1984)	200.0	X	200.0	300.0	DC	22.1	371.0	344.0	1.60	1.27	1.35	0.51	0.17	0.11
<b>NagasakaHPRC1 0-32</b>		200.0	X	200.0	300.0	DC	22.1	371.0	344.0	1.60	1.27	0.77	0.51	0.33	0.19
<b>Ohue2D16RS</b>	Ohue <i>et al.</i> (1985)	200.0	X	200.0	400.0	DC	32.0	369.0	316.0	2.12	2.01	0.53	0.46	0.14	0.26
<b>Ohue4D13RS</b>		200.0	X	200.0	400.0	DC	29.9	370.0	316.0	2.13	2.65	0.54	0.53	0.15	0.27
<b>OnoCA025C</b>	Ono <i>et al.</i> (1989)	200.0	X	200.0	300.0	DC	25.8	361.0	426.0	1.66	2.13	1.00	0.73	0.26	0.39
<b>LejanoCB060C</b>	Lejano <i>et al.</i> (1992)	278.0	X	278.0	323.0	DC	46.3	441.0	414.0	1.29	4.12	0.98	1.13	0.74	0.21
<b>LejanoCB070T</b>		278.0	X	278.0	323.0	DC	46.3	441.0	414.0	1.29	4.12	0.98	0.26	-0.26	0.21
<b>XiaoFHC2-0.34</b>	Xiao & Yun (2002)	510.0	X	510.0	1778.0	HH	62.1	473.0	445.0	3.53	3.10	0.80	0.41	0.34	0.20
<b>XiaoFHC4-0.34</b>		510.0	X	510.0	1778.0	HH	62.1	473.0	525.0	3.53	3.10	0.64	0.40	0.33	0.25
<b>XiaoFHC5-0.2</b>		510.0	X	510.0	1778.0	HH	64.1	473.0	445.0	3.53	3.10	0.53	0.35	0.20	0.30
<b>XiaoFHC6-0.2</b>	Xiao and Martirosyan (1998)	510.0	X	510.0	1778.0	HH	64.1	473.0	524.0	3.53	3.10	0.53	0.35	0.20	0.30
<b>XiaoHC4-8L16- T6-0.1P</b>		254.0	X	254.0	508.0	DC	86.0	510.0	449.0	2.11	2.46	0.83	0.38	0.10	0.21
<b>XiaoHC4-8L16- T6-0.2P</b>		254.0	X	254.0	508.0	DC	86.0	510.0	449.0	2.11	2.46	0.83	0.56	0.19	0.21
<b>SezenNo. 1</b>	Sezen & Moehle (2006)	457.2	X	457.2	1473.2	DC	21.1	434.4	476.0	3.76	2.48	0.24	0.40	0.15	0.78
<b>SezenNo. 2</b>		457.2	X	457.2	1473.2	DC	21.1	434.4	476.0	3.76	2.48	0.24	0.46	0.61	0.78
<b>SezenNo. 4</b>		457.2	X	457.2	1473.2	DC	21.8	434.4	476.0	3.76	2.48	0.24	0.37	0.15	0.78
<b>LeBorgne2L06</b>	Leborgne (2012)	406.4	X	406.4	1473.2	DC	21.6	451.6	459.2	4.00	2.45	0.57	0.38	0.19	0.41
<b>LeBorgne2H06</b>		406.4	X	406.4	1473.2	DC	23.0	451.6	459.2	4.00	2.45	0.57	0.39	0.41	0.41
<b>Bett1-1</b>	Bett <i>et al.</i> (1985)	304.8	X	304.8	457.2	DC	29.9	462.0	413.7	1.64	2.45	0.19	0.45	0.10	0.73

<b>Ramirez00-U</b>		304.8	X	304.8	457.2	DC	34.5	372.3	455.1	1.64	2.45	0.34	0.52	0.00	0.23
<b>Ramirez50T-U</b>	Ramirez & Jirsa	304.8	X	304.8	457.2	DC	35.2	372.3	455.1	1.64	2.45	0.34	0.41	-0.07	0.23
<b>Ramirez100T-U</b>	(1980)	304.8	X	304.8	457.2	DC	38.6	372.3	455.1	1.64	2.45	0.34	0.32	-0.12	0.23
<b>Ramirez120C-U</b>		304.8	X	304.8	457.2	DC	30.7	448.2	455.1	1.64	2.45	0.34	0.62	0.19	0.23
<b>OgawaLC-12</b>	Ogawa <i>et al.</i>	500.0	X	500.0	1100.0	C	24.1	347.7	384.7	2.30	0.91	0.52	0.00	0.25	0.21
	(1990)														
<b>Woods3</b>		457.2	X	457.2	1473.2	DC	17.3	448.2	372.3	3.52	3.13	0.08	0.42	0.61	1.09
<b>Woods4</b>	Woods (2009)	457.2	X	457.2	1473.2	DC	18.6	441.3	372.3	3.52	2.47	0.21	0.41	0.39	0.73
<b>PandeyA-1</b>		300.0	X	300.0	800.0	C	32.5	380.2	396.6	2.94	2.68	0.09	0.25	0.03	0.92
<b>PandeyB-1</b>	Pandey <i>et al.</i>	300.0	X	300.0	650.0	C	28.8	380.2	396.6	2.39	2.68	0.15	0.43	0.03	0.55
	(2008)														
<b>ShiraiC-2</b>	Shirai <i>et al.</i>	278.0	X	278.0	323.0	DC	39.6	496.2	414.0	1.29	4.12	0.98	1.23	0.78	0.21
	(1996)														
<b>NguyenU0</b>		200.0	X	400.0	350.0	DC	59.5	540.0	300.0	0.90	3.93	0.58	0.97	0.42	0.26
<b>NguyenU90</b>	Nguyen (2005)	400.0	X	200.0	350.0	DC	59.5	540.0	300.0	1.87	3.93	0.27	0.69	0.42	0.53
<b>EsakiH-2-1/5</b>		200.0	X	200.0	400.0	DC	23.0	361.7	364.4	2.12	2.65	0.64	0.62	0.20	0.26
<b>EsakiH-2-1/3</b>		200.0	X	200.0	400.0	DC	23.0	361.7	364.4	2.12	2.65	0.79	0.70	0.33	0.21
<b>EsakiHT-2-1/5</b>	Esaki (1996)	200.0	X	200.0	400.0	DC	20.2	361.7	364.4	2.12	2.65	0.64	0.65	0.20	0.40
<b>EsakiHT-2-1/3</b>		200.0	X	200.0	400.0	DC	20.2	361.7	364.4	2.12	2.65	0.79	0.68	0.33	0.32
<b>EsakiH-1-1/3</b>		200.0	X	200.0	200.0	DC	22.8	361.7	364.4	1.06	2.65	1.59	1.05	0.33	0.11

## APPENDIX B: ESTIMATION OF CRITICAL SHEAR CRACK ANGLE FROM PHOTOGRAPHIC EVIDENCE

In some cases, orthophotographs of specimens with shear cracking were provided (e.g. Cotofana & Popa, 2009), which made the measurement rather simple and straightforward. In other cases, however, normal photos were provided, thus corrections had to be applied, in order to get an accurate angle value.

The derivation is purely geometry-based, i.e. the required angle is the inverse tangent of the height,  $h_{act}$ , of the column cross-section over an effective length,  $L_{eff,act}$  (Figure B-2). So, if one acquires the observed angle, cross-section height and effective length from the photo, then with the right corrections the actual  $L_{eff}$  can be inferred, the actual  $h$  is known, so the actual  $\vartheta$  can be calculated. The corrections applied are summarised below and in Eq. B-1 – B-5 (whatever is known in advance is given in green, the measured values are given in red and the calculated ones in blue font):

- 1) Due to the rotation of some photographs about the longitudinal axis of the column, the observed section height that has to be divided by the observed effective length in order to get the observed  $\vartheta$  is lower than the height of the element's section ( $h_{obs} \leq h_{act}$ ). This can easily be calculated based on trigonometry, so long as the rotation  $\varphi$  is known. From Figure B-1, it can be seen that the sine and cosine of  $\varphi$  can be calculated as a function of  $h_{obs}$ ,  $b_{obs}$ ,  $h_{act}$  and  $b_{act}$ . Simultaneously, the scale of the photos' dimensions is unknown. So,  $h_{meas}$  and  $b_{meas}$  are measured horizontally on the photo and relate to the  $h_{obs}$  and  $b_{obs}$ , being effectively the multiplication of the latter by the scale. Therefore, dividing the sine by the cosine cancels out the scale and directly yields the tangent of the rotation of the section,  $\varphi$ . The equations follow:

$$\sin(\varphi) = \frac{b_{obs}}{b_{act}} = \frac{b_{meas} \times scale}{b_{act}}; \cos(\varphi) = \frac{h_{obs}}{h_{act}} = \frac{h_{meas} \times scale}{h_{act}} \quad (B-1)$$

$$\varphi = \tan^{-1} \left( \frac{b_{meas}/b_{act}}{h_{meas}/h_{act}} \right) \quad (B-2)$$

$$h_{obs} = \cos(\varphi) \times h_{act} \quad (B-3)$$

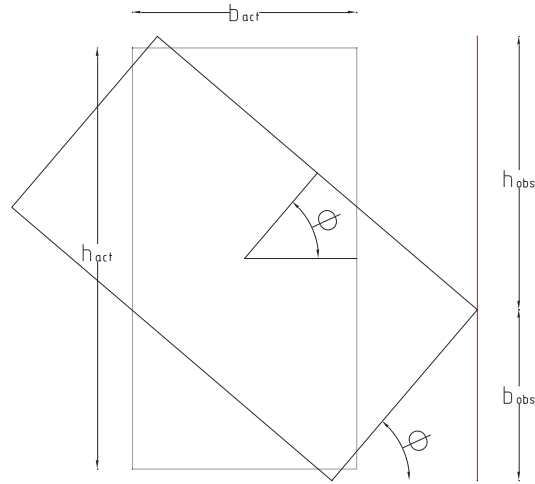


Figure B-1: Cross-section of the rotated column and observed dimensions, instead of the actual ones.

- 2) When the direction of the photo is upwards or downwards, perspective can distort the image, therefore the observed effective length does not equal the actual effective length.

If it's downwards (Figure B-2, top), then the actual  $L_{eff}$  is lower than the observed one, as explained in the figure ( $L_{eff,act} \leq L_{eff,obs}$ ). If it's upwards (Figure B-2, middle), then the inverse is real ( $L_{eff,act} \geq L_{eff,obs}$ ). In each case, if this correction is not made, an angle different to the required one will be calculated, i.e.  $\vartheta'_{act}$ , instead of  $\vartheta_{act}$  (Figure B-2). However, it's fairly easy to correct it in such ideal cases, where the inclination  $\vartheta_2$  is known, since the ratio  $L_{eff,act}/L_{eff,obs}$  can be directly computed from the measured values, no matter the scale. Nevertheless, the situation is more complicated in real photos, being closer to the bottom part of Figure B-2. In such cases, an approximation of the angle and, consequently, the ratio has to be made. This depends both on the two angles  $\vartheta_2$  and  $\vartheta_3$  and on the part of the column where the diagonal crack is located. It was mainly based on engineering judgement, during the measurements. Applying the aforementioned corrections, the angle is calculated as follows:

$$L_{eff,act} = \frac{L_{eff,act}}{L_{eff,obs}} \times \frac{h_{obs}}{\tan(\theta_{obs})} \quad (B-4)$$

$$\theta_{act} = \tan^{-1} \left( \frac{h_{act}}{L_{eff,act}} \right) \quad (B-5)$$

Other sources of errors include low resolution images that might lead to slight inaccuracies, capturing an inclined photo, so that vertical lines are not exactly vertical or extreme lateral drift,

causing again the vertical lines to be slightly inclined, e.g. in photos of axial collapse state. These, however, were not so frequently encountered and they were considered less influential than the abovementioned sources of errors - at least for this database's specimens.

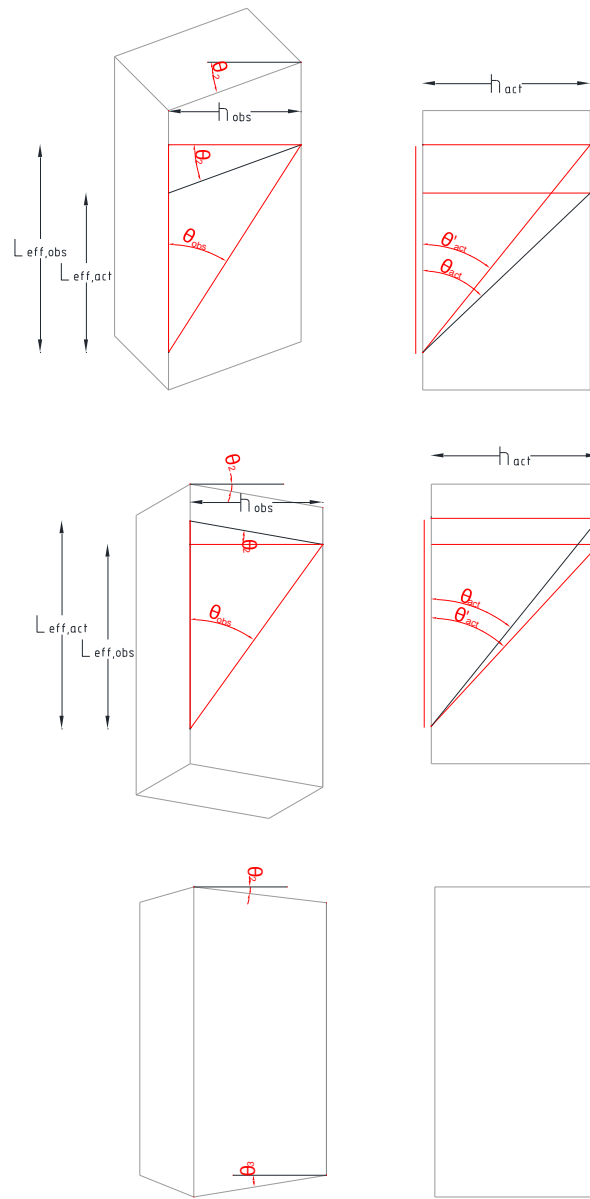


Figure B-2: Distortion of the column dimensions, due to the perspective; downwards (top), upwards (middle) and the common realistic case (bottom).



## APPENDIX C: SPECIMEN DESIGN DRAWINGS

In this appendix, the detailed as-built design drawings of the sub-base (Figure C-1), SC (Figure C-2) and FSC specimens (Figure C-3) are presented.

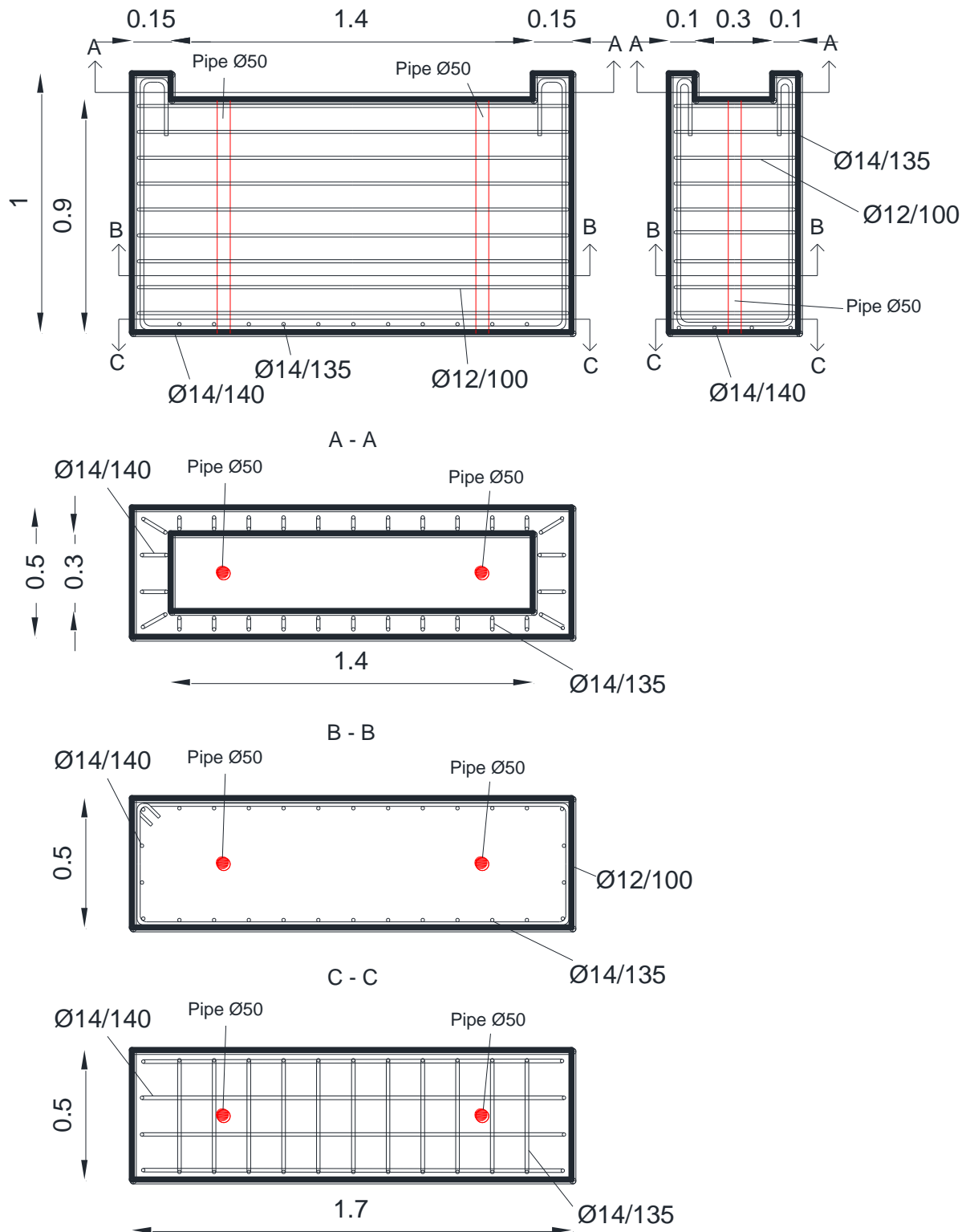


Figure C-1: As-built design drawings of sub-base.

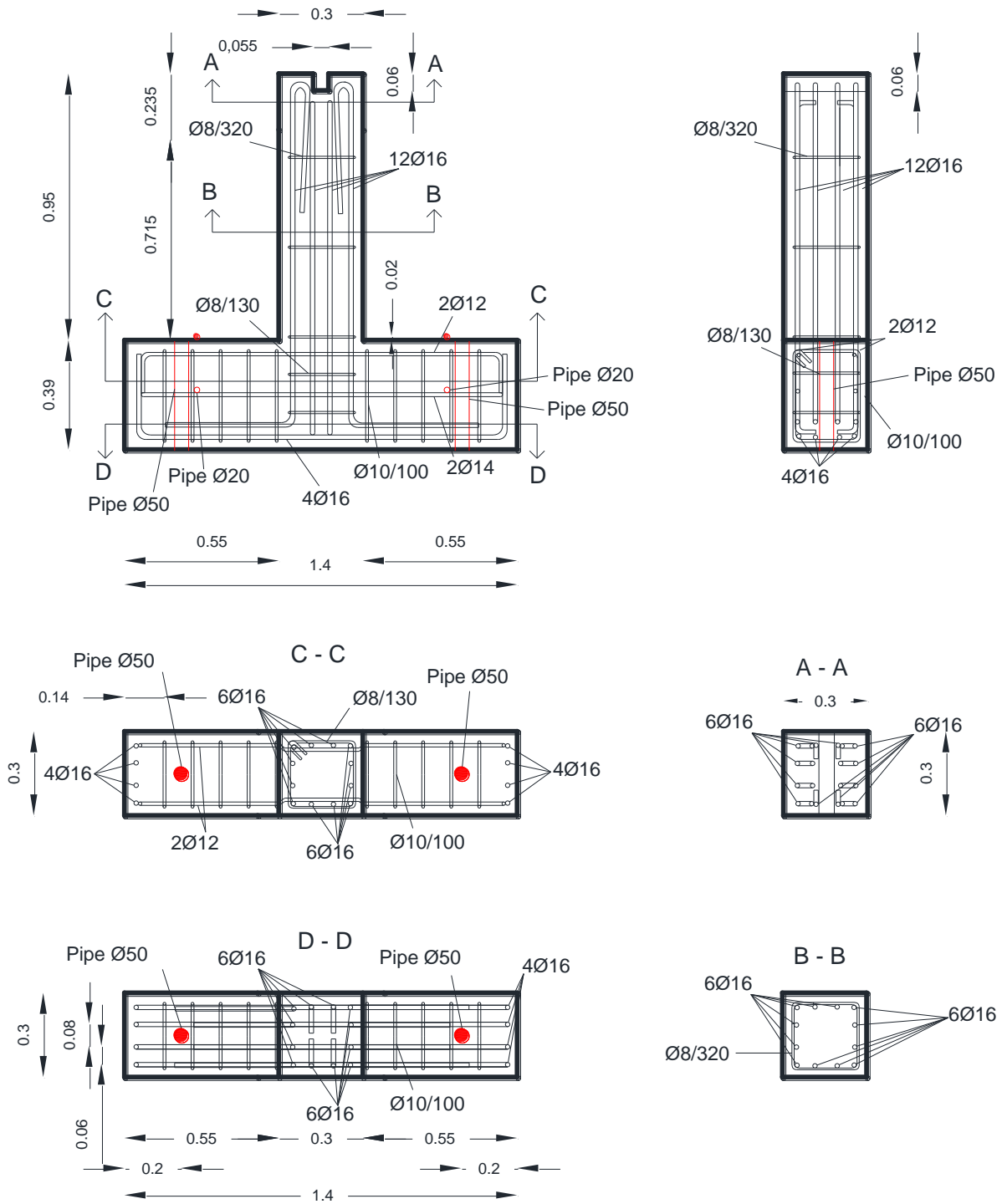


Figure C-2: As-built design drawings of SC specimens.

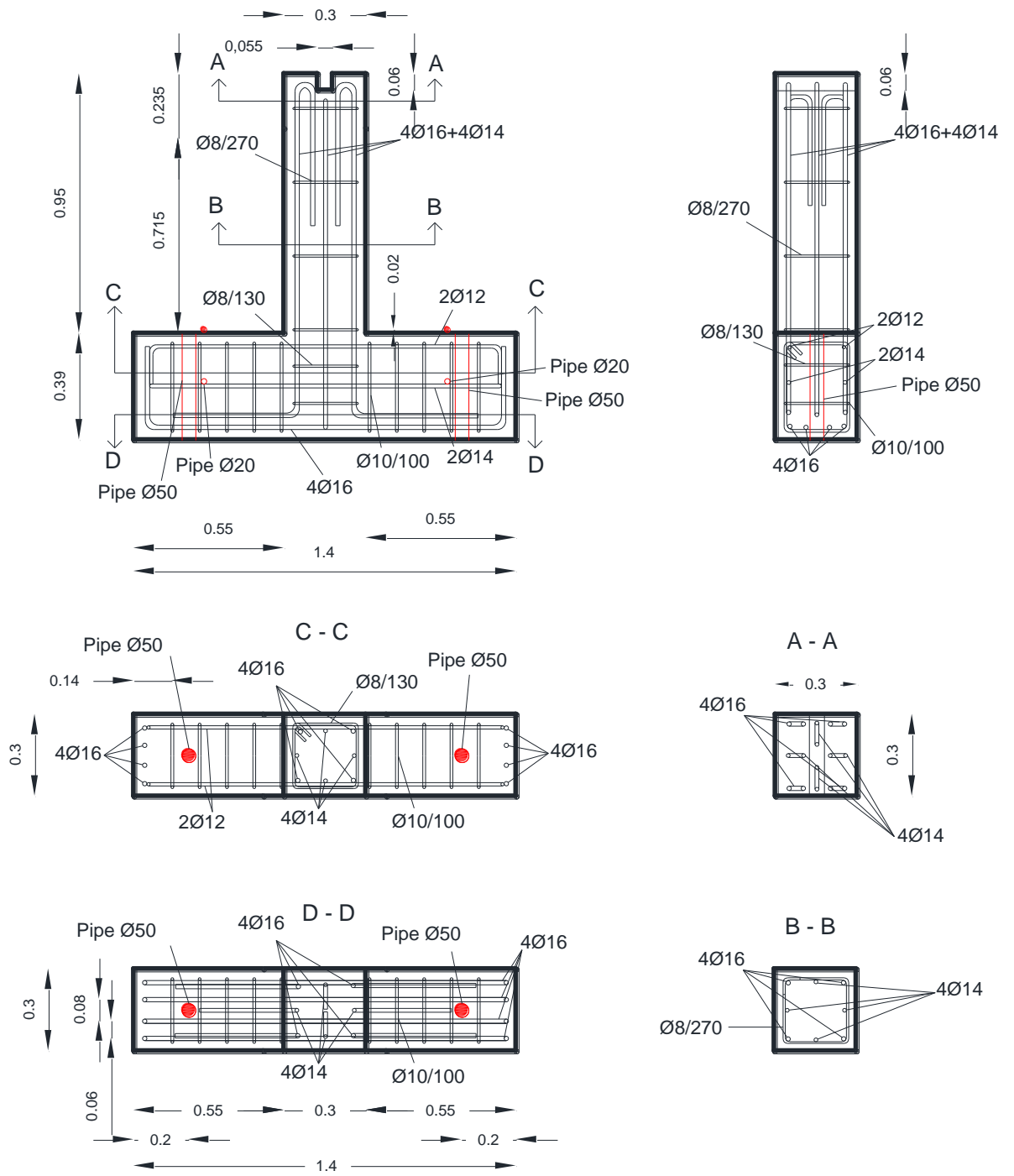


Figure C-3: As-built design drawings of FSC specimens.



## APPENDIX D: ACTUAL HYSTERETIC RESPONSE AND SMOOTHING

---

In this appendix, the hysteretic responses of the tested specimens are presented as recorded. The recording and control loop frequency (10 Hz) resulted in recording various “anomalies” in the applied force from the actuators or the displacement recorded by the draw-wire sensor.

These anomalies are generally either not captured at all in experimental tests, having a far lower recording frequency, or they are smoothed out for the sake of clarity, as also done in chapter 7 of the current work.

The method used in this thesis to smooth out the graphs results in the envelope of the hysteretic response being obtained. It is herein presented:

- 1) The time ranges were defined, wherein the horizontal displacement and the horizontal force should be increasing. Similarly the ranges, wherein they should be decreasing. This was possible, because the displacement history is an input in the procedure, so the respective ranges (increasing or decreasing) are known a priori. However, the command and the response of the system has a lag. Therefore, a variable accounting for this was also included in the timings.
- 2) A “2-point moving max” function is used in the increasing ranges and a “2-point moving min” in the decreasing ones. This applies both to the displacements and the forces.
- 3) In the case of in-cycle degradation, which was observed (for brief periods) in most of the specimens, a manual correction has to be made, because although the displacement is increasing, the force is decreasing or vice-versa. So, in order to avoid having the corrected force assuming a constant value instead of decreasing, it was manually changed to obtain the real response. This was done with the displacements, as well, wherever there seemed to be unrealistic results, however these cases were very limited.

Using “moving average” functions, instead, would result in a smoothed version which would not represent the actual envelope of each cycle of the response of the specimen, but envelopes of smaller area.

Also, were this categorisation (increasing/decreasing) not included, it would result in wrong results either in the descending or in the ascending branches.

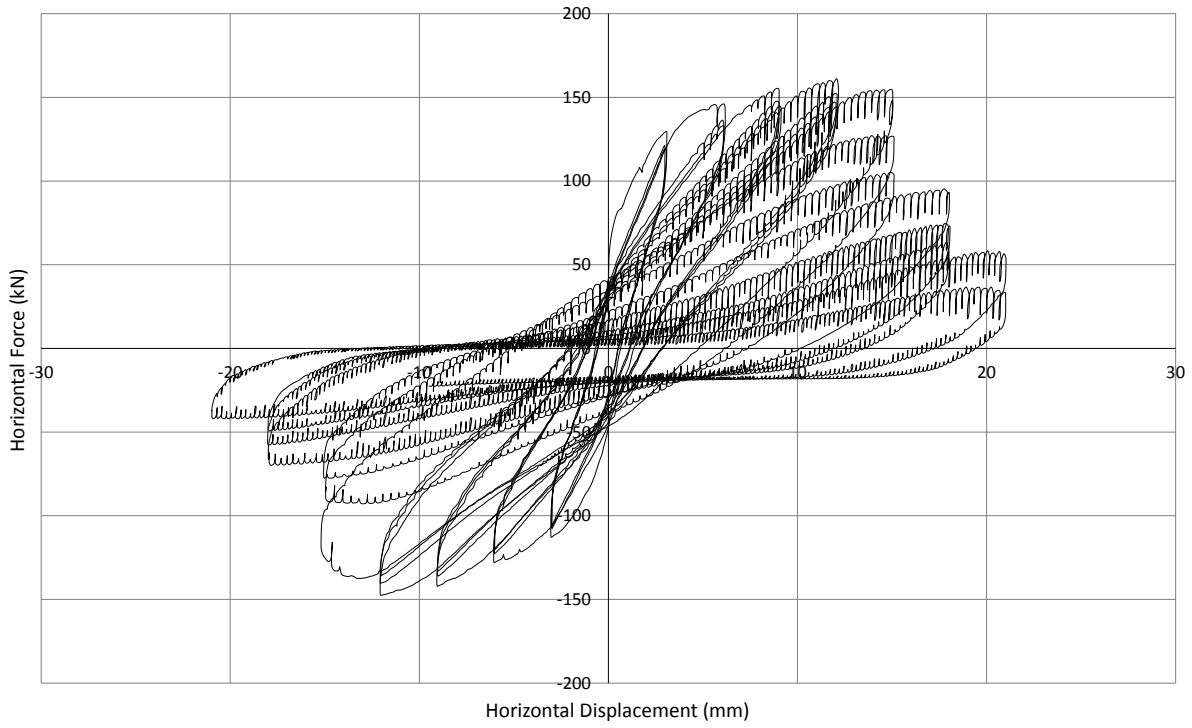


*Figure D-1: Response of specimen FSC\_1 without smoothing.*

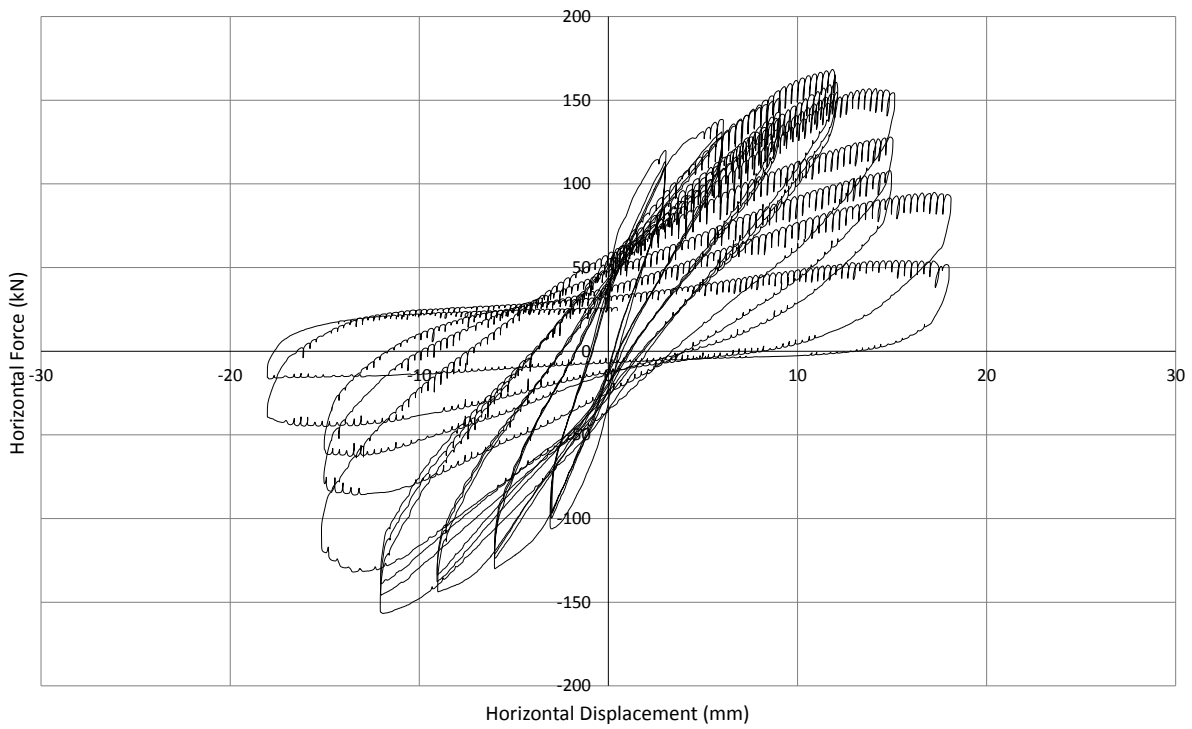


*Figure D-2: Response of specimen FSC\_2 without smoothing.*

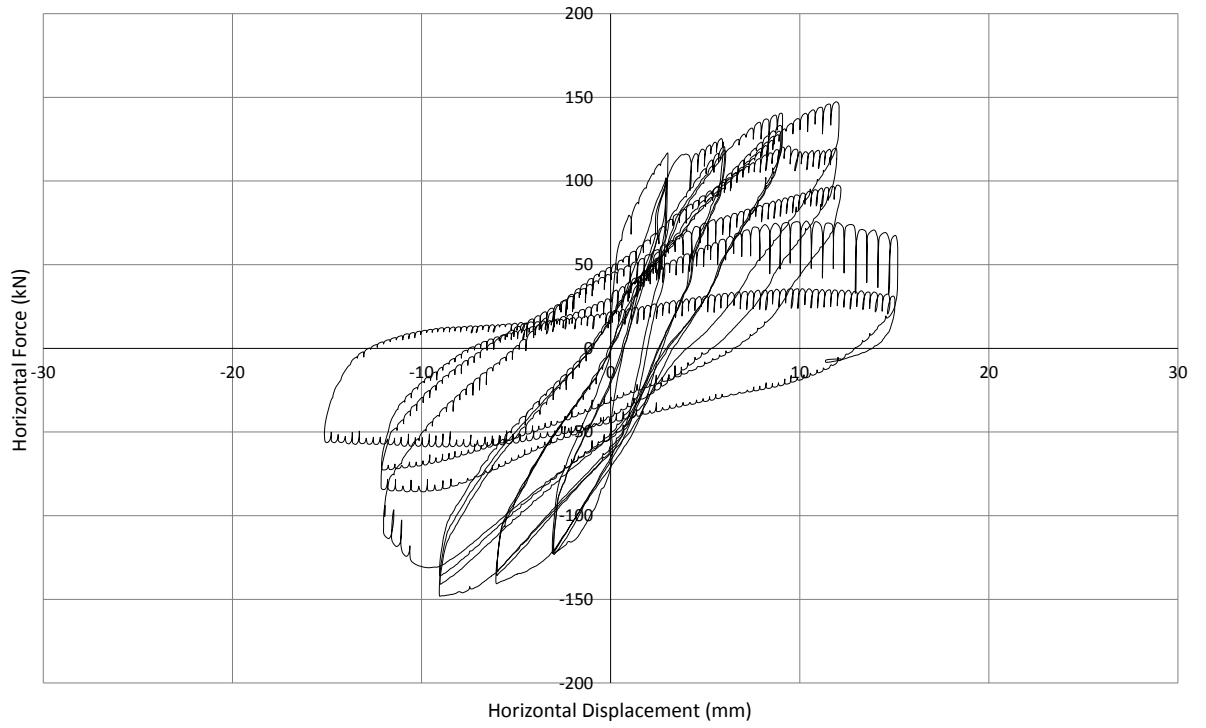


Figure D-3: Response of specimen FSC\_3 without smoothing.

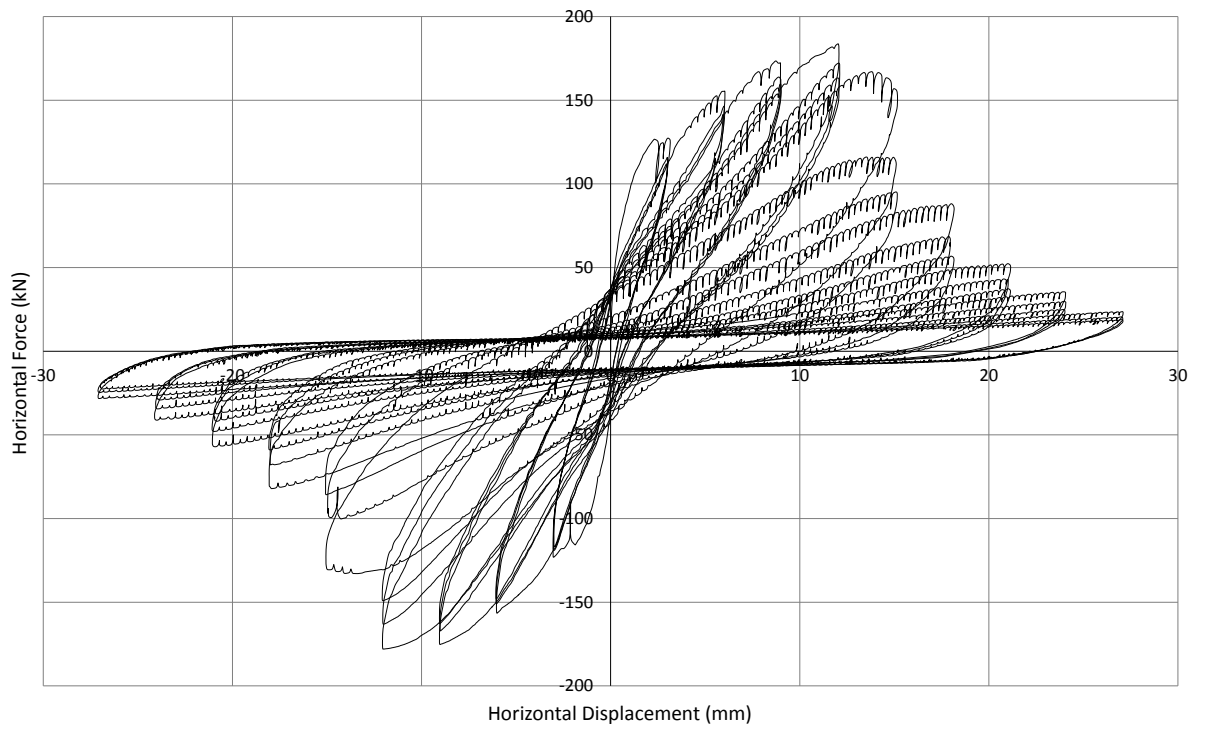


Figure D-4: Response of specimen SC\_1 without smoothing.

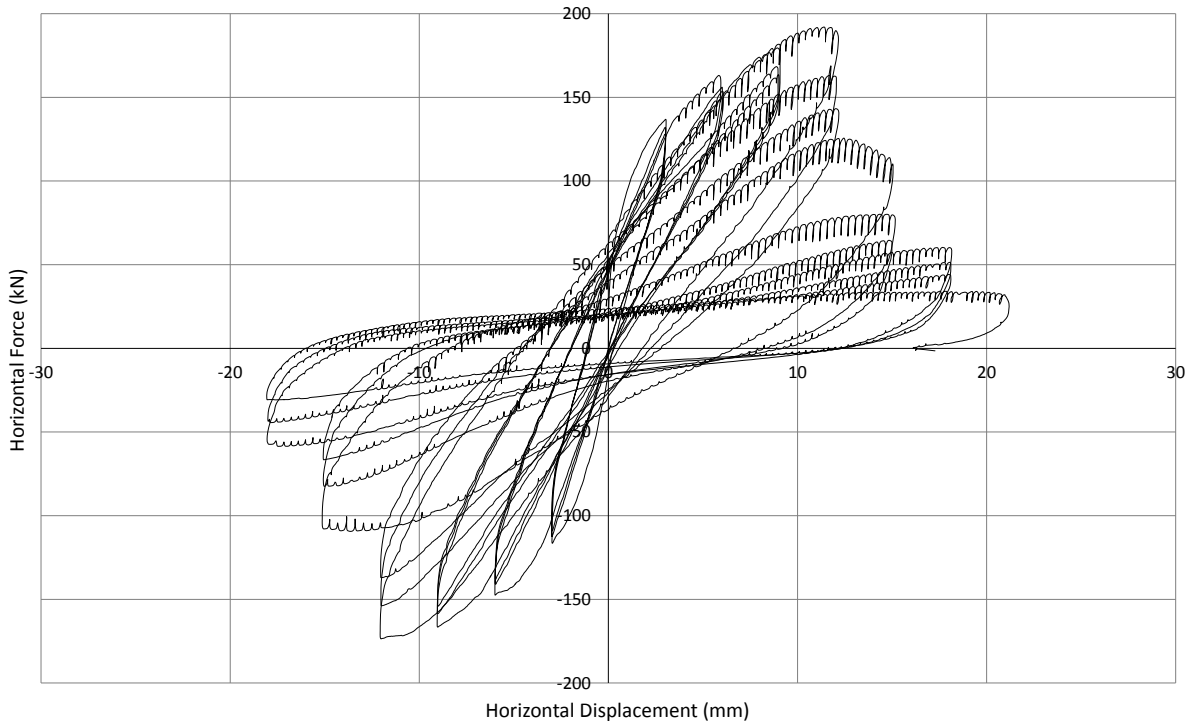


Figure D-5: Response of specimen SC\_2 without smoothing.

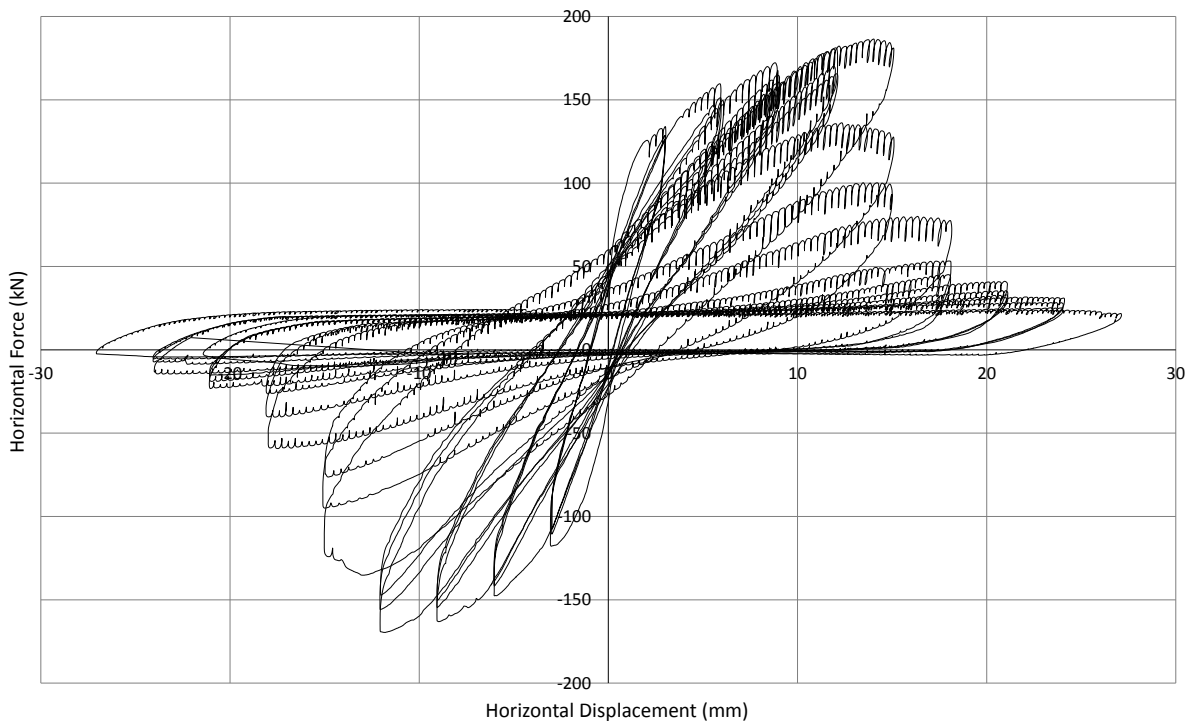


Figure D-6: Response of specimen SC\_3 without smoothing.

## LIST OF REFERENCES

---

- Aboutaha, R.S., Engelhardt, M.D., Jirsa, J.O. & Kreger, M.E. (1999) **“Rehabilitation of Shear Critical Concrete Columns by Use of Rectangular Steel Jackets”**, *ACI Structural Journal*, 96(1), 68-78.
- Adam, C. & Ibarra, L.F. (2014) **“Seismic Collapse Assessment”**, *Encyclopedia of Earthquake Engineering*, Springer-Verlag Berlin Heidelberg 2014. doi: 10.1007/978-3-642-36197-5\_248-1
- American Society of Civil Engineers (ASCE) (2006) **“Seismic Rehabilitation of Existing Buildings”**, *ASCE/SEI 41-06*, American Society of Civil Engineers.
- Applied Technology Council (ATC) (2009) **“Effects of Strength and Stiffness Degradation on Seismic Response”**, *FEMA P440A*, Washington, D.C., USA.
- Arakawa, T., Arai, Y., Mizoguchi, M. & Yoshida, M. (1989) **“Shear Resisting Behavior of Short Reinforced Concrete Columns Under Biaxial Bending-Shear”**, *Transactions of the Japan Concrete Institute*, 11, 317-324.
- ASTM International (2011) **“Standard Test Methods for Cyclic (Reversed) Load Test for Shear Resistance of Vertical Elements of the Lateral Force Resisting Systems for Buildings”**, *Report ASTM E2126-11*, West Conshohocken, PA, www.astm.org. doi:10.1520/E2126-11
- Bairan, J.M. & Mari, A.R. (2007) **“Multiaxial-coupled analysis of RC cross-sections subjected to combined forces”**, *Engineering Structures*, 29(8), 1722–1738. doi:10.1016/j.engstruct.2006.09.007
- Baradaran-Shoraka, M. & Elwood, K.J. (2013) **“Mechanical Model for Non Ductile Reinforced Concrete Columns”**, *Journal of Earthquake Engineering*, 17(7), 937–957. doi:10.1080/13632469.2013.794718
- Berry, M., Parrish, M. & Eberhard, M. (2004) **“PEER Structural Performance Database. User’s Manual (Version 1.2)”**, Pacific Earthquake Engineering Research Center, University of California, Berkeley.
- Bett, B., Klingner, R. & Jirsa, J. (1985) **“Behavior of strengthened and repaired reinforced concrete columns under cyclic deformations”**, *PMFSEL REPORT NO. 85-3*, Phil M. Ferguson Structural Engineering Laboratory, Department of Civil Engineering / Bureau of Engineering Research, The University of Texas at Austin.
- Beyer, K., Dazio, A. & Priestley, M.J.N. (2011) **“Shear Deformations of Slender Reinforced Concrete Walls under Seismic Loading”**, *ACI Structural Journal*, 108(2), 167–177.
- Biskinis, D., Roupakias, G. & Fardis, M. (2004) **“Degradation of shear strength of reinforced concrete members with inelastic cyclic displacements”**, *ACI Structural Journal*, 101(6), 773–783.
- Biskinis, D. & Fardis, M.N. (2013) **“Stiffness and cyclic deformation capacity of circular RC columns with or without lap-splices and FRP wrapping”**, *Bulletin of Earthquake Engineering*, 11(5), 1447–1466. doi:10.1007/s10518-013-9442-7
- Calabrese, A., Almeida, J.P. & Pinho, R. (2010) **“Numerical Issues in Distributed Inelasticity Modeling of RC Frame Elements for Seismic Analysis”**, *Journal of Earthquake Engineering*, 14(S1), 38–68. doi:10.1080/13632461003651869
- Ceresa, P., Petrini, L. & Pinho, R. (2007) **“Flexure-Shear Fiber Beam-Column Elements for Modeling Frame Structures Under Seismic Loading — State of the Art”**, *Journal of Earthquake Engineering*, 11(S1), 46–88. doi:10.1080/13632460701280237

- Ceresa, P., Petrini, L., Pinho, R. & Sousa, R. (2009) **"A fibre flexure–shear model for seismic analysis of RC-framed structures"**, *Earthquake Engineering and Structural Dynamics*, 38(5), 565–586.  
doi:10.1002/eqe.894
- Cervenka, V., Jendele, L. & Cervenka, J. (2016) **"ATENA Program Documentation, Part 1: Theory"**, Praha, Czech Republic.
- Chang, G.A. (1993) **"Seismic energy based damage analysis of bridge columns"**, *PhD Thesis*, University at Buffalo, State University of New York.
- Choi, H. & Kim, J. (2011) **"Progressive collapse-resisting capacity of RC beam–column sub-assembly"**, *Magazine of Concrete Research*, 63(4), 297–310. doi:10.1680/macrc.9.00170
- Coleman, J. & Spacone, E. (2001) **"Localization Issues in Force-Based Frame Elements"**, *Journal of Structural Engineering*, 127(11), 1257–1265. doi:10.1061/(ASCE)0733-9445(2001)127:11(1257)
- Collins, M. & Mitchell, D. (1997) **"Prestressed concrete structures"**, Response Publications, Canada.
- Cotofana, D. & Popa, V. (2009) **"Displacement capacity for shear controlled reinforced concrete columns subjected to cyclic loading. Experimental study"**, *Mathematical Modelling in Civil Engineering*, 1, 5–14.
- Elwood, K. & Moehle, J.P. (2003) **"Shake table tests and analytical studies on the gravity load collapse of reinforced concrete frames"**, *PEER 2003/01*, University of California, Berkeley.
- Elwood, K. (2004) **"Modelling failures in existing reinforced concrete columns"**, *Canadian Journal of Civil Engineering*, 31(5), 846–859. doi:10.1139/1.04-040
- Elwood, K.J. & Moehle, J.P. (2005a) **"Axial capacity model for shear-damaged columns"**, *ACI Structural Journal*, 102(4), 578–587.
- Elwood, K.J. & Moehle, J.P. (2005b) **"Drift Capacity of Reinforced Concrete Columns with Light Transverse Reinforcement"**, *Earthquake Spectra*, 21(1), 71–89. doi:10.1193/1.1849774
- Elwood, K.J. & Moehle, J.P. (2006) **"Idealized Backbone Model for Existing Reinforced Concrete Columns and Comparisons with FEMA 356 Criteria"**, *Structural Design of Tall And Special Buildings*, 15, 553–569. doi:10.1002/tal.382
- Elwood, K.J. & Moehle, J.P. (2008a) **"Dynamic collapse analysis for a reinforced concrete frame sustaining shear and axial failures"**, *Earthquake Engineering & Structural Dynamics*, 37(7), 991–1012. doi:10.1002/eqe.787
- Elwood, K.J. & Moehle, J.P. (2008b) **"Dynamic shear and axial-load failure of reinforced concrete columns. Journal of structural engineering"**, *Journal of Structural Engineering*, 134(7), 1189–1198. doi:10.1061/(ASCE)0733-9445(2008)134:7(1189)
- Esaki, F. (1996) **"Reinforcing effect of steel plate hoops on ductility of R/C square columns"**, In *11th World Conference on Earthquake Engineering*, Acapulco, Mexico, Paper No. 189.
- European Committee for Standardization (CEN) (2004) **"Eurocode 2: Design of concrete structures — Part 1-1: General rules and rules for buildings"**, *EN 1992-1-1: 2004*.
- European Committee for Standardization (CEN) (2005) **"Eurocode 8. Design of structures for earthquake resistance. Part 3: Assessment and retrofitting of buildings"**, *EN 1998-3: 2005*.
- Fardis, M.N. (2014) **"RC Members in Cyclic Loading: Strength, Deformation Capacity, Failure Modes"**, In *8th International Conference AMCM 2014*, Wroclaw, Poland, 23–42.

- Filippou, F.C., Ambrisi, A.D. & Issa, A. (1992) **“Nonlinear Static and Dynamic Analysis of Reinforced Concrete Subassemblages”**, Report No. UCB/EERC 92–08, University of California, Berkeley.
- Filippou, F.C., Gregori, J.N., Sosa, P.M. & Fern, M.A. (2007) **“A 3D numerical model for reinforced and prestressed concrete elements subjected to combined axial, bending, shear and torsion loading”**, *Engineering Structures*, 29(12), 3404–3419. doi:10.1016/j.engstruct.2007.09.001
- General Services Administration (GSA) (2013) **“Alternate Path Analysis & Design Guidelines for Progressive Collapse Resistance”**.
- Ghannoum, W.M., Moehle, J.P. & Bozorgnia, Y. (2008) **“Analytical Collapse Study of Lightly Confined Reinforced Concrete Frames Subjected to Northridge Earthquake Ground Motions”**, *Journal of Earthquake Engineering*, 12(7), 1105–1119. doi:10.1080/13632460802003165
- Ghannoum, W. & Moehle, J. (2012) **“Shake-Table Tests of a Concrete Frame Sustaining Column Axial Failures”**, *ACI Structural Journal*, 109(3), 393–403.
- Ghannoum, W., Saouma, V., Haussmann, G., Polkinghorne, K., Eck, M. & Kang, D.-H. (2012) **“Experimental investigations of loading rate effects in reinforced concrete columns”**, *Journal of Structural Engineering*, 138(8), 1032–1041. doi:10.1061/(ASCE)ST.1943-541X.0000540
- Giberson, M. (1967) **“The response of nonlinear multi-story structures subjected to earthquake excitation”**, *PhD Thesis*, California Institute of Technology, Pasadena, California.
- Griira, M. & Saatcioglu, M. (1996) **“Concrete columns confined with welded reinforcement grids”**, *OCEERC 96-05*, Ottawa Carleton Earthquake Engineering Research Center, Ottawa, Canada.
- Guner, S. & Vecchio, F.J. (2012) **“Simplified Method for Nonlinear Dynamic Analysis of Shear-Critical Frames”**, *ACI Structural Journal*, 109(5), 727–737.
- Haselton, C., Liel, A. & Deierlein, G. (2009) **“Simulating structural collapse due to earthquakes: model idealization, model calibration, and numerical solution algorithms”**, In *COMPADYN 2009 Computational Methods in Structural Dynamics and Earthquake Engineering*, Rhodes, Greece.
- He, Q. & Yi, W. (2008) **“Experimental Study on Collapse-Resistant Behavior of RC Beam-Column Sub-structure considering Catenary Action”**, In *14th World Conference on Earthquake Engineering*, Beijing, China.
- Hellesland, J. & Scordelis, A.C. (1981) **“Analysis of R.C. bridge columns under imposed deformations”**, In *Proceedings of the IABSE Colloquium on advanced mechanics of reinforced concrete*, 545–559.
- Henkhaus, K.W., Ramirez, J.A. & Pujol, S. (2009) **“Simultaneous Shear and Axial Failures of Reinforced Concrete Columns”**, In *ATC & SEI 2009 Conference on Improving the Seismic Performance of Existing Buildings and Other Structures*, San Francisco, California, United States, 536–546.
- Henkhaus, K., Pujol, S. & Ramirez, J. (2013) **“Axial Failure of Reinforced Concrete Columns Damaged by Shear Reversals”**, *Journal of Structural Engineering*, 139(7), 1172–1180. doi:10.1061/(ASCE)ST.1943-541X.0000673.
- Hsu, T.T.C. (1988) **“Softened Truss Model Theory for Shear and Torsion”**, *Structural Journal*, 85(6), 624–635.
- Hsu, T.T.C. (1998) **“Unified Approach to Shear Analysis and Design”**, *Cement and Concrete Composites*, 20(6), 419–435. doi:10.1016/S0958-9465(98)00028-6
- Hsu, T.T.C. & Zhu, R.R.H. (2002) **“Softened Membrane Model for Reinforced Concrete Elements in Shear”**, *ACI structural journal*, 99(4), 460 – 469.

- Huang, X. & Kwon, O. (2015) **“Numerical models of RC elements and their impacts on seismic performance assessment”**, *Earthquake Engineering & Structural Dynamics*, 44(2), 283–298. doi:10.1002/eqe.2471
- International Federation for Structural Concrete (fib) (2010) **“Model Code 2010: First Complete Draft”**.
- Izzuddin, B.A., Vlassis, A.G., Elghazouli, A.Y. & Nethercot, D.A. (2008) **“Progressive collapse of multi-storey buildings due to sudden column loss - Part I: Simplified assessment framework”**, *Engineering Structures*, 30(5), 1308–1318. doi:10.1016/j.engstruct.2007.07.011
- Jahromi, H.Z., Izzuddin, A.B., Nethercot, A.D., Donahue, S., Hadjioannou, M., Williamson, E.B., Engelhardt, M., Stevens, D., Marchand, K. & Waggoner, M. (2012) **“Robustness Assessment of Building Structures under Explosion”**, *Buildings*, 2(4), 497–518. doi:10.3390/buildings2040497
- Kabeyasawa, T., Tasai, A. & Igarashi, S. (2001) **“An economical and efficient method of strengthening reinforced concrete columns against axial load collapse during major earthquake”**, In *The Third U.S.-Japan Workshop on Performance-Based Earthquake Engineering Methodology for Reinforced Concrete Building Structures, PEER 2002/02*, Seattle, Washington, 399–412.
- Kappos, A.J., & Panagopoulos, G. (2011) **“RCCOLA-NET: A computer program for the analysis of the inelastic response of reinforced concrete sections”**, Laboratory of Reinforced Concrete and Masonry Structures, Department of Civil Engineering, Aristotle University of Thessaloniki.
- Kato, D., Zhuzhen, L.I., Yatsutsuka, T. & Nakamura, Y. (2006) **“Axial load capacity of RC columns with various reinforcing details and concrete strength”**, In *1st European Conference on Earthquake Engineering and Seismology*, Geneva, Switzerland, Paper Number: 347, 1–10.
- Kato, D., Miyajima, Y. & Nakamura, Y. (2009) **“Evaluating Method of Deformation at Losing Point of Axial Load Carrying Capacity of RC Columns”**, *Journal of Asian Architecture and Building Engineering*, 8(2), 501–508. doi:10.3130/jaabe.8.501
- Kim, J. & Mander, J. (1999) **“Truss modeling of reinforced concrete shear-flexure behavior”**, *Technical Report MCEER-99-0005*, University at Buffalo, State University of New York, Buffalo, New York.
- Kogoma, I., Hayashida, T. & Minowa, C. (1992) **“Experimental studies on the collapse of RC columns during strong earthquake motions”**, In *10th World Conference on Earthquake Engineering*, Balkema, Rotterdam, Netherlands, 3013–3017.
- Lam, S., Wu, B., Wong, Y., Wang, Z., Liu, Z. & Li, C. (2003) **“Drift capacity of rectangular reinforced concrete columns with low lateral confinement and high-axial load”**, *Journal of Structural Engineering*, 129(6), 733–742. doi:10.1061/(ASCE)0733-9445(2003)129:6(733)
- Leborgne, M.R. (2012) **“Modeling the Post Shear Failure Behavior of Reinforced Concrete Columns”**, *PhD Thesis*. The University of Texas at Austin.
- LeBorgne, M.R. & Ghannoum, W.M. (2013) **“Analytical Element for Simulating Lateral-Strength Degradation in Reinforced Concrete Columns and Other Frame Members”**, *Journal of Structural Engineering*, 140(7), 04014038. doi:10.1061/(ASCE)ST.1943-541X.0000925
- Leborgne, M.R. & Ghannoum, W.M. (2014) **“Calibrated analytical element for lateral-strength degradation of reinforced concrete columns”**, *Engineering Structures*, 81, 35–48. doi:10.1016/j.engstruct.2014.09.030
- Lee, C. & Filippou, F. (2009) **“Efficient beam-column element with variable inelastic end zones”**, *Journal of structural engineering*, 135(11), 1310–1319. doi:10.1061/(ASCE)ST.1943-541X.0000064

- Lee, D. & Elnashai, A. (2001) **“Seismic analysis of RC bridge columns with flexure-shear interaction”**, *Journal of Structural Engineering*, 127(5), 546–553. doi:10.1061/(ASCE)0733-9445(2001)127:5(546)
- Lee, J.-Y. & Watanabe, F. (2003) **“Predicting the longitudinal axial strain in the plastic hinge regions of reinforced concrete beams subjected to reversed cyclic loading”**, *Engineering Structures*, 25(7), 927–939. doi:10.1016/S0141-0296(03)00026-9
- Lejano, B.A., Shirai, N., Adachi, H. & Ono, A. (1992) **“Deformation properties and shear resistance mechanism of reinforced concrete column with high and fluctuating axial force”**, In *10th World Conference on Earthquake Engineering*, Balkema, Rotterdam, Netherlands, 3007–3012.
- Lejano, B.A., Adachi, H., Shirai, N. & Nakanishi, M. (1995) **“Deformation characteristics of RC columns subjected to high and fluctuating axial load”**, *Journal of Structural and Construction Engineering (Transactions of Architectural Institute of Japan)*, 60(467), 93–104. doi:10.3130/aijs.60.93\_1
- Levenberg, K. (1944) **“A method for the solution of certain non-linear problems in least squares”**, *Quarterly of Applied Mathematics*, 2(2), 164 – 168. doi:10.1090/qam/10666
- Lew, H.S., Bao, Y., Pujol, S. & Sozen, M.A. (2014) **“Experimental study of reinforced concrete assemblies under column removal scenario”**, *ACI Structural Journal*, 1119(4), 881–892.
- Li, Y., Lu, X., Guan, H. & Ye, L. (2011) **“Improved tie force method for progressive collapse resistance design of RC frame structures”**, *Engineering Structures*, 33(10), 2931-2942. doi:10.1016/j.engstruct.2011.06.017
- Li, Y., Lu, X., Guan, H. & Ye, L. (2014) **“Progressive Collapse Resistance Demand of Reinforced Concrete Frames under Catenary Mechanism”**, *ACI Structural Journal*, 111(5), 1225–1234.
- Liel, A. (2008) **“Assessing the collapse risk of California’s existing reinforced concrete frame structures: Metrics for seismic safety decisions”**, *PhD Thesis*, Stanford University.
- Lignos, D. & Krawinkler, H. (2012) **“Sidesway collapse of deteriorating structural systems under seismic excitations”**, *John A. Blume Earthquake Engineering Center Technical Report 177*, Stanford Digital Repository.
- Lodhi, M. (2012) **“Seismic Evaluation of Reinforced Concrete Columns and Collapse of Buildings”**, *PhD Thesis*, The Ohio State University.
- Lynn, A.C., Moehle, J.P., Mahin, S.A. & Holmes, W.T. (1996) **“Seismic Evaluation of Existing Reinforced Concrete Building Columns”**, *Earthquake Spectra*, 12(4), 715–739. doi:10.1193/1.1585907
- Lynn, A. (2001) **“Seismic evaluation of existing reinforced concrete building columns”**, *PhD Thesis*, University of California at Berkeley.
- Marini, A. & Spacone, E. (2006) **“Analysis of Reinforced Concrete Elements Including Shear Effects”**, *ACI Structural Journal*, 103(5), 645–656.
- Martinelli, L. (2008) **“Modeling Shear-Flexure Interaction in Reinforced Concrete Elements Subjected to Cyclic Lateral Loading”**, *ACI Structural Journal*, 105(6), 675–684.
- Maruyama, K. & Jirsa, J.O. (1979) **“Shear behavior of reinforced concrete members under bidirectional reversed lateral loading”**, *CESRL Report No. 79-1*, Department of Civil Engineering, Structures Research Laboratory, University of Texas at Austin, Texas.
- Matamoros, A.B. & Von Ramin, M. (2005) **“Estimating the drift ratio at axial load failure of reinforced concrete columns on the basis of a model to calculate shear strength”**, In *Proceedings of the First*

NEES/E-Defense Workshop on Collapse Simulation of Reinforced Concrete Building Structures, PEER Report 2005/10, Berkeley, 261–274.

Matamoros, A., Matchulat, L. & Woods, C. (2008) **“Axial load failure of shear critical columns subjected to high levels of axial load”**, In *14th World Conference on Earthquake Engineering*, Beijing, China.

Matamoros, A. & Woods, C. (2010) **“Drift at Axial Failure of R/C Columns Most Vulnerable to Collapse”**, In *Structures Congress 2010*, Orlando, Florida, United States, 1817–1827. doi:10.1061/41130(369)166

Matchulat, L. (2009) **“Mitigation of collapse risk in vulnerable concrete buildings”**, *MSc Thesis*, University of Kansas.

Matsukawa, K., Maeda, M., Al-Washali, H. & Takahashi, K. (2012) **“Research for Collapse of R/C Frame Composed of Shear and Flexure Column”**, In *15th World Conference on Earthquake Engineering*, Lisbon, Portugal.

Matsukawa, K., Liu, X. & Maeda, M. (2013) **“Process of Collapse for RC Frame Including Shear Column”**, In *10th International Conference on Urban Earthquake Engineering*, Tokyo Institute of Technology, Tokyo, Japan, 817–824.

Mazars, J., Kotronis, P., Ragueneau, F. & Casaux, G. (2006) **“Using multifiber beams to account for shear and torsion. Applications to concrete structural elements”**, *Computer Methods in Applied Mechanics and Engineering*, 195(52), 7264–7281. doi:10.1016/j.cma.2005.05.053

Mazars, J. & Millard, A. (2009) **“Dynamic behavior of concrete and seismic engineering”**, *ISTE Ltd and John Wiley & Sons, Inc.*

Mergos, P. & Kappos, A. (2008) **“A distributed shear and flexural flexibility model with shear–flexure interaction for R/C members subjected to seismic loading”**, *Earthquake Engineering & Structural Dynamics*, 37(12), 1349–1370. doi:10.1002/eqe.812

Mergos, P.E. & Kappos, A.J. (2012) **“A gradual spread inelasticity model for R/C beam–columns, accounting for flexure, shear and anchorage slip”**, *Engineering Structures*, 44, 94–106. doi:10.1016/j.engstruct.2012.05.035

Mergos, P. & Kappos, A. (2013a) **“Analytical study on the influence of distributed beam vertical loading on seismic response of frame structures”**, *Earthquakes and Structures*, 5(2), 239–259.

Mergos, P. & Kappos, A. (2013b) **“Damage Analysis of Reinforced Concrete Structures with Substandard Detailing”**, In M. Papadrakakis, M. Fragiadakis, & V. Plevris (eds.) *Computational Methods in Earthquake Engineering : Volume 2. Computational Methods in Applied Sciences*, 30, 149–176. doi:10.1007/978-94-007-6573-3\_8

Moharrami, M., Koutromanos, I. & Panagiotou, M. (2015) **“Analysis of shear-dominated RC columns using the nonlinear truss analogy”**, *Earthquake Engineering & Structural Dynamics*, 44, 677–694. doi:10.1002/eqe.2480

Mohr, S., Bairán, J.M. & Marí, A.R. (2010) **“A frame element model for the analysis of reinforced concrete structures under shear and bending”**, *Engineering Structures*, 32(12), 3936–3954. doi:10.1016/j.engstruct.2010.09.005

Mostafaei, H. & Kabeyasawa, T. (2007) **“Axial-shear-flexure interaction approach for reinforced concrete columns”**, *ACI Structural Journal*, 104(2), 218–226.

- Murray, J.A. & Sasani, M. (2013) **“Seismic shear-axial failure of reinforced concrete columns vs . system level structural collapse”**, *Engineering Failure Analysis*, 32, 382–401.  
doi:10.1016/j.engfailanal.2013.04.014
- Nagasaka, T. (1982) **“Effectiveness of Steel Fiber as Web Reinforcement in Reinforced Concrete Columns”**, *Transactions of the Japan Concrete Institute*, 4, 493-500.
- Nagasaka, T. (1984) **“Effectiveness of Steel Fiber Reinforcement on Improving Carrying Capacities and Deformation Characteristics of Reinforced Concrete Columns”**, In *8th World Conference on Earthquake Engineering*, 553–560.
- Nakamura, T. & Yoshimura, M. (2002) **“Gravity load collapse of reinforced concrete columns with brittle failure modes”**, *Journal of Asian Architecture and Building Engineering*, 27(3), 21–27.  
doi:10.3130/jaabe.1.21
- Nakamura, T. & Yoshimura, M. (2012) **“Simulation of Old Reinforced Concrete Column Collapse by Pseudo-dynamic Test Method”**, In *15th World Conference on Earthquake Engineering*, Lisbon, Portugal.
- Nakamura, T. & Yoshimura, M. (2014) **“Gravity Load Collapse of Reinforced Concrete Columns with Decreased Axial Load”**, In *2nd European Conference on Earthquake Engineering and Seismology*, Istanbul, Turkey.
- NEHRP Consultants Joint Venture (2010) **“Program Plan for the Development of Collapse Assessment and Mitigation Strategies for Existing Reinforced Concrete Buildings”**, *NIST GCR 10-917-7*.
- Nguyen, X.H. (2005) **“Behaviour of reinforced concrete short columns subjected to multi-directional loading”**, *PhD Thesis*, School of Civil and Environmental Engineering, Nanyang Technological University.
- Ogawa, J., Hoshi, M. & Abe, Y. (1990) **“Crack ratio and spall off ratio of reinforced concrete columns”**, In *8th European Conference on Fracture ECF 8: Fracture Behaviour and Design of Materials and Structures*, Torino, 805–810.
- Ohue, M., Morimoto, H., Fujii, S., and Morita, S. (1985) **“The Behavior of R.C. Short Columns Failing in Splitting Bond-Shear Under Dynamic Lateral Loading”**, *Transactions of the Japan Concrete Institute*, 7, 293-300.
- Ono, A., Shirai, N., Adachi, H. & Sakamaki, Y. (1989) **“Elasto-Plastic Behavior of Reinforced Concrete Column With Fluctuating Axial Force”**, *Transactions of the Japan Concrete Institute*, 11, 239-246.
- Ousalem, H., Kabeyasawa, T., Tasai, A. & Ohsugi, Y. (2002) **“Experimental study on seismic behavior of reinforced concrete columns under constant and variable axial loadings”**, *Proceedings of the Japan Concrete Institute*, 24(2), 229–234.
- Ousalem, H., Kabeyasawa, T., Tasai, A. & Iwamoto, J. (2003) **“Effect of hysteretic reversals on lateral and axial capacities of reinforced concrete columns”**, *Proceedings of the Japan Concrete Institute*, 25(2), 367–372.
- Ousalem, H., Kabeyasawa, T. & Tasai, A. (2004) **“Evaluation of ultimate deformation capacity at axial load collapse of reinforced concrete columns”**, In *13th World Conference on Earthquake Engineering*, Vancouver, B.C., Canada, Paper No. 370.
- Ousalem, H. & Kabeyasawa, T. (2006) **“Drift at axial load failure under cracked-region-sway mechanism for reinforced concrete columns”**, *Proceedings of the Japan Concrete Institute*, 28(2), 223–228.
- Ozcebe, G. & Saatcioglu, M. (1989) **“Hysteretic shear model for reinforced concrete members”**, *Journal of Structural Engineering*, 115(1), 132–148. doi:10.1061/(ASCE)0733-9445(1989)115:1(132)

- Palmisano, F. (2014) **“Mitigation of Progressive Collapse by the Activation of the Elasto-Plastic Catenary Behaviour of R.C. Slab Structures”**, *The Open Construction and Building Technology Journal*, 8, 122–131. doi:10.2174/1874836801408010122
- Pandey, G.R., Mutsuyoshi, H. & Maki, T. (2008) **“Seismic performance of bond controlled RC columns”**, *Engineering Structures*, 30(9), 2538–2547. doi:10.1016/j.engstruct.2008.02.001
- Paulay, T. (1978) **“A consideration of P-delta effects in ductile reinforced concrete frames”**, *Bulletin of the New Zealand Society for Earthquake Engineering*, 11(3), 151–160.
- Perus, I., Biskinis, D., Fajfar, P., Fardis, M.N., Grammatikou, S., Krawinkler, H. & Lignos, D. (2014) **“The SERIES database of RC elements”**, In *2nd European Conference on Earthquake Engineering and Seismology*, Istanbul, Turkey.
- Petrangeli, M., Pinto, P. & Ciampi, V. (1999) **“A Fibre Element for Cyclic Bending and Shear. I: Theory”**, *Journal of Engineering Mechanics*, 125(9), 994–1001. doi:10.1061/(ASCE)0733-9399(1999)125:9(994)
- Pham, T. & Li, B. (2013) **“Seismic Behavior of Reinforced Concrete Columns with Light Transverse Reinforcement under Different Lateral Loading Directions”**, *ACI Structural Journal*, 110(5), 833–844.
- Pilitsis, V.G., Papanikolaou, V.K., Tegos, I.A. & Stylianidis, K.A. (2015) **“A novel mechanism for restraining seismic actions in ductile bridges: analytical modeling and experimental verification”**, In *COMPADYN 2015 Computational Methods in Structural Dynamics and Earthquake Engineering*, Crete Island, Greece.
- Pincheira, J., Dotiwala, F. & D’Souza, J. (1999) **“Seismic analysis of older reinforced concrete columns”**, *Earthquake Spectra*, 15(2), 245–272. doi:10.1193/1.1586040
- Priestley, M., Verma, R. & Xiao, Y. (1994) **“Seismic shear strength of reinforced concrete columns”**, *Journal of Structural Engineering*, 120(8), 2310–2329. doi:10.1061/(ASCE)0733-9445(1994)120:8(2310)
- Ramirez, H. & Jirsa, J.O. (1980) **“Effect of axial load on shear behavior of short RC columns under cyclic lateral deformations”**, *PMFSEL REPORT No. 80-1*, Phil M. Ferguson Structural Engineering Laboratory, Department of Civil Engineering, The University of Texas at Austin.
- Ranzo, G. & Petrangeli, M. (1998) **“A Fibre Finite Beam Element with Section Shear Modelling for Seismic Analysis of RC Structures”**, *Journal of Earthquake Engineering*, 2(3), 443–473. doi:10.1080/13632469809350330
- Ravi Mullapudi, T. & Ayoub, A. (2010) **“Modeling of the seismic behavior of shear-critical reinforced concrete columns”**, *Engineering Structures*, 32(11), 3601–3615. doi:10.1016/j.engstruct.2010.08.004
- Refaeilzadeh, P., Tang, L. & Liu, H. (2009) **“Cross Validation”**, In L. Liu & M. T. Özsu (Eds.), *Encyclopedia of Database Systems* (1st ed), Springer US.
- Reinhorn, A.M., Roh, H., Sivaselvan, M., Kunnath, S.K., Valles, R.E., Madan, A., Li, C., Lobo, R. & Park, Y.J. (2009) **“IDARC2D Version 7.0: A Program for the Inelastic Damage Analysis of Structures”**, *Technical Report MCEER-09-0006*, University at Buffalo, State University of New York, Buffalo, New York.
- Ricles, J., Yang, Y. & Priestley, M. (1998) **“Modeling nonductile R/C columns for seismic analysis of bridges”**, *Journal of Structural Engineering*, 124(4), 415–425. doi:10.1061/(ASCE)0733-9445(1998)124:4(415)
- Roufaiel, M.S.L. & Meyer, C. (1987) **“Analytical Modeling of Hysteretic Behavior of R/C Frames”**, *Journal of Structural Engineering*, 113(3), 429–444. doi:10.1061/(ASCE)0733-9445(1987)113:3(429)
- Saatcioglu, M. & Ozcebe, G. (1989) **“Response of reinforced concrete columns to simulated seismic loading”**, *ACI Structural Journal*, 86(1), 3–12.

- Saatcioglu, M., Alsiwat, J. & Ozcebe, G. (1992) "**Hysteretic behavior of anchorage slip in R/C members**", *Journal of Structural Engineering*, 118(9), 2439–2458. doi:10.1061/(ASCE)0733-9445(1992)118:9(2439)
- Salonikios, T.N., Kappos, A.J., Tegos, I.A. & Penelis, G.G. (1999) "**Cyclic Load Behavior of Low-Slenderness Reinforced Concrete Walls : Design Basis and Test Results**", *ACI Structural Journal*, 96(4), 649–661.
- Saritas, A. & Filippou, F.C. (2009) "**Inelastic axial-flexure–shear coupling in a mixed formulation beam finite element**", *International Journal of Non-Linear Mechanics*, 44(8), 913–922. doi:10.1016/j.ijnonlinmec.2009.06.007
- Sasani, M., Bazan, M. & Sagioglu, S. (2007) "**Experimental and analytical progressive collapse evaluation of actual reinforced concrete structure**", *ACI Structural Journal*, 104(6), 731–739.
- Sasani, M. & Sagioglu, S. (2008) "**Progressive Collapse Resistance of Hotel San Diego**", *Journal of Structural Engineering*, 134(3), 478–488. doi:10.1061/(ASCE)0733-9445(2008)134:3(478)
- Sasani, M. & Sagioglu, S. (2010) "**Gravity load redistribution and progressive collapse resistance of 20-story reinforced concrete structure following loss of interior column**", *ACI Structural Journal*, 107(6), 636–644.
- Scott, M.H. & Fenves, G.L. (2006) "**Plastic Hinge Integration Methods for Force-Based Beam – Column Elements**", *Journal of Structural Engineering*, 132(2), 244–252. doi:10.1061/(ASCE)0733-9445(2006)132:2(244)
- Sezen, H. (2000) "**Seismic behavior and modeling of reinforced concrete building columns**", *PhD Thesis*, University of California, Berkeley.
- Sezen, H. & Moehle, J. (2004) "**Shear strength model for lightly reinforced concrete columns**", *Journal of Structural Engineering*, 130(11), 1692–1703. doi:10.1061/(ASCE)0733-9445(2004)130:11(1692)
- Sezen, H. & Moehle, J. (2006) "**Seismic tests of concrete columns with light transverse reinforcement**", *ACI structural journal*, 103(6), 842–849.
- Sezen, H. (2008) "**Shear deformation model for reinforced concrete columns**", *Structural Engineering and Mechanics*, 28(1), 39–52. doi:10.12989/sem.2008.28.1.039
- Sezen, H. & Chowdhury, T. (2009) "**Hysteretic model for reinforced concrete columns including the effect of shear and axial load failure**", *Journal of Structural Engineering*, 135(2), 139–146. doi:10.1061/(ASCE)0733-9445(2009)135:2(139)
- Sivaselvan, M. & Reinhorn, A. (1999) "**Hysteretic models for cyclic behavior of deteriorating inelastic structures**", *Technical Report MCEER-99-0018*, University at Buffalo, State University of New York, Buffalo, New York.
- Shirai, N., Lejano, B.A., Adachi, H. & Nakanishi, M. (1996) "**Flexure and shear behavior of high strength reinforced concrete column subjected to high and fluctuating axial load**", In *11th World Conference on Earthquake Engineering*, Acapulco, Mexico, Paper No. 1199.
- Simpson, B. & Matamoros, A. (2012) "**Criteria for Evaluating the Effect of Displacement History and Span-to-Depth Ratio on the Risk of Collapse of R/C Columns**", In *15th World Conference on Earthquake Engineering*, Lisbon, Portugal.
- Soleimani, D., Popov, E. & Bertero, V. (1979) "**Nonlinear Beam Model for R/C Frame Analysis**", In *Proceedings of 7th Conference on Electronic Computation*, Structural Division ASCE, Washington, 483-509.

- Spacone, E., Filippou, F. & Taucer, F. (1996) "**Fibre beam-column model for non-linear analysis of R/C frames: Part I. Formulation**", *Earthquake Engineering & Structural Dynamics*, 25(7), 711–725. doi:10.1002/(SICI)1096-9845(199607)25:7<711::AID-EQE576>3.0.CO;2-9
- Starossek, U. (2009) "**Progressive collapse of structures**", Thomas Telford Ltd.
- Tagami, J., Suzuki, N., Kaneko, T. & Maruta, M. (2005) "**Dynamic loading test of reinforced concrete columns for identification of strain rate effect**", In *1st NEES/E-Defense Workshop on Collapse Simulation of Reinforced Concrete Building Structures*, Berkeley, California, 291–304.
- Takayanagi, T., Derecho, A. T., and Corley, W. G. (1979) "**Analysis of inelastic shear deformation effects in R/C structural wall systems**", In *Proceedings of the Nonlinear Design of R/C Structures, CSCE-ASCE-ACI-FIB International Symposium, University of Waterloo Press, Waterloo, Ontario, Canada*, 545-579.
- Thom, C. (1983) "**The Effects of Inelastic Shear on the Seismic Response of Structures**", *PhD Thesis*, University of Auckland.
- Tran, C.T.N. (2010) "**Experimental and analytical studies on the seismic behavior of reinforced concrete columns with light transverse reinforcement**", *PhD Thesis*, Nanyang Technological University.
- Tran, C.T.N. & Li, B. (2013) "**Ultimate displacement of reinforced concrete columns with light transverse reinforcement**", *Journal of Earthquake Engineering*, 17(2), 282–300. doi:10.1080/13632469.2012.730117
- Uchida, Y. & Uezono, Y. (2003) "**Judging collapse of SRC and RC columns failed by shear**", *Journal of Structural and Construction Engineering (Transactions of Architectural Institute of Japan)*, 68(566), 177–184. doi:10.3130/aijs.68.177\_2
- Umehara, H. & Jirsa, J.O. (1982) "**Shear strength and deterioration of short reinforced concrete columns under cyclic deformations**", *PMFSEL REPORT No. 82-3*, Phil M. Ferguson Structural Engineering Laboratory, Department of Civil Engineering, The University of Texas at Austin.
- Umemura, H. & Ichinose, T. (2004) "**Experimental study on the effects of loading history on the ductility capacity of reinforced concrete members**", In *13th World Conference on Earthquake Engineering*, Vancouver, B.C., Canada, Paper No. 1301.
- Valles, R.E., Reinhorn, A.M., Kunnath, S.K., Li, C. & Madan, A. (1996) "**IDARC2D, Version 4.0 : A Computer Program for the Inelastic Damage Analysis of Buildings**", *Technical Report NCEER-96-0010*, University at Buffalo, State University of New York, Buffalo, New York.
- Vecchio, F. & Collins, M. (1986) "**The modified compression-field theory for reinforced concrete elements subjected to shear**", *ACI Journal Proceedings*, 83(2), 219–231.
- Vecchio, F.J. & Emara, M.B. (1992) "**Shear Deformations in Reinforced Concrete Frames**", *ACI Structural Journal*, 89(1), 46–56.
- Vlassis, A.G., Izzuddin, B.A., Elghazouli, A.Y. & Nethercot, D.A. (2008) "**Progressive collapse of multi-storey buildings due to sudden column loss - Part II: Application**", *Engineering Structures*, 30(7), 1424–1438. doi:10.1016/j.engstruct.2007.08.011
- Wibowo, A. (2013) "**Drift Capacity of Lightly Reinforced Soft Storey Structures**", *Jurnal Rekayasa Sipil*, 7(2), 166–177.
- Wibowo, A., Wilson, J. L., Lam, N. T. K. & Gad, E. F. (2014) "**Drift performance of lightly reinforced concrete columns**", *Engineering Structures*, 59, 522–535. doi:10.1016/j.engstruct.2013.11.016

- Wilson, E. (2002) **“Three dimensional static and dynamic analysis of structures: a physical approach with emphasis on earthquake engineering - Third Edition”**, *Computers & Structures, Inc.*, Berkeley, California, USA.
- Woods, C. (2009) **“Displacement demand effects in vulnerable reinforced concrete columns”**, *MSc Thesis*, University of Kansas.
- Woods, C. & Matamoros, A. (2010) **“Effect of Longitudinal Reinforcement Ratio on the Failure Mechanism of R/C Columns Most Vulnerable to Collapse”**, In *9th US National Conference and 10th Canadian Conference on Earthquake Engineering*, Toronto, Canada.
- Wu, C., Kuo, W.W., Yang, Y.Y., Hwang, S., Elwood, K.J., Loh, C. & Moehle, J.P. (2008a) **“Collapse of a nonductile concrete frame: Shaking table tests”**, *Earthquake Engineering & Structural Dynamics*, 38(2), 205–224. doi:10.1002/eqe.853
- Wu, C., Su, R., Hwang, S. & Yang, Y. (2008b) **“Shake Table Tests on Reinforced Concrete Short Columns Failing in Shear”**, In *14th World Conference on Earthquake Engineering*, Beijing, China.
- Xiao, Y. & Martirosyan, A. (1998) **“Seismic Performance of High-Strength Concrete Columns”**, *Journal of Structural Engineering*, 124(3), 241-251. doi:10.1061/(ASCE)0733-9445(1998)124:3(241)
- Xiao, Y. & Yun., H.W. (2002) **“Experimental studies on full-scale high-strength concrete columns”**, *ACI Structural Journal* 99(2), 199-207.
- Xu, G. & Ellingwood, B.R. (2011) **“An energy-based partial pushdown analysis procedure for assessment of disproportionate collapse potential”**, *Journal of Constructional Steel Research*, 67(3), 547–555. doi:10.1016/j.jcsr.2010.09.001
- Yi, W., He, Q., Xiao, Y. & Kunnath, S.K. (2008) **“Experimental Study on Progressive Collapse Resistance of Reinforced Concrete Frame Structures”**, *ACI Structural Journal*, 105(4), 433–439.
- Yoshimura, M. & Yamanaka, N. (2000) **“Ultimate limit state of RC columns”**, In *The Second U.S.-Japan Workshop on Performance-Based Earthquake Engineering Methodology for Reinforced Concrete Building Structures*, PEER 2000/10, Sapporo, Hokkaido, Japan, 313–328.
- Yoshimura, M. & Nakamura, T. (2002) **“Axial collapse of reinforced concrete short columns”**, In *The Fourth US-Japan Workshop on Performance-Based Earthquake Engineering Methodology for Reinforced Concrete Building Structures*, PEER 2002/21, Toba, Japan, 187–198.
- Yoshimura, M., Takaine, Y. & Nakamura, T. (2003) **“Collapse drift of reinforced concrete columns”**, In *The Fifth U.S.-Japan Workshop on Performance-Based Earthquake Engineering Methodology for Reinforced Concrete Building Structures*, PEER 2003/11, Hakone, Japan, 239–253.
- Yoshimura, M., Takaine, Y. & Nakamura, T. (2004) **“Axial collapse of reinforced concrete columns”**, In *13th World Conference on Earthquake Engineering*, Vancouver, B.C., Canada, Paper No. 1699.
- Yoshimura, M. (2008) **“Formulation of Post-Peak Behavior of old Reinforced Concrete Columns until Collapse”**, In *14th World Conference Earthquake Engineering*, Beijing, China.
- Yu, J. & Tan, K.H. (2013) **“Experimental and numerical investigation on progressive collapse resistance of reinforced concrete beam column sub-assemblages”**, *Engineering Structures*, 55, 90–106. doi:10.1016/j.engstruct.2011.08.040
- Zhou, X., Higashi, Y., Jiang, W. & Shimizu, Y. (1985) **“Behavior of Reinforced Concrete Column Under High Axial Load”**, *Transactions of the Japan Concrete Institute*, 7, 385-392.

Zhou, X., Satoh, T., Jiang, W., Ono, A. & Shimizo, Y. (1987) "**Behavior of Reinforced Concrete Short Column Under High Axial Load**", *Transactions of the Japan Concrete Institute*, 9, 541-548.

Zhu, L., Elwood, K.J. & Haukaas, T. (2007) "**Classification and seismic safety evaluation of existing reinforced concrete columns**", *Journal of Structural Engineering*, 133(9), 1316–1330.

doi:10.1061/(ASCE)0733-9445(2007)133:9(1316)

Zimos, D.K., Mergos, P.E. & Kappos, A.J. (2015) "**Shear Hysteresis Model for Reinforced Concrete Elements Including the Post-Peak Range**", In *COMPADYN 2015 Computational Methods in Structural Dynamics and Earthquake Engineering*, Crete Island, Greece.

Zimos, D.K., Papanikolaou, V.K., Mergos, P.E. & Kappos, A.J. (2016) "**Effect of Axial Load Redistribution in Progressive Collapse of Existing R/C Structures**", In *National Conference on Concrete Structures*, Thessaloniki, Greece.